Slow-wave substrate integrated waveguides for applications in RF and millimeter-wave frequency bands

Matthieu Bertrand

UNIVERSITÉ DE GRENOBLE

THÈSE

Pour obtenir le grade de

DOCTEUR DE LA COMMUNAUTÉ UNIVERSITÉ GRENOBLE ALPES

Spécialité : **NANO ELECTRONIQUE ET NANO TECHNOLOGIES**

Arrêté ministériel : 25 mai 2016

Présentée par

Matthieu BERTRAND

Thèse dirigée par **Philippe FERRARI** et **Emmanuel PISTONO,**
Co-encadrée par Darine KADDOUR et Vincent PUYAL
préparée au sein du **Laboratoire IMEP-LAHC**
dans **l'École Doctorale E.E.A.T.S**

Guides à ondes lentes intégrés dans le substrat pour les applications en bandes RF et millimétriques

Thèse soutenue publiquement le **09 Novembre 2017**,
devant le jury composé de :

M. Stéphane BILA
Directeur de recherche CNRS, XLIM, Limoges, Président du jury
M. Hervé AUBERT
Professeur à l'Institut National Polytechnique de Toulouse, Rapporteur
M. Maurizio BOZZI
Professeur à l'Université de Pavie, Rapporteur
Mme. Anne-Laure FRANC
Maître de conférences à l'Institut National Polytechnique de Toulouse, Examinatrice
M. Philippe FERRARI
Professeur à l'Université Grenoble-Alpes, Membre
M. Emmanuel PISTONO
Maître de conférences à l'Université Grenoble-Alpes, Membre
Mme. Darine KADDOUR
Maître de conférences à l'Institut National Polytechnique de Grenoble, Membre
M. Vincent PUYAL
Ingénieur de recherche au CEA-LETI, Membre invité
Mme. Edith CLAVEL
Maître de conférences à l'Université Grenoble-Alpes, Membre invité
M. Hervé LEGAY
Expert Ingénierie Antennes, THALES Alenia Space, Membre invité
M. Laurent PETIT
Responsable Projet R&T, Expert Hyperfréquences, RADIALL, Membre Invité

To my parents, family, friends and the One who made all things...

First of all, I would like to express my special appreciation and thanks to Prof. Philippe Ferrari, Dr. Emmanuel Pistono, as well as Dr. Darine Kaddour and Dr. Vincent Puyal. It was a true pleasure to work under your supervision, you have been an incredible source of motivation all along the way. Thank you for allowing me to grow as a young researcher, I learned so much thanks to your competence and attention.

I believe that this work is also the result of multiple and rich interactions with other members of the radio-frequency research group, thank you to all of them for the great scientific atmosphere they have built over the years. I would also like to thank M. Nicolas Corrao for his patience and useful support during the measurement campaigns.

A significant part of this work relies on strong partnership with foreign research teams, for that I am especially grateful to Mehmet Kaynak, Ariana Serrano and Gustavo Rehder for their trust and support.

I would like to thank my office mates and friends in IMEP LAHC, Isaac Silva, Frédéric Parment, Zyad Iskandar, Ayssar Serhan, Anh Tu Ho, Cyril Guers, Ramin Kayatzadeh, Vipin Velayudhan, Victoria Nasserdine, Pierre Ferris, Alessandro Niembro, Giuseppe Acri, Mohamad Awad, Hamza Hallak, Ekta Sharma and so on. It was a great pleasure to work alongside you.

Thank you to all my friends for the joy and encouragement that you shared with me in so many occasions. Especially, I would like to thank Samuel and Corentin for always supporting me in the pursuit of my ambitions.

I would like to thank my sister Johanna and her husband Bastien, you were always there to support me and you refreshed my motivation many times. Your wonderful daughter Elia is yet too young to read these lines, still her vibrant happiness was a powerful boost when I needed it the most. I also would like to thank my brother Jérémie, your sincere encouragements up to to the final months were precious, even as you were far away.

Finally, I owe my deepest gratitude to my parents, Claudie and Régis. Thank you for your unfailing love and support. This work closes a chapter of my life, you made all of it possible through countless sacrifices.

Matthieu Bertrand

The second half of the twentieth century has seen major technological progress taking place in our modern societies. The emergence of the telecommunication networks could be one of the most visible. Thanks to a great number of scientific and technological breakthroughs, these networks have evolved toward greater complexity and efficiency. As a result, in these two last decades the consumer electronic market has become economically significant. Furthermore, its development has also created new services, which in turn became new activities.

The current trend is mainly driven by the increasing demand of high-definition multimedia applications. In practice, that means greater data rates and larger frequency bandwidths. In order to provide such bandwidths the next generations of wireless communications are oriented toward the higher frequencies, especially the millimeter-wave bands. In fact, because higher frequency waves are more rapidly attenuated in free-space than their low-frequency counterparts, the future networks will also have to reduce emitter to receiver distance. Therefore, the number of so-called base stations will dramatically increase.

From the technology point-of-view, all these evolutions lead to emerging new challenges. More precisely, the wireless transmission circuits will have to be able to operate at high frequencies with reasonable efficiencies, rely on a low-cost technologies and compact solutions. In this context, a technology developed since nearly fifteen years, the substrate integrated waveguide (SIW), has progressively emerged as one of the promising waveguide topologies for antennas, filters and other passive components. Based on low-cost fabrication process, it overcomes many limitations of the conventional planar transmission lines such as interference sensitivity, reduced quality factor at higher frequencies and power handling restrictions. Also, as an integrated version of the conventional rectangular waveguides, it benefits from nearly half a century of theoretical and technological research and development legacy.

However, one of the limiting characteristics of the substrate integrated waveguide is its dimensions, especially at lower frequencies. As a result, the miniaturization techniques dedicated to this technology remain an active field of research. In this context, this work focuses on the development of miniaturized passive circuits such as filters, couplers and waveguides. First, a miniaturization technique based on the use of slow-wave propagation is studied for printed circuits technology at frequencies below 20 GHz. Secondly, as a first step toward the application of the same principle at very high frequencies in advanced technologies, two different technological solutions for the realization of integrated waveguides on interposers are proposed. The first one is based on the use of copper nano-wires grown inside an alumina nano-porous membrane. The second one is based on the through-silicon-via technology and applied on high-resistivity silicon wafers. These two separate technologies are developed in collaboration with the University of Sao Paulo, Brazil, and the IHP institute in Germany, respectively.

The first chapter is an introduction, which lays down the fundamental electromagnetism equations which are the basis of this work. It also provides an historical background on waveguide technology and slow-wave structures.

The second chapter describes the slow-wave substrate integrated waveguide (SW-SIW) topology in detail as well as the underlying principles of operation. Some the-

oretical derivations are presented as well as parametric analysis of its performance. These theoretical derivations are developed in a general context, not only dedicated to substrate integrated waveguide topology. Hence, they could be useful for further application to other kind of slow-wave structures.

Then, chapter 3 and 4 are dedicated to the description of design methods for non-resonant and resonant passive circuits, respectively. In chapter 3, the design of couplers in both SIW and SW-SIW is presented along with measurements. In chapter 4, the same procedure is applied to the synthesis of coupled cavity filters.

Finally, chapter 5 is dedicated to the integration of waveguides on interposer technologies. Because of process requirements, layered waveguides with thickness disparities and dielectric constant variations have to be considered. In order to confirm the results of commercial simulation software, a theoretical and numerical analysis of the propagation was therefore developed. Then, test features are designed and measurement results are presented.

Contents

1 Introduction **1**

1.1 Theoretical framework . . . 2

1.1.1 Maxwell's equations . . . 2

1.1.2 Transmission lines . . . 5

1.1.3 Waveguides . . . 6

1.2 Technological context, the integration of rectangular waveguides . . . 7

1.2.1 Origin, principle and main applications of rectangular waveguides 7

1.2.2 The integrated rectangular waveguide . . . 11

1.2.3 Beyond integration, the miniaturization techniques . . . 14

1.3 The slow-wave concept, a tool for the miniaturization of integrated waveguides . . . 18

1.3.1 General considerations . . . 18

1.3.2 Historical background and main applications . . . 21

1.3.3 The existing slow-wave topologies for SIW . . . 23

1.4 Conclusion . . . 23

References . . . 25

2 Theoretical description of a Slow-Wave Substrate Integrated Waveguide Technology **35**

2.1 Introduction . . . 36

2.2 General considerations . . . 36

2.2.1 Useful properties of periodic structures . . . 36

2.2.2 Velocity, stored energy and transmitted power . . . 38

2.2.3 Increased dissipation, a consequence of the velocity reduction . . . 40

2.2.4 In practice: the required spatial energies separation . . . 42

2.2.5 Discussion . . . 46

2.3 Slow-wave effect induced by a uniform distribution of blind via holes in a parallel-plate waveguide configuration . . . 47

2.3.1 Definition of the topology and associated simulation methods . . . 47

2.3.2 Physical properties . . . 50

2.3.3 Parametric analysis for large wavelengths . . . 57

2.4 A Slow-wave substrate integrated waveguide . . . 62

2.4.1 Motivations and modelling . . . 62

2.4.2 Electrical performance . . . 63

2.4.3 Brief parametric analysis . . . 65

2.4.4 Design rules . . . 68

2.5 Conclusion . . . 70

References . . . 71

3 Miniaturization of non resonant circuits in X-band 73
3.1 Introduction . . . 74
3.1.1 Motivations behind the resonant/non-resonant circuits distinction 74
3.1.2 Overview of SIW coupler technologies . . . 74
3.2 Design of couplers in SIW and SW-SIW technologies in X-band . . . 76
3.2.1 Short-slot coupler principle of operation and theory . . . 76
3.2.2 Design in SIW technology . . . 78
3.2.3 Design in SW-SIW technology . . . 83
3.3 Measurement results and retro-simulations . . . 94
3.3.1 Measurement results . . . 94
3.3.2 Fabrication process variations and retro-simulations . . . 97
3.4 Conclusion . . . 102
References . . . 103

4 Miniaturization of resonant circuits in X-band 107
4.1 Introduction . . . 108
4.1.1 Overview of SIW filter technologies . . . 108
4.1.2 Slow-wave topology for the miniaturization of SIW filters . . . 111
4.2 Implementation of a synthesis method in SIW technology . . . 112
4.2.1 Global description . . . 112
4.2.2 Implementation and verification . . . 117
4.3 Development of the synthesis method in SW-SIW technology . . . 123
4.3.1 Application of the classical synthesis method . . . 123
4.3.2 Homogenisation of the blind-via distribution . . . 127
4.3.3 Development of a segmentation algorithm for fast optimization . 131
4.3.4 Algorithmic implementation . . . 139
4.4 Measurement results and perspectives . . . 141
4.4.1 5^{th}-order, 1 GHz bandwidth filter in SW-SIW technology . . . 141
4.4.2 5^{th}-order, 0.5 GHz bandwidth filter in SW-SIW technology . . . 142
4.4.3 3-rd order, 1 GHz bandwidth filter in HM-SW-SIW technology . 143
4.4.4 Retro-simulation based on fabrication issues and perspectives . . 144
4.5 Conclusion . . . 147
References . . . 148

5 Integration of waveguides in advanced technologies for millimeter-wave frequencies 151
5.1 Introduction . . . 152
5.2 Analytical modelling of inhomogeneous integrated waveguides and numerical resolution . . . 153
5.2.1 The solution of Maxwell's equations in inhomogeneous rectangular waveguides . . . 154
5.2.2 Numerical resolution strategy and algorithm definition . . . 156
5.3 Validation of the implemented resolution . . . 162
5.3.1 The IHP HR-Si interposer technology . . . 162
5.3.2 The MnM interposer technology . . . 167

5.4 Design of test features on IHP interposer . . . 169
5.4.1 Broadband transitions from G-CPW to integrated waveguide . . 169
5.4.2 0-dB and 3-dB Couplers . . . 173
5.5 Design of test features on the Nano-porous Alumina Membrane interposer as an alternative to the TSV process . . . 176
5.5.1 Broadband transition from G-CPW to integrate waveguide . . . 177
5.5.2 Other passive circuits . . . 178
5.5.3 Measurement results . . . 179
5.6 Prospects and conclusion . . . 185
References . . . 186

6 Conclusion **189**

Chapter 1

Introduction

Contents

1.1 Theoretical framework 2

1.1.1 Maxwell's equations 2

1.1.2 Transmission lines 5

1.1.3 Waveguides 6

1.2 Technological context, the integration of rectangular waveguides 7

1.2.1 Origin, principle and main applications of rectangular waveguides 7

1.2.2 The integrated rectangular waveguide 11

1.2.3 Beyond integration, the miniaturization techniques 14

1.3 The slow-wave concept, a tool for the miniaturization of integrated waveguides 18

1.3.1 General considerations 18

1.3.2 Historical background and main applications 21

1.3.3 The existing slow-wave topologies for SIW 23

1.4 Conclusion 23

References 25

In this first chapter, the aim is to place the work of this thesis into its context. Firstly, section 1.1 will be dedicated to the fundamental electromagnetism equations in order to introduce the notions of wave and propagation. The practical implementation of structures carrying such waves will then be detailed, making the distinction between transmission lines and waveguides.

Secondly, the historical background of waveguide development will be given in section 1.2, leading to the concept of integration and modern high frequency electronics. In this part, the integrated form of the rectangular waveguide will be presented. While offering significant advantages, its miniaturization remains a necessity, this is why several miniaturization techniques have been developed and will be explained here.

Finally, coming to the subject of this work, the slow-wave principle will be described, and placed in its historical context in section 1.3. As an alternative miniaturization technique, existing topologies will be detailed and a conclusion will be given.

1.1 Theoretical framework

1.1.1 Maxwell's equations

Electromagnetism theory relies on a set of four differential equations which can be expressed in local form by (1.1)-(1.4). They were first established in 1864 by Scottish physicist James Clerk Maxwell (1831-1879) under a different formulation of 20 equations of 20 variables. Maxwell effort was aimed at giving a mathematical formulation of Faraday's principles regarding electricity and magnetism. In 1881, Olivier Heaviside (1850-1925) reduced the complexity down to four equations, now commonly known as Maxwell's equations.

$$\boldsymbol{\nabla} \cdot \boldsymbol{\mathcal{D}} = \rho \tag{1.1}$$

$$\boldsymbol{\nabla} \cdot \boldsymbol{\mathcal{B}} = 0 \tag{1.2}$$

$$\boldsymbol{\nabla} \times \boldsymbol{\mathcal{H}} = \boldsymbol{\mathcal{J}} + \frac{\partial \boldsymbol{\mathcal{D}}}{\partial t} \tag{1.3}$$

$$\boldsymbol{\nabla} \times \boldsymbol{\mathcal{E}} = -\frac{\partial \boldsymbol{\mathcal{B}}}{\partial t} \tag{1.4}$$

This set of equations relates several physical quantities. First it deals with the magnetic field $\boldsymbol{\mathcal{H}}$, electric field $\boldsymbol{\mathcal{E}}$ as well as magnetic and electric flux densities $\mathbf{B}$ and $\mathbf{D}$ (also called displacement vector). Electrical charges contributions are introduced through the current density $\boldsymbol{\mathcal{J}}$ and charge density ρ. In order to have a complete definition of the electromagnetic problem, constitutive relations (1.5)-(1.6) are necessary, they provide the relation between field quantities and flux densities (or inductions) for a given material, in this case it is assumed isotropic and homogeneous.

$$\boldsymbol{\mathcal{D}} = \varepsilon \boldsymbol{\mathcal{E}} \tag{1.5}$$

$$\boldsymbol{\mathcal{B}} = \mu \boldsymbol{\mathcal{H}} \tag{1.6}$$

In these two relations, ε and μ are respectively called electrical permittivity and magnetic permeability. For dielectric materials, one usually define for simplicity the relative permittivity ε_r as the ratio between its actual permittivity ε and that of the vacuum ε_0. For a lossless material, both ε and μ are real numbers. Most of existing materials exhibit only dielectric losses, a complex permittivity written as $\varepsilon = \varepsilon' - j\varepsilon''$ is therefore adopted. The contribution of the imaginary part of ε is described by its so-called loss-tangent $\tan\delta$ defined in equation (1.7).

$$\tan\delta = \frac{\omega\varepsilon'' + \sigma}{\omega\varepsilon'} \tag{1.7}$$

For all the work presented here, a steady state harmonic regime is assumed so that the four Maxwell equations can be conveniently expressed using complex notations (1.8)-(1.11). In that case, all vector field, current and charges density quantities are replaced by their equivalent complex quantities $\boldsymbol{E}$, $\boldsymbol{H}$, $\boldsymbol{D}$, $\boldsymbol{B}$, $\boldsymbol{J}$ and ρ. For simplicity the complex charge density is still written ρ. The time-derivative operation is then equivalent to a multiplication by a factor $j\omega$, where ω is the angular frequency.

$$\boldsymbol{\nabla} \cdot \boldsymbol{D} = \rho \tag{1.8}$$

$$\boldsymbol{\nabla} \cdot \boldsymbol{B} = 0 \tag{1.9}$$

$$\boldsymbol{\nabla} \times \boldsymbol{H} = \boldsymbol{J} + j\omega\boldsymbol{D} \tag{1.10}$$

$$\boldsymbol{\nabla} \times \boldsymbol{E} = -j\omega\boldsymbol{B} \tag{1.11}$$

Let now assume a free-of-charge medium, so that both $\boldsymbol{J}$ and ρ disappear from the equations. One of the great contributions of Maxwell was the introduction of the displacement vector $\boldsymbol{\mathcal{D}}$ in the equations. Interestingly enough, it provided the coupling between the two curl equations (1.10)-(1.11) necessary to establish the possibility of electromagnetic wave propagation. To highlight this fact, let's take the curl of (1.10):

$$\boldsymbol{\nabla} \times (\boldsymbol{\nabla} \times \boldsymbol{H}) = j\omega\boldsymbol{\nabla} \times \boldsymbol{D} \tag{1.12}$$

Then, by applying (1.5) and (1.6) to (1.11) we have :

$$\boldsymbol{\nabla} \times \boldsymbol{D} = -j\omega\varepsilon\mu\boldsymbol{H} \tag{1.13}$$

As a consequence, vector identity (1.14) applied to the left term of (1.12) leads to (1.15), the divergence of magnetic field being zero.

$$\boldsymbol{\nabla} \times (\boldsymbol{\nabla} \times \boldsymbol{A}) = \boldsymbol{\nabla}(\boldsymbol{\nabla} \cdot \boldsymbol{A}) - \boldsymbol{\nabla}^2\boldsymbol{A} \tag{1.14}$$

$$\left[\boldsymbol{\nabla}^2 + \mu\varepsilon\omega^2\right]\boldsymbol{H} = 0 \tag{1.15}$$

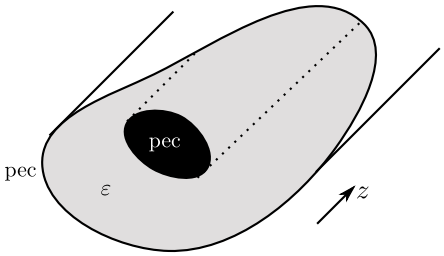

Figure 1.1 – General form of a closed uniform waveguide.

This last equation could also be obtained for the electric field, it is a well-known propagation equation which has for solution waves propagating at a velocity $c = (\varepsilon\mu)^{-1/2}$. In other words, Maxwell equations predict the propagation of electromagnetic fields at a velocity defined by the medium properties ε and μ.

The focus of this work will be on guided waves, which mean that we are interested in confining the electromagnetic field in a limited area of space delimited by boundary conditions. In practice, such a confinement is used to carry electromagnetic energy from one point to another with low attenuation. In fact, the use of guided waves is dominant in electronics, that is because any circuit rely on the information to be transferred from one point to another in a well-controlled manner.

Several structures realize this function in electronics. Most of these structures are uniform, which means that the boundary conditions are independent of the longitudinal coordinate, for instance z as illustrated in Figure 1.1 for a closed structure. Ideally, it is only made of perfect electric conductors (pec) and an ideal dielectric.

In this case, the problem boils down to the analysis of the cross-section, i.e in planes defined by $z = C^{te}$. Based on these hypothesis, an electromagnetic wave will propagate accordingly to specific field patterns, called "modes of propagation". A mode represents a certain field distribution which is solution of Maxwell equations considering the proper boundary conditions. From the mathematical point of view, a mode can be defined by a frequency-dependant complex number γ called propagation constant. Accordingly, all field components of the mode will follow along z a variation in $exp(-\gamma z)$. Its real part, the attenuation constant α, reflects the dissipation while the imaginary part β is the phase constant, related to the guided wavelength λ by $\beta = 2\pi/\lambda$. As we will see, the guided wavelength is a function of frequency but also takes into account the boundary conditions. It can strongly differ from the free-space wavelength $\lambda_0 = c/f$, where c is the light velocity in the considered medium.

In fact, by separating variations in the transverse section and longitudinal directions the derivation of (1.15) can readily lead to the so-called dispersion relation [1–3]:

$$\beta^2 = k^2 - k_c^2 = \left(\frac{\omega}{c}\right)^2 - k_c^2 \tag{1.16}$$

In this equation, the longitudinal phase constant β is related to the angular frequency $\omega = 2\pi f$ and a fixed wavenumber k_c called cut-off wavenumber. The latter can be expressed as a function of the cut-off frequency ω_c by $k_c = \omega_c/c$. Depending on the geometry, k_c can take different values. All of that being said, a distinction

is in general drawn between multi-conductor structures called transmission lines or single-conductor structures usually called waveguides.

1.1.2 Transmission lines

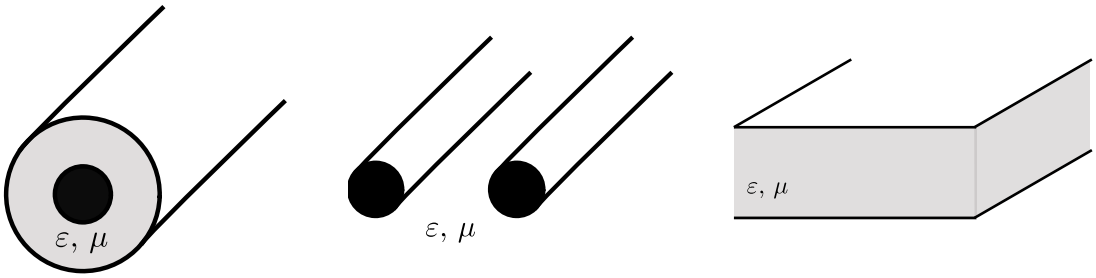

Figure 1.2 – Examples of TEM transmission lines: (a) Coaxial cable, (b) two-wire cable and (c) parallel-plate waveguide.

To begin with, the multi-conductor transmission lines are extensively used for nearly all modern high-frequency telecommunications, low-frequency power management or digital electronics. As examples, the coaxial cable, the two-wire cable, the parallel-plates waveguide (see Figure 1.2) are located in this category. An important characteristic of these waveguides is that they can carry signal at any frequency, making them very suitable for diverse applications. In fact, it can be shown that a specific mode, called Transverse Electro-Magnetic (TEM), will exist for any frequency because thanks to the presence of several conductors. This mode is said to be transverse because its field components are located in the transverse section only. For higher frequencies, an infinite number of modes will be able to carry energy, they are called Transverse Electric (TE) and Transverse Magnetic (TM). In this classification, the TE modes do not have any electric field component in the propagation direction. Similarly, the TM modes have transverse magnetic field only. In general, these higher-order modes are suppressed by different techniques, mainly because they are source of dispersion, unwanted radiation or dissipation.

The illustration of the dispersion relation is called dispersion diagram. In the general transmission line case, β as a function of ω for the TEM mode looks like Figure 1.3. Because of the presence of several conductors, there is no cut-off frequency, ie. $k_c = 0$. Physically, a potential applied between the conductors will propagate along the line for any frequency. In this particular case, the dispersion relation is very simple, it is a linear progression following $\beta = \omega/c$.

In practice, these transmission line topologies are often implemented in more realistic environment where imperfect conductors and dielectrics are involved. Also, different dielectrics are usually combined, resulting in the existence of quasi- TEM, TE and TM modes. However, the fundamental properties are generally still obtained considering relatively low losses and limited frequencies. Some of the most common topologies are illustrated in Figure 1.4, namely the microstrip line, the coplanar waveguide (CPW) and the stripline. All these three examples are usually printed technologies, realised by metallic deposition and selective removal on a thin dielectric surface. This fact is

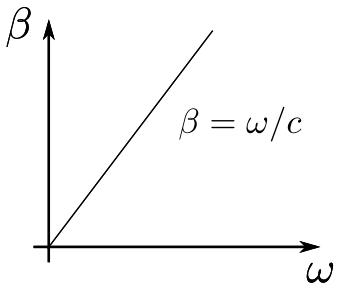

Figure 1.3 – General form of a transmission line dispersion diagram.

of great interest because it means that compact electronic circuits can be fabricated at an affordable cost while using a simple fabrication process.

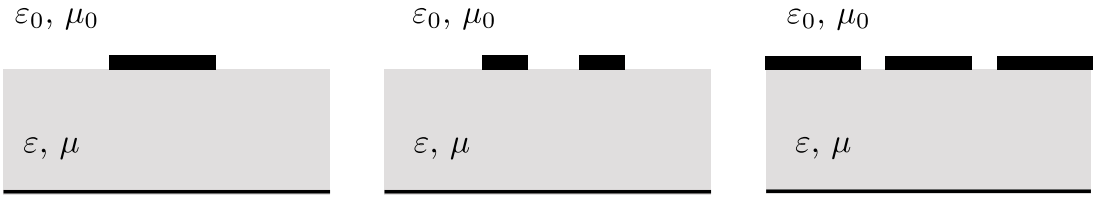

Figure 1.4 – Examples of quasi-TEM transmission line: (a) Microstrip, (b) stripline and (c) coplanar waveguide (CPW).

Among other things, the invention of such technologies has created a significant growth in the electronic market since the 1970's. It has led to the development of low-cost devices for telecommunications, computing, etc. Obviously, the recent developments are more and more related to the semi-conductor industries, which provided even more miniaturized environment for the integration of highly complex analog and digital functions. That being said, the adopted transmission line topologies for these circuits remain essentially based on scaled versions of microstrip or CPW.

1.1.3 Waveguides

The rectangular waveguide is not part of this category as it is only made of one conductor. In fact, it is generally taken as the typical example of single-conductor waveguide in the electromagnetism textbooks [1–3]. In most cases, these waveguides are characterised by a "pipe" shape, meaning that the wave is enclosed in a specific region by metallic boundaries, able to propagate in a single longitudinal direction. Three examples are given in Figure 1.5, the rectangular waveguide, the ridge rectangular waveguide, as well as the circular waveguide.

The fundamental difference between the two categories is that waveguides do not support TEM modes, and thus cannot operate at low frequencies. In a nutshell, for a mode to propagate along the waveguide, it is necessary that it satisfies the boundary conditions. In particular, the electric field should have no tangential component on the outer metallic boundaries. For large wavelengths - ie. small frequencies -, such a condition can simply not be fulfilled. This is the reason why a cut-off behaviour is observed on the dispersion diagram, as illustrated in the general case for the first

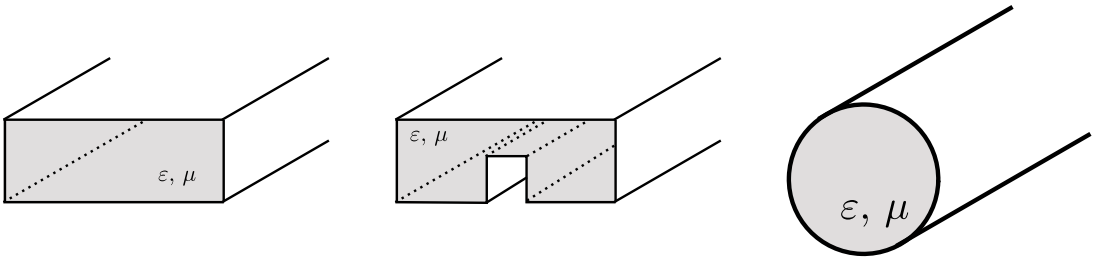

Figure 1.5 – Examples of waveguides: (a) Rectangular, (b) Ridge rectangular and (c) Circular.

propagating mode in Figure 1.6. Below the cut-off angular frequency ω_c the waveguide cannot carry any energy. In this case, $k_c \neq 0$.

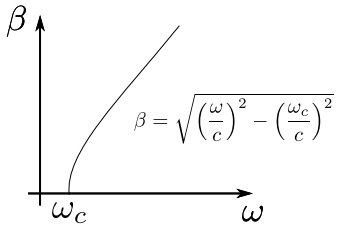

Figure 1.6 – General form of a waveguide dispersion diagram.

1.2 Technological context, the integration of rectangular waveguides

1.2.1 Origin, principle and main applications of rectangular waveguides

1.2.1.1 Beginning of the XX's century, the first significant developments

Fully metallic waveguides have been studied since the end of the nineteen century [4], mostly by physicists Lord Rayleigh [5] in 1897. His work intended to demonstrate the existence of solutions to the recently established Maxwell equations for waves propagating in cylindrical metallic waveguides. Such waves would be able to transport energy along one direction in well-defined modes. As radio communications were mainly focused on large wavelength, these developments received not much attention in the beginning of the twentieth century.

However, about three decades later much work had been done in the realization of high-power microwave sources for science experimental purpose. Following the invention of the Triode in 1906, the Barkhausen-Kurz oscillator based on the vacuum-tube technology was invented in 1920. Further research works led to the existence of useful power sources operating above 10 GHz in the 1930's. As a consequence, the technological knowledge available at that time led to more attention given to the somehow forgotten one conductor waveguide. Both technological and theoretical main findings

were related to the works of Georges C. Southworth at Bell Telephone Laboratories (BLT) and Wilmer L. Barrow at Massachusetts Institute of Technology (MIT) (see Figure 1.7). The irony is that both researchers were not aware of each other investigations until a few months before the official papers were published.

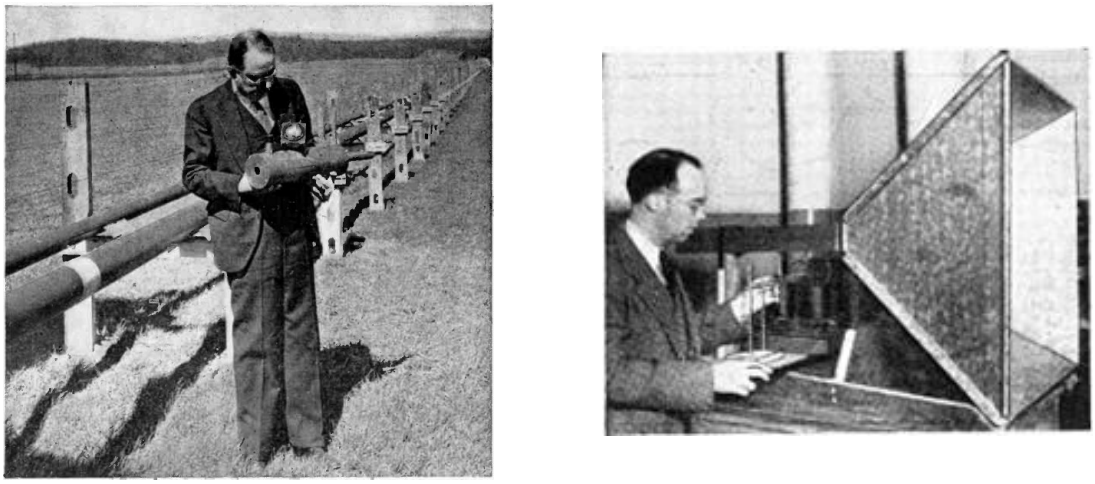

Figure 1.7 – (a) G.C Southworth, conducting some of the work done at Holmdel , N.J., on electrical wave guides (Jan 2, 1935) [6]), (b) W.L. Barrow, standing next to his invented first modern horn antenna (1938) [7].

The former came to the idea of investigating the hollow waveguides for communication applications, attracted by the possibility of carrying a very high number of channels. However, for more and more obvious reasons, he came to the conclusion that this technology would be of better use in antennas, rather than long-range communications.

The latter was in charge of developing accurate plane detection in fog conditions, and therefore mainly investigated antennas and electromagnetic propagation at short-wavelengths. After establishing the principles of horn antenna he eventually came to the issue of energy feeding into these kind of structures, which led to the hollow waveguide (see Figure 1.8). After leading theoretical and practical works he became the Director of MIT Radar School and performed research in the MIT Radiation Laboratory, which provided much of the waveguide technology at that time.

1.2.1.2 General principles

A rectangular waveguide has a very simple shape, it is defined by its width W and height H (see Figure 1.9). In general, it is filled with air or empty. The resolution of Maxwell equations in this structure leads to the complete definition of the set of modes with associated power dissipation, it can be readily found in [1–3].

The set of modes is usually arranged by considering two integers which indicate the field variations along x and y, resp. n and m. Based on this principle, TE and TM modes are therefore written TE_{nm} and TM_{nm}, where n and m take independent values. The corresponding cut-off frequencies are denoted $f_{c,nm}$, they are given by (1.17) where

Figure 1.8 – (a) Rectangular horn antenna [8], (b) Circular horn antenna [9], (c) Rectangular waveguides [10].

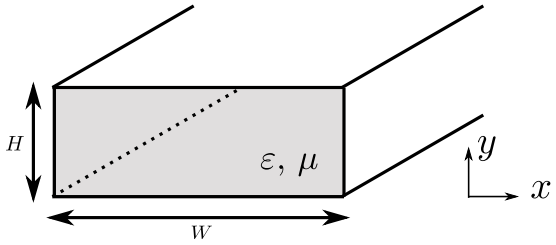

Figure 1.9 – Rectangular waveguide dimensions.

$c = (\varepsilon\mu)^{-1/2}$ stands for the light velocity in the filling material. Moreover, it can be shown that $n = m = 0$ is not a solution because it would correspond to a TEM propagation. Also, TM_{nm} modes are only existing for $n, m \geq 1$.

$$f_{c,nm} = \frac{c}{2\pi}\sqrt{\left(\frac{n\pi}{W}\right)^2 + \left(\frac{m\pi}{H}\right)^2} \tag{1.17}$$

If $W > H$, the first mode to propagate is the TE_{10}, starting at $f_{c,10} = c/2W$. It is worth mentioning that the cut-off frequency is inversely proportional to the waveguide lateral dimension, this point constitutes a major issue for low-frequency applications. Then, the order of apparition of the higher order modes will depend on the ratio W/H. If $W > 2H$, the TE_{20} starts to propagate at twice the TE_{10} cut-off frequency. In this case, only the TE_{10} is able to propagate between $f_{c,10}$ and $2f_{c,10}$. This frequency range is thus called the "mono-mode frequency band". Because of the single-mode operation, a low dispersion is observed in this frequency band. In practice, most circuits operate in this regime. The field distributions associated with TE_{10} and TE_{20} are illustrated in Figure 1.10.

1.2.1.3 Main applications of the rectangular waveguide

The development of the waveguide technology has a lot to do with radar applications, especially during World War II. The MIT Radiation Laboratory developed most of the theory and microwave components in this period. Because of its low attenuation, high-power handling capabilities as well as very high isolation, the rectangular waveguide offered an immediate advantage over existing technologies. Several components

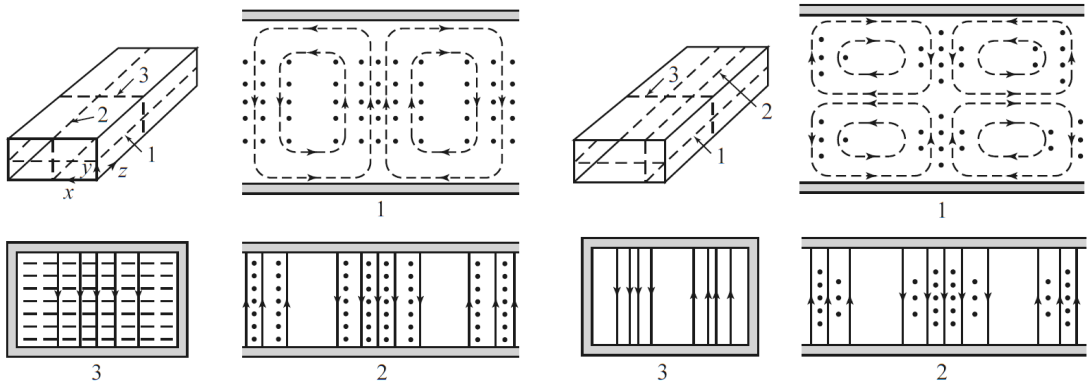

Figure 1.10 – (a) TE_{10} and (b) TE_{20} field lines [1] (solid lines for electric field, dashed line for magnetic field).

have been developed such as couplers, filters, power dividers, antennas, orthomode transducers etc...

In the second half of the XXth century, it naturally became more and more dedicated to small volume and very high performance applications. In fact, the development of the consumer electronic market has relied on microwave planar circuits. It has been made possible thanks to the use of planar transmission lines like the slotline, microstrip or the coplanar waveguide [11–13]. They are mainly two reasons for this orientation. First, these planar solutions offered a direct economic advantage because they relied on a cheap fabrication process, thus compensating research investments. Secondly, these solutions could be more easily interfaced with semi-conductor platforms, thus opening the possibility of manufacturing monolithic microwave integrated circuits (MMIC) [14–16].

At the same time, the waveguide technology became prominent in applications requiring either mechanical robustness, high-power signals, resistance to interferences, or extremely low loss. Not surprisingly, satellite and airborne markets therefore represent an important part of the waveguide applications. As an illustration, a commercialized filter in Ka band is illustrated in Figure 1.11(a). In addition, because of transmission line limitations at millimeter-wave frequencies, the waveguide technology also provided a good platform for radio-astronomy low-noise receivers [17, 18] (see Figure 1.11(b)).

While offering significantly high performance compared to planar solutions, the major drawback of this technology is obviously its size and fabrication complexity, directly resulting in higher costs. For defense purpose or advanced science research projects, these issues are generally anticipated. For mass production of consumer electronics however, these two elements make the choice of planar solutions much more coherent.

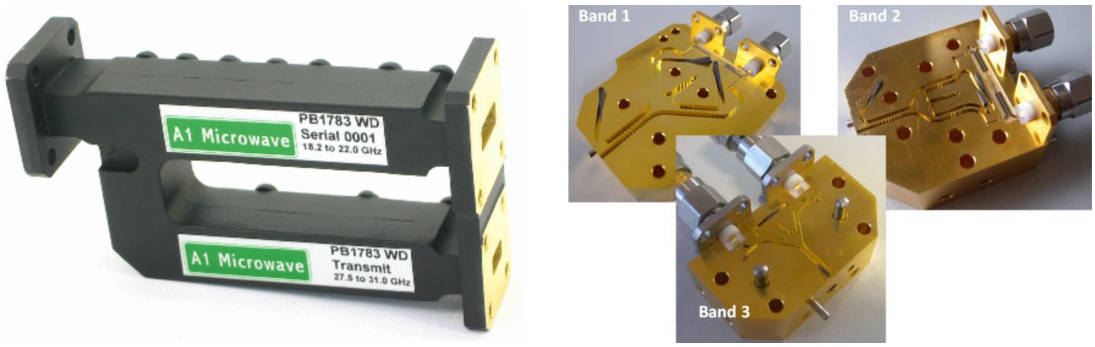

(a) (b)

Figure 1.11 – (a) Ka-Band diplexer for satellite communications from A1 Microwave [19] and (b) Superconducting mixers (SIS) embedded in waveguide technology from the NOMEA receiver (72-373 GHz) [18].

1.2.2 The integrated rectangular waveguide

1.2.2.1 Principle of Substrate Integrated Waveguide

As we have seen in sub-section 1.1.2, the transmission lines are nowadays fabricated in planar forms. The integration of these technologies on thin dielectrics or semi-conductors has been a driving force for the reduction of costs production.

In 1994, F. Shigeki introduced the concept of integrated waveguides [20], which was soon followed by the circuit publication of a "Waveguide filters having a layered dielectric structure" [21], illustrated in Figure 1.12(a). Based on high dielectric low temperature co-fired ceramic, the authors created vertical via holes which were plated with a conductive material, thus achieving resonant cavities. Then, in 1998, a power divider [22] as well as a slot antenna [23] were published (see Figure 1.12(b) and 1.12(c)). The horizontal walls of the waveguide were realized by conductive plates deposited on dielectric substrates, while the lateral continuous vertical walls were imitated by closely arranged plated via holes.

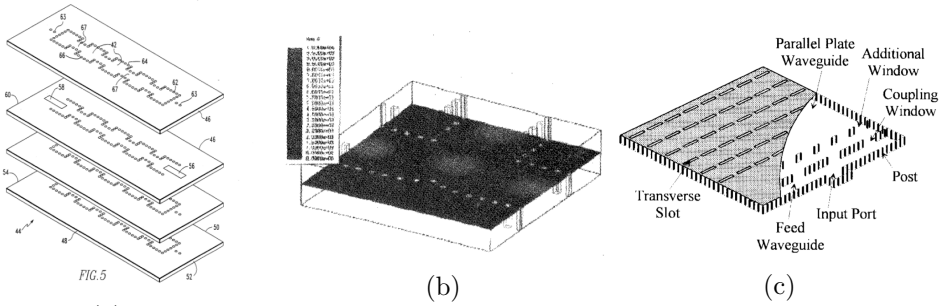

(a) (b) (c)

Figure 1.12 – (a) Waveguide filter in LTCC technology (1995) [21], (b) power divider in glass ceramic (1998) [22] and (c) slot antenna in Teflon substrate (1998) [23].

The authors of these first realizations intended to use the integrated waveguide

as a separate component, mostly because its excitation was rather complex. Finally, the idea did not gain any more attention until the work of D. Deslandes (2001), who dedicated its PhD thesis to the extension of the integrated waveguide as a platform which could integrated both active and passive functions of a full transceiver [24]. The integrated form of the rectangular waveguide took the name of "Substrate Integrated Waveguide" (SIW), and became a very important research topic in the microwave community. In comparison with the existing planar solutions, SIW exhibited high quality factors, quasi-perfect isolation from the environment as well as high power-handling capabilities. Obviously, these properties where largely inherited from the rectangular waveguide technology. However, the main difference between the two is the very low fabrication cost of SIW, as it only relies on drilling and hole plating processes.

A general geometry of a SIW is illustrated in Figure 1.13. In most cases, the lateral walls are made of circular via holes, however it can also be based on rectangular trenches such as in [25–27]. As for rectangular waveguides, the main geometrical parameters of a SIW are its width W and height H. Two other parameters are introduced, the via-holes diameter d and their longitudinal separation s.

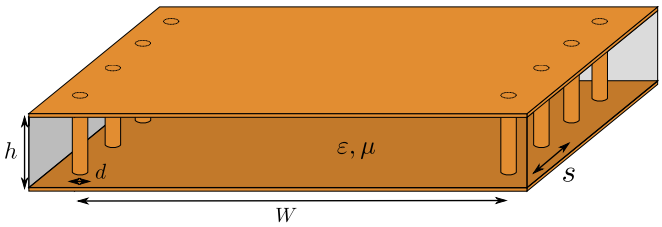

Figure 1.13 – SIW geometry.

The literature on the subject is highly exhaustive. In IEEE Xplore only, it is addressed in more than 1500 journal and magazine articles, and about 3200 conference papers. The fundamental design rules for the proper operation of SIW were investigated in [24]. They will be quickly listed here.

Because of the inherent periodical character of SIW, it exhibits some additional properties compared to the rectangular waveguide. From the modal perspective, the SIW does not support TM modes because the associated longitudinal currents cannot travel along the lateral walls, creating a very strong radiation between the via holes. The design rules for d and s are generally defined in relation with the cut-off wavelength λ_c, related to the cut-off frequency f_c by $f_c = 1/\left(\lambda_c\sqrt{\varepsilon\mu}\right)$. These design rules are based on three different principles listed below:

- Minimize the leakage between the via holes
- Avoid the presence of bandgaps within the operating frequency band
- Limit the mechanical impact of drilling by avoiding very high densities of holes

The design rules were analysed in detail in [24] and [28]. First, the condition $s > d$ should be followed for obvious practical reasons. Then by combining all considerations, the two following rules were given:

$$0.05 < \frac{s}{\lambda_c} < 0.25 \tag{1.18}$$

$$s \leq 2d \tag{1.19}$$

The upper boundary of equation (1.18) is related to bandgap considerations, while its lower one reflects an arbitrary mechanical consideration which aims at avoiding unnecessary drilling. Secondly, (1.19) is a sufficient condition for negligible leakage losses. Once all these conditions are satisfied, the SIW can be seen as a rectangular waveguide of width W_{eff}, which expression has taken several forms, the most simple being that of [29] (4.13). Other work related to more elaborate approximations can be found in [30].

$$W_{eff} = W - \frac{d^2}{0.95s} \tag{1.20}$$

1.2.2.2 Overview of existing realizations

As already mentioned, the amount of research and development effort dedicated to the SIW technology is significant. In fact, thanks to more than half a century of research legacy on rectangular waveguides, the development of the SIW technology has been relatively fast. In 2017, it is now a technology which has demonstrated its interest in a wide frequency range, from a few GHz to the beginning of the millimeter-wave bands.

From the process point of view, it has been adapted in various context, including conventional Printed Circuit Board (PCB) (Figure 1.14(a)) [31–37], low-temperature co-fired ceramic (LTCC) (Figure 1.14(b)) [38–40], textile materials (Figure 1.14(c)) [41, 42] etc. The development of 3D-Printed structures (Figure 1.14(d)) is also investigated in [43–45], as well as CMOS technology for sub-THz frequencies (Figure 1.14(e)) [46–48].

Nowadays, most of the passive functions have been realized in SIW technology, including couplers [35, 49, 50], filters [33, 38, 51, 52], power dividers [31, 32, 53, 54], antennas [46, 55, 56], feeding networks [57–60], attenuators [61–63], phase shifters [64–66] etc. The incorporation of active functions to form oscillators and amplifiers has also been investigated [67–71]. Some examples among all these different realizations are illustrated in Figure 1.15.

Beyond the development of several key circuit components and assembly, some work is related to the improvement of intrinsic SIW performance. In order to reduce the attenuation and obtain higher quality factors, empty versions of the SIW were proposed. For instance, an air-filled SIW was developed by F. Parment [72]. A slightly different waveguide with continuous lateral walls was also developed by Belenguer et al. [73].

Finally, tunable SIW components such as filters, antennas and VCO were realized [74] in order to address multiple channels in communication protocols and reduce the occupied area.

The SIW technology offers many advantages as compared to the conventional planar transmission lines, however it has inherited from the rectangular waveguide its

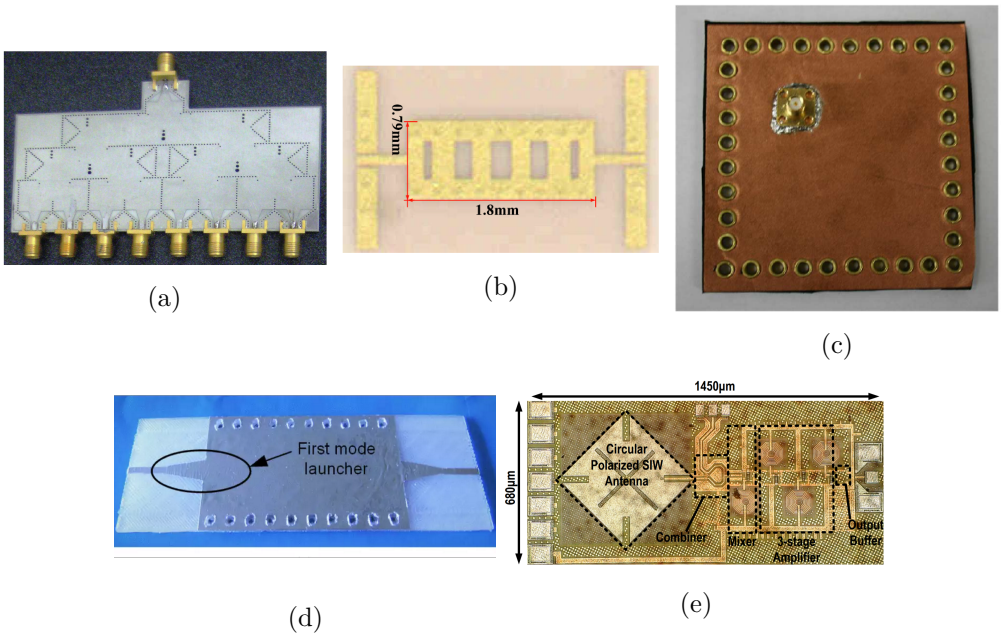

(a) (b) (c) (d) (e)

Figure 1.14 – (a) SIW eight way power divider in PCB [31], (b) SIW Filter in LTCC [38], (c) SIW Cavity resonator in textile material [42], (d) 3D-printed SIW [43], (e) SIW Antenna in CMOS 65 nm [46].

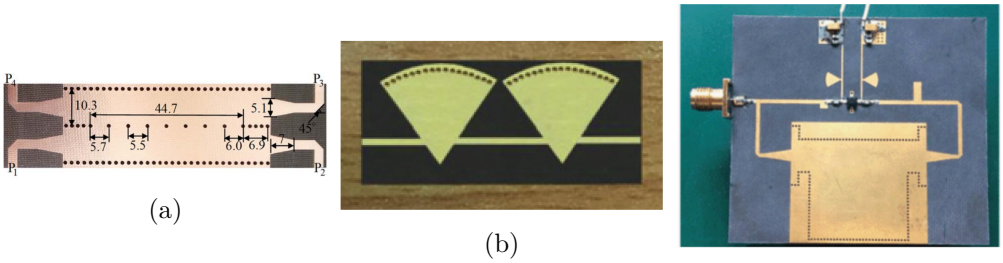

(a) (b) (c)

Figure 1.15 – (a) SIW multi-aperture coupler [31], (b) SIW 2nd order cavity filter [51], (c) Low phase-noise oscillator based on SIW dual-mode filter[68].

main limitation, i.e. its dimensions. As seen before, the lateral dimension W is directly related to the operating frequency, so that transmission line based circuits are usually more compacts at low frequencies. For this reason, several techniques have been developed to overcome this issue and propose compact SIW circuits, they will be presented in the next section.

1.2.3 Beyond integration, the miniaturization techniques

The miniaturization techniques for SIW circuits are often dependent on the topology and operation principle. This if for example the case of multi-mode considerations, which are mostly used only for filters. In this first chapter, we will focus on the broader aspects of it. Namely, without specifying the kind of SIW circuit, what are

the techniques that already provides miniaturized waveguides ? In Chapter 3 and 4, the state-of-the-art miniaturization techniques related to couplers and filters will be respectively dealt more in detail.

The miniaturization can be seen from two complementary different angles. On one side, given an operating frequency and thus a corresponding cut-off frequency, the miniaturization consists in trying to reduce the width W by modifications of the geometry. On the other side, the dual approach is about reducing the cut-off frequency for a given W. These two approaches are two faces of the same problem, one or the other description is used depending on the context. Once again, the development of compact SIW is often related to general hollow waveguides miniaturization techniques, which were conducted as earlier as in the 1940's [75].

1.2.3.1 The ridge SIW

This first solution is in fact the integrated version of a well known metallic waveguide called "Ridge waveguide", depicted in Figure 1.16 in single and double configurations. Its principle was first published in 1947 by S. B. Cohn [76], who analysed its propagation characteristics, impedance and cut-off frequencies. By inserting one or two ridges in the center of the waveguide, Cohn demonstrated that "ridge wave guide has a lower cutoff frequency, impedance and greater higher-mode separation than a plain rectangular wave guide of the same width and height" [76]. This waveguide is mainly used for impedance matching because it exhibits lower impedance values that the conventional version. It is especially useful for transitions between planar transmission lines and rectangular waveguides as in [77].

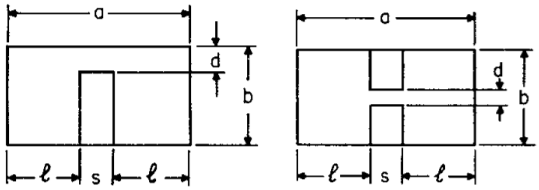

(a) (b)

Figure 1.16 – (a) Single and (b) double ridge rectangular waveguide cross-section [78].

Thanks to the possibility of multilayer configuration in printed-circuit-board technology, the ridge concept has been adapted as soon as in 2007 for broadband transitions from microstrip to SIW [79] (Figure 1.17(a)). The ridge can be realized by using blind via holes connected to the bottom metallic layer only. It was shown that it provided an interesting 37 % expansion of the monomode bandwidth [82], as well as lateral miniaturization up to 40% [83]. In [80], the authors demonstrated that a metal strip connecting all via-holes could be used to remove the bandgap effect related to the periodicity and improve the bandwidth to three times that of the usual SIW. Finally, a factor of five was achieved by combining different dielectric constant layers [81]. These last two configurations are illustrated in Figures 1.17(b)-1.17(c).

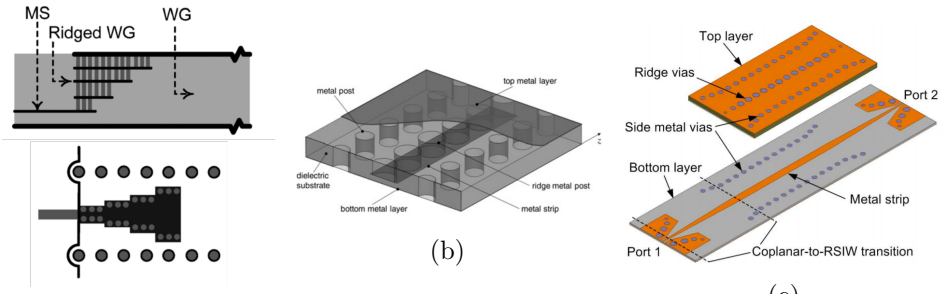

(a) (b) (c)

Figure 1.17 – (a) Transition from microstrip to SIW based on Ridge SIW [79], (b) Ridge waveguide with connection of the blind via holes for band-gap removal [80], and (c) Ridge waveguide with two dielectric constants for optimal bandwidth enhancement [81]

1.2.3.2 The Folded waveguides

This second technique also relies on a multilayer configuration. The idea is to fold the rectangular waveguide in order to reduce its lateral occupation. It was first introduced in W. L. Barrow in 1941 [75], who tried to obtain very low cut-off frequencies for given outer dimensions by folding the wave path inside the waveguide (see Figure 1.18(a)). In this waveguide, the miniaturization is directly related to the number of bends.

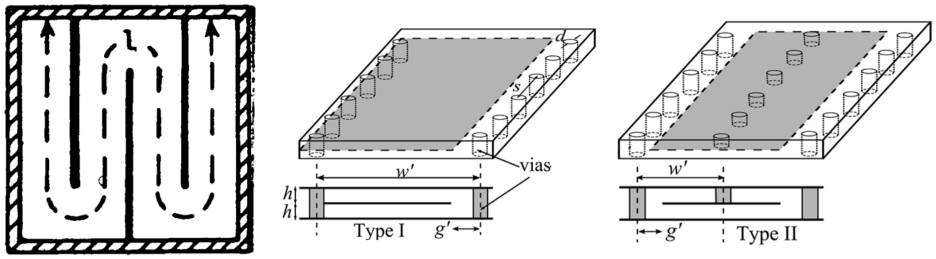

(a) (b) (c)

Figure 1.18 – (a) Folded rectangular waveguide as introduced by W. L. Barrow [75], (b) Folded SIW in C,(c) and T shapes [84].

It was first adapted in SIW in 2004 [85], and later applied to the design of several passive components. In general, the folded SIW takes either a "C-" or "T-shape", respectively illustrated in Figure 1.18(b) and 1.18(c). This is mainly because more complex topologies would require additional layers, and thus greater costs. The T-shape has the advantage of presenting a vertical symmetric field distribution over the C-shape, facilitating the excitation. A "L-shaped" was also introduced in [86] for the feeding of folded tapered slot antenna.

From the modelling point of view, several theoretical investigations have been led, which among other things concluded that the "C-shape" folded SIW could provide very similar propagation characteristics as the SIW, depending on the ratio g'/h, where g' and h are shown on Figure 1.18(b) [87, 88]. Interesting theoretical derivations have

also been more recently performed based on a variational analysis [89].

In practice, most realizations have been done in PCB technology, but it is worth mentioning that this miniaturization technique has been very recently chosen for the fabrication of SIW in the IBM 130-nm CMOS technology around 200 GHz [90]. It has also attracted attention for the design of compact filters in LTCC technology [91–93], which offers the possibility of stacking an important number of layers.

1.2.3.3 The partial-mode waveguides

Finally, this last approach is based on symmetry considerations. As illustrated in Figure 1.19(a), the vertical magnetic symmetry which characterizes the fundamental mode of the SIW can be replaced by an open-circuit condition without introducing a significant difference in the propagation characteristics. The propagating mode in this open structure is therefore called half-mode. The lateral dimension of the half-mode waveguide is approximately half that of the SIW having the same cut-off frequency, it is in reality slightly larger than that because of the imperfect open-circuit condition. For this configuration, the thinner the substrate the lower the leakage loss, as the parasitic capacitance of the aperture is more and more negligible. However, using thin substrates will also increase metallic dissipation so a trade-off is required. The concept was first introduced in 2006 [94] and rapidly applied to the design of power dividers [95, 96] and couplers [97, 98]. It was also later applied to the design of filters, which used quarter- or even height-mode resonant cavities (see Figure 1.19(b) and 1.19(c), respectively.)

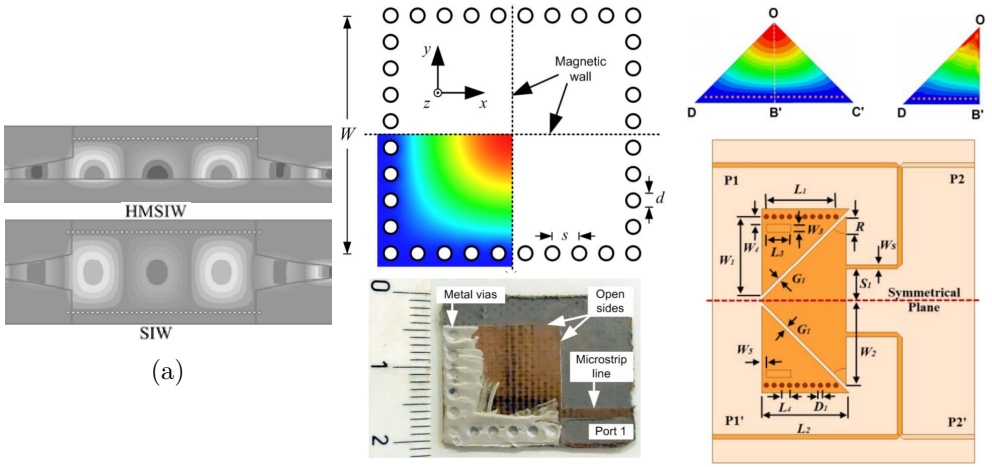

(a) (b) (c)

Figure 1.19 – (a) Electric field amplitude in SIW vs. half-mode SIW [95], (b) Quarter-mode resonant cavity [99] and (c) Filter based on quarter- and heigth-mode resonant cavities [100].

Obviously, such a waveguide is subject to radiation, this drawback can be limited by using thin substrates. Furthermore, the fringing fields can be used to couple adjacent waveguides or cavities.

From the modelling point of view, semi-analytical solutions were performed in [101], as well as a variational analysis in [102]. The modelling of such a structure is more complex than that of the SIW because it exhibits a strong electric field on the open side.

1.3 The slow-wave concept, a tool for the miniaturization of integrated waveguides

1.3.1 General considerations

1.3.1.1 Definitions and physical principle

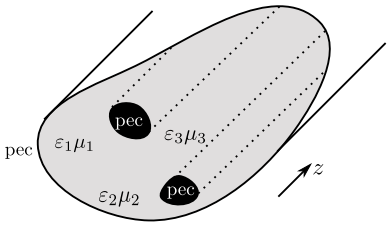

Figure 1.20 – General form of a uniform waveguide.

Before introducing the slow-wave technologies, let's first define the terms in a general context. A general uniform waveguide topology is illustrated in Figure 1.20. The cross section could contain either different metallic conductors, magnetic or dielectric materials.

As already mentioned in section 1.1.1, a wave propagating inside such a waveguide is characterized by its phase constant β and angular frequency ω. By definition, its phase velocity v_p is the velocity at which the phase of the wave travels in space, and is defined as (1.21). It can be seen as the velocity at which an observer should travel along the waveguide in order to keep in state with this wave. A second velocity is called group velocity, v_g, it is the velocity at which the overall shape of the waves' amplitudes - or modulation - travels through space. This velocity is also often interpreted as the velocity at which the energy or information propagates, it is given by (1.22).

$$v_p = \frac{\omega}{\beta} \tag{1.21}$$

$$v_g = \frac{\partial\omega}{\partial\beta} \tag{1.22}$$

By definition, for a non dispersive propagating mode such as the lossless TEM mode, the phase velocity does not depend on frequency, which implies that the phase constant β is a linear function of ω. In that case, it follows that $v_p = v_g$. However, if this velocity does vary, the group velocity will differ from the phase velocity.

Considering equation (1.15), the free space phase velocity (and therefore the group velocity) in a specific material is fixed by its intrinsic properties ε and μ, in particular $v_p = v_g = c = 1/\sqrt{\varepsilon\mu}$. For a guided wave however, dispersion occurs so that phase

and group velocities can greatly differ from the free space value. As explained in [103], in a closed uniform waveguide waves propagates at velocities greater than the light velocity, they are commonly called "Fast-waves". This is equivalent to say that the guided wavelength λ is greater than the free space wavelength.

On the contrary, some structures can exhibit lower velocities compared to free-space propagation. These waves are therefore called "Slow-waves" and characterized by smaller guided wavelengths. The velocity reduction can be obtained by specific spatial variations of materials properties in the transverse section, as shown in Figure 1.20. Another method relies on the introduction of periodicity in the propagation direction, either in materials properties or in the boundary conditions.

In order to quantify the velocity reduction a common definition of a so-called slow-wave factor (swf) is adopted [103]. This factor is defined as the ratio between the free-space velocity in vacuum c_0 and actual phase velocity in the considered waveguide v_p (see (1.23)). This factor is also called effective refractive index defined in optics. It can also be expressed as the ratio of free-space and guided wavelengths λ_0 and λ, or phase constants β_0 and β. Usually, an effective relative permittivity ε_{reff} is introduced, integrating both magnetic and electrical effects in one single parameter (as in [103]). In this definition, ε_{reff} contains the contribution of material properties (ε_r, μ_r), as well as any additional slow-wave mechanism.

$$swf = \frac{c_0}{v_p} = \frac{\lambda_0}{\lambda} = \frac{\beta}{\beta_0} = \sqrt{\varepsilon_{reff}} \tag{1.23}$$

From the definition given above, a slow-wave structure is characterised by a swf greater than 1. However, based on this definition most existing waveguides (TEM or not) are slow-wave structures, because they contain dielectric materials with $\varepsilon_r > 1$. For convenience, a second definition of slow-wave factor may be used to remove this ambiguity. It is defined as the ratio between the phase velocity in a given wave-guiding structure v_p^{ref} taking the material properties into account, and v_p, the one achieved through additional geometry and materials modifications (see (1.24)).

$$SWF = \frac{v_p^{ref}}{v_p} = \frac{\lambda^{ref}}{\lambda} = \frac{\beta}{\beta^{ref}} \tag{1.24}$$

Besides, if the reference waveguide supports a TEM mode so that its phase velocity can be expressed as $v_p^{ref} = c_0/\sqrt{\varepsilon_r}$, then the following relation between the two definitions can be derived:

$$SWF = \frac{v_p^{ref}}{v_p} = \frac{swf}{\sqrt{\varepsilon_r}} \tag{1.25}$$

As a result, the effective relative permittivity becomes:

$$\varepsilon_{reff} = \varepsilon_r SWF^2 \tag{1.26}$$

1.3.1.2 Practical conditions for the slow-wave propagation

For a given waveguide, the strictly necessary condition to be fulfilled in order to achieve lower velocity is the spatial separation of electric and magnetic energies, either in transverse or longitudinal directions. Some physical insight about this required physical separation will be given in Chapter 2. In practice, this separation can be achieved by two different means, which correspond to two distinct slow-wave structures classes [103].

Figure 1.21 – (a) MIS Microstrip and coplanar waveguide (left and right, resp.), (b) Shottky-contact microstrip transmission line.

The first one exhibits energies separation in the transverse section. This can be realized by special geometries made of different materials. Common examples of these structures are the metal-insulator-semiconductor (MIS) planar transmission lines (Figure 1.21(a)), such as the microstrip [104] and coplanar waveguide [105]. The Shottky-contact microstrip is also an example of such slow-wave structures (see Figure 1.21(b)) [106]. In these transmission lines, the spatial separation of energies can be explained by the fact that the conductive property of the doped layer is confining the electric energy in the insulator while the magnetic field is not really affected.

In the second category, the spatial energy separation is performed in the longitudinal axis. It can be realized by periodic variations of either materials properties or boundaries. It is true that some work has been conducted in relation with the former method, especially through semiconductor periodical doping as in [107] (Figure 1.22(a)). However, the latter solution is adopted in most cases for its simpler practical implementation. The helix waveguide is generally taken as an example, it is given in Figure 1.22(b). The planar meander line is also given as a planar illustration in 1.22(c)

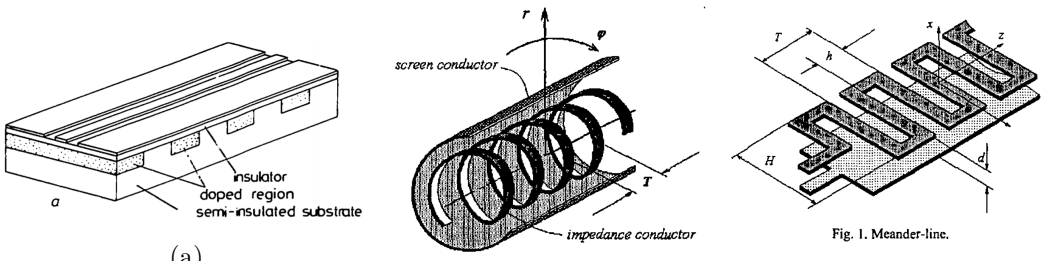

Figure 1.22 – (a) Coplanar waveguide on periodically doped semiconductor [107], (b) Helix waveguide and (c) Meander line [108].

Interestingly, the mathematical demonstration can be found in [109] that guided

wave problems can only lead to slow-wave solutions if it includes either dielectric boundaries or non uniform, periodic boundaries. Detailed developments by L. Brillouin on the slow-wave propagation in periodic structures can also be found in [110].

1.3.2 Historical background and main applications

Slow-wave structures began their apparition in the early 1940's for their capability to establish efficient interaction with electron beams. More precisely, it started in the context of radar applications, where these interactions were used to amplify RF waves. The amplification was based on transferring kinetic energy from electrons to a propagating wave. Based on this principle, the first slow-wave structure was called "klystron", a high-frequency vacuum tube invented in 1939 by W. Hansen and the Varian brothers, illustrated in Figure 1.23(a). In these amplifiers, the slow-wave propagation was achieved by cascading resonant cavities, which resulted in narrow-band operation [103].

In this amplifier, the slow-wave propagation was necessary because the interaction requires close velocities between the wave and the electrons, which move in vacuum at a lower velocity than the light. This interaction was further enhanced by R. Kompfner, who realized in 1943 a broadband amplification based on a non-resonant helix structure, called "travelling-wave tube" (TWT), illustrated in Figure 1.23(b).

Improved versions of these devices are still in use for radar, satellite communications, television broadcasting as well as particle accelerators. Oscillators have also been developed based on the same principles.

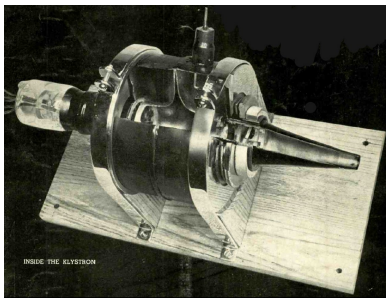

(a)

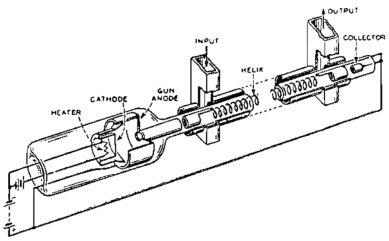

(b)

Figure 1.23 – (a) First fabricated klystron [111], (b) Travelling-wave tube principle of operation [112].

During the 1960's, the development of integrated microwave circuits provided a good opportunity to develop layered structures with potential slow-wave propagation. This concept was demonstrated for the first time in 1969 for a metal-insulator-semiconductor microstrip structure [113] on silicon. It was followed by several topologies including the Schottky contact transmission line [106]. Thanks to an external bias, this last structure was used to create a variable slow-wave effect [114]. As explained in [103], planar periodic structures gained attention in the early 1970's for the development of wide-band coupled microstrip lines [115]. Since then, the research on planar periodic and layer structures continued until today.

In the meantime, slow-wave planar structures have also been used for miniaturization purpose. In microwave passive circuit design, specific functions such as filters, antennas and couplers are realized by the combination of physical phenomenon such as interference, resonance and couplings. These phenomenon are very often dependant on wavelengths, so that specific properties can be obtained for given dimensions. It also means that in general these passive circuits generally occupy much larger areas than the active ones, which are made of increasingly smaller transistors. For example, a floating straight transmission line has intrinsic resonance frequencies which are directly related to the ratio of the propagation velocity by its physical length. Therefore, for a given frequency a miniaturized structure can be obtained if the velocity is accordingly reduced. Obviously, the challenge lies in the effort to make such slow-wave structures as efficient in terms of dissipation as the original ones.

In printed-circuit-board technology, a high number of topologies have been developed in the recent years, some of them are illustrated in Figure 1.24. Figure 1.24(a) shows spoof surface plasmon based transmission lines, for compact designs, reduced attenuation and limited cross-talks [116]. Compact couplers, such as the "rat-race" illustrated in Figure 1.24(b), was obtained by using a high slow-wave factor microstrip structure [117]. In Figure 1.24(c), a filter based on six slow-wave resonators is illustrated [118]. One could also mention the use of defected ground [119] and electromagnetic band-gap [120] which often exhibits slow-wave propagation.

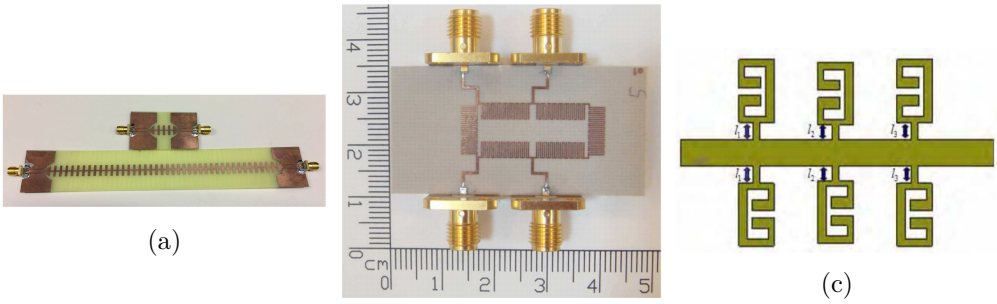

(a) (b) (c)

Figure 1.24 – (a) Spoof surface plasmon based slow-wave transmission lines [116], (b) Rat-race coupler[117], and (c) Six-resonator low-pass filter based on slow-wave resonators [118].

Concerning integrated technologies, the design of compact and low-loss passive circuits is a real challenge. It is especially true for the newly addressed millimeter-wave bands, in which parasitic couplings are more and more limiting and high conduction losses result in poor quality factors. In this context, slow-wave structures do not only provide miniaturized circuits, but may also lead to higher quality factors [121–123]. This is the case of the slow-wave coplanar waveguide, which geometry prevents conduction losses in the semiconductor by shielding the electric field (see Figure 1.25(a)). Meander lines were also used to realize compact couplers in silicon-based integrated passive device (IPD) technologies [124], as shown in Figure 1.25(b). A band-pass filter using a slow-wave microstrip topology was presented in [125], it is illustrated in

Figure 1.25(c).

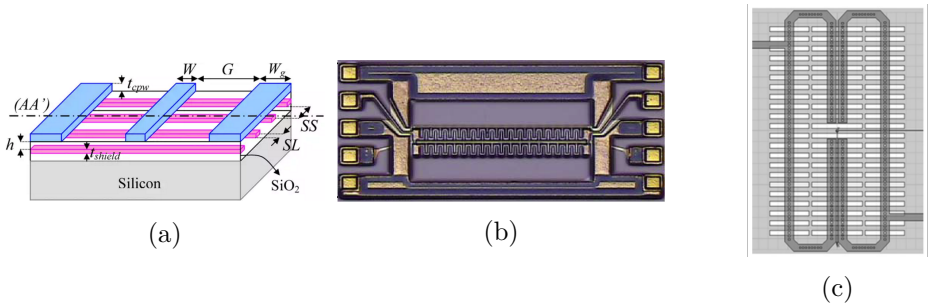

(a) (b) (c)

Figure 1.25 – (a) Slow-wave coplanar waveguide topology [123], (b) Slow-wave coupler in silicon-based IPD technology [124], (c) Miniaturized slow-wave microstrip filter in CMOS 65 nm technology [125].

1.3.3 The existing slow-wave topologies for SIW

The miniaturization of SIW circuits is generally performed through the techniques presented in section 1.2.3. However, in order to be efficient these techniques require in general important structural modifications. For this reason, a slow-wave strategy could be beneficial if it was able to reduce the dimensions while requiring no significant topology change.

Until now, three different topologies have been published, all of which are for the moment implemented in printed-circuit-board technology. The first one was introduced by A. Niembro in 2014 [126], it relies on the use of blind via holes to separate the spatial distribution of electric and magnetic fields. It is illustrated in Figure 1.26(a), and will be presented more in details in Chapter 2.

The two other topologies are based on a same idea, which is that of loading the top cover of the SIW either with polyline [127] or lumped inductors [128] to create an additional inductive effect. They are both illustrated in Figure 1.26(b) and 1.26(c), respectively.

In the two last cases, the inductive loading brings a reduction in both lateral and longitudinal directions between 35 and 40%. In addition, the second solution provides miniaturization factors in both directions which can be independently adjusted by changing the inductances value.

1.4 Conclusion

In this first chapter, a short electromagnetism background was given. The context of guided waves propagation in which this work can be placed was defined. For any wave propagation, the definitions of both phase and group velocities were recalled. From these definitions, the notion of slow-wave propagation was introduced, as well as its quantification through the slow-wave factor.

In order to introduce the SIW concept, a brief history of waveguides and especially rectangular waveguide was given. It was shown that the integration of this technol-

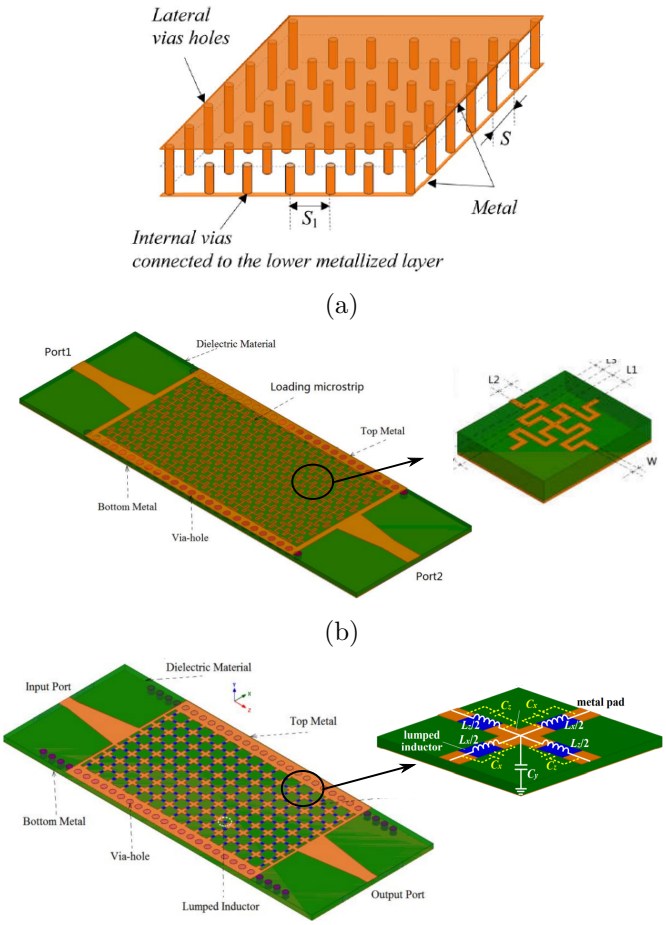

Figure 1.26 – Existing SW-SIW technologies based on (a) blind via insertion [126], (b) polyline [127], and (c) lumped inductors loading on top cover [128].

ogy in thin dielectrics emerged later than the integration of transmission lines, which started in the 1960's. The SIW attracted the attention of the research community around 2005, and it is now a very intense field of development.

While being an interesting alternative to the planar transmission lines for high frequencies, this technology suffers from large dimensions at lower ones. In order to tackle this limitation, several miniaturizations techniques have been developed, they were presented in this chapter.

In this work, we propose a miniaturization technique based on the slow-wave concept. Before presenting the other existing slow-wave integrated waveguide topologies, the history and main applications of this concept were given.

References

[1] D. Pozar, *Microwave Engineering, 4th Edition*. Wiley, 2011.

[2] R. Collin, *Field Theory of Guided Waves*. IEEE Press, 1991.

[3] S. J. Orfanidis, *Electromagnetic Waves and Antennas*. Rutgers University, 2014.

[4] K. S. Packard, "The origin of waveguides: A case of multiple rediscovery," *IEEE Transactions on Microwave Theory and Techniques*, vol. 32, no. 9, pp. 961–969, Sep. 1984.

[5] L. R. F.R.S., "Xviii. on the passage of electric waves through tubes, or the vibrations of dielectric cylinders," *Philosophical Magazine Series 5*, vol. 43, no. 261, pp. 125–132, 1897.

[6] Wikipedia. [Online]. Available: https://en.wikipedia.org/wiki/Waveguide_(electromagnetism)

[7] Wikipedia. [Online]. Available: https://en.wikipedia.org/wiki/Horn_antenna

[8] Labvolt company. [Online]. Available: https://www.labvolt.com/

[9] ELVA-1 Company. [Online]. Available: http://www.elva-1.com/

[10] Pasternack Enterprises, Inc. [Online]. Available: https://www.pasternack.com/

[11] R. Garg and K. C. Gupta, "Expressions for wavelength and impedance of a slotline (letters)," *IEEE Transactions on Microwave Theory and Techniques*, vol. 24, no. 8, pp. 532–532, Aug. 1976.

[12] T. G. Bryant and J. A. Weiss, "Parameters of microstrip transmission lines and of coupled pairs of microstrip lines," *IEEE Transactions on Microwave Theory and Techniques*, vol. 16, no. 12, pp. 1021–1027, Dec. 1968.

[13] C. P. Wen, "Coplanar waveguide, a surface strip transmission line suitable for nonreciprocal gyromagnetic device applications," in *Proc. G-MTT International Microwave Symposium*, Dallas, TX, May 1969, pp. 110–115.

[14] A. J. Kelly, H. C. Okean, and S. J. Foti, "Low noise microwave and millimeter wave integrated circuit mixers," in *Proc. IEEE-MTT-S International Microwave Symposium*, Palo Alton, CA, May 1975, pp. 146–148.

[15] R. Sorrentino and G. Leuzzi, "Full-wave analysis of integrated transmission lines on layered lossy media," *Electronics Letters*, vol. 18, no. 14, pp. 607–608, July 1982.

[16] J. Magarshack, "Microwave integrated circuits on gaas," in *Proc. 12th European Microwave Conference*, Helsinki, Finland, Sep. 1982, pp. 5–15.

[17] B. Billade, O. Nystrom, D. Meledin, E. Sundin, I. Lapkin, M. Fredrixon, V. Desmaris, H. Rashid, M. Strandberg, S. E. Ferm, A. Pavolotsky, and V. Belitsky, "Performance of the first alma band 5 production cartridge," *IEEE Transactions on Terahertz Science and Technology*, vol. 2, no. 2, pp. 208–214, Mar. 2012.

[18] J. Y. Chenu, A. Navarrini, Y. Bortolotti, G. Butin, A. L. Fontana, S. Mahieu, D. Maier, F. Mattiocco, P. Serres, M. Berton, O. Garnier, Q. Moutote, M. Parioleau, B. Pissard, and J. Reverdy, "The front-end of the NOEMA interferometer," *IEEE Transactions on Terahertz Science and Technology*, vol. 6, no. 2, pp. 223–237, Mar.

[19] A1 Microwave company. [Online]. Available: http://www.a1microwave.com/

[20] F. Shigeki, "Waveguide line," Japanese Patent 06 053 711, 1994.

[21] A. Piloto, K. Leahy, B. Flanick, and K. Zaki, "Waveguide filters having a layered dielectric structure," 1995.

[22] H. Uchimura, T. Takenoshita, and M. Fujii, "Development of the "laminated waveguide"," in *IEEE MTT-S International Microwave Symposium Digest*, vol. 3, Baltimore, MD, June 1998, pp. 1811–1814.

[23] M. Ando, J. Hirokawa, T. Yamamoto, A. Akiyama, Y. Kimura, and N. Goto, "Novel single-layer waveguides for high-efficiency millimeter-wave arrays," *IEEE Transactions on Microwave Theory and Techniques*, vol. 46, no. 6, pp. 792–799, Jun. 1998.

[24] D. Deslandes, "Etude et developpement du guide d'ondes integre au substrat pour la conception de systemes en ondes millimetriques," Ph.D. dissertation, Ecole Polytechnique, Montreal, 2005.

[25] F. Parment, A. Ghiotto, T. P. Vuong, J. M. Duchamp, and K. Wu, "Air-filled substrate integrated waveguide for low-loss and high power-handling millimeter-wave substrate integrated circuits," *IEEE Transactions on Microwave Theory and Techniques*, vol. 63, no. 4, pp. 1228–1238, Apr. 2015.

[26] ——, "Double dielectric slab-loaded air-filled siw phase shifters for high-performance millimeter-wave integration," *IEEE Transactions on Microwave Theory and Techniques*, vol. 64, no. 9, pp. 2833–2842, Sep. 2016.

[27] T. Djerafi, D. Hammou, K. Wu, and S. O. Tatu, "Ring-shaped substrate integrated waveguide wilkinson power dividers/combiners," *IEEE Transactions on Components, Packaging and Manufacturing Technology*, vol. 4, no. 9, pp. 1461–1469, Sep. 2014.

[28] D. Deslandes and K. Wu, "Accurate modelling, wave mechanisms, and design considerations of a substrate integrated waveguide," *IEEE Transactions on Microwave Theory and Techniques*, vol. 54, no. 6, pp. 2516–2526, June 2006.

[29] Y. Cassivi, L. Perregrini, P. Arcioni, M. Bressan, K. Wu, and G. Conciauro, "Dispersion characteristics of substrate integrated rectangular waveguide," *IEEE Microwave and Wireless Components Letters*, vol. 12, no. 9, pp. 333–335, Sep. 2002.

[30] F. Taringou and J. Bornemann, "Return-loss investigation of the equivalent width of substrate-integrated waveguide circuits," in *IEEE MTT-S International Microwave Workshop Series on Millimeter Wave Integration Technologies*, Sitges, Spain, Sep. 2011, pp. 140–143.

[31] R. Kazemi, R. Sadeghzadeh, and A. Fathy, "A new compact wide band 8-way SIW power divider at x-band," in *Proc. Antennas and Propagation Conference (LAPC)*, Loughborough, United Kingdom, Jan. 2011, pp. 1–4.

[32] G. Li, K. Song, F. Zhang, and Y. Zhu, "Novel four-way multilayer SIW power divider with slot coupling structure," *IEEE Microwave and Wireless Components Letters*, vol. 25, no. 12, pp. 799–801, Dec. 2015.

[33] Z. C. Hao, W. q. Ding, and W. Hong, "Developing low-cost -band SIW bandpass filters using the commercially available printed-circuit-board technology," *IEEE Transactions on Microwave Theory and Techniques*, vol. 64, no. 6, pp. 1775–1786, June 2016.

[34] B. Muneer, Z. Qi, and X. Shanjia, "A broadband tunable multilayer substrate integrated waveguide phase shifter," *IEEE Microwave and Wireless Components Letters*, vol. 25, no. 4, pp. 220–222, Apr. 2015.

References

[35] A. Doghri, T. Djerafi, A. Ghiotto, and K. Wu, "Substrate integrated waveguide directional couplers for compact three-dimensional integrated circuits," *IEEE Transactions on Microwave Theory and Techniques*, vol. 63, no. 1, pp. 209–221, Jan. 2015.

[36] P. Wu, S. Liao, and Q. Xue, "A substrate integrated slot antenna array using simplified feeding network based on higher order cavity modes," *IEEE Transactions on Antennas and Propagation*, vol. 64, no. 1, pp. 126–135, Jan. 2016.

[37] Z. Yang, B. Luo, J. Dong, and T. Yang, "X-band low-phase noise oscillator employing substrate integrated waveguide dual-mode filter," *Electronics Letters*, vol. 51, no. 6, pp. 494–495, Mar. 2015.

[38] K. Wang, S. Wong, G. Sun, Z. Chen, L. Zhu, and Q. Chu, "Synthesis method for substrate-integrated waveguide bandpass filter with even-order chebyshev response," *IEEE Transactions on Components, Packaging and Manufacturing Technology*, vol. 6, no. 1, pp. 126–135, Jan. 2016.

[39] J. X. Xu, X. Y. Zhang, X. L. Zhao, and Q. Xue, "Synthesis and implementation of LTCC bandpass filter with harmonic suppression," *IEEE Transactions on Components, Packaging and Manufacturing Technology*, vol. 6, no. 4, pp. 596–604, Apr. 2016.

[40] T. Tajima, H. J. Song, and M. Yaita, "Compact THz LTCC receiver module for 300 GHz wireless communications," *IEEE Microwave and Wireless Components Letters*, vol. 26, no. 4, pp. 291–293, Apr.

[41] R. Moro, S. Agneessens, H. Rogier, and M. Bozzi, "Wearable textile antenna in substrate integrated waveguide technology," *Electronics Letters*, vol. 48, no. 16, pp. 985–987, Aug. 2012.

[42] R. Moro, S. Agneessens, H. Rogier, A. Dierck, and M. Bozzi, "Textile microwave components in substrate integrated waveguide technology," *IEEE Transactions on Microwave Theory and Techniques*, vol. 63, no. 2, pp. 422–432, Feb. 2015.

[43] C. Tomassoni, R. Bahr, M. Tentzeris, M. Bozzi, and L. Perregrini, "3d printed substrate integrated waveguide filters with locally controlled dielectric permittivity," in *46th European Microwave Conference (EuMC)*, London, United Kingdom, Oct., pp. 253–256.

[44] M. Bozzi, C. Tomassoni, L. Perregrini, R. Bahr, and M. Tentzeris, "Additive manufacturing of substrate integrated waveguide components," in *Proc. IEEE MTT-S International Microwave Workshop Series on Advanced Materials and Processes for RF and THz Applications (IMWS-AMP)*, Chengdu, China, July 2016, pp. 1–4.

[45] S. Moscato, M. Pasian, M. Bozzi, L. Perregrini, R. Bahr, T. Le, and M. M. Tentzeris, "Exploiting 3d printed substrate for microfluidic siw sensor," in *Proc. European Microwave Conference (EuMC)*, Paris, France, Sep. 2015, pp. 28–31.

[46] Y. Shang, H. Yu, C. Yang, Y. Liang, and W. M. Lim, "A 239-281ghz sub-thz imager with 100 mhz resolution by cmos direct-conversion receiver with on-chip circular-polarized siw antenna," in *Proc. IEEE Custom Integrated Circuits Conference*, San Jose, CA, Sep. 2014, pp. 1–4.

[47] H. J. Tang, G. Q. Yang, J. X. Chen, W. Hong, and K. Wu, "Millimeter-wave and terahertz transmission loss of cmos process-based substrate integrated waveguide," in *IEEE/MTT-S International Microwave Symposium Digest*, Montreal, QC, Canada, June 2012, pp. 1–3.

[48] M. S. Mahani and G. Roberts, "A sub-thz folded substrate integrated waveguide in ibm 130 nm cmos process," in *Proc. Global Symposium on Millimeter-Waves (GSMM)*, Montreal, QC, Canada, May 2015, pp. 1–3.

[49] Z. Hao, W. Hong, J. Chen, H. Zhou, and K. Wu, "Single-layer substrate integrated waveguide directional couplers," *Microwaves, Antennas and Propagation, IEE Proceedings*, vol. 153, no. 5, pp. 426–431, Oct. 2006.

[50] Z. Liu and G. Xiao, "Design of SIW-based multi-aperture couplers using ray tracing method," *IEEE Transactions on Components, Packaging and Manufacturing Technology*, vol. 7, no. 1, pp. 106–113, Jan. 2017.

[51] Q. Liu, D. Zhou, S. Wang, and Y. Zhang, "Highly-selective pseudoelliptic filters based on dual-mode substrate integrated waveguide resonators," *Electronics Letters*, vol. 52, no. 14, pp. 1233–1235, June 2016.

[52] L. Silvestri, E. Massoni, M. Bozzi, L. Perregrini, C. Tomassoni, and A. Coves, "A new class of SIW filters based on periodically perforated dielectric substrate," in *46th European Microwave Conference (EuMC)*, London, United Kindgom, 2016, pp. 775–778.

[53] M. Pasian, L. Silvestri, C. Rave, M. Bozzi, L. Perregrini, A. F. Jacob, and K. K. Samanta, "Substrate-integrated-waveguide e-plane 3-dB power-divider/combiner based on resistive layers," *IEEE Transactions on Microwave Theory and Techniques*, vol. 65, no. 99, pp. 1498 – 1510, May 2017.

[54] T. Li and W. Dou, "Broadband substrate-integrated waveguide t-junction with arbitrary power-dividing ratio," *Electronics Letters*, vol. 51, no. 3, pp. 259–260, Feb. 2015.

[55] M. Mujumdar and A. Alphones, "Eighth-mode substrate integrated resonator antenna at 2.4 GHz," *IEEE Antennas and Wireless Propagation Letters*, vol. 15, pp. 853–856, Sep. 2015.

[56] D. Guan, C. Ding, Z. Qian, Y. Zhang, Y. Guo, and K. Gong, "Broadband high gain SIW cavity-backed circular polarized array antenna," *IEEE Transactions on Antennas and Propagation*, vol. 64, no. 99, pp. 1493 – 1497, Jan. 2016.

[57] P. Wu, S. Liao, and Q. Xue, "A substrate integrated slot antenna array using simplified feeding network based on higher order cavity modes," *IEEE Transactions on Antennas and Propagation*, vol. 64, no. 1, pp. 126–135, Jan. 2016.

[58] D. Mencarelli, A. Morini, F. Prudenzano, G. Venanzoni, F. Bigelli, O. Losito, and M. Farina, "Broadband single-layer slotted array antenna in siw technology," *IEEE Antennas and Wireless Propagation Letters*, vol. 15, pp. 263–265, June 2016.

[59] K. Tekkouk, M. Ettorre, L. L. Coq, and R. Sauleau, "Multibeam siw slotted waveguide antenna system fed by a compact dual-layer rotman lens," *IEEE Transactions on Antennas and Propagation*, vol. 64, no. 2, pp. 504–514, Feb. 2016.

[60] T. Djerafi, N. J. G. Fonseca, and K. Wu, "Planar ku-band 4x4 nolen matrix in siw technology," *IEEE Transactions on Microwave Theory and Techniques*, vol. 58, no. 2, pp. 259–266, Feb. 2010.

[61] R. F. Xu, A. J. Farrall, and P. R. Young, "Analysis of loaded substrate integrated waveguides and attenuators," *IEEE Microwave and Wireless Components Letters*, vol. 24, no. 1, pp. 62–64, Jan. 2014.

[62] Z. Liu, L. Zhu, and G. Xiao, "A novel microwave attenuator on multilayered substrate integrated waveguide," *IEEE Transactions on Components, Packaging and Manufacturing Technology*, vol. 6, no. 7, pp. 1106–1112, July 2016.

[63] D. S. Eom and H. Y. Lee, "Broadband half mode substrate integrated waveguide attenuator in 7.29 - 14.90 ghz," *IEEE Microwave and Wireless Components Letters*, vol. 25, no. 9, pp. 564–566, Sep. 2015.

[64] I. Boudreau, K. Wu, and D. Deslandes, "Broadband phase shifter using air holes in substrate integrated waveguide," in *Proc. IEEE MTT-S International Microwave Symposium*, Baltimore, MD, June 2011, pp. 1–4.

[65] M. Ebrahimpouri, S. Nikmehr, and A. Pourziad, "Broadband compact siw phase shifter using omega particles," *IEEE Microwave and Wireless Components Letters*, vol. 24, no. 11, pp. 748–750, Nov. 2014.

[66] B. Muneer, Z. Qi, and X. Shanjia, "A broadband tunable multilayer substrate integrated waveguide phase shifter," *IEEE Microwave and Wireless Components Letters*, vol. 25, no. 4, pp. 220–222, Apr. 2015.

[67] W. Huang, J. Zhou, and P. Chen, "An x-band low phase noise free-running oscillator using substrate integrated waveguide dual-mode bandpass filter with circular cavity," *IEEE Microwave and Wireless Components Letters*, vol. 25, no. 1, pp. 40–42, Jan. 2015.

[68] Z. Yang, B. Luo, J. Dong, and T. Yang, "X-band low-phase noise oscillator employing substrate integrated waveguide dual-mode filter," *Electronics Letters*, vol. 51, no. 6, pp. 494–495, Mar. 2015.

[69] T. V. Duong, W. Hong, V. H. Tran, T. A. Vu, W. C. Huang, and P. N. Choubey, "An alternative technique to minimize the phase noise of x-band oscillators using improved group delay siw filters," *IEEE Microwave and Wireless Components Letters*, vol. 27, no. 2, pp. 153–155, Feb. 2017.

[70] M. Abdolhamidi and M. Shahabadi, "X-band substrate integrated waveguide amplifier," *IEEE Microwave and Wireless Components Letters*, vol. 18, no. 12, pp. 815–817, Dec. 2008.

[71] K. W. Eccleston, "Siw distributed amplifier: Analysis, prospects and challenges," in *Proc. IEEE MTT-S International Conference on Numerical Electromagnetic and Multiphysics Modeling and Optimization (NEMO)*, Beijing, China, 2016, pp. 1–2.

[72] F. Parment, "Guides d´onde integrés au substrat (siw) multicouches à haute performance pour des circuits millimétriques à faible coût," Ph.D. dissertation, Universite Grenoble Alpes, Grenoble, 2016.

[73] A. Belenguer, H. Esteban, and V. E. Boria, "Novel empty substrate integrated waveguide for high-performance microwave integrated circuits," *IEEE Transactions on Microwave Theory and Techniques*, vol. 62, no. 4, pp. 832–839, Apr. 2014.

[74] K. Entesari, A. P. Saghati, V. Sekar, and M. Armendariz, "Tunable siw structures: Antennas, vcos, and filters," *IEEE Microwave Magazine*, vol. 16, no. 5, pp. 34–54, June 2015.

[75] W. L. Barrow and H. Schaevitz, "Hollow pipes of relatively small dimensions," *Electrical Engineering*, vol. 60, no. 3, pp. 119–122, Mar. 1941.

[76] S. B. Cohn, "Properties of ridge wave guide," *Proceedings of the IRE*, vol. 35, no. 8, pp. 783–788, Aug. 1947.

[77] H.-W. Yao, A. Abdelmonem, J.-F. Liang, and K. A. Zaki, "Analysis and design of microstrip-to-waveguide transitions," *IEEE Transactions on Microwave Theory and Techniques*, vol. 42, no. 12, pp. 2371–2380, Dec. 1994.

[78] S. Hopfer, "The design of ridged waveguides," *IRE Transactions on Microwave Theory and Techniques*, vol. 3, no. 5, pp. 20–29, Oct. 1955.

[79] Y. Ding and K. Wu, "Substrate integrated waveguide-to-microstrip transition in multilayer substrate," *IEEE Transactions on Microwave Theory and Techniques*, vol. 55, no. 12, pp. 2839–2844, Dec. 2007.

[80] M. Bozzi, S. A. Winkler, and K. Wu, "Broadband and compact ridge substrate-integrated waveguides," *IET Microwaves, Antennas Propagation*, vol. 4, no. 11, pp. 1965–1973, Nov. 2010.

[81] S. Moscato, R. Moro, M. Pasian, M. Bozzi, and L. Perregrini, "Two-material ridge substrate integrated waveguide for ultra-wideband applications," *IEEE Transactions on Microwave Theory and Techniques*, vol. 63, no. 10, pp. 3175–3182, Oct. 2015.

[82] C. Li, W. Che, P. Russer, and Y. L. Chow, "Propagation and band broadening effect of planar ridged substrate-integrated waveguide (rsiw)," in *Proc. International Conference on Microwave and Millimeter Wave Technology*, vol. 2, Nanjing, China, Apr. 2008, pp. 467–470.

[83] Y. L. Chow and W. Che, "Successive siw (substrate integrated waveguides) types for width reductions by physical reasoning and formulas by analytical (use of) mom," in *Proc. International Conference on Microwave and Millimeter Wave Technology*, vol. 4, Nanjing, China, Apr. 2008, pp. 1746–1749.

[84] N. Nguyen-Trong, T. Kaufmann, L. Hall, and C. Fumeaux, "Variational analysis of folded substrate-integrated waveguides," *IEEE Microwave and Wireless Components Letters*, vol. 25, no. 6, pp. 352–354, June 2015.

[85] N. Grigoropoulos and P. R. Young, "Compact folded waveguides," in *Proc. European Microwave Conference, 2004.*, vol. 2, Amsterdam, The Netherlands, Oct. 2004, pp. 973–976.

[86] A. Doghri, A. Ghiotto, T. Djerafi, and K. Wu, "Corrugated siw l-folded antipodal parabolic tapered slot antenna," in *Proc. Asia Pacific Microwave Conference*, Kaohsiung, Taiwan, Dec. 2012, pp. 893–895.

[87] W. Che, L. Geng, K. Wu, and Y. L. Chow, "Theoretical investigation and experimental verification of compact folded substrate integrated waveguide," in *Proc. European Microwave Conference*, Munich, Germany, Oct. 2007, pp. 380–383.

[88] W. Che, L. Geng, K. Deng, and Y. L. Chow, "Analysis and experiments of compact folded substrate-integrated waveguide," *IEEE Transactions on Microwave Theory and Techniques*, vol. 56, no. 1, pp. 88–93, Jan. 2008.

[89] N. Nguyen-Trong, T. Kaufmann, L. Hall, and C. Fumeaux, "Variational analysis of folded substrate-integrated waveguides," *IEEE Microwave and Wireless Components Letters*, vol. 25, no. 6, pp. 352–354, June 2015.

[90] M. S. Mahani and G. W. Roberts, "A mmwave folded substrate integrated waveguide in a 130-nm cmos process," *IEEE Transactions on Microwave Theory and Techniques*, vol. 65, no. 8, pp. 2775–2788, Aug. 2017.

[91] H. Y. Chien, T. M. Shen, T. Y. Huang, W. H. Wang, and R. B. Wu, "Miniaturized bandpass filters with double-folded substrate integrated waveguide resonators in ltcc," *IEEE Transactions on Microwave Theory and Techniques*, vol. 57, no. 7, pp. 1774–1782, July 2009.

[92] R. Zhang, Z. Wang, B. Yan, and R. Xu, "Fsiw cavity filter and derivative fsiw cavity and its filters with ltcc technology," in *Proc. Asia Pacific Microwave Conference*, Singapore, Singapore, Dec. 2009, pp. 1360–1363.

[93] L. S. Wu, X. L. Zhou, and W. Y. Yin, "A novel multilayer partial h-plane filter implemented with folded substrate integrated waveguide (fsiw)," *IEEE Microwave and Wireless Components Letters*, vol. 19, no. 8, pp. 494–496, Aug. 2009.

[94] W. Hong, B. Liu, Y. Wang, Q. Lai, H. Tang, X. X. Yin, Y. D. Dong, Y. Zhang, and K. Wu, "Half mode substrate integrated waveguide: A new guided wave structure for microwave and millimeter wave application," in *Proc. Joint 31st International Conference on Infrared Millimeter Waves and 14th International Conference on Teraherz Electronics*, Sep. 2006, pp. 219–219.

[95] B. Liu, W. Hong, L. Tian, H.-B. Zhu, W. Jiang, and K. Wu, "Half mode substrate integrated waveguide (hmsiw) multi-way power divider," in *Proc. Asia-Pacific Microwave Conference*, Yokohama, Japan, Dec. 2006, pp. 917–920.

[96] J. Chen, W. Hong, P. Yan, B. Liu, Y. Wang, and K. Wu, "Design of a six-port junction using half-mode substrate integrated waveguide," in *Proc. Asia-Pacific Microwave Conference*, Bangkok, Thailand, Dec. 2007, pp. 1–4.

[97] B. Liu, W. Hong, Y. Q. Wang, Q. H. Lai, and K. Wu, "Half mode substrate integrated waveguide (hmsiw) 3-db coupler," *IEEE Microwave and Wireless Components Letters*, vol. 17, no. 1, pp. 22–24, Jan. 2007.

[98] B. Liu, W. Hong, Y. Zhang, J. x. Chen, and K. Wu, "Half-mode substrate integrated waveguide (hmsiw) double-slot coupler," *Electronics Letters*, vol. 43, no. 2, pp. 113–114, Jan. 2007.

[99] S. Moscato, C. Tomassoni, M. Bozzi, and L. Perregrini, "Quarter-mode cavity filters in substrate integrated waveguide technology," *IEEE Transactions on Microwave Theory and Techniques*, vol. 64, no. 8, pp. 2538–2547, Aug. 2016.

[100] P. Li, H. Chu, and R. S. Chen, "Design of compact bandpass filters using quarter-mode and eighth-mode siw cavities," *IEEE Transactions on Components, Packaging and Manufacturing Technology*, vol. 7, no. 6, pp. 956–963, June 2017.

[101] Q. Lai, C. Fumeaux, W. Hong, and R. Vahldieck, "Characterization of the propagation properties of the half-mode substrate integrated waveguide," *IEEE Transactions on Microwave Theory and Techniques*, vol. 57, no. 8, pp. 1996–2004, Aug. 2009.

[102] N. Nguyen-Trong, T. Kaufmann, and C. Fumeaux, "A semi-analytical solution of a tapered half-mode substrate-integrated waveguide with application to rapid antenna optimization," *IEEE Transactions on Antennas and Propagation*, vol. 62, no. 6, pp. 3189–3200, June 2014.

[103] K. Wu, *Slow Wave Structures.* John Wiley and Sons, Inc., 2001.

[104] J. P. K. Gilb and C. A. Balanis, "Mis slow-wave structures over a wide range of parameters," *IEEE Transactions on Microwave Theory and Techniques*, vol. 40, no. 12, pp. 2148–2154, Dec. 1992.

[105] S. Chen, R. Vahldieck, J. Huang, and M. Kim, "Field theory analysis of slow-wave propagation on silicon based coplanar mis transmission lines," in *IEEE MTT-S International Microwave Symposium Digest*, vol. 1, San Francisco, CA, June 1996, pp. 291–294.

[106] D. Jager, "Slow-wave propagation along variable schottky-contact microstrip line," *IEEE Transactions on Microwave Theory and Techniques*, vol. 24, no. 9, pp. 566–573, Sep. 1976.

[107] Y. Fukuoka and T. Itoh, "Slow-wave propagation on mis periodic coplanar waveguide," *Electronics Letters*, vol. 19, no. 2, pp. 37–38, Jan. 1983.

[108] Y. N. Pchelnikov, "Advantages of slowed electromagnetic waves," in *Proc. IEEE SoutheastCon*, Columbia, SC, Aug. 2002, pp. 375–380.

[109] K. Zhang and D. Li, *Electromagnetic theory for microwaves and optoelectronics.* Springer Science, 2013.

[110] L. Brillouin, "Wave guides for slow waves," *Journal of Applied Physics*, vol. 19, no. 11, pp. 1023–1041, 1948.

[111] [Online]. Available: http://www.americanradiohistory.com/Archive-Electronics/40s/Electronics-1940-11.pdf

[112] [Online]. Available: http://www.americanradiohistory.com/Archive-Tele-Tech/Tele-Tech-1953-04.pdf

[113] H. Hasegawa, M. Furukawa, and H. Yanai, "Properties of microstrip line on si-sio2 system," *IEEE Transactions on Microwave Theory and Techniques*, vol. 19, no. 11, pp. 869–881, Nov. 1971.

[114] J. M. Jaffe, "A high-frequency variable delay line," *IEEE Transactions on Electron Devices*, vol. 19, no. 12, pp. 1292–1294, Dec. 1972.

[115] A. Podell, "A high directivity microstrip coupler technique," in *G-MTT International Microwave Symposium*, Newport Beach, CA, May 1970, pp. 33–36.

[116] A. Kianinejad, Z. N. Chen, and C. W. Qiu, "Design and modeling of spoof surface plasmon modes-based microwave slow-wave transmission line," *IEEE Transactions on Microwave Theory and Techniques*, vol. 63, no. 6, pp. 1817–1825, June 2015.

[117] W. S. Chang and C. Y. Chang, "A high slow-wave factor microstrip structure with simple design formulas and its application to microwave circuit design," *IEEE Transactions on Microwave Theory and Techniques*, vol. 60, no. 11, pp. 3376–3383, Nov. 2012.

[118] J. J. Shi, M. S. Chen, and X. L. Wu, "A design of ku-band slow-wave bandpass filter," in *Proc. International Conference on Microwave and Millimeter Wave Technology*, Chengdu, China, May 2010, pp. 2063–2066.

[119] H.-M. Kim and B. Lee, "Bandgap and slow/fast-wave characteristics of defected ground structures (dgss) including left-handed features," *IEEE Transactions on Microwave Theory and Techniques*, vol. 54, no. 7, pp. 3113–3120, July 2006.

[120] V. Zhurbenko, V. Krozer, and P. Meincke, "Miniature microwave bandpass filter based on ebg structures," in *Proc. European Microwave Conference*, Manchester, UK, Sep. 2006, pp. 792–794.

[121] T. S. D. Cheung and J. R. Long, "Shielded passive devices for silicon-based monolithic microwave and millimeter-wave integrated circuits," *IEEE Journal of Solid-State Circuits*, vol. 41, no. 5, pp. 1183–1200, May 2006.

[122] I. C. H. Lai, H. Tanimoto, and M. Fujishima, "Characterization of high q transmission line structure for advanced cmos processes," *IEICE Transactions on Electronics*, vol. 89, no. 12, pp. 1872–1879, Dec. 2006.

[123] A. L. Franc, E. Pistono, G. Meunier, D. Gloria, and P. Ferrari, "A lossy circuit model based on physical interpretation for integrated shielded slow-wave cmos coplanar waveguide structures," *IEEE Transactions on Microwave Theory and Techniques*, vol. 61, no. 2, pp. 754–763, Feb. 2013.

[124] C. H. Tseng and Y. T. Chen, "Design and implementation of new 3-db quadrature couplers using pcb and silicon-based ipd technologies," *IEEE Transactions on Components, Packaging and Manufacturing Technology*, vol. 6, no. 5, pp. 675–682, May 2016.

[125] B. Yang, E. Skafidas, and R. J. Evans, "Slow-wave slot microstrip transmission line and bandpass filter for compact millimetre-wave integrated circuits on bulk complementary metal oxide semiconductor," *IET Microwaves, Antennas Propagation*, vol. 6, no. 14, pp. 1548–1555, Nov. 2012.

[126] A. Niembro-Martin, V. Nasserddine, E. Pistono, H. Issa, A.-L. Franc, T.-P. Vuong, and P. Ferrari, "Slow-wave substrate integrated waveguide," *IEEE Transactions on Microwave Theory and Techniques*, vol. 62, no. 8, pp. 1625–1633, Aug. 2014.

[127] H. Jin, K. Wang, J. Guo, S. Ding, and K. Wu, "Slow-wave effect of substrate integrated waveguide patterned with microstrip polyline," *IEEE Transactions on Microwave Theory and Techniques*, vol. 64, no. 6, pp. 1717–1726, June 2016.

[128] H. Jin, Y. Zhou, Y. M. Huang, and K. Wu, "Slow-wave propagation properties of substrate integrated waveguide based on anisotropic artificial material," *IEEE Transactions on Antennas and Propagation*, no. 99, pp. 1–1, 2017.

Chapter 2

Theoretical description of a Slow-Wave Substrate Integrated Waveguide Technology

Contents

2.1 Introduction 36

2.2 General considerations 36

2.2.1 Useful properties of periodic structures 36

2.2.2 Velocity, stored energy and transmitted power 38

2.2.3 Increased dissipation, a consequence of the velocity reduction . . 40

2.2.4 In practice: the required spatial energies separation 42

2.2.5 Discussion 46

2.3 Slow-wave effect induced by a uniform distribution of blind via holes in a parallel-plate waveguide configuration 47

2.3.1 Definition of the topology and associated simulation methods . . 47

2.3.2 Physical properties 50

2.3.3 Parametric analysis for large wavelengths 57

2.4 A Slow-wave substrate integrated waveguide 62

2.4.1 Motivations and modelling 62

2.4.2 Electrical performance 63

2.4.3 Brief parametric analysis 65

2.4.4 Design rules 68

2.5 Conclusion 70

References 71

2.1 Introduction

In this second chapter, the main objective is to introduce a theoretical perspective on the proposed slow-wave substrate integrated waveguide (SW-SIW) topology.

In order to derive its main characteristics, some general theoretical considerations will first be introduced in section 2.2. The results presented in this first part rely mostly on periodic structures properties. An attempt to describe the slow-wave effect as based on energy considerations will be presented, with a specific focus on the spatial separation necessity. Then, a quantitative analysis is performed considering an ideal parallel-plate configuration, which aims at relating energy space distribution and slow-wave effect. The impact on dielectric and metallic dissipations is also dealt with.

In section 2.3, the theoretical results will be applied to a slow-wave parallel-plate waveguide. This configuration is used as a first step toward the SW-SIW, which differs only by the addition of lateral via holes. The insertion of blind via holes inside the waveguide is presented as a way to obtain a significant slow-wave effect. In this section, an approximate model based on the previously introduced energy considerations will be detailed. Finally, a parametric analysis showing the impact of several geometric parameters is performed.

Finally, the effect of additional lateral via holes to create a closed waveguide is described in section 2.4. Its main properties are then compared to the conventional SIW.

2.2 General considerations

2.2.1 Useful properties of periodic structures

As mentioned in the introduction, the velocity reduction can be achieved by two different means. The first one is to create a specific arrangement of materials in the transverse section, such as different dielectrics, semi-conductors or more complex materials. The second one relies on the introduction of spatially periodic boundary conditions or material properties in the longitudinal direction. In this work we will focus on the second kind of slow-wave structures, and more precisely based on periodic boundary conditions.

First of all, some precisions will be given on velocity definitions in the context of periodic structures. Let's consider a solution of Maxwell equations in a lossless s-periodic structure along z-axis. This mode is defined by its phase constant β, so that electric field can be written as in (2.1) in the cartesian coordinate system. The same formulation could also be used for magnetic field. Under the assumption that $\bar{\boldsymbol{E}}$ is a s-periodic function of z this form satisfies Floquet's theorem.

$$\boldsymbol{E} = \bar{\boldsymbol{E}}(x, y, z)e^{-j\beta z}e^{j\omega t} \tag{2.1}$$

Furthermore, a Fourier expansion of $\bar{\boldsymbol{E}}$ can be used because of its periodicity, resulting in equation (2.2), where again s is the period length.

$$\bar{\boldsymbol{E}}(x,y,z) = \sum_n \boldsymbol{E_n}(x,y)e^{-j(\frac{2\pi n}{s})z} \tag{2.2}$$

The modal field $\boldsymbol{E}$ is therefore an infinite sum of harmonic fields. These spatial harmonics, also called Hartree harmonics do not necessary satisfy the boundary conditions when considered alone. By integration of the last exponential in the sum one obtains (2.3), where β_n is defined by (2.4).

$$\boldsymbol{E}(x,y,z) = \sum_n \boldsymbol{E_n}(x,y)e^{-j(\beta_n z-\omega t)} \tag{2.3}$$

$$\beta_n = \beta + \frac{2\pi n}{s} \quad , -\infty < n < +\infty \tag{2.4}$$

Consequently, each of every harmonic has a separate phase constant β_n, which corresponds to a phase velocity v_{pn} (see (2.5)).

$$v_{pn} = \frac{\omega}{\beta_n} = \frac{\omega}{\beta + \frac{2\pi n}{s}} \tag{2.5}$$

The zero-order harmonic ($n = 0$) has a phase constant β, defining all other phase constants by addition of the term $\frac{2\pi n}{s}$. Therefore, only the determination of β is necessary to define all other phase constants. Interestingly, the group velocity v_{gn} is constant and equal to that of the zero-order harmonic v_{g0} (see (2.6)), it will thus be written v_g.

$$v_{gn} = \left(\frac{\partial \beta_n}{\partial \omega}\right)^{-1} = \left(\frac{\partial \beta}{\partial \omega}\right)^{-1} = v_g \tag{2.6}$$

In the following paragraph two theorems will be introduced in the context of lossless periodic structures, they were derived by Bell and other authors. These two theorems are of particular interest in the context of slow-wave structures. The demonstrations of these two theorems are readily available in [1] and [2]. A periodic waveguide of longitudinal period s is considered, an arbitrary transverse cut plane of section S_t is also defined. The total volume of one section is denoted V. The two theorems are given below, as stated in [1].

Theorem 1 *The time-average stored electrical energy per period is equal to the time-average stored magnetic energy per period in the pass bands.*

Theorem 2 *The time-average power flow in the pass bands is equal to the group velocity times the time-average stored electrical and magnetic energy per period divided by the period.*

The mathematical representations of these two theorems are given by equations (2.7) and (2.8), respectively.

$$\iiint_V \frac{1}{4}\varepsilon \boldsymbol{E}\cdot\boldsymbol{E}^* dV - \iiint_V \frac{1}{4}\mu \boldsymbol{H}\cdot\boldsymbol{H}^* dV = W_e - W_m = 0 \tag{2.7}$$

$$\frac{1}{2}\,\mathrm{Re}\iint_{S_t}\boldsymbol{E}\times\boldsymbol{H}^{*}dS=\left[\iiint_{V}\left(\frac{1}{4}\varepsilon\boldsymbol{E}\cdot\boldsymbol{E}^{*}+\frac{1}{4}\mu\boldsymbol{H}\cdot\boldsymbol{H}^{*}\right)dV\right]\frac{v_g}{s} \tag{2.8}$$

This last result can be of high interest for understanding the slow-wave mechanism, as it relates energies and a velocity quantity v_g.

In the literature, a common feature of all slow-wave topologies is the spatial separation of electric and magnetic energies. Let's first consider why is is a necessary feature of slow-wave propagation. This separation principle is generally evoked along with the necessity to increase stored energy in the structure [3]-[4]. However, authors usually then describe specific cases where L-C models are available for example. To our best knowledge, a general explanation of this principle was not given in any book or paper. We will try to highlight the reasons behind the necessity to spatially separate energies in a general case and define some quantitative analysis for an hypothetical ideal structure.

2.2.2 Velocity, stored energy and transmitted power

2.2.2.1 Phase and group velocities in the waveguide context

From the considerations given above, and especially the second theorem, some insight can be given concerning the velocity reduction. However, the slow-wave factor is usually defined by a ratio of phase, instead of group velocities.

In the context of TEM modes and transmission lines in general, the equivalence is straightforward as $v_p = v_g$.

For non-TEM modes, as for instance in rectangular waveguides (integrated or not), the only source of dispersion, i.e. of inequality between v_g and v_p is the existence of cut-off frequencies. It manifests itself by very strong variations of both v_p and v_g for varying frequencies. These variations can be interpreted in the context of the multiple-reflection model, as illustrated in Figure 2.1 [5] for the fundamental mode in a rectangular waveguide. As frequency increases, the reflected waves angle of incidence on the lateral walls will change, thus affecting directly its projected velocity in the longitudinal direction.

For such a waveguide, the phase and group velocities expressions are given by (2.9) and (2.10), respectively. In these expressions, c stands for the light velocity in the considered medium. At the cut-off frequency, v_p tends to infinity, while v_g is 0.

$$v_p=\frac{\omega}{\beta}=\frac{c}{\sqrt{1-\frac{{\omega_c}^2}{\omega}}} \tag{2.9}$$

$$v_g=\frac{\partial\omega}{\partial\beta}=c\sqrt{1-\frac{{\omega_c}^2}{\omega}} \tag{2.10}$$

In these conditions, the slow-wave factor can only be calculated using the group velocity if two conditions are fulfilled. First, the cut-off frequencies should be identical between the reference waveguide and the slow wave one. Secondly, the slow-wave effect should be introducing no additional dispersion, affecting only the intrinsic velocity c. In practice, conditions for a low dispersion should be required. Ideally, the proposed

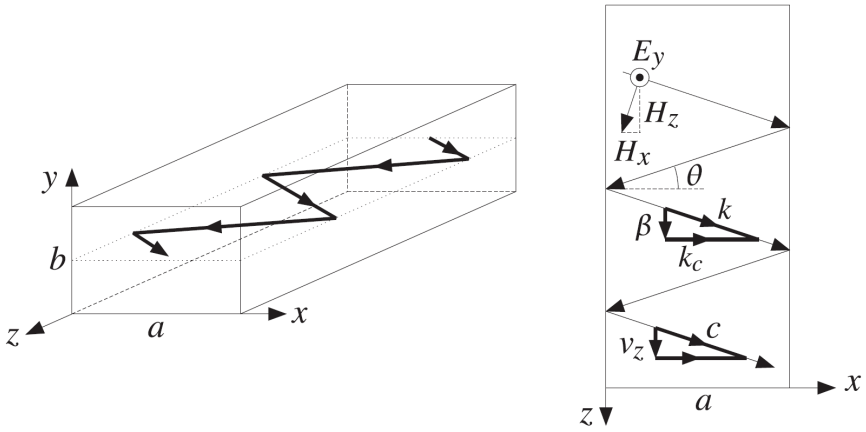

Figure 2.1 – Schematic representation of the multiple reflection model for the fundamental mode in rectangular waveguide [5].

SW-SIW technology should satisfy these conditions. We will consider such a case in the following developments.

2.2.2.2 Increased stored energy for velocity reduction

Let's consider two waveguides, WG1 and WG2. WG1 is the reference waveguide, so that SWF will be calculated for WG2 by comparison to WG1. Both of them are either periodic or uniform along the direction of propagation. That being said, suppose that WG2 is a modified version of WG1 which aims at exhibiting a reduced velocity compared to WG1. An important point is that each structure is assumed to carry the same amount of power, at the same frequency. The periodicity (or uniformity) of the boundary conditions in the propagation direction makes it then possible to apply the theorems given above for any unit-cell of arbitrary length s. The equality (2.11) can therefore be obtained by applying (2.8) for both WG1 and WG2. In these equations, W_{e1}, W_{m1}, and v_{g1} are associated to WG1, while W_{e2}, W_{m2}, and v_{g2} to WG2, respectively.

$$[W_{e1} + W_{m1}] \frac{v_{g1}}{s} = [W_{e2} + W_{m2}] \frac{v_{g2}}{s} \tag{2.11}$$

Therefore, the velocities ratio which is the slow-wave factor can be expressed as the stored energies ratio:

$$SWF = \frac{v_{g1}}{v_{g2}} = \frac{W_{e2} + W_{m2}}{W_{e1} + W_{m1}} \tag{2.12}$$

Then, the loss-less hypothesis is considered to express this ratio as function of either magnetic or electric energies ratio as in (2.13):

$$SWF = \frac{W_{e2}}{W_{e1}} = \frac{W_{m2}}{W_{m1}} \tag{2.13}$$

This last equation states that the reduction in velocity is directly proportional to the stored energy in a unit-cell, while transmitted power is constant.

2.2.3 Increased dissipation, a consequence of the velocity reduction

The slow-wave effect is mainly targeted for two distinct goals. Historically, the motivation for reduced velocities is to be found in the electron-beam technologies dedicated either to RF signals amplification or particle acceleration by energy transfer from an incoming EM wave. In both cases, the velocity of the EM wave had to be slowed down to that of the particles, thus increasing the transfer of energies. On the other side, the more recent attention given to the slow-wave topologies is interested in the consequence of the velocity reduction, which is the reduction of the guided wavelengths, and thus of passive circuits dimensions. While in the first case the goal was the maximisation of the interaction between an electron beam and an electromagnetic wave, in the second case it is to realise compact and efficient passive circuits.

In order to realise such passive circuits it is obviously necessary to have efficient waveguides. In particular, the attenuation of a travelling wave along these waveguides should be minimum for a given phase shift. In microwave engineering, this property is translated by the quality factor Q, defined as :

$$Q = \frac{\beta}{2\alpha} \tag{2.14}$$

Therefore, the highest the quality factor, the better. More precisely, β reflects the slow-wave factor (see (1.24)), while α the power dissipation. Let's now consider the slow-wave effect from this perspective. An ideal slow-wave structure would be able to maximise β while keeping α at a minimum, which would lead to greater quality factors. However in reality, both attenuation and phase constant are related, as we will see in this paragraph.

Considering low losses, the theorems (2.7)-(2.8) related to energy considerations in periodical structures are assumed to be still valid. Of course, the higher the dissipation in both metal and dielectrics the less valid this assumption will be. We will also assume that the field amplitudes are not merely modified by the losses introduction, so that a good estimation of the attenuation can be obtained based on the lossless field values. First of all, the expressions for transmitted and dissipated powers will be given [5].

The time-averaged transmitted power along the waveguide is given by the time-averaged Poynting vector $\mathbf{\Pi}$ flux in the transverse section:

$$P_t = \iint_{S_t} \mathbf{\Pi}.\boldsymbol{dS} = \iint_{S_t} \frac{1}{2}\,\mathrm{Re}\{\boldsymbol{E} \times \boldsymbol{H}^*\}\boldsymbol{dS} \tag{2.15}$$

Then, by considering low losses the different attenuation contributions can be obtained. The time-averaged power attenuation per meter in the dielectrics is given by (2.16), which in combination with (2.17) gives the related attenuation α_d. In these equations, the material permittivity is denoted ε and its loss tangent $tan\delta$.

$$P_d = \iint_S \frac{1}{2}\omega\varepsilon tan\delta|\boldsymbol{E}|^2 dS \tag{2.16}$$

$$\alpha_d = \frac{P_d}{2P_t} \tag{2.17}$$

On the other hand, the induced currents on the metallic parts can be used to compute an estimation of the conductive losses. They are first estimated through (2.18), where $\boldsymbol{n}$ represents the considered surface normal unit vector.

$$\boldsymbol{J_s} = \boldsymbol{n} \times \boldsymbol{H} \tag{2.18}$$

Then, an integration is performed in (2.19) taking into account the surface impedance R_s to obtain the dissipated power per meter.

$$P_c = \int_C \frac{1}{2} R_s \boldsymbol{J_s}^2 dl \tag{2.19}$$

The corresponding attenuation constant is finally obtained in a similar way as for the dielectric attenuation by (2.20). The total attenuation α is obtained by adding these two contributions.

$$\alpha_c = \frac{P_c}{2P_t} \tag{2.20}$$

From these equations, a first interesting result can be extracted. Using the expression of SWF given by (2.13), if both reference and slow-wave waveguides are made of the same dielectric, one obtains:

$$SWF = \frac{W_{e2}}{W_{e1}} = \frac{\iiint_V \frac{1}{4}\varepsilon |\boldsymbol{E_2}|^2 dV}{\iiint_V \frac{1}{4}\varepsilon |\boldsymbol{E_1}|^2 dV} = \frac{\iiint_V \frac{1}{2}\omega\varepsilon tan\delta |\boldsymbol{E_2}|^2 dV}{\iiint_V \frac{1}{2}\omega\varepsilon tan\delta |\boldsymbol{E_1}|^2 dV} \tag{2.21}$$

For uniform waveguides, $|\boldsymbol{E}|^2$ does not depend on the longitudinal direction, so that the triple integrals ratio can be reduced to that of the transverse integrals. Then, by dividing top an bottom integrals by two times the transmitted power P_t, the SWF can be written as the ratio of dielectric attenuations:

$$SWF = \frac{\iint_{S_t} \frac{1}{2}\omega\varepsilon tan\delta |\boldsymbol{E_2}|^2 dS}{\iint_{S_t} \frac{1}{2}\omega\varepsilon tan\delta |\boldsymbol{E_1}|^2 dS} = \frac{\iint_{S_t} \frac{1}{2}\omega\varepsilon tan\delta |\boldsymbol{E_2}|^2 dS/2P_t}{\iint_{S_t} \frac{1}{2}\omega\varepsilon tan\delta |\boldsymbol{E_1}|^2 dS/2P_t} = \frac{\alpha_{d2}}{\alpha_{d1}} \tag{2.22}$$

This states that for a slow-wave waveguide filled with a single lossy dielectric, the corresponding attenuation will increase by the same factor as the factor by which the velocity is reduced.

For periodic waveguides, the triple integrals correspond to the total time-averaged dissipated power per unit-cell. Therefore it can be said that the dissipation per unit-cell for WG2 is multiplied by SWF compared to WG1. In general, if the period length s is a small fraction of wavelength then the same conclusion as in the uniform case can be considered.

Regarding metallic losses, a general conclusion is hardly obtained, as the current distribution will greatly depend on the adopted slow-wave topology.

2.2.4 In practice: the required spatial energies separation

2.2.4.1 Qualitative considerations

In order to apply the two theorems given above it is necessary to consider a lossless structure. Let's assume a uniform cylindrical waveguide carrying power through electromagnetic field over its cross-section.

Three hypothetical waveguides are considered in Figure 2.2, they are considered as filled with an homogeneous dielectric with also some metallic inclusion. The first one on the left is the reference waveguide. Second and third waveguides on the right have the same cross-section area but it is assumed that fields separation is achieved so that electric field (b) or magnetic field (c) are confined in a specific area. Obviously, some material modifications would be necessary in reality for this separation to occur but these are not considered here for simplicity.

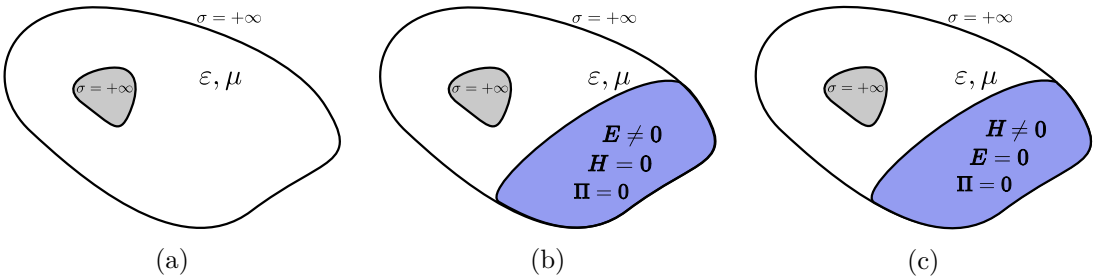

Figure 2.2 – Considered ideal cases: (a) Reference waveguide, (b) with electric field confinement and (c) with magnetic field confinement.

Let assume that all of these three waveguides carry the same amount of power along the direction of propagation. The flux of Poynting vector over the cross-section is therefore the same for (a), (b) and (c). In that case, the group velocity reduction is proportional to the increase in total stored energy (see (2.8)). Moreover, electric energy W_e equals magnetic energy W_m so we can choose arbitrarily one of them for interpretation.

Let's first consider case (b). In order to increase W_e it is necessary to increase the overall electric field strength. However, doing so without changing the amplitudes of the magnetic components would result in a greater power flow. In order to maintain this flow, let us imagine the extreme case where the magnetic field is completely removed from a specific domain. The field separation leads to a separation between the power flow and the electric energy, thus creating the possibility of increasing only the latter.

In case (c) the dual reasoning is applied so that the electric field is removed from one part of the cross-section. That means only magnetic energy, as part of W_m is stored in this region. Also, this field does not contribute directly to the Poynting vector flux because $\boldsymbol{E} = 0$. Therefore, the overall flux has to be maintained by increasing field amplitudes in the remaining region. If magnetic field amplitude can be adjusted independently in the region where $\boldsymbol{E} = 0$, the overall energy and therefore the group velocity can be tuned.

In reality, avoiding the presence of magnetic field in some specific region as in (b) is relatively complicated as no magnetic conductor is available. In practice, confinement of the electric field as in (c) is much easier to realize thanks to additional capacitive effects. In the next paragraph, a quantitative analysis of the relationship between field confinement and velocity reduction is presented.

2.2.4.2 A quantitative analysis for ideal parallel-plate configurations

Considering a strongly idealistic framework, some quantification of the velocity reduction can be achieved, it is be demonstrated in this paragraph. The parallel plate waveguide (PPW) configuration is chosen because in this particular case an estimation of velocity reduction can be derived directly from field separation parameters. Furthermore, the rectangular waveguide and its integrated counterpart - which is the object of this thesis - are based on this configuration with the addition of lateral walls.

For simplicity the slow-wave factor is defined relatively to a reference structure which exhibits a given velocity (see (1.24)). Using this definition, the slow-wave factor is greater than one if the wave velocity is reduced compared to that of the reference structure.

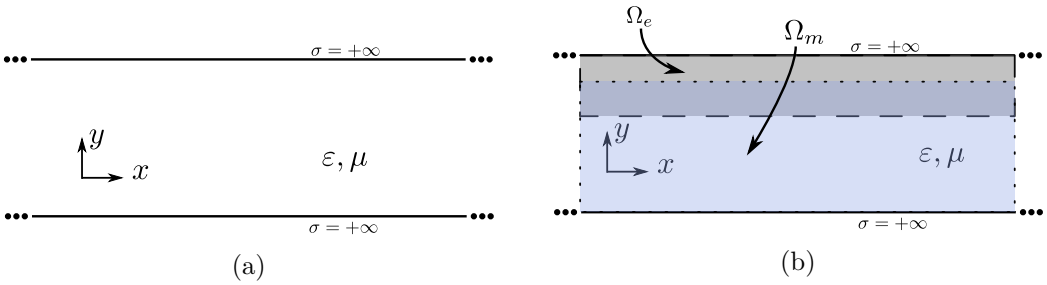

Figure 2.3 – Considered PPW: (a) Reference waveguide, (b) modified waveguide.

The propagation is analysed in z-direction. Several hypothesis concerning both reference and slow-wave waveguides are listed below, these two waveguides are illustrated in Figure 2.3. They are considered infinite in x-direction, so that an arbitrary portion of it between two values of x coordinate is analysed. If periodic variations are to be introduced in this direction, a unit cell length should be considered.

Let's first consider the reference parallel-plate waveguide (2.3(a)), the following hypothesis are made:

- The top and bottom metallic walls are perfect electric conductors (PEC)
- It is filled with an homogeneous loss-less medium of permittivity ε and permeability μ.
- Only the first TEM mode is considered, so that energy distribution (both electric and magnetic) is equally distributed in the transverse section of the reference waveguide.

Based on these hypothesis, it follows that the power flux is also distributed homogeneously in the transverse section. The electric and magnetic fields vectors for the considered mode in this structure are denoted $\boldsymbol{E_1}$ and $\boldsymbol{H_1}$, respectively.

A second waveguide is considered (Figure 2.3(b)), it is based on the same geometry but some further assumptions are made. It is assumed that by adding some metal or dielectric parts the electric field is confined in the cross-section sub-domain Ω_e. These additional structures are not represented here for simplicity. The magnetic field is also limited to a domain called Ω_m.

The total cross-section is written Ω. Also, because the first mode only is analysed (TEM), group velocity equals phase velocity (no dispersion).

Some further hypothesis are considered concerning the field distribution:

- The electric field is similar to that of the reference waveguide in Ω_e except by a real scale factor a_e.
- The magnetic field is similar to that of the reference waveguide in Ω_m except by a real scale factor a_m.

These two hypothesis can be written using the indicator functions for each sub-domains, $\mathbb{1}_e$ and $\mathbb{1}_m$ respectively. They are defined as $\mathbb{1}_e = 1$ in Ω_e, and 0 elsewhere (and resp. for $\mathbb{1}_m$ in Ω_m).

$$\boldsymbol{E_2}(x,y,z) = a_e \boldsymbol{E_1}(x,y,z)\mathbb{1}_e(x,y) \tag{2.23}$$

$$\boldsymbol{H_2}(x,y,z) = a_m \boldsymbol{H_1}(x,y,z)\mathbb{1}_m(x,y) \tag{2.24}$$

Let's now focus on the energy distribution following these assumptions. The total stored energy in a cell of length s can be written as in equation (2.25), the (x,y,z) dependence is not written for clarity.

$$W_{e2} = s\int_\Omega \varepsilon \|\boldsymbol{E_2}\|^2 dS = a_e^2 s\int_\Omega \varepsilon \|\boldsymbol{E_1}\|^2 \mathbb{1}_e dS = a_e^2 s\int_{\Omega_e} \varepsilon \|\boldsymbol{E_1}\|^2 dS \tag{2.25}$$

Now, this expression can be further simplified using the fact that the energy is homogeneously distributed in the reference waveguide. By introducing the areas of Ω, Ω_e and Ω_m, written S, S_e and S_m respectively, (2.25) can be simplified into:

$$W_{e2} = a_e^2 s\frac{S_e}{S}\int_\Omega \varepsilon \|\boldsymbol{E_1}\|^2 dS = a_e^2\frac{S_e}{S}W_{e1} \tag{2.26}$$

A similar expression can be derived with the magnetic field:

$$W_{m2} = a_m^2 s\frac{S_m}{S}W_{m1} \tag{2.27}$$

As a consequence, the SWF can be calculated using (2.13), leading to (2.28).

$$SWF = a_e^2\frac{S_e}{S} = a_m^2\frac{S_m}{S} \tag{2.28}$$

In addition, this equality provides an expression for the ratio of electric and magnetic amplitude scale factors a_e and a_m, as function of the surfaces involved in the field separation :

$$\frac{a_e}{a_m} = \sqrt{\frac{S_m}{S_e}} \tag{2.29}$$

A second relation will be derived from the equality of transmitted power. By equating the Poynting vector flux in both waveguides the relation (2.30) is readily obtained. The second equality is based on the fact that both electric and magnetic fields are non-zero in $\Omega_e \cap \Omega_m$ only, so that all the transmitted power is contained in this area.

$$\int_\Omega \boldsymbol{E_1} \times \boldsymbol{H_1^*} dS = \int_\Omega \boldsymbol{E_2} \times \boldsymbol{H_2^*} dS = a_e a_m \int_{\Omega_e \cap \Omega_m} \boldsymbol{E_1} \times \boldsymbol{H_1^*} dS \tag{2.30}$$

Then, using the fact that the transmitted power is equally distributed in the transverse section of the reference waveguide, the last integral on the right hand-side of the equation can be seen as a fraction of the first one on the left. For that, the intersection of Ω_e and Ω_m area is denoted by S_{em}:

$$\int_\Omega \boldsymbol{E_1} \times \boldsymbol{H_1^*} dS = a_e a_m \frac{S_{em}}{S} \int_\Omega \boldsymbol{E_1} \times \boldsymbol{H_1^*} dS \tag{2.31}$$

By consequence, one obtains:

$$a_e a_m \frac{S_{em}}{S} = 1 \tag{2.32}$$

Finally, one can notice that both the ratio and the product of a_e and a_m were derived, respectively by (2.29) and (2.32). Therefore, both of them can be extracted:

$$a_e = \left(\frac{S}{S_{em}}\right)^{1/2} \left(\frac{S_m}{S_e}\right)^{1/4} \tag{2.33}$$

$$a_m = \left(\frac{S}{S_{em}}\right)^{1/2} \left(\frac{S_e}{S_m}\right)^{1/4} \tag{2.34}$$

Then, using (2.28) SWF becomes:

$$SWF = \frac{\sqrt{S_m S_e}}{S_{em}} \tag{2.35}$$

This last equation relates directly the velocity reduction to the field confinement. Let now assume that a small amount of metal inclusion is necessary to confine the electric field in Ω_e (such an hypothesis can be justified by the fact that the electric field lines are very easily captured by thin wires for example). At the same time, magnetic field lines will avoid these obstacles without changing significantly, so that $S_m \approx S$ and $S_{em} \approx S_e$. The following simplified forms for SWF, a_e and a_m can therefore be derived:

$$SWF = \sqrt{\frac{S}{S_e}} \tag{2.36}$$

$$a_e = SWF^{3/2} \tag{2.37}$$

$$a_m = SWF^{1/2} \tag{2.38}$$

These equations provide an estimation of the increase in electric and magnetic field strength for a given slow-wave factor, itself resulting from a confinement of the electric energy in the transverse section. Yet these results are obtained in an idealistic framework, but it could provide physical insight for existing slow-wave structures. A final result can be of interest, that of the averaged wave impedance $< Z_{w2} >$. By calculating the ratio of the field components, one arrives to the following expression:

$$< Z_{w2} >= \frac{1}{S}\int_{\Omega}\frac{|\boldsymbol{E_2}|}{|\boldsymbol{H_2}|}dS = \frac{a_e}{a_m}\frac{1}{S}\int_{\Omega_e\cap\Omega_m}\frac{|\boldsymbol{E_1}|}{|\boldsymbol{H_1}|}dS \tag{2.39}$$

Again, the right-side integral is a fraction of the integral over Ω, so that:

$$< Z_{w2} >= \frac{a_e}{a_m}\frac{S_{em}}{S^2}\int_{\Omega}\frac{|\boldsymbol{E_1}|}{|\boldsymbol{H_1}|}dS = \sqrt{\frac{S_e}{S}} < Z_{w1} >= \frac{< Z_{w1} >}{SWF} \tag{2.40}$$

The averaged impedance in the slow-wave case is therefore related to the reference impedance by a factor $1/SWF$.

2.2.5 Discussion

The simplified expressions derived above were obtained thanks to several hypothesis, some of them being relatively restrictive. Similar expressions can be found for existing topologies which do not respect these hypothesis. As an example, the effective permittivity derived by Hasegawa for the microstrip line on Si-SiO_2 is expressed by the square root of the two layers thickness ratios [6].

Moreover, it is interesting to note that similar results can be obtained using the same concepts for slow-wave quasi-TEM structures where a loss-less LC transmission line model can be adopted. Actually, the slow-wave effect in most of these structures is generally interpreted on the basis of such a model. Among others, this category of transmission lines includes for example the capacitively [7, 8], inductively-loaded [9] CPW, as well as slow-wave microstrip [10]. In general, the slow-wave effect is produced by an increase in the capacitance per unit-length. Let's consider the case of a loaded transmission line where this capacitance is increased from a nominal value C to a new value C_{sw} by inserting metallic fingers (as in the case of the S-CPW [8]). The effect on the inductance is considered negligible, as often verified in most of these structures. Both reference and slow-wave equivalent circuits are represented in Figure 2.5. Real currents and voltage along the lines are introduced in both cases for the calculation.

By considering the ratios of stored energies the slow-wave factor can then be reduced to the following expressions:

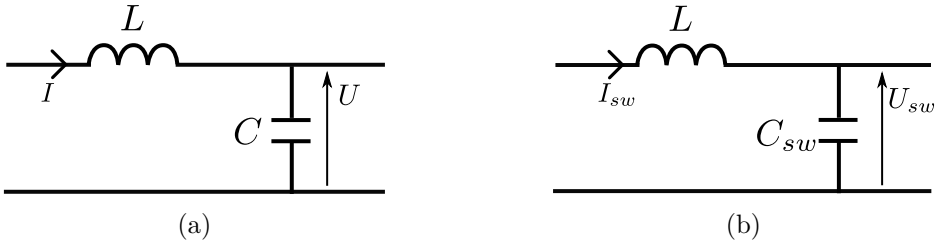

Figure 2.4 – Considered ideal LC models: (a) Reference and (b) Slow-wave transmission line.

$$SWF = \frac{C_{sw}U_{sw}^2}{CU^2} = \frac{LI_{sw}^2}{LI^2} = \frac{I_{sw}^2}{I^2} \tag{2.41}$$

Then, by forcing the equality of transmitted power $U_{sw}I_{sw} = UI$ we obtain:

$$SWF = \frac{C_{sw}U_{sw}^2}{CU^2} = \frac{U^2}{U_{sw}^2} \tag{2.42}$$

By replacing the voltage ratio by SWF in the middle term the expected expression is obtained (usually directly derived through $v_p = \sqrt{1/LC}$):

$$SWF = \sqrt{\frac{C_{sw}}{C}} \tag{2.43}$$

This ratio of capacitance could be related to equation (2.36), in the sense that an increase in capacitance is generally obtained by confining the electric field in a smaller area S_e. Finally, the change in voltage and current along the slow-wave transmission line can be derived from (2.42) and (2.43):

$$U_{sw} = \frac{U}{\sqrt{SWF}} \tag{2.44}$$

$$I_{sw} = \frac{I}{\sqrt{SWF}} \tag{2.45}$$

An ideal framework was used for the derivation of general principles and simplified expressions. The following sections will now focus on the application of these results to the slow-wave topology presented in this work.

2.3 Slow-wave effect induced by a uniform distribution of blind via holes in a parallel-plate waveguide configuration

2.3.1 Definition of the topology and associated simulation methods

2.3.1.1 Description of the loaded parallel-plate waveguide topology

The idea behind the proposed SW-SIW is to confine the electrical field in the upper part of the SIW. In order to achieve that, a uniform distribution of blind via holes

is inserted inside the waveguide, as depicted in Figure 2.5. The properties of a wave travelling along such a waveguide depend on the effect produced by the blind via holes combined with its successive reflections on the lateral walls. For simplicity, these two effects are considered separately in the following analysis. First, the parallel-plate configuration (without any lateral via holes) will be analysed in this section to exhibit the impact of the capacitive loading. Then, we will focus on the SW-SIW, its closed integrated version.

For these two waveguides, several geometric parameters need to be defined. The inner height of the waveguide is h, its lateral dimension is W and the lateral holes diameter is d_{ext}. Then, the internal via holes diameter and height are called d and h_v, respectively. Moreover, the fabrication process requires that they shall be covered by copper lands, whos diameter and thickness are d_p and h_p, respectively. Finally, the spacing between the via holes - both external and internal - is denoted s, it is identical in longitudinal and transverse directions.

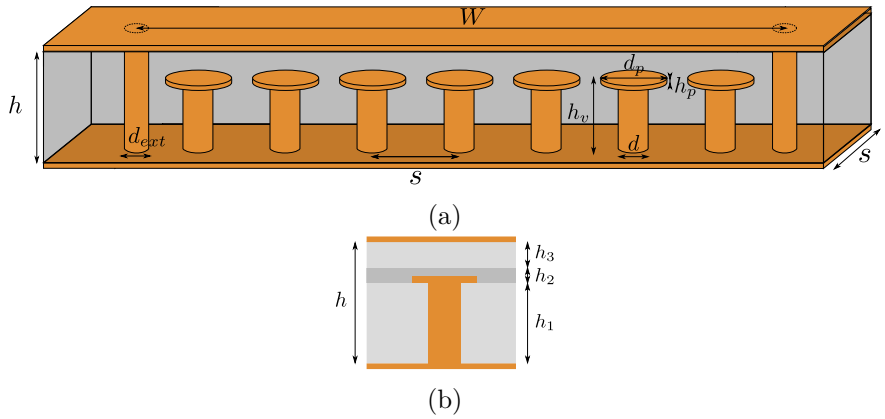

Figure 2.5 – General topology of the proposed SW-SIW: (a) SW-SIW unit-cell, (b) Technology stack-up.

In practice, for all realizations presented in this manuscript the waveguide is made out of two RO4003 layers ($\varepsilon_r = 3.55$, $tan\delta = 0.0027$), stacked together by a RO4450F prepreg ($\varepsilon_r = 3.54$, $tan\delta = 0.004$). As illustrated in Figure 2.5, the bottom RO4003 layer thickness h_1 is 0.813 mm while the top one is $h_3 = 0.203$ mm. The intermediate RO4450F layer has a thickness h_2 of 0.102 mm. For this topology, the via height h_v is therefore equal to h_1. Finally, a copper land of thickness $h_p = 0.035$ mm was considered.

2.3.1.2 Simulation methods

In order to study the electrical performance of the introduced waveguides, different simulation strategies were adopted. As for most non-TEM waveguides, the relevant parameter is the propagation constant $\gamma = \alpha + j\beta$. An ideal slow-wave structure would be able to increase dramatically the phase constant β while limiting the increase in the attenuation α.

2.3. Slow-wave effect induced by a uniform distribution of blind via holes in a parallel-plate waveguide configuration

The usual simulation strategy for a given topology is the extraction of the scattering matrix S of two different sections of waveguides, so that a two-line method can be applied to extract both attenuation and phase constant. However, such a method has several disadvantages. First, the set of lengths has to be carefully chosen in order to avoid resonances during the extraction [11]. Also, a proper estimation of the attenuation can only be obtained with relatively long waveguides. Finally, from the practical point of view, this method requires two simulations as well as a mathematical post-processing.

A more straight-forward strategy is the use of the eigen-mode solver in HFSS [12]. As described in [13, 14], closed periodic waveguides can be analysed through their unit-cell only. In order to obtain the propagation constant, an equivalent resonator is defined with specific boundary conditions, as illustrated in Figure 2.6.

(a) (b)

Figure 2.6 – Principle of the eigen-mode simulation: (a) Periodic waveguide, (b) equivalent resonant unit-cell.

More precisely, the propagation term $e^{-j\beta z}$ is replaced by a phase shift $e^{-j\varphi}$ between two opposite faces of the unit-cell. This is imposed by applying "Master" and "Slave" boundaries. Technically, the field on the slave boundary $\boldsymbol{E_s}$ should be a delayed version of that on the master boundary $\boldsymbol{E_m}$. The output data of the solver is a frequency at which the boundary conditions are satisfied, that is for which $\beta = \varphi/s$. Then, by varying φ between 0 and a maximum angle of π, a curve of dispersion $\beta(\omega)$ can be directly obtained. In reality, the output frequency ω' is a complex value, the real part being the physical resonance frequency while the imaginary part expresses dissipation in the resonator (and thus attenuation). The following equations are implemented to recover the attenuation constant from this complex frequency.

$$\omega = Re(\omega') \tag{2.46}$$

$$\alpha = Im(\omega')\frac{d\beta}{d\omega} \tag{2.47}$$

Such a method has many advantages, among them is the fact that it provides a reduced computation time as compared to full-wave simulations. Also, field values are in general more accurately calculated because of the reduced computed volume.

In most cases, this last simulation strategy will be adopted.

2.3.2 Physical properties

2.3.2.1 Dispersion diagram, Fields separation

The considered loaded parallel-plate waveguide (LPPW) unit-cell is illustrated in Figure 2.7. Propagation is analysed in the x-z plane so that the wavenumber has two components, respectively on x and z-axis. The sweep over the wavenumber values is realised by two independent pairs of master-slave boundaries, one in the x-direction, and the other in z-direction.

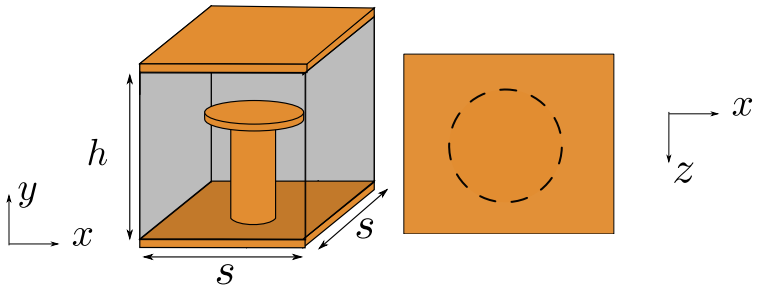

(a) (b)

Figure 2.7 – Unit-cell of the studied loaded PPW: (a) 3D view, (b) Top view.

First of all, the fields associated with the first mode solution (quasi-TEM) are illustrated in Figure 2.8 for a propagation in the x-direction. Top and bottom metals are represented in HFSS by conductive boundaries so that they do not appear in the figure. The geometrical parameters for this simulation are that which will be used for most of the circuits presented in this work, ie. $s = 0.8$ mm, $d = 0.4$ mm, $h_v = 0.813$ mm, $d_p = 0.6$ mm and $h_p = 0.035$ mm. Electrical field is mainly confined in the upper part of the waveguide, between the blind via hole and the top metal layer. Simultaneously, magnetic field strength is mainly present from bottom to top without significant amplitude variation.

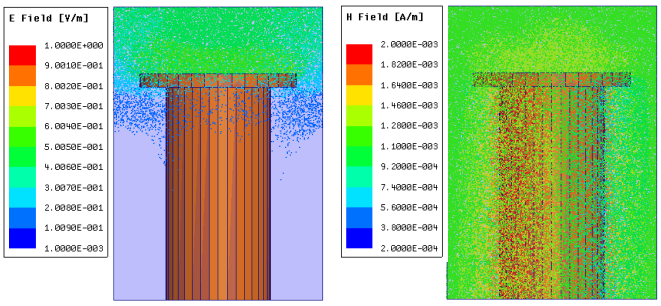

(a) (b)

Figure 2.8 – Fields amplitude in the loaded parallel-plate waveguide unit-cell: (a) Electric field, (b) Magnetic field.

Dispersion curves for the first propagating mode are illustrated in Figure 2.9 for two different propagation directions. These two cases represent extreme configurations,

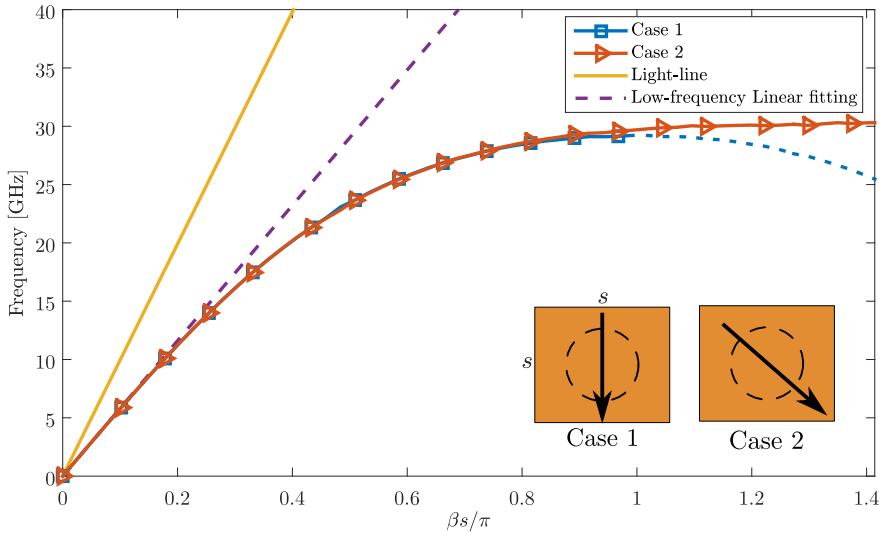

Figure 2.9 – Dispersion diagram for the loaded parallel-plate waveguide.

either the propagation is only on x or z axis (Case 1), or with an inclination of 45 degrees in respect to these two axes (Case 2). For an easier interpretation, the light-line is also represented considering a relative permittivity of 3.55, as well as a linear fitting of the low frequency results.

Thanks to the spatial periodicity, the dispersion diagram has to be simulated for a phase-shift limited only to π over the unit-cell. The complete curves (including the higher order harmonics) could be obtained by translation (see section 2.2.1). Moreover, because the period in Case 2 is increased by a factor $\sqrt{2}$, a separation between the two results can be observed for large phase shifts.

In addition, because the blind via hole becomes electrically larger as frequency increases the dispersion becomes also more and more visible. This phenomenon manifests itself in the tendency of the dispersion curve to move away from the linear progression. However, for phase shifts lower than 0.2π (ie. a period lower than a tenth of wavelength) a quasi linear progression can be observed.

On the overall, a very similar behaviour is observed between the two configurations, thus demonstrating that the introduced slow-wave effect is not dependent on the direction of propagation for lower frequencies. This point is important because when lateral walls are added to form a closed waveguide the wave propagates at a frequency dependant angle of incidence. Therefore, it means that in this case no dispersion is added by this angular change.

Finally, the SWF along with the corresponding effective permittivity are given in Figure 2.10 as functions of frequency. The SWF is referenced to the light velocity in the considered medium $c_0/\sqrt{\varepsilon_r}$, which is the phase (and group) velocity of the fundamental parallel plate waveguide mode. The same kind of observation as for the dispersion diagram can be done, with a very close behaviour observed in both propagation directions. Finally, both SWF and ε_{reff} are increasing functions of frequency, with maximum values around 30 GHz, the frequency at which half a wavelength is contained in a single unit-cell (see Figure 2.9).

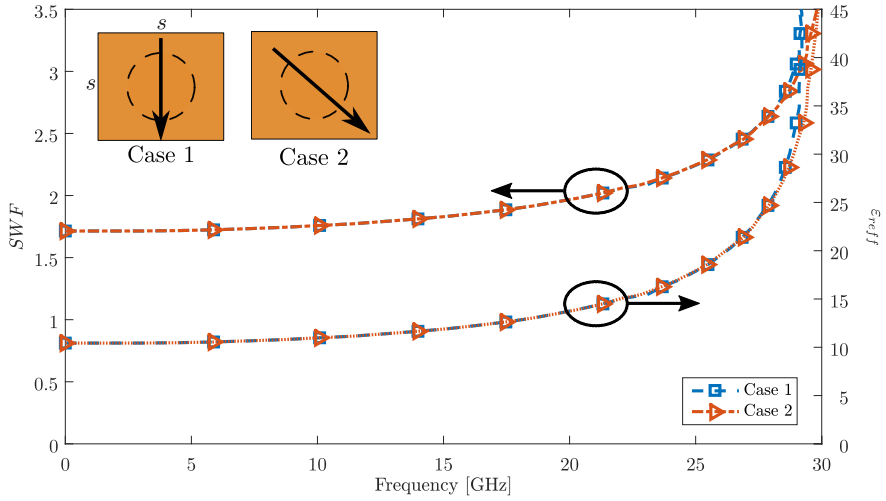

Figure 2.10 – Slow-wave factor and effective permittivity for the loaded parallel-plate waveguide first mode.

Because of the periodic nature of the loaded parallel plate waveguide, group velocity varies in inverse proportion compared to the stored energy in the unit-cell. For a weakly dispersive waveguide, phase and group velocities are equal and therefore SWF can be calculated based on energy considerations. As observed in Figure 2.9, a low dispersion regime can be observed at low frequencies, because the unit-cell is electrically very small. Let's consider the energies distribution in this context.

The loaded parallel-plate waveguide is compared to its non-loaded counterpart. The exact same unit-cell dimensions are adopted for the analysis. As the field separation is mainly defined along the vertical coordinate y, an integration of electric and magnetic energies is performed in a restrained volume $V(y)$ following expressions (2.48) and (2.49), where the volume $V(y)$ is defined as $\{M(x', y', z'), 0 \leq x', z' \leq s, 0 \leq y' \leq y\}$ (see Figure 2.11).

$$I_e(y) = \int_{V(y)} W_e dV \tag{2.48}$$

$$I_m(y) = \int_{V(y)} W_m dV \tag{2.49}$$

Prior to the computation of these integrals, all fields were normalised to obtain an identical transmitted power of 1 W, the results are illustrated in Figure 2.11 as function of the normalised coordinate y/h or a frequency of 1 GHz. Many observations can be made, first of all in both waveguides the total energy is equally magnetic and electric, as the curves converge to the same point for $y/h = 1$, that is when all the volume is taken into account. This total energy is 4.3 nJ in the loaded case and 2.64 nJ otherwise. By neglecting dispersion these values provides an estimated slow-wave factor of 1.63 (see equation (2.13)). By comparison, the value estimated through the dispersion diagram is 1.71, representing an difference of about 4.6%.

Secondly, the uniform waveguide exhibits an homogeneous energy distribution, visible by the linear progression of the curves. For the loaded waveguide however, this

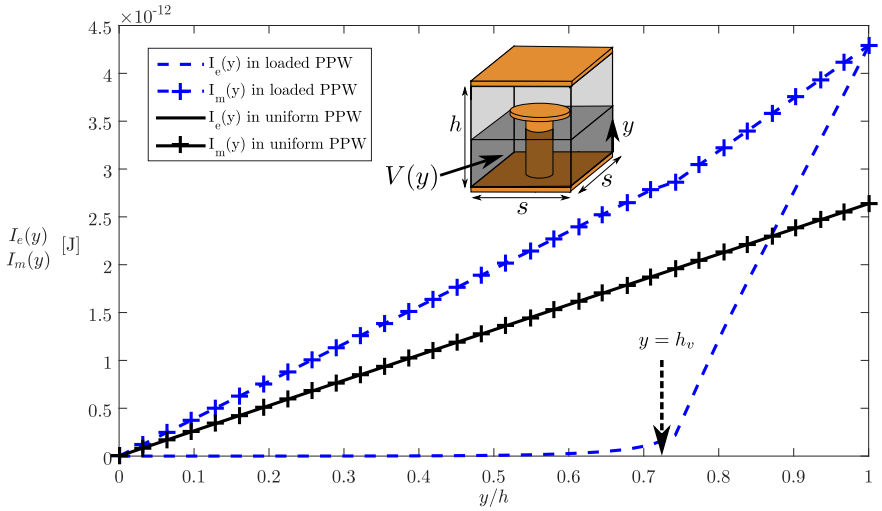

Figure 2.11 – Energies distribution in both uniform and loaded waveguides at 1 GHz.

linear trend is only visible for the magnetic field. The electric energy is mainly present in the higher part of the waveguide. The copper land is positioned at $h_v = 0.813$ mm from the lower plate, i.e. at a normalised height of 0.73. The electric energy contained below this copper land $I_e(y)$ is estimated to 0.18 nJ, that is about 4% of the total energy. By neglecting this quantity, we could come closer to the ideal case previously analysed, where the electric field would only be considered in the higher part of the waveguide. Simultaneously, magnetic field is still present everywhere else, except inside the blind via hole.

Let's consider the application of the ideal case derived formulas in this context. Because of the 3D configuration, the domains Ω_e and Ω_m are now volumes instead of surfaces, which volumes are denoted V_e and V_m. Their graphical definitions are illustrated in Figure 2.12(a) and 2.12(b), respectively. The impact of the transition from surface to volume considerations is expected to be small for low frequencies. In this case it is facilitated by the fact that the energy separation mostly occurs on the transverse directions rather the longitudinal one.

Based on the obtained field distribution, the following approximations are performed. The electric field is considered to be only present in the top of the waveguide. However, in the case of small and distant via holes the penetration of the electric field in the bottom part may not be negligible. For this reason, a penetration depth in the lower part is taken into account, it is defined by the distance from the copper land to the edge of the unit cell Δ. The magnetic field still occupies all the available volume, that is all of the unit cell minus the blind via hole.

A slow-wave factor was then derived by analogy with equation (2.50) using volumetric considerations:

$$SWF = \sqrt{\frac{V_m}{V_e}} \tag{2.50}$$

Two cases are considered for the expression of SWF depending on the distance

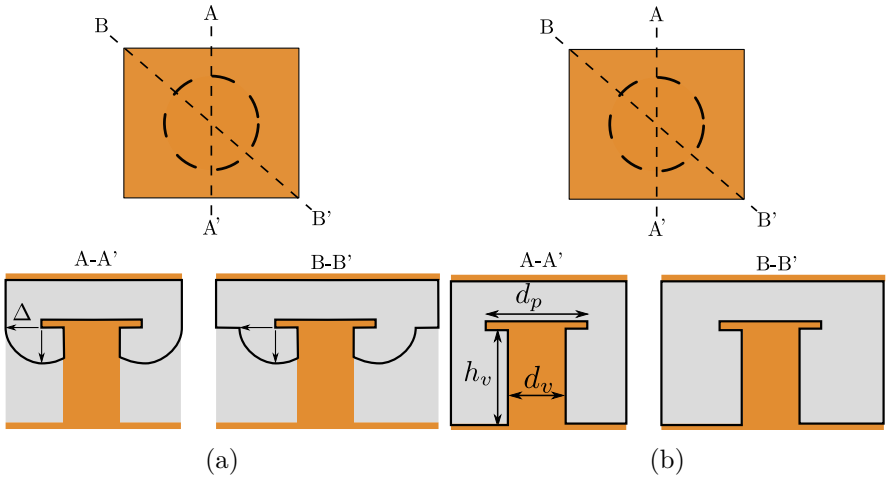

Figure 2.12 – Definitions of magnetic and electric domains in the loaded parallel-plate waveguide unit-cell: (a) Electric field, (b) Magnetic field.

Δ. First, if $\Delta \leq d_p/2 - d_v/2$ then all field lines penetrating in the bottom part are considered pointing to the copper land. The expression for SWF therefore becomes:

$$SWF = \sqrt{\frac{s^2h - h_v\pi(d_v/2)^2 - h_p\pi(d_p/2)^2 + (\pi\Delta)^2 d_p/2}{s^2(h - h_v) - h_p\pi(d_p/2)^2}} \tag{2.51}$$

However, if the copper land diameter is reduced so that $\Delta > d_p/2 - d_v/2$, then the expression for the penetration region is slightly more complicated, it is given below:

$$SWF = \sqrt{\frac{s^2h - h_v\pi(d_v/2)^2 - h_p\pi(d_p/2)^2 + (\pi\Delta)^2 d_p/2 - 1/4\pi d_v\Delta^2\,(\theta - sin\theta)}{s^2(h - h_v) - h_p\pi(d_p/2)^2}} \tag{2.52}$$

$$\theta = acos\left(\frac{d_p - d_v}{2\Delta}\right) \tag{2.53}$$

Numerical computation of these expressions for the dimensions given previously leads to $SWF = 1.68$, which is very close to the simulated 1.71 value. In this estimation, the hypothesis of the ideal case are not all respected, especially the fact that the field lines are bended, however it already provides a close approximation.

2.3.2.2 Losses contributions

For a closed waveguide without any magnetic materials, the losses are in general divided into metallic and dielectric ones. As already shown in section 2.2.3 in an ideal structure, if only one dielectric material is used the dielectric attenuation α_d is directly related to the group velocity reduction, that is the slow-wave factor in the low-dispersion regime (see (2.22)). By considering a loss tangent of 0.0024 in the waveguide this result can be compared with the simulation of the loaded waveguide. The relevant parameter to be plotted is the ratio of dielectric attenuations in loaded and reference

waveguides, respectively α_d^{lppw} and α_d^{ppw}, as a function of frequency. Then, this ratio can be compared to the SWF. Because a low-dispersion is required, the frequency sweep is limited to 0-15 GHz. The results are illustrated in Figure 2.13.

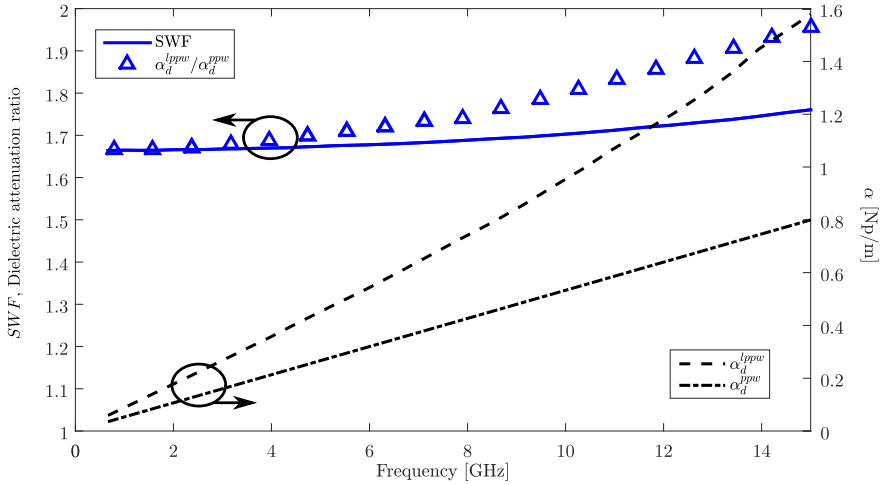

Figure 2.13 – Comparison between slow-wave factor and dielectric attenuation ratio for the parallel-plate configurations ($s = 0.8$ mm, $h = 1.118$ mm, $h_v = 0.813$ mm, $d_v = 0.4$ mm, $h_p = 0.035$ mm and $d_p = 0.6$ mm)

A very good agreement is obtained on the left side of the plot. At low frequencies, the increase in dielectric dissipation in this region is equal to the reduction in velocity SWF. In other word, if such a structure could exhibit negligible metallic losses, it would provide the same increase in β and α at low frequencies. The quality factor of such a waveguide would therefore be that of the conventional parallel-plate waveguide.

At higher frequencies, dispersion increases and the equality between the attenuation ratio and SWF is less and less valid. As example the ratio of attenuations is 7% greater than the slow-wave factor for a frequency of 11 GHz, which is the frequency of most devices in SW-SIW presented in this work. In fact, as shown in the dispersion diagram 2.9, the group velocity (derivative of $\omega(\beta)$) tends to 0 when the frequency reaches 30 GHz, while phase velocity (ω/β) is still positive. As a consequence, the dissipation of power per meter reaches very high value.

Concerning the metallic losses, dissipation occurs through induced currents in metallic parts. In order to analyse the different contributions, two different simulations were performed. First, all dielectric losses were removed by assigning $tan\delta = 0$ and then a perfect electric condition was applied successively to the blind via hole and top/bottom plates. All obtained attenuations are compared with that of the uniform waveguide in Figure 2.14

First of all, let's consider the attenuation obtained with a PEC condition on the blind via hole. In this case, only the loss induced by current circulation on both top and bottom parallel plates is taken into account. A factor of about 2 is observed between the loaded waveguide and the reference one. This ratio is slightly larger than the SWF in this range of frequency, which is around 1.7. In the ideal theoretical case studied previously, the magnetic field amplitude in the slow-wave waveguide is increased by a

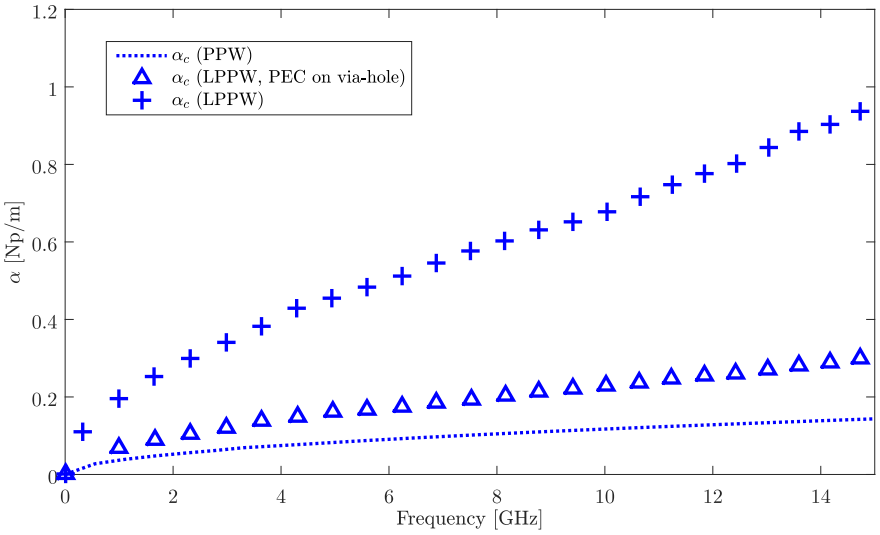

Figure 2.14 – Comparison between metallic attenuations for the parallel-plate configuration ($s = 0.8$ mm, $h = 1.118$ mm, $h_v = 0.813$ mm, $d_v = 0.4$ mm, $h_p = 0.035$ mm and $d_p = 0.6$ mm).

factor a_m (see (2.34)). As a consequence, the induced currents and the attenuation should be increased by a_m and a_m^2, respectively. An interesting agreement is obtained, as the computation of a_m^2 gives 1.94 in this context. This factor is slightly higher than SWF because the volume in which the magnetic field exists V_m is restrained. In the end, a strong reduction of the quality factor could not be related to an increased dissipation in these plates, as it is mostly compensated by the velocity reduction. Finally, an important increase in dissipation is observed when the impact of the blind via hole is fully taken into account. As one can notice, the total metallic attenuation is about 3 times greater in this case. In fact, as much as twice the amount of power dissipated in the parallel plates is lost in the blind via hole. This is obviously the main contribution to the degradation of Q as we will see.

Let's now consider the relative impact of the two contributions. The quality factor of the loaded parallel-plate waveguide can be expressed as in (2.54):

$$Q = \frac{\beta^{lppw}}{2\alpha^{lppw}} \approx \frac{SWF\beta^{ppw}}{2\left(\alpha_c^{lppw} + SWF\alpha_d^{ppw}\right)} \tag{2.54}$$

As shown before, the reduction of the phase velocity by SWF leads to an identical increase of α_d for limited values of frequency. Thus, one shouldn't expect the dielectric contribution to degrade significantly the quality factor. On the other hand, α_c is more strongly affected by the insertion of the blind via hole, in this case it is multiplied by about 5.5 for a SWF of 1.7. This significant increase is therefore responsible for the degradation of the quality factor. Furthermore, the increase of α_c is not merely a function of frequency, the factor of 5.5 being approximately respected from 1 GHz to 15 GHz. As a result, the quality factor degradation is also not really dependent on the frequency (see Figure 2.15), an average reduction of 35% can be observed here.

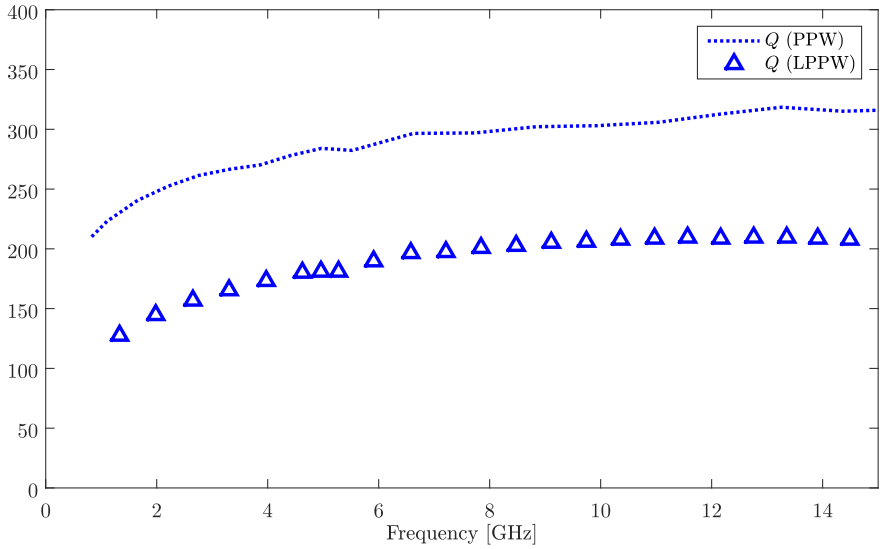

Figure 2.15 – Quality factors of PPW and LPPW ($s = 0.8$ mm, $h = 1.118$ mm, $h_v = 0.813$ mm, $d_v = 0.4$ mm, $h_p = 0.035$ mm and $d_p = 0.6$ mm).

Finally, it is worth mentioning that for higher frequencies the dielectric dissipation is more important than the metallic one. This is observed for many transmission lines and waveguides. The metallic attenuation usually follows approximately the square root of the frequency while the dielectric one follows a linear progression. As a result, at the frequency of 11 GHz used for most of the circuits presented in this thesis, the dielectric attenuation is dominant, but it is not yet enough dominant to retrieve the same quality factor as in the uniform waveguide. In practice, working at higher frequencies to limit the influence of the metallic loss would lead to greater dispersion as well, a trade-off is therefore required.

A parametric analysis on the different geometric parameters involved will be given in the next section. In order to apply the theoretical derivations given before, a low frequency of 1 GHz exhibiting low dispersion was chosen for all simulations. In this case, an estimation of the slow-wave factor can be derived more rigorously.

Yet, the relative proportions of α_c^{lppw} and α_d^{lppw} in the loaded waveguide evolves when frequency changes, we have seen that their respective increase compared to α_c^{ppw} and α_d^{ppw} does not vary significantly. This relative change is the key factor for determining the evolution of the quality factor, therefore the analysis presented in the low frequency regime does provide insight for higher frequencies as well.

2.3.3 Parametric analysis for large wavelengths

The main parameter which defines the slow-wave effect is the height of the blind via hole h_v. Also, the copper land diameter has some influence as it is the metallic part which prevents the electric field from reaching the lower part of the waveguide. The influence of these two parameters in terms of slow-wave and quality factors are illustrated in Figure 2.16 for a low frequency of 1 GHz. In this figure, h_v is normalised to the total height of the waveguide h. Also, d_p is normalised to the unit-cell length

s, so that $d_p/s = 1$ is obtained if the copper lands of adjacent via holes are touching each other. In addition, the simplified model theoretical values given by (2.51)-(2.53) are also illustrated for comparison.

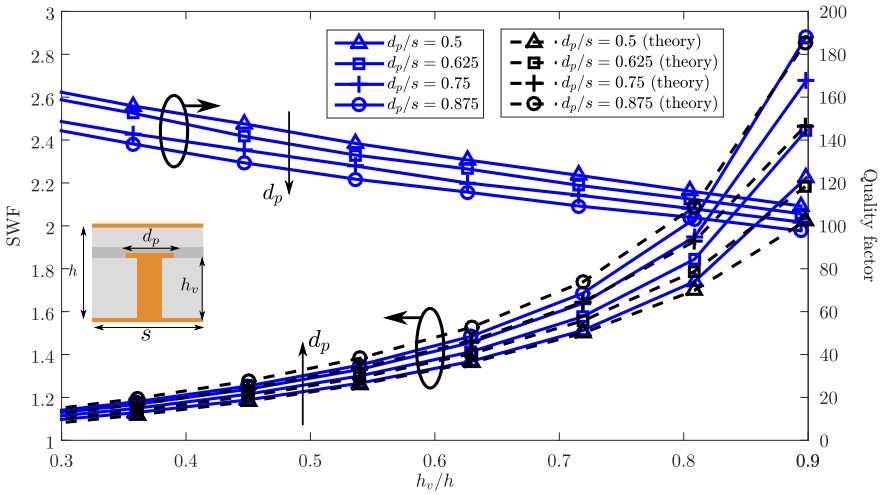

Figure 2.16 – Influence of via height h_v and copper land diameter d_p on SWF and quality factor at 1 GHz. These results were obtained for $s = 0.8$ mm, $h = 1.118$ mm, $d_v = 0.4$ mm and $h_p = 0.035$ mm

First of all, one can notice that the theoretical derivations provide a rather good estimation of the SWF as a function of both h_v and d_p. A maximum deviation of about 10% is obtained for very strong capacitive effect, i.e. $h_v/h = 0.9$.

Concerning the influence of the via height h_v, the slow-wave factor evolves following roughly an $\frac{1}{\sqrt{\ }}$ law, as the volume which contains the electric field V_e is inversely proportional to h_v. For an intermediate copper land diameter of $0.75s$, SWF ranges from 1.35 to 2.68 if h_v/h is increased from 0.3 to 0.9. At the same time, the quality factor is reduced by 40%, showing that the attenuation is increasing more "rapidly" than the slow-wave factor when increasing h_v. As shown in the loss contributions analysis, this would not be the case if only dielectric losses were involved. The reduction of the quality factor is mainly due to the extra dissipation which occurs on the surface of the blind via-hole.

In order to better understand the decrease observed for the quality factor, the same parametric variations are applied but the attenuation is illustrated. More precisely, the two contributions, namely metallic and dielectric dissipations are separated. The variations of both α_c and α_d are illustrated in Figure 2.17.

The dielectric attenuation follows the trend of SWF, as expected in theory. α_c rises very rapidly as function of h_v/h, it exhibits variations by a factor 1:4 in this observation range. Once again, the reason for this sharp increase lies in two facts. First, a greater confinement of the electric field leads to a greater SWF, and thus an accordingly increased magnetic field energy. Secondly, this energy is distributed in a smaller volume because of the presence of the via, so it requires even greater magnetic field and induces accordingly strong currents. Finally, as the via hole gets taller the integration path for these currents is also increasing. As a result, such a significant

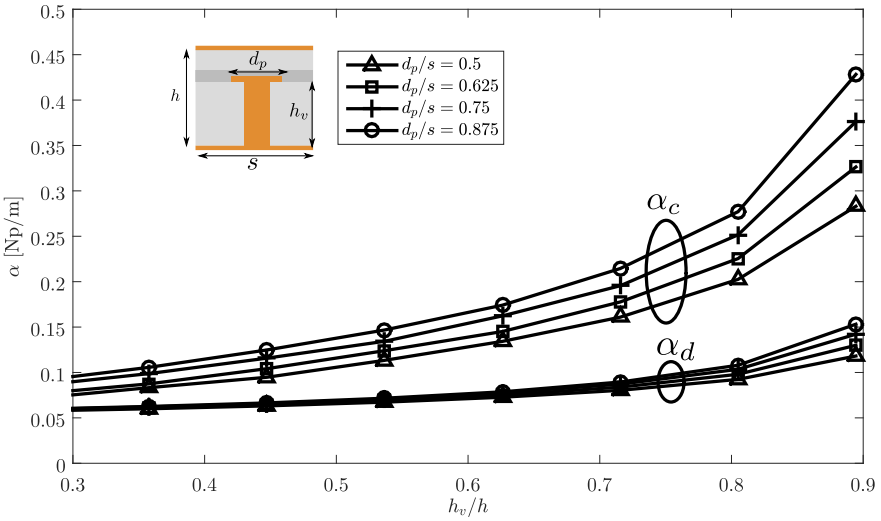

Figure 2.17 – Influence of via height h_v and copper land diameter d_p on metallic and dielectric attenuations at 1 GHz. These results were obtained for $s = 0.8$ mm, $h = 1.118$ mm, $d_v = 0.4$ mm and $h_p = 0.035$ mm, $tan\delta = 0.0024$, $\varepsilon_r = 3.55$

increase can be obtained, leading to the decrease of the quality factor.

In these conditions, a trade-off between quality factor and miniaturisation is required depending on the application. Both attenuation and SWF are evolving as increasing functions of the height h_v. That is because a greater h_v directly corresponds to a confinement of the electric field in a smaller volume. A similar conclusion is obtained when the copper land diameter is increased, which reduces the penetration of electric field in the lower part of the waveguide.

A second analysis was performed, that of the influence of the via hole diameter d_v. Once again, the parametric analysis was done in combination with a variation of the copper land diameter, so that large via holes with no copper lands can be compared to very thin via holes with large copper lands. The results are illustrated in Figure 2.18. Also, the theoretical estimation of SWF is added for comparison. In order to respect the geometrical constraint $d_p > d_p$, the number of copper land diameter d_p variations is adjusted for each value of d_v. Finally, the normalisation is again performed relatively to the unit-cell dimension $s = 0.8$ mm.

First of all, it is interesting to note that both SWF and Q, are decreasing functions of d_v/s. As a consequence, for a given copper land diameter d_p, a better quality factor as well as miniaturisation can be obtained with thinner via holes. That being said, if low losses are targeted, the copper land should be as small as possible. On the contrary, miniaturisation can be maximised if this copper land is extended. As an example, suppose that $d_v/s = 0.25$, by adjusting d_p, SWF or Q will be affected by variations of $\pm 15\%$, but each one in opposite directions.

Concerning the theoretical prediction of SWF, a rather good estimation is obtained between the extreme values of both d_v/s and d_p/s.

The different contributions to the attenuation are illustrated in Figure 2.19. First of all, the scale of the y-axis was increased, as the variations generated by changes in

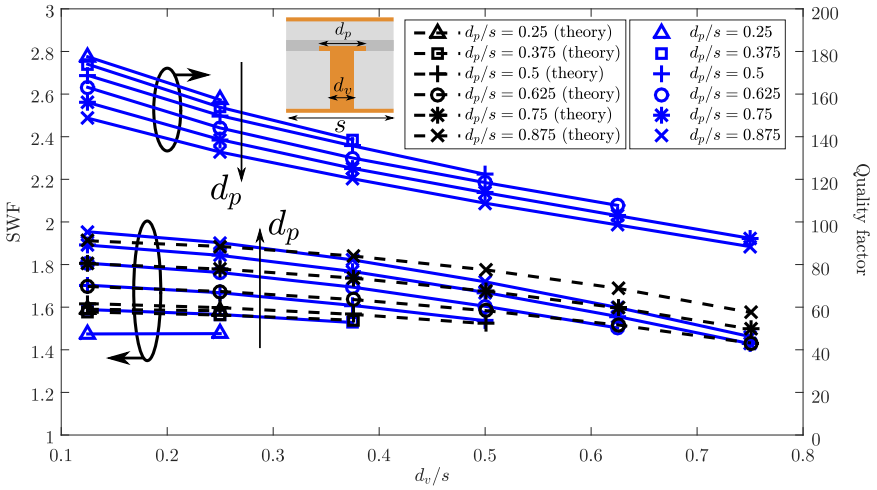

Figure 2.18 – Influence of via diameter d_v and copper land diameter d_p on SWF and Q. These results were obtained for $s = 0.8$ mm, $h = 1.118$ mm, $h_v = 0.813$ mm, $h_p = 0.035$ mm, $tan\delta = 0.0024$, and $\varepsilon_r = 3.55$

d_v are less significant that the ones of h_v. For d_v/s lying between 0.1 and 0.8, the dielectric attenuation α_d is reduced of maximum 30% in the case of large copper lands. As expected, it follows the variations of SWF. On the contrary, it is interesting to notice that α_c is an increasing function of d_v, with variations up to 65%. In fact, the increase of d_v results in a reduction of V_m, thus increasing the magnetic energy density and therefore the magnetic field amplitude. At the same time, the metallic surface exposed to the magnetic field is also expanded, inevitably leading to greater dissipation. On the other hand, the use of wide copper lands also leads to larger values of α_c. This can be interpreted by the strong relation between d_p and SWF, which in turns relates to the magnetic field amplitude.

As a conclusion, the slow-wave factor does not strongly depend on the via diameter d_v, but much more on the use of large copper land diameter d_p. As for the quality factor, it appears to be profitable to use thin via-holes to limit the metallic dissipation while limiting d_p.

Finally, a last analysis is performed, that of the size of the unit-cell s. As shown before, the unit-cell dimension needs to be small compared to the guided wavelength, otherwise higher dispersion occurs. Furthermore, small unit-cells should be preferred as they provide less geometrical constraints in any circuit design procedure. Until now, the results show that it is more interesting to use thin via holes, with large copper lands if the miniaturisation has to be maximised.

Let's consider the case of a thin via hole ($d_v/s = 0.25$) with a large copper land diameter ($d_p/s = 0.75$) which creates a strong fields separation. According to Figure 2.18, it provides $SWF = 1.84$ and $Q = 170$. A quality factor of nearly 190 could be achieved by reducing d_p to a value of 0.3 mm, however SWF would drop to 1.57 because the amount of fringing field becomes very important. Now, instead of reducing only d_p, the spacing s and the via diameter d_v are also scaled down. In other words, the comparison lies between a small number of large copper lands on top of thin via

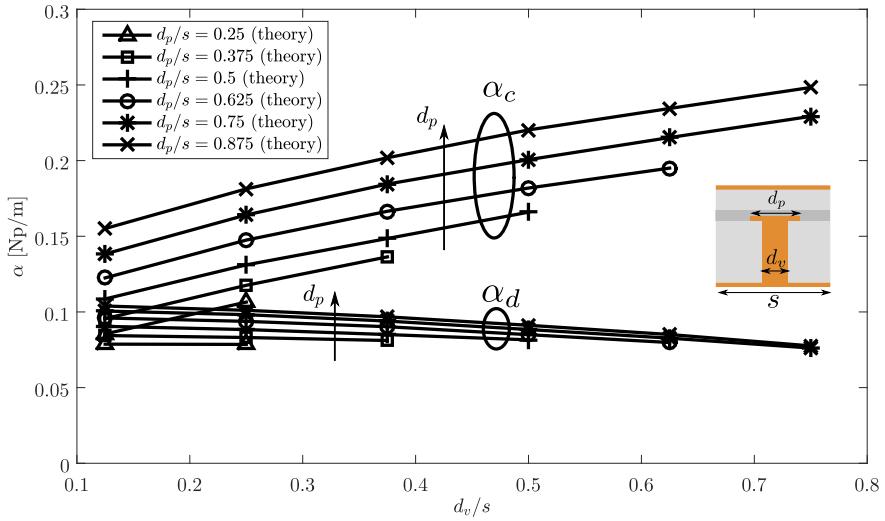

Figure 2.19 – Influence of via diameter d_v and copper land diameter d_p on the attenuation. These results were obtained for $s = 0.8$ mm, $h = 1.118$ mm, $h_v = 0.813$ mm, $h_p = 0.035$ mm, $tan\delta = 0.0024$, and $\varepsilon_r = 3.55$

holes, versus a more important number of via holes with smaller copper lands. In this comparison, the fixed parameter is the copper density in the unit-cell $\pi d_p^2/s^2$ (seen from the top plate). As a consequence, both d_p, s and d_v are scaled by the same factor. The only parameters which are not scale are the copper land thickness h_p and the via height h_v. The results are illustrated in Figure 2.20.

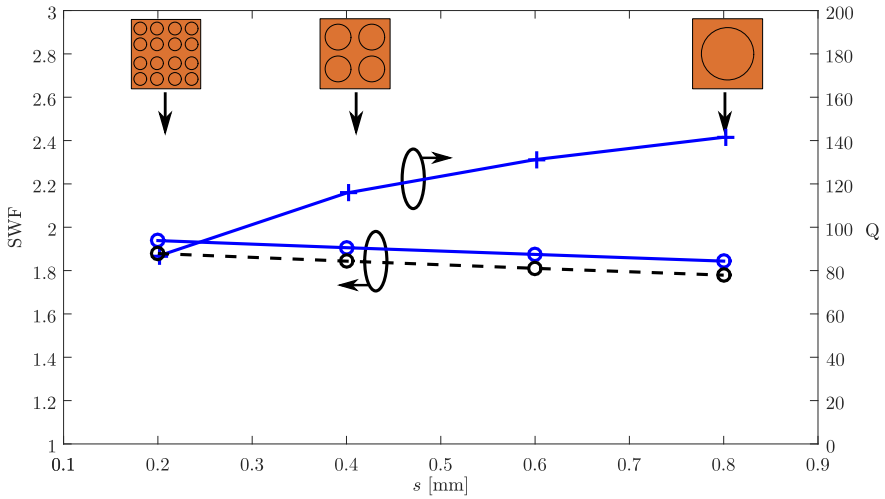

Figure 2.20 – Influence of unit-cell size s for on SWF and Q. The dotted lines correspond to theoretical estimations.

Four different configurations were simulated, starting from $s = 0.2$ mm to 0.8 mm. First, the slow-wave factor is not really affected by the change in s. If the unit-cell size is divided by four it is only increased by 5%. The theoretical estimation of SWF follows this weak variations, as both d_v, d_p and s are scaled by the same factor. On the

contrary, the quality factor exhibits a strong dependence on s. In this particular case, a value of 87 is obtained for $s = 0.2$ mm, while it is 141 for $s = 0.8$ mm, representing a variation of more than 60%. Because SWF is nearly constant, so should be the dielectric losses. The main factor for the strong reduction in Q is therefore the metallic dissipations. Mostly because h_v is not scaled at the same time as the other parameters, the amount of metallic surfaces per unit length is dependent on the unit cell dimension s. In other words, for smaller unit cells the relative quantity of metallic surfaces in the LPPW compared to the PPW is greater, thus leading to higher attenuation and lower quality factor.

As a conclusion, while at the same time a small unit-cell should be preferred for design flexibility and reduced dispersion, it also leads to significant quality factor degradation. On the overall, the best performance could be obtained in this case for relatively large cells with $s = 0.8$ mm, thin via holes of diameter $d_v = 0.4$ mm and copper-land diameter d_p chosen accordingly to the priority, either miniaturisation or high quality factor. For most of the design presented in this work, it was fixed to 0.6 mm.

2.4 A Slow-wave substrate integrated waveguide

2.4.1 Motivations and modelling

Following the analysis of the loaded parallel-plate waveguide, the properties of its closed counterpart as given in Figure 2.5 will now be presented. As for the SIW, the idea of the introduced SW-SIW is to confine the electromagnetic wave between two lateral walls, realised by copper-plated through via holes. For simplicity, the distance between these via holes is considered identical to that of the blind via holes s. In such a waveguide, the propagation in the longitudinal direction is the result of successive reflections on the lateral walls, which act as metallic boundaries.

The SIW is usually assimilated to its rectangular waveguide counterpart through the introduction of the effective width W_{eff} (see (4.13)). The angle at which the wave propagates inside the waveguide is frequency dependant in order to satisfy the lateral boundary conditions. This condition is expressed by equation (2.55) for the first mode, where β stands for the phase constant in the longitudinal direction, k_c is the cut-off wavenumber and k is the free-space wavenumber. For homogeneous waveguides, k is given by ω/c and k_c by ω_c/c, where $\omega_c = 2\pi f_c$ is the cut-off angular frequency. The cut-off wavenumber k_c can also be related to the effective lateral dimension W_{eff}.

$$\beta^2 = k^2 - k_c^2 = \left(\frac{\omega}{c}\right)^2 - \left(\frac{\omega_c}{c}\right)^2 = \left(\frac{\omega}{c}\right)^2 - \left(\frac{\pi}{W_{eff}}\right)^2 \tag{2.55}$$

The previous expression can be derived thanks to two important properties. First, the homogeneous material inside the waveguide should be non dispersive as well as isotropic, in the sense that wave velocity does not depend on the direction of propagation. In our case, the LPPW exhibits low dispersion for large wavelengths (see Figure 2.9), as well as a relatively good isotropy (see Figure 2.10), the same formalism was therefore adopted. The phase constant for the SW-SIW was therefore approxi-

mated by the following expression, where SWF is the slow-wave factor estimated in the LPPW configuration by equations (2.51)-(2.53).

$$\beta^2 = \left(\frac{\omega}{c}SWF\right)^2 - \left(\frac{\omega_c}{c}SWF\right)^2 = \left(\frac{\omega}{c}SWF\right)^2 - \left(\frac{\pi}{W_{eff}}\right)^2 \tag{2.56}$$

Because the wave propagation velocity is reduced in all directions, the miniaturisation of the waveguide occurs not only in the lateral dimension (as for the Ridge waveguide [15]), but also in the longitudinal one. Therefore, the relevant miniaturisation factor of the SW-SIW is not SWF but rather SWF^2.

In the next section, we will show some simulation results comparing SIW and SW-SIW.

2.4.2 Electrical performance

The analysed SW-SIW is made of 8 blind via holes separated by $s = 0.8\ mm$. Its width W is set to $9s$ so that the spacing is equally distributed along the transverse section. To begin with, the electric and magnetic field amplitudes are represented in Figure 2.21 at the first mode cut-off frequency of 6.6 GHz.

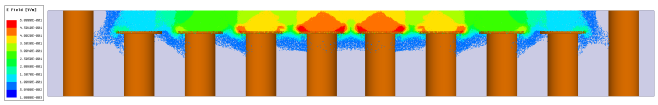

(a)

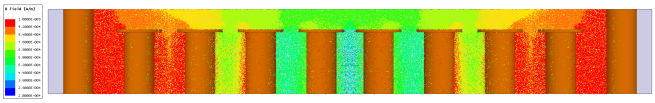

(b)

Figure 2.21 – Fields amplitude in the SW-SIW at the cut-off frequency: (a) Electric field, (b) Magnetic field.

The dispersion diagram of the unit-cell is represented in Figure 2.22 for the two first modes. In the same graphic are also represented the curves corresponding to the SIW having the same cut-off frequencies. In comparison with the LPPW, the SW-SIW exhibits a high-pass characteristic with a strong dispersion at low frequencies, then the trends are similar with a maximum frequency of about 30 GHz. For a given frequency and mode, the phase constant of SW-SIW is significantly greater than that of the SIW, demonstrating the presence of the slow-wave effect.

The following analysis was limited to the mono-mode bandwidth, as it is of higher interest for most of circuit designs. The SWF as defined by the ratio of phase constants in SW-SIW and SIW, is illustrated in Figure 2.23. It is also compared to that of the LPPW. Both waveguides provide similar slow-wave factors, the maximum difference being of only 2% in the observed bandwidth. Concerning the SW-SIW, a small variation can be observed at lower frequencies, it is readily explained by the fact that the two compared waveguides do not have the absolutely same cut-off frequency.

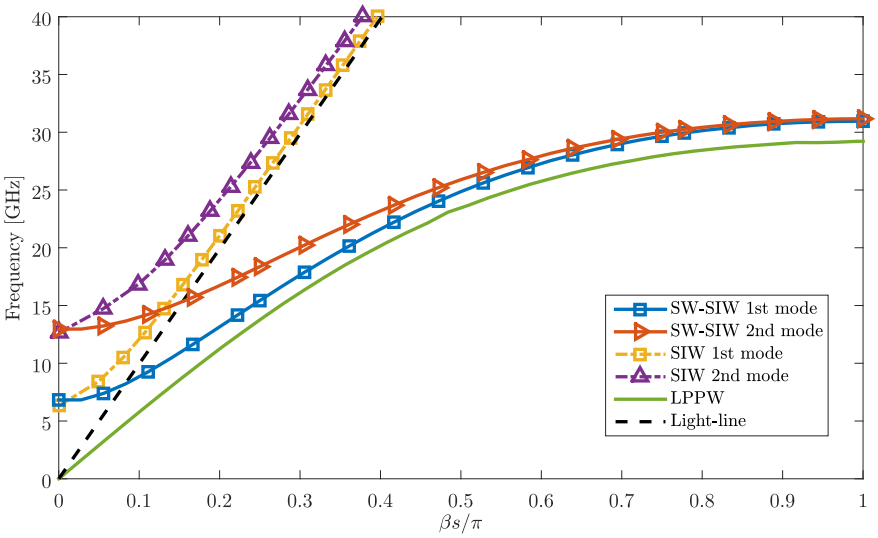

Figure 2.22 – Dispersion diagram of the two first modes in SW-SIW compared to LPPW and SIW.

That being said, a value of approximately 1.73 is maintained for all the mono-mode bandwidth.

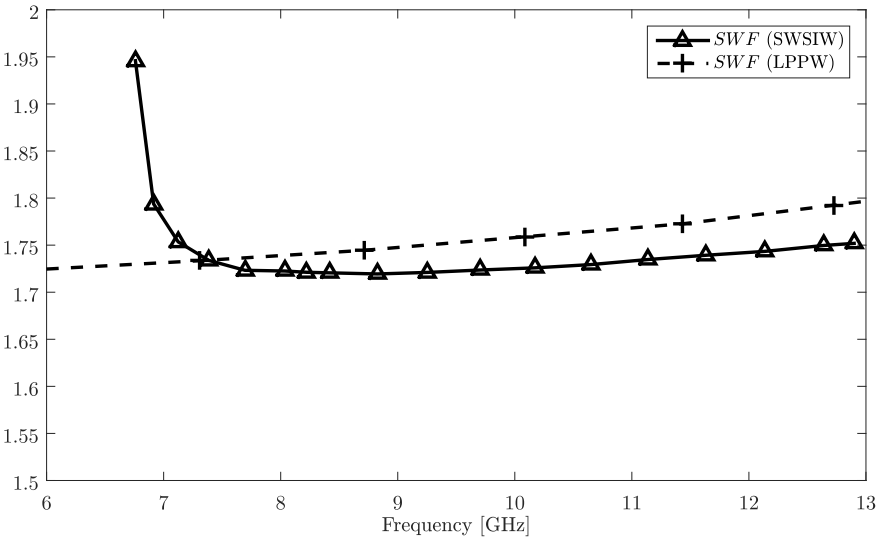

Figure 2.23 – Compared SWF of LPPW and SW-SIW.

Thanks to the fact that SWF is almost constant, the comparison of the quality factors is equivalent to the comparison of the attenuations. First of all, SIW and SW-SIW quality factors are compared while all conductors are considered as perfect conductors (PEC). Once again, the idea is to verify the theoretical prediction that dielectric dissipation is increased at the inverse rate as the velocity is decreased (see section 2.2.3), thus maintaining the quality factor. By observing the two curves on the top of the figure one can see that this principle is verified, with a maximum deviation

of 8%.

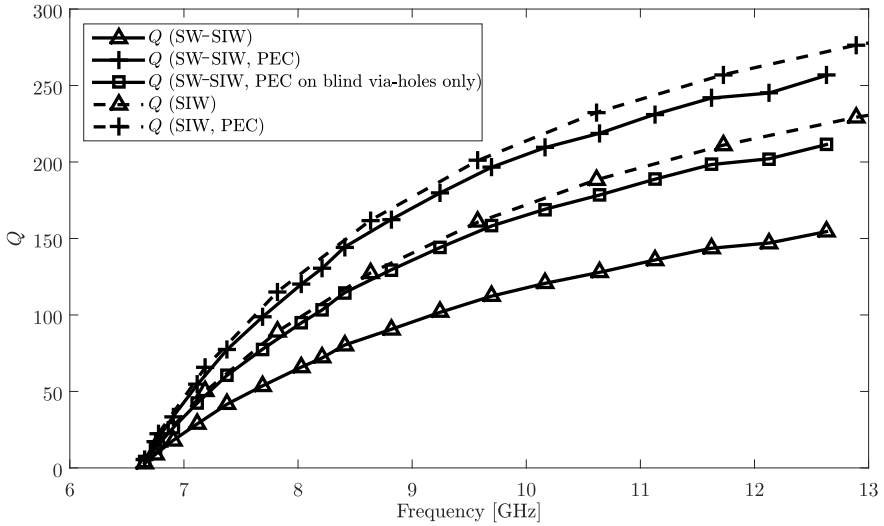

Figure 2.24 – Compared quality factors of SIW and SW-SIW.

When all losses contributions are taken into account, the SW-SIW quality factor is lower than that of the SIW by about 32%. Then, if dissipation is removed on the surface of the blind via hole one obtains similar values as for the SIW, ie. about 180 at 11 GHz. The degradation of the quality factor is therefore very close to that observed in the LPPW. The parametric analysis conclusions for the LPPW are still valid in the SW-SIW, as long as the distribution of blind via holes remains homogeneous.

2.4.3 Brief parametric analysis

In this last section, the influence of the two main geometric parameters is detailed. The first one is the blind via height h_v, the second one is the spacing s.

First, the phase constant obtained as a function of frequency for the first mode is illustrated for various values of h_v/h in Figure 2.25.

On the same figure, the theoretical evaluation of β from (2.56) is also plotted for comparison. In addition, two curves of SIW waveguides are added. The one on the right corresponds to the case $h_v = 0$, its width is thus W. The second one has a reduced width so that its cut-off frequency matches that of the SW-SIW with the maximum slow-wave effect.

Without any blind via hole (i.e $h_v/h = 0$), the simulated cut-off frequency is 11.4 GHz. By inserting via holes, the cut-off frequency is decreased at a rapid rate, leading to a cut-off at 5.76 GHz for $h_v/h = 0.8$, which is nearly half that of the SIW with identical dimensions. At the same time, the phase constant slope is increasing, demonstrating that longitudinal miniaturization is also achieved.

Finally, theoretical prediction shows a very good agreement with the simulation. A maximum deviation for the cut-off frequency of 3.5% is obtained for $h_v/h = 0.8$, which corresponds to a high SWF. In this extreme case, the difference on the phase constant is less than 6% on all the mono-mode bandwidth.

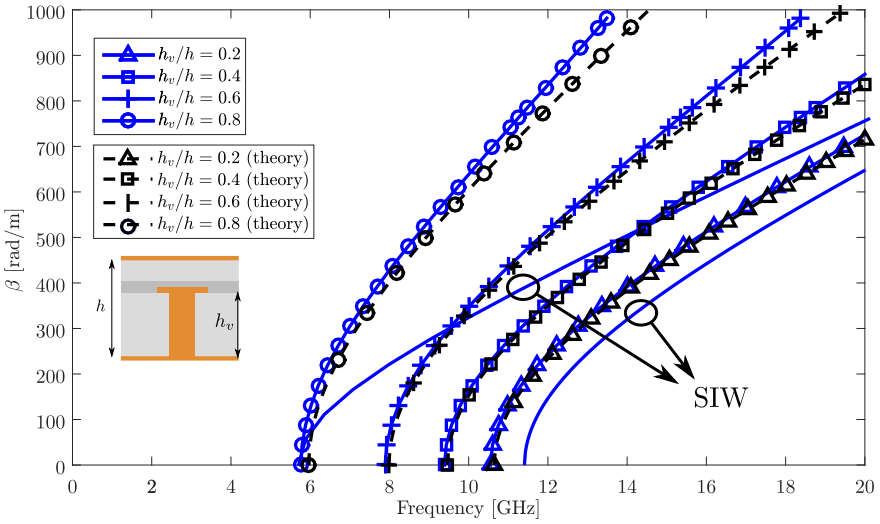

Figure 2.25 – Influence of the via height h_v on the SW-SIW phase constant ($W = 9s$, $s = 0.8$ mm, $h = 1.118$ mm, $d_p = 0.6$ mm, $h_p = 0.035$ mm, $tan\delta = 0.0024$, and $\varepsilon_r = 3.55$)

The corresponding attenuation and quality factor are illustrated in Figure 2.26. As already showed in Figure 2.24, the quality factor of SW-SIW is lower than that of the SIW. In other words, the increase which is obtained in phase constant is not fully compensated by the increase in attenuation, so that the overall figure of merit is degraded.

As one can see in these two figures, the same kind of conclusions can be drawn as for the parallel plate configuration. The attenuation increase is stronger than that of the phase constant, therefore leading to a degradation of the quality factor. If the priority is set on the miniaturization, a ratio $h_v/h = 0.8$ can provide a division of the occupied area by nearly four, as both β and f_c are divided by approximately two. This miniaturization comes at the price of a 35% reduction in the quality factor.

Secondly, the number of via holes is increased by adjusting the spacing s. As for the LPPW, both d_v, d_p and s are scaled simultaneously to maintain an equal apparent density of metallic surface as seen from the top cover. The procedure is very similar to that of Figure 2.20. Also, the external via holes were replaced by equivalent metallic walls in order to observe only the influence of the blind via holes distribution. For this simulation, the height h_v was fixed to the value used for the circuits presented in Chapter 3 and 4, i.e 0.813 mm. The spacing s is expressed as a fraction of the cut-off wavelength λ_c, that is $2W$.

As expected, the adjustment of s from very small values ($\lambda_c/72$, i.e. 31 via holes in the transverse section), to relatively large ones ($\lambda_c/18$, i.e. 9 via holes in the transverse section) has little effect on the phase constant. In this range of variation, the cut-off frequency lies between 6.34 GHz and 6.62 GHz, that is a variation of $\pm 2\%$. This small sensitivity is correctly represented by the model as well.

On the other hand, as seen for the LPPW configuration the attenuation should be a lot more influenced by this geometrical parameter. Both α and Q are represented in

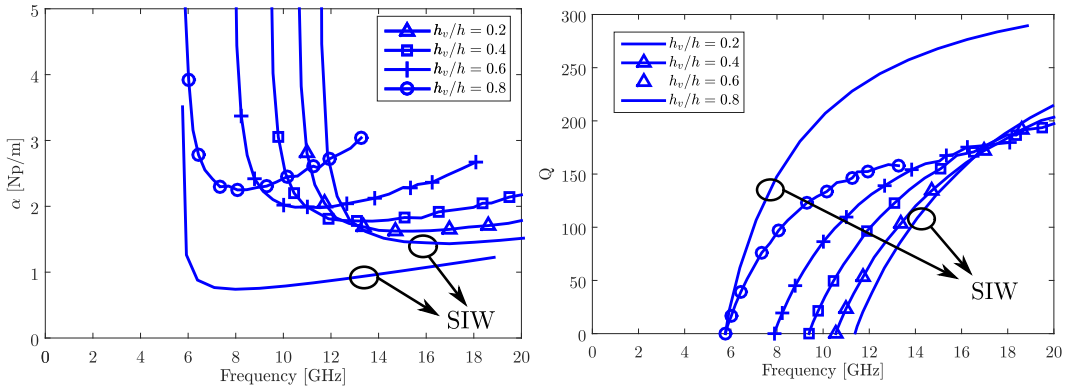

(a) (b)

Figure 2.26 – Influence of the via height h_v on the SW-SIW (a) attenuation constant and (b) quality factor ($W = 9s$, $s = 0.8$ mm, $h = 1.118$ mm, $d_p = 0.6$ mm, $h_p = 0.035$ mm, $tan\delta = 0.0024$, and $\varepsilon_r = 3.55$).

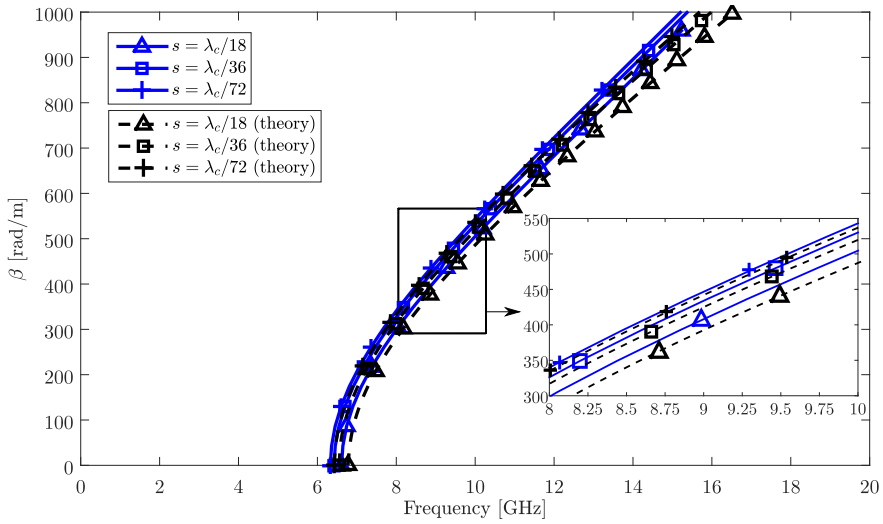

Figure 2.27 – Influence of the unit cell dimension s on the SW-SIW phase constant ($s = 0.8$ mm, $h = 1.118$ mm, $d_p = 0.6$ mm, $h_p = 0.035$ mm, $tan\delta = 0.0024$, and $\varepsilon_r = 3.55$)

Figure 2.28 for the same variations of s.

By contrast with the phase constant, the attenuation constant is rapidly increased if the number of via holes is multiplied in the transverse section, leading to a significant degradation of the quality factor. In this range of observation, the quality factor at 10 GHz drops down from 122 to 81 in the worst case.

As a conclusion, a trade-off has to be defined depending on the required quality factor and design flexibility. In one hand, using smaller unit cells will release the geometrical constraints and ease the design but will lead to lower quality factors. For non resonant passive components which do not rely on precise effects such as weak couplings this approach can be of high interest. Indeed, the distributed slow-wave

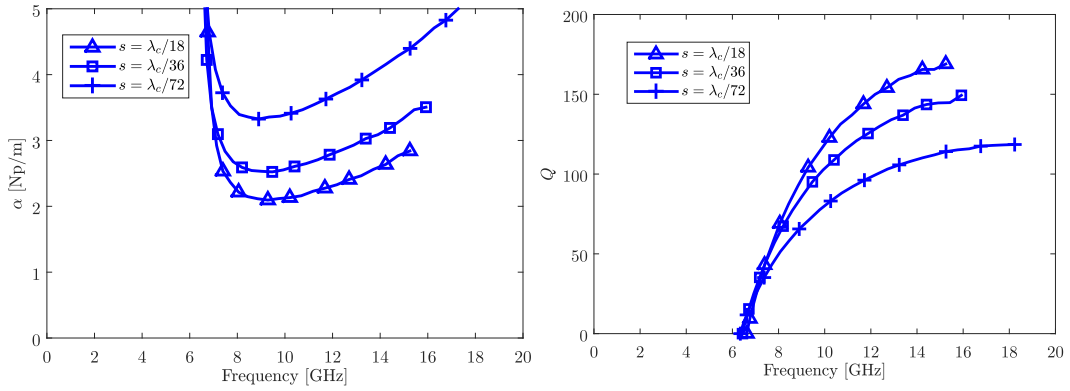

(a) (b)

Figure 2.28 – Influence of the unit cell size s on the SW-SIW (a) attenuation constant and (b) quality factor ($W = 7.2$ mm, $h = 1.118$ mm, $h_p = 0.035$ mm, $tan\delta = 0.0024$, and $\varepsilon_r = 3.55$).

effect can be completely integrated in an equivalent homogeneous substrate, so that the simulation process can be as fast as in SIW. We will focus on this point in Chapter 3.

On the contrary, for circuits such as filters which require high quality factors and precise couplings, s can be increased to reduce the insertion loss. In this case, the design procedure should then carefully take the greater discrete character of the waveguide into account. This problematic will be dealt with in Chapter 4.

2.4.4 Design rules

Based on the previous analysis, the following design rules can be defined for a given miniaturization goal, i.e. a given value of SWF. We consider a technology stack-up which does not contains dielectric variations to be coherent with the obtained conclusions. In circuit design, one should keep in mind that the occupied area of a SW-SIW circuit will be about that of its counterpart in SIW divided by SWF^2.

First of all, considering the standard copper conductivity and dielectric constants available, a reasonable upper limit for SWF can be set at two, which leads to a surface reduction by four. For higher SWF, we believe that even by adjusting all via hole dimensions, a degradation of the quality factor below 50% would be hardly obtained.

Once the SWF value is defined, an estimation of the maximum spacing s can be obtained by aiming at a distributed effect for easier circuit design. Let's consider an operation frequency f placed at the center of the mono-mode frequency band. The cut-off frequency is therefore defined as $f_c = \frac{2}{3}f$. The maximum frequency in the mono-mode operation is $2f_c$, it is associated to the smaller guided wavelength $\lambda(2f_c)$. For instance, a distributed assumption can be expressed by $\lambda(2f_c) \leq 10s$. Furthermore, based on the expression of β given by (2.56), one can easily derive the following relation:

$$\lambda(2f_c) = \frac{c_0/\sqrt{3\varepsilon_r}}{f_c SWF} \tag{2.57}$$

Then, the following upper limit for s can be defined:

$$s \leq \frac{c_0}{10\sqrt{3\varepsilon_r} f_c SWF} \tag{2.58}$$

We did not define explicit lower limit for s, however one should keep in mind that reducing s quickly leads to an increased attenuation and degraded quality factor. The upper limit as defined by (2.58) can for instance be adopted as initial value.

This spacing can be used in the lateral walls as well for simplicity of design. The upper limit fixed for s is in fact more restricting than that given by [16] (see (1.18)). The definition of the lateral walls can be completed by setting $d_{ext} = s/2$, as it is often chosen in SIW. Finally, using the expression of the effective width (4.13) and the cut-off frequency value the waveguide lateral dimension W can be estimated.

In general, metallic layer thickness follow standard format, so that the choice of h_p is somehow already pre-defined, for instance 17 or 35 µm. Then, h_v and h can be defined considering the commercialized material thickness's. As a first approximation, they can be related to the SWF by the following expression, which is readily derived from 2.36 by neglecting the fringing field.

$$SWF \approx \frac{h}{h - h_v - h_p} \tag{2.59}$$

Depending on the material availability, a combination of h and h_v leading to the proper SWF can be defined.

In the end, the only parameters remaining are the diameters d_v and d_p. Already, fabrication constraints generally impose that d_p should be greater than d_v from a certain margin in order to ensure a functional copper plating process. In our case, the rule was $d_p \geq d_v + 200\,\mu m$. Based on the parametric analysis, the following rules can be applied. First, for a given SWF, thinner via holes do provide greater quality factors, at the condition of reducing the copper land diameter accordingly. Thus, let assume that the minimum available drilling diameter is chosen for d_v. By evaluating SWF using (2.51)-(2.53) for different values of d_p, the targeted value can be obtained.

This procedure should be finalized by performing a simulation of the obtained waveguide, to confirm and if necessary adjust the dimensions.

The circuits presented in this thesis have been developed in parallel with the modelling work detailed in this chapter. As a consequence, the dimensions which were selected do not necessary represent the exact optimal configuration, however they provide already interesting results as first realisations.

2.5 Conclusion

In this chapter, the theoretical underlying principles for the SW-SIW topology were given. Based on some properties of periodic structures, the slow-wave phenomenon was related to energy considerations. More precisely, the requirement for magnetic and electric energies spatial separation was highlighted. By adopting an ideal framework in a parallel-plate waveguide configuration, an explicit formulation of the slow-wave factor was derived, as well as informations about field amplitudes, impedance and losses contributions.

In practice, the energy separation is achieved in SIW by inserting blind via holes, limiting the extent of the electric field to the top part of the waveguide. Thanks to the use of an homogeneous distribution of these via holes, the analysis was reduced to that of a loaded parallel-plate configuration (LPPW) in a first step. Using the ideal case considerations, an estimation of the slow-wave factor was carried out. Then, the impacts of several geometric parameters on the velocity reduction and attenuation were analysed.

Then, the performance of the SW-SIW was compared to that of the SIW, showing a good agreement with the conclusions obtained for the LPPW. Based on the theoretical approximations performed in the LPPW configuration, an expression for the phase constant in SW-SIW was derived.

Finally, a brief parametric analysis of the SW-SIW was performed and design rules were derived. In future works a model for the attenuation could be derived, so that the optimum dimensions of the SW-SIW could be obtained more accurately through analytical calculations. Furthermore, dielectric constant variations among the different layers could also be investigated.

References

[1] D. A. Watkins, *Topics in electromagnetic theory.* Wiley, 1958.

[2] R. Collin, *Field Theory of Guided Waves.* IEEE Press, 1991.

[3] H. Jin, K. Wang, J. Guo, S. Ding, and K. Wu, "Slow-wave effect of substrate integrated waveguide patterned with microstrip polyline," *IEEE Transactions on Microwave Theory and Techniques*, vol. 64, no. 6, pp. 1717–1726, June 2016.

[4] A. Niembro-Martin, V. Nasserddine, E. Pistono, H. Issa, A.-L. Franc, T.-P. Vuong, and P. Ferrari, "Slow-wave substrate integrated waveguide," *IEEE Transactions on Microwave Theory and Techniques*, vol. 62, no. 8, pp. 1625–1633, Aug. 2014.

[5] S. J. Orfanidis, *Electromagnetic Waves and Antennas.* Rutgers University, 2014.

[6] H. Hasegawa, M. Furukawa, and H. Yanai, "Properties of microstrip line on si-sio2 system," *IEEE Transactions on Microwave Theory and Techniques*, vol. 19, no. 11, pp. 869–881, Nov. 1971.

[7] E. H. Bottcher, H. Pfitzenmaier, E. Droge, and D. Bimberg, "Millimetre-wave coplanar waveguide slow wave transmission lines on inp," *Electronics Letters*, vol. 32, no. 15, pp. 1377–1378, July 1996.

[8] A. Bautista, A. L. Franc, and P. Ferrari, "Accurate parametric electrical model for slow-wave cpw and application to circuits design," *IEEE Transactions on Microwave Theory and Techniques*, vol. 63, no. 12, pp. 4225–4235, Dec. 2015.

[9] J. Selga, P. Velez, J. Bonache, and F. Martin, "Slow wave ebg-based transmission lines and applications," in *Proc. International Conference on Electromagnetics in Advanced Applications (ICEAA)*, Cairns, Australia, Sep. 2016, pp. 484–486.

[10] J. S. Hong and M. J. Lancaster, "Capacitively loaded microstrip loop resonator," *Electronics Letters*, vol. 30, no. 18, pp. 1494–1495, Sep. 1994.

[11] G. F. Engen and C. A. Hoer, "Thru-reflect-line: An improved technique for calibrating the dual six-port automatic network analyzer," *IEEE Transactions on Microwave Theory and Techniques*, vol. 27, no. 12, pp. 987–993, Dec. 1979.

[12] Ansoft, "ANSYS HFSS, 3D Full-wave Electromagnetic Field Simulation." [Online]. Available: http://www.ansoft.com/products/hf/hfss/

[13] F. Xu, A. Patrovsky, and K. Wu, "Fast simulation of periodic guided-wave structures based on commercial software," *Microwave and Optical Technology Letters*, vol. 49, no. 9, pp. 2180–2182, June 2007.

[14] F. Xu, K. Wu, and W. Hong, "Equivalent resonant cavity model of arbitrary periodic guided-wave structures and its application to finite-difference frequency-domain algorithm," *IEEE Transactions on Microwave Theory and Techniques*, vol. 55, no. 4, pp. 697–702, Apr. 2007.

[15] M. Bozzi, S. A. Winkler, and K. Wu, "Broadband and compact ridge substrate-integrated waveguides," *IET Microwaves, Antennas Propagation*, vol. 4, no. 11, pp. 1965–1973, Nov. 2010.

[16] D. Deslandes, "Etude et developpement du guide d'ondes integre au substrat pour la conception de systemes en ondes millimetriques," Ph.D. dissertation, Ecole Polytechnique, Montreal, 2005.

Chapter 3

Miniaturization of non resonant circuits in X-band

Contents

3.1 Introduction 74

3.1.1 Motivations behind the resonant/non-resonant circuits distinction 74

3.1.2 Overview of SIW coupler technologies 74

3.2 Design of couplers in SIW and SW-SIW technologies in X-band 76

3.2.1 Short-slot coupler principle of operation and theory 76

3.2.2 Design in SIW technology 78

3.2.3 Design in SW-SIW technology 83

3.3 Measurement results and retro-simulations 94

3.3.1 Measurement results 94

3.3.2 Fabrication process variations and retro-simulations 97

3.4 Conclusion 102

References 103

3.1 Introduction

3.1.1 Motivations behind the resonant/non-resonant circuits distinction

In this first chapter dedicated to circuits design, the slow-wave topology previously introduced will be applied to non resonant circuits in X-band, more precisely 0-dB and 3-dB couplers around 11 GHz. The slow-wave effect will be applied to existing SIW topologies, showing interesting miniaturization capabilities without any change in the principles of operation. But first, the motivations for the distinction between resonant and non-resonant circuits that led to chapters 3 and 4 separation will be briefly discussed.

On one hand, circuits such as filters and resonant antennas rely on precisely adjusted phase conditions in order to obtain a specific response at a given frequency. For periodic structures such as the SW-SIW with a period of about one tenth of a wavelength, such conditions will not be completely independent on the blind via holes placement. This is also the case for regions where a precise inter-resonator coupling has to be achieved, as well as in the vicinity of radiating slots or apertures. For this reason, this placement has to be properly taken into account during the design procedure, as shown in the next chapter for coupled cavity filters.

On the other hand, non resonant circuits such as power dividers, couplers and interconnects have generally broadband properties which do not rely on very precise local effects such as weak couplings. In that case, the blind via holes placement is not very critical in most of the regions as soon as the slow-wave effect is homogeneously distributed in the waveguide.

For such via hole distributions (i.e. homogeneous both in transverse and longitudinal directions), an equivalent effective permittivity can be introduced. Thus, fast simulations can be performed because of the absence of blind via holes. Once again, such an equivalent model would not be suitable for filters or antennas as it is unable to translate the local influence of a blind via hole on coupling phenomenon or radiation for instance. Before going into these details, a brief overview of current miniaturised couplers in SIW will be given in section 3.1.2. Then, the design of the reference 0-dB and 3-dB couplers in SIW is presented (section 3.2.2). Pivoting to the SW-SIW, a description of an equivalent waveguide is given in 3.2.3.1. This equivalent waveguide can be used to design couplers as in section 3.2.3.2. Finally, measurement results are presented and compared with simulation and state-of-the-art couplers in section 3.3.

3.1.2 Overview of SIW coupler technologies

Couplers are essential building blocks in micro-wave circuits, they operate different functions depending on the application. In some cases, they can be used to separate an input signal in two different ones, while affecting one of the two by a certain amount of phase shift. This function is especially useful for realising mixers, phase shifters and antenna feeding networks. As the SIW technology provides a good platform for carrying relatively high-power signals while avoiding parasitics coupling, it has been

extensively studied in this context. Different architecture of feeding networks such as Nolen [1, 2] or Butler [3, 4] matrices have already been realised.

They are also used to extract a small fraction of a travelling signal along a waveguide, thus providing information about its amplitude and phase. This extraction can also be directional, in the sense that the coupler will be able to differentiate between two opposite travelling directions. The main application of such a component is the measurement of scattering parameters. Couplers are indeed a critical component of any vector network analyser (VNA).

While these circuits provide interesting functions, one of their weakness is generally the occupied area. Especially for strong coupling coefficients, a large coupling region is necessary to bring the power from the main path to the coupled one. In SIW technology, several techniques were used to miniaturize these structures, they are described hereafter.

First of all, most of SIW couplers are based on one of two different topologies, the slot-based and the ring-shaped couplers. As depicted in Figure 3.1, the former is based on coupled modes travelling in adjacent waveguides through apertures, either performed in the waveguide broad [4, 5] or side [6] walls. The latter is based on the well-known ring shaped (or rat-race) coupler, it was first applied in SIW in 2006 [7] but was introduced as early as in 1947 by Tyrrell [8] in conventional rectangular waveguide. The power distribution in this case is caused by a specific standing-wave pattern along the ring.

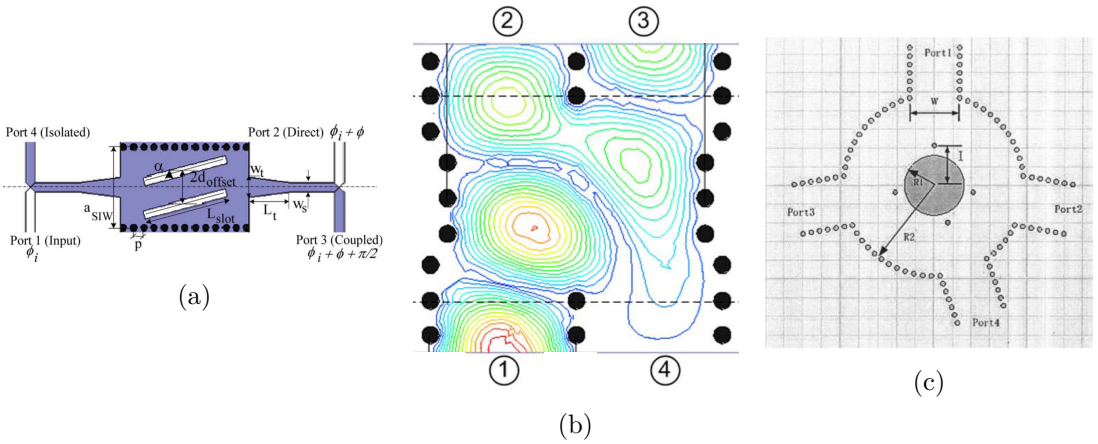

Figure 3.1 – Three examples of existing SIW coupling topologies (a) Broad-wall aperture [5] (b) Side-wall aperture (short-slot) [6] and (b) Ring [7].

Let's consider the miniaturization potential of these existing solutions. For coherence all the comparisons are done by taking only the coupling region into account. Already, the two-layer broad-wall coupling mechanism offers obviously an interesting area reduction, at the cost of a more complex fabrication. In [5], the coupling region area is only $0.54\lambda_0^2$, where λ_0 stands for the free-space wavelength at center-frequency in the substrate permittivity. By applying the half-mode strategy, this area was reduced to $0.37\lambda_0^2$ in [9].

Regarding the side-wall coupling topologies, the short-slot coupler from [6] occupies

a normalised area of $1.6\lambda_0^2$. In [10] the half-mode principle was applied and led to an area of $1.07\lambda_0^2$. Also, by combining this strategy with a ridge waveguide, a surface of $0.47\lambda_0^2$ was obtained in [11].

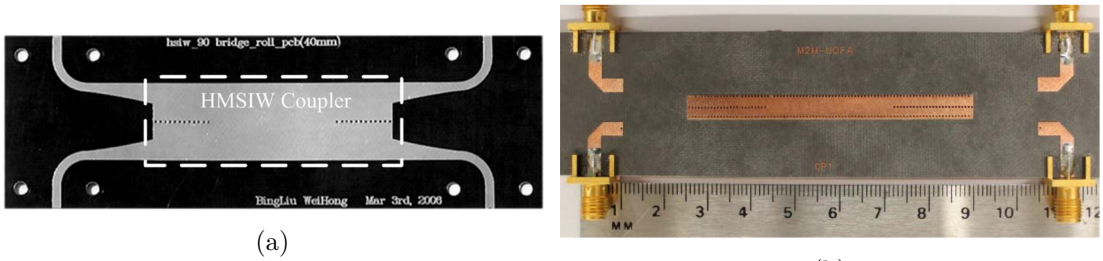

(a) (b)

Figure 3.2 – Miniaturised side-wall couplers based on (a) Half-mode SIW [10] and (b) Ridge, half-mode SIW [11].

The ring topology has a greater size, with an occupied area of $4\lambda_0^2$ in [7]. For this reason, several attempts to reduce the dimensions of this topology have been published (see Figure 3.3). In [12], a T-folded SIW was used to reduce its size to about $0.96\lambda_0^2$. Also, the combined use of ridge waveguide and electromagnetic band-gap (EBG) loading have demonstrated even further miniaturization up to $0.54\lambda_0^2$ in [13].

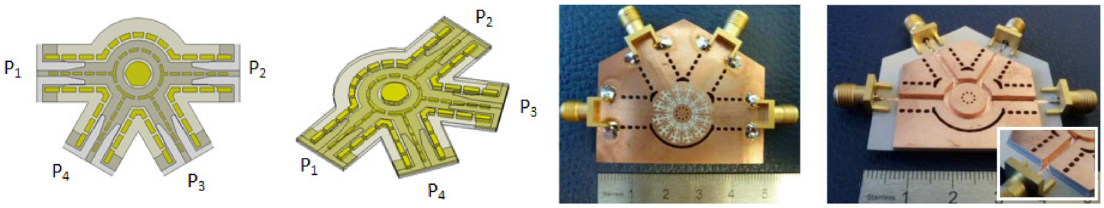

(a) (b)

Figure 3.3 – Miniaturised ring couplers (a) T-Folded [12] and (b) Ridge, EBG-loaded [13].

In this context, this work intends to demonstrate the possibility of realising compact couplers using the slow-wave effect. The short-slot topology was selected for its simple formulation and wide use in antenna feeding networks.

3.2 Design of couplers in SIW and SW-SIW technologies in X-band

3.2.1 Short-slot coupler principle of operation and theory

The short-slot coupler topology was first introduced by Riblet in 1950 [14] along with its theoretical description. It was also described by R. Levy in [15] and then used in a lot of different rectangular waveguide based applications. Since 2005 several realizations of this short-slot coupler in SIW technology have been demonstrated (see [6, 16–20]).

Given its simple formulation it was therefore chosen to demonstrate the size reduction provided by the slow-wave topology.

Basically, its operation principle relies on the interference of two propagating modes, the fundamental TE_{10} and TE_{20}. It is illustrated in its SIW implementation form in Figure 3.4. In order to provide the required interference, a larger waveguide is inserted between the four waveguide access. For practical reasons the access waveguide are operating in their mono-mode frequency band, carrying only a propagating TE_{10}. However, both TE_{10} and TE_{20} modes can propagate in the enlarged middle section and provide the power division functionality.

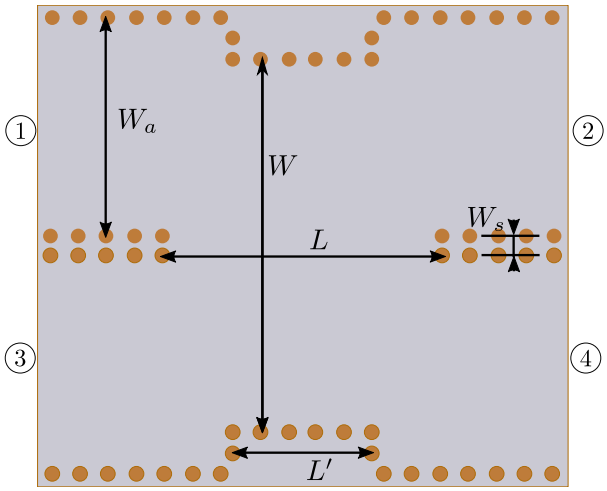

Figure 3.4 – Topology of short-slot coupler in SIW technology.

The geometric parameters defining this device are denoted W_a,W_s, W, L and L'. The frequency of operation defines the access waveguides width W_a for mono-mode operation. The waveguide separation wall defined by W_s is not a critical parameter, an arrangement of one or two via holes is sufficient to avoid unwanted coupling. The fundamental parameters responsible for the interference phenomenon are those defining the center region size, namely L and W. An analysis of the scattering matrix based on even-odd mode analysis is presented in [6]. By considering both the interference pattern required for the power division and the minimisation of return loss they obtained design equations for W and L, given by (3.1) and (3.2), respectively. In these equations, $|S_{41}|$ stands for the coupled power to the opposite port, k is the free space wavenumber at the operating frequency and n is a positive integer. The secondary parameter L' is tuned by full-wave simulation in HFSS.

$$W = \frac{\pi}{k}\sqrt{\frac{\left[\pi\left(2n+1\right)+4sin^{-1}|S_{41}|\right]\left[3\pi\left(2n+1\right)-4sin^{-1}|S_{41}|\right]}{8sin^{-1}|S_{41}|\left[\pi\left(2n+1\right)-2sin^{-1}|S_{41}|\right]}} \tag{3.1}$$

$$L = \frac{\left(2n+1\right)\pi}{2\sqrt{k^2-\left(\frac{\pi}{W}\right)^2}} \tag{3.2}$$

To evaluate the performance of the SW-SIW technology, the design was realised in SIW and SW-SIW for two power division ratios, 3-dB and 0-dB. The latter corresponds to the so-called crossover. The design steps along with simulation results are detailed in the following sections.

For both the SIW and SW-SIW technologies, fabrication was performed on the same technology stack, presented previously in 2.5. In this configuration, the average relative permittivity of 3.55 was considered. Finally, an operating frequency of 11 GHz was chosen.

3.2.2 Design in SIW technology

3.2.2.1 Coupler design

By considering the case where $|S_{41}| = 1/\sqrt{2}$, design equations (3.1) and (3.2) reduce to (3.3) and (3.4), where λ_0 is the free-space wavelength at 11 GHz considering the substrate dielectric constant.

$$W = \lambda_0 \sqrt{\frac{(n+1)(3n+1)}{4n+1}} \tag{3.3}$$

$$L = \lambda_0 \sqrt{\frac{(n+1)(3n+1)}{12}} \tag{3.4}$$

The numerical values obtained for $n = 1, 2, 3$ are listed in Table 3.1. In fact, n should be as small as possible for area reduction, as W and L are increasing sequences of n. For $n \geq 2$ the width W is greater than 22.11 mm, which leads to the possible propagation of TE_{30} mode at the operating frequency, thus $n = 1$ was selected.

n	1	2	3
W [mm]	18.31	22.11	25.39
L [mm]	11.82	19.15	26.43

Table 3.1 – Theoretical dimensions of the interference region in SIW technology for a 3-dB coupler

In order to lie approximately in the center of the mono-mode bandwidth of the access waveguides W_a was set to 11.2 mm for a first cut-off frequency of 7.25 GHz. Thus, the second mode starts to propagate at about 14.5 GHz. A double row of via holes separated by $W_s = 0.6$ mm was inserted between the accesses to provide a sufficient isolation.

The coupler was implemented in HFSS and full-wave simulations were carried out to obtain the optimized response illustrated in Figure 3.5 and Figure 3.6. The final geometric parameters are $W = 19.7$ mm, $L = 14.92$ mm and $L' = 8.8$ mm. The value of W is relatively close to that provided by the theory, however L is much larger than its initial value. As mentioned in [6],[21][22] this is related to the non negligible influence of the evanescent TE_{30} mode for short-slot topology.

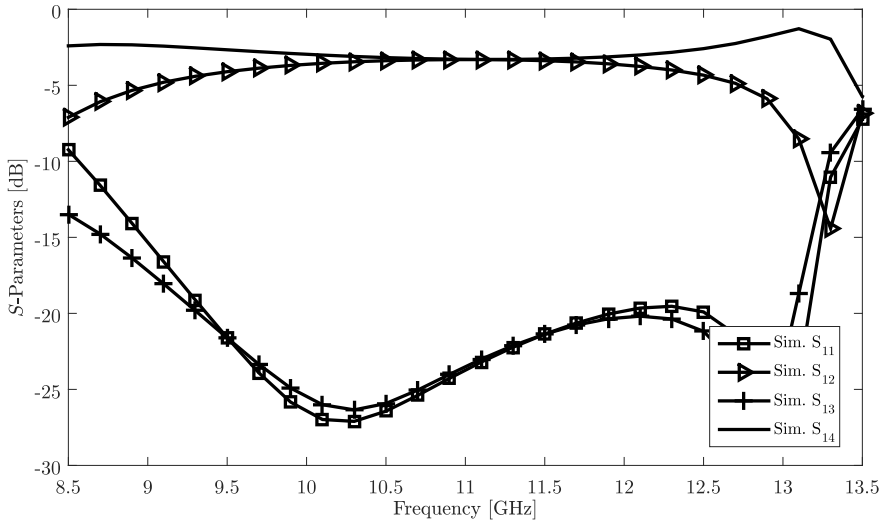

Figure 3.5 – Simulated S-Parameters of the optimized 3-dB coupler in SIW technology.

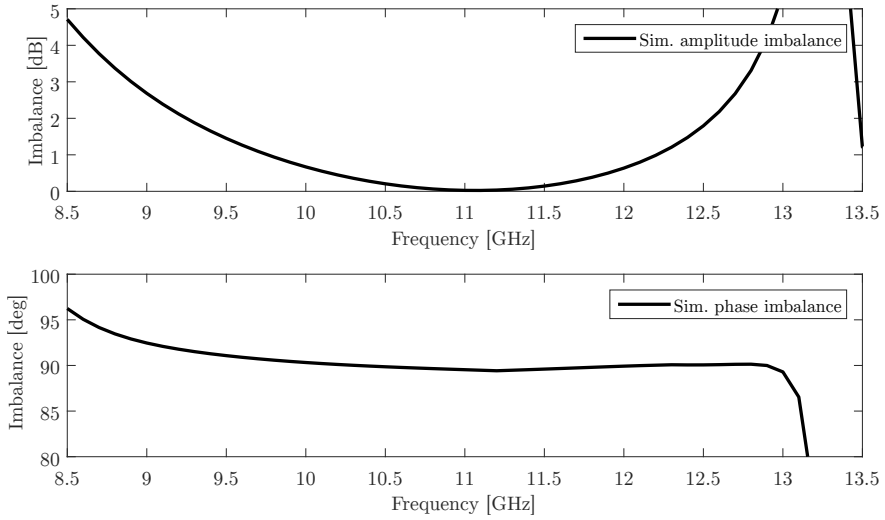

Figure 3.6 – Simulated S-Parameters imbalance of the optimized 3-dB coupler in SIW technology.

Simulated return loss as well as isolation are greater than 15 dB from 9 to 13.1 GHz. Amplitude imbalance remains lower than 1 dB between 9.7 and 12.3 GHz. Within this same frequency range, phase imbalance is lower than 0.7 degrees. Finally, an insertion loss of 3.3 dB at the center frequency of 11 GHz is obtained.

3.2.2.2 Crossover design

The crossover, or also named 0-dB coupler should convey all input power to the diametrically opposite port. The same equations can be used to set the initial geometric dimensions, but this time the amplitude of the transmission coefficient S_{41} should be

set to 1 instead of $1/\sqrt{2}$. In that case, design equations can be reduced to (3.5) and (3.6).

$$W = \frac{\lambda_0}{2}\sqrt{\frac{(2n+3)(6n+1)}{8n}} \tag{3.5}$$

$$L = \frac{\lambda_0}{2}\sqrt{\frac{(2n+3)(6n+1)}{12}} \tag{3.6}$$

The computed dimensions for $n = 1, 2, 3$ are given in Table 3.2. Once again both W and L are increasing sequences of n. $n = 3$ was chosen as starting point for the optimization. Since these devices were first dedicated to be part of a butler matrix, in which longer crossover makes the realization of the phase shifter easier (as explained in [6]). Moreover, both access waveguide width W_a and wall separation W_s were fixed at the same values as for the 3-dB coupler.

n	1	2	3
W [mm]	15.14	17.26	19.32
L [mm]	12.36	19.93	27.32

Table 3.2 – Theoretical dimensions of the interference region in SIW technology for a 0-dB coupler.

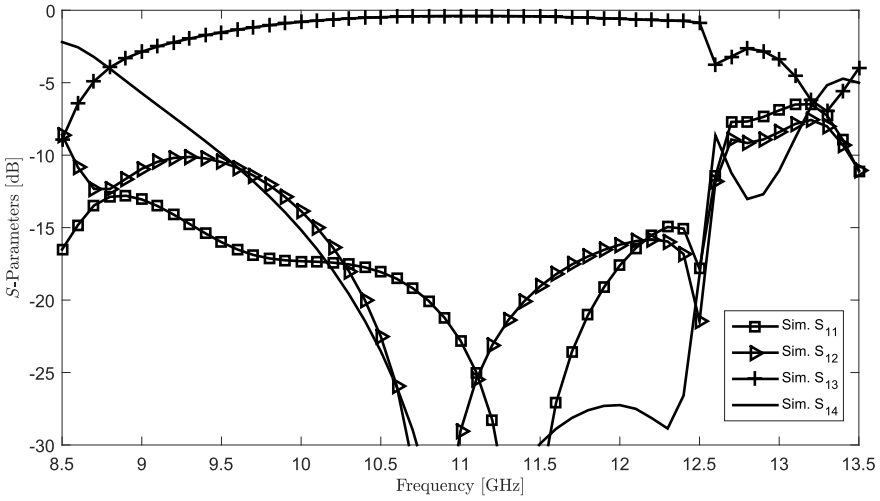

Figure 3.7 – Simulated 0-dB coupler in SIW technology.

After optimization, final dimensions of 19.7 mm and 29.32 mm were obtained for W and L, respectively. Also, the optimized length of the narrower region L' was found at 23.2 mm. An illustration of the simulated crossover is given in Figure 3.7. An insertion loss of 0.4 dB was achieved at 11 GHz, while return loss remains higher than

15 dB between 9.3 and 12.6 GHz. Finally, isolation of both ports 2 and 3 is better than 15 dB between 10 and 12.6 GHz.

3.2.2.3 Feeding structures and de-embedding

The incident power is transferred from a quasi-TEM (grounded coplanar waveguide) feeding line to the integrated waveguide through a broadband transition, as illustrated in Figure 3.8. A coplanar waveguide configuration was chosen for its higher design flexibility than its microstrip counterpart. Thanks to this flexibility, a reduced insertion loss is also obtained at the connector transition. The connectors that were used for all circuits are end-launch connectors 1092-03A-6 from Southwest Microwave company [23], operating up to 40 GHz.

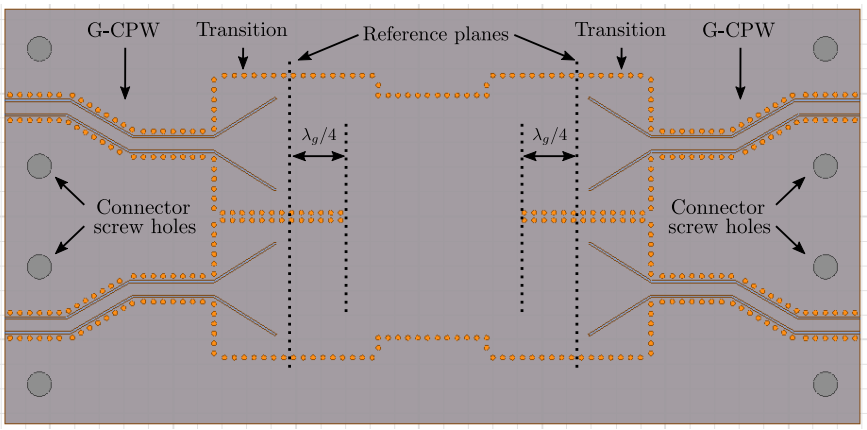

Figure 3.8 – Full coupler topology in SIW technology, with transitions and feeding lines.

In addition, via holes were used to connect lateral grounds of the coplanar waveguide, resulting in a grounded coplanar waveguide (G-CPW) configuration. Actually, these ground connections also help removing unwanted propagation modes such as the coupled-slot mode [24]. A transverse view of the G-CPW is given in Figure 3.9 as well as its dimensions for a 50 Ω characteristic impedance in Table 3.3.

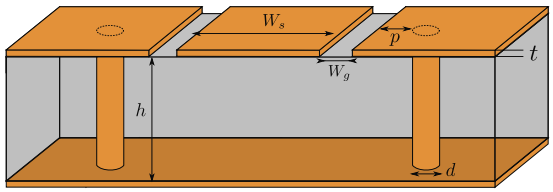

Figure 3.9 – Grounded Coplanar Waveguide (G-CPW) geometry for SIW couplers.

Several transitions from transmission lines to SIW are available in the literature. The main existing topologies are given in [25] and illustrated in Figure 3.10. From left to right, are illustrated the microstrip tapered transition (3.10(a)), the coplanar

Parameter	h	W_g	W_s	p	t	d
Value [mm]	1.113	0.18	1	0.16	0.035	0.4

Table 3.3 – Grounded Coplanar Waveguide (G-CPW) dimensions for SIW couplers.

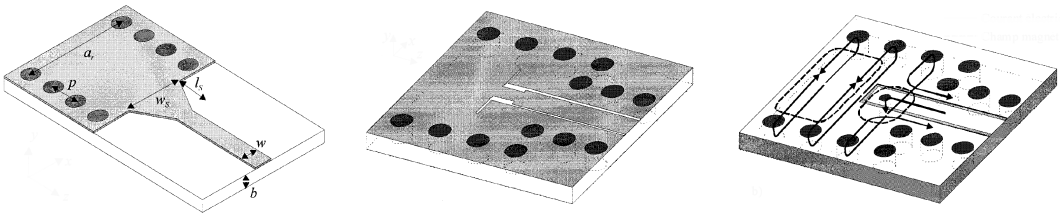

(a) (b) (c)

Figure 3.10 – Different types of transitions from quasi-TEM transmission line to SIW as given in [25]: (a) Microstrip tapered transition, (b) Coplanar slot transition and (c) coplanar current probe.

slot transition (3.10(b)) and the coplanar current probe (3.10(c)). In our context, thanks to the presence of a ground as back metal in the access line, a vertical electric field component is introduced, which couples to that of the first waveguide mode. Therefore, a simple quarter-wavelength tapered transition was adopted by analogy with the microstrip transition, which relies on the same field matching principles.

A de-embedding procedure is applied in order to measure the two previously presented devices, positioning the reference planes at a quarter wavelength distance from the coupling slot inside the waveguide, as depicted in Figure 3.8. The same electrical length was applied in SW-SIW couplers so that a coherent comparison between the two topologies can be done.

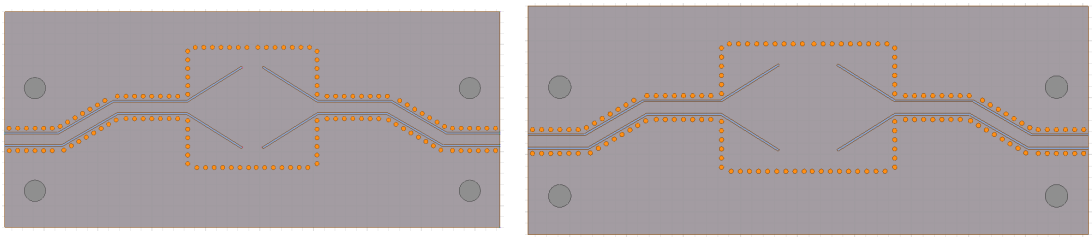

(a) (b)

Figure 3.11 – De-embedding structures for the extraction of two-ports parasitics matrices: (a) Through and (b) Line.

In general, a four-port de-embedding procedure would be required to take into account the coupling occurring between accesses, such as in [26]. Yet, because of the relatively large distance between the feeding lines this coupling was not taken into account. For this reason, a two-port "Through-Line" de-embedding [27] was performed to extract the two-port chain matrices including both connectors, feeding lines and transitions to SIW. The Through and Line circuits are illustrated in Figure 3.11, the

exact same propagation path as for the couplers was implemented, to the exception of the coupling between the ports.

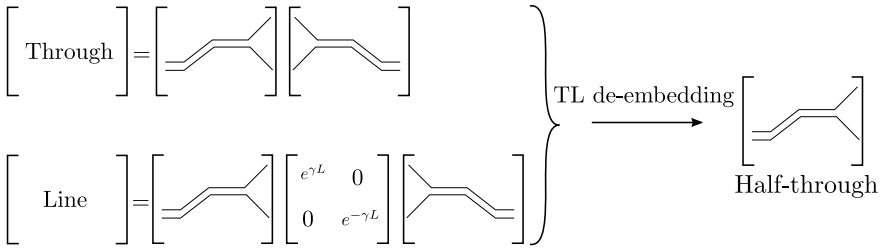

Figure 3.12 – Extraction of Half-Through by the through-line de-embedding procedure.

If Through and Line quadripoles are symmetric, the de-embedding is able to provide the matrix representation of the so-called Half-Through, as illustrated in Figure 3.12. Beside, it is necessary to have a 90-degrees phase shift at 11 GHz between the two de-embedding structures to maximize the accuracy, as for the conventional Through-Reflect-Line (TRL) calibration [28].

Then, this last matrix is inverted, transformed into its scattering matrix and exported in a *.s2p* file. Finally, a circuit simulation in Agilent Design System (ADS) was performed with Data Items boxes to remove the access contribution for each port separately (see Figure 3.13). In this simulation, the full measurement of the coupler was inserted as a 4-port circuit and each access was represented by the inverted extracted Half-Through matrices.

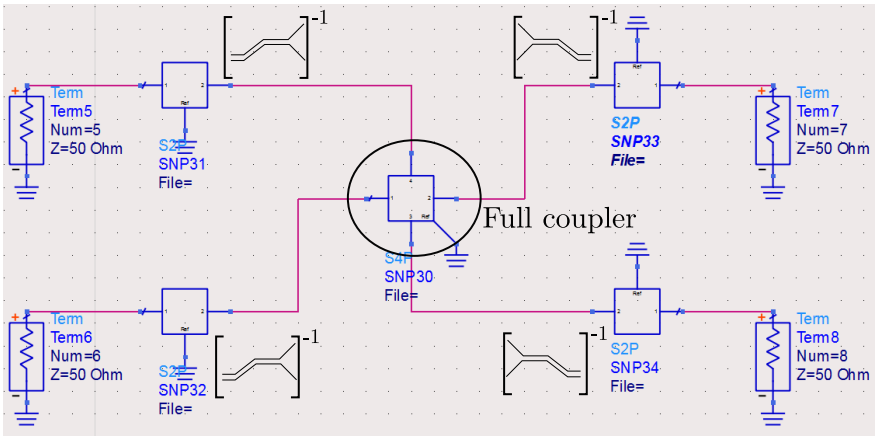

Figure 3.13 – Circuit simulation of the coupler in ADS for removal of access influence.

3.2.3 Design in SW-SIW technology

3.2.3.1 Introduction of an equivalent medium

The SW-SIW topology adopted for the design of couplers is that of a SIW with blind via holes filling all the transverse section, as depicted in Figure 3.14. The complete

filling was motivated by the idea of distributing the slow-wave effect equally from one lateral wall to the other. The different geometric parameters for the blind via holes and substrate are the same as defined in 2.3.2.1. However, because of the reduced guided wavelength, lateral via holes diameter d_{ext} was set to 0.2 mm instead of 0.4 mm, this was done in order to keep similar proportions as in SIW.

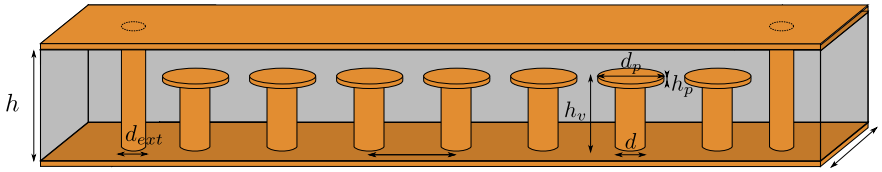

Figure 3.14 – Schematic view of the SW-SIW used for the design of couplers.

For such a uniform distribution in the waveguide, an effective medium approach was adopted. The idea is to be able to remove the blind via holes in the waveguide and compensate their absence by an increase in either permittivity or permeability of an equivalent substrate (see Figure 3.15).

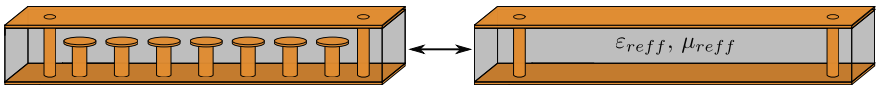

Figure 3.15 – Principle of the equivalent medium approach for uniform distribution of blind via holes.

In order to be able to replace the discrete loading by an equivalent medium, long wavelengths compared to the period $s = 0.8$ mm have to be considered. A precise estimation of the slow-wave effect can be done by using the Eigenmode solver in HFSS. This effective parameter is extracted by considering the slow-wave effect observed when loading a parallel plate waveguide with the same blind via holes (see Chapter 2). With all the dimensions given previously, an ε_{reff} of 10.45 at 11 GHz was found, which leads to a guided wavelength greater than 8.4 mm. Hence, the period is less than a tenth of a wavelength at the operating frequency, validating the distributed assumption.

Two main parameters can be used to define the equivalence between the two waveguides, the phase velocity v_p and the mode impedance Z_m. The former describes the slow-wave effect while the latter dictates the ratio between electric and magnetic fields. Moreover, as the equivalent SIW can be assimilated to a dielectric filled rectangular waveguide, as explained in [25], these two parameters can be expressed by equations (3.7) and (3.8). In these two equations, ω_c stands for the cut-off frequency of the first propagating mode.

$$v_p = \sqrt{\frac{1}{\mu_{reff}\varepsilon_{reff}}} \frac{1}{\sqrt{1 - \frac{{\omega_c}^2}{\omega}}} \tag{3.7}$$

$$Z_m = \sqrt{\frac{\mu_{reff}}{\varepsilon_{reff}}} \frac{1}{\sqrt{1 - \frac{\omega_c}{\omega}^2}} \tag{3.8}$$

That being said, two different approaches can be defined. The first one consists in trying to match the slow-wave effect by an increase in either ε_{reff} or μ_{reff} without focusing attention on the impedance level. A second approach consists in adjusting both parameters to match more precisely the SW-SIW properties.

First of all, it is worth mentioning that the simulations of SW-SIW components imply the use of a de-embedding algorithm to remove the port discontinuities. Excitation ports used in HFSS for waveguide structures are called "Waveports" (for "Waveguide Ports"). The simulation produces S-Parameters which corresponds to a semi-infinite waveguide of identical cross-section as that of the port feeding the 3-D structure. In other words, HFSS assumes that the simulated design feeding accesses are of identical cross-section as the waveport geometry. If we apply this principle to the SIW and SW-SIW we obtain the configurations illustrated in Figure 3.16. Each metallic part in the port is assumed to represent an infinite object, therefore the via holes are interpreted as longitudinal walls. The de-embedding may not be strictly necessary for SIW, as the discontinuity induced by the lateral via holes are located in the regions of very weak electrical fields. On the contrary, a significant change in field distribution occurs at the excitation port for SW-SIW. This discontinuity can be reduced by placing blind via holes inside the port itself, but it is still not negligible. Interestingly, this solution also reduces the cut-off frequency of the feeding waveguide to a close value to that of the SW-SIW, thus avoiding some numerical issues.

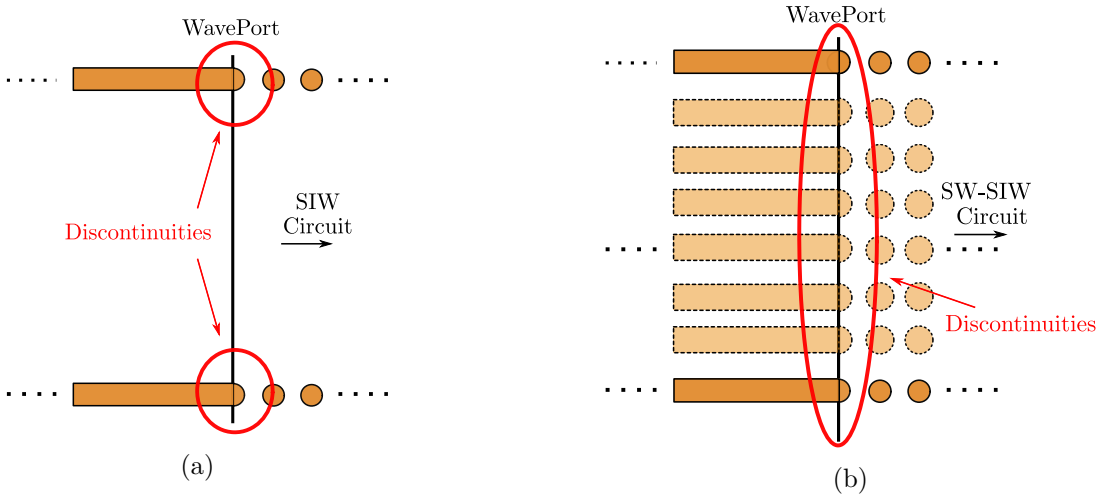

Figure 3.16 – Waveguide excitation port principle of operation for both (a) SIW and (b) SW-SIW.

In this context, the use of an equivalent waveguide which has the same impedance level as that of the SW-SIW, as for the second approach, is not really relevant. In fact, once the normalisation is performed inside the waveguide, only relative changes in impedance will have an impact, not absolute values. The simulated S-Parameters

of both real and equivalent structures can be very similar, while both of them are normalised to their specific mode impedance.

In practice, let's assume that a certain velocity reduction is achieved by the insertion of a uniform blind via holes distribution. This velocity reduction has to be modelled in the equivalent waveguide by an increase of the product of μ_{reff} and ε_{reff}. In order to retrieve the good phase velocity, the slow-wave factor can for example be absorbed in the permittivity by putting $\varepsilon_{reff} = SWF^2\varepsilon_r$ (as in (1.26)). In the meantime, the permeability remains $\mu_{reff} = 1$.

Let's first validate the use of the equivalent waveguide in the context of a straight section. The relevance of this model in coupler design will be further shown in the design description. For simplicity, we will consider here the feeding waveguides of the couplers. These waveguides were chosen to have the same cut-off frequency as that of the SIW couplers, ie. 7.25 GHz. Considering 7 blind via holes in the transverse section, this condition is satisfied for a width W_a of 6.6 mm. As the mode impedance is not the same between the two models, only the phase of the transmission coefficient S_{21} (related to the phase constant) are compared.

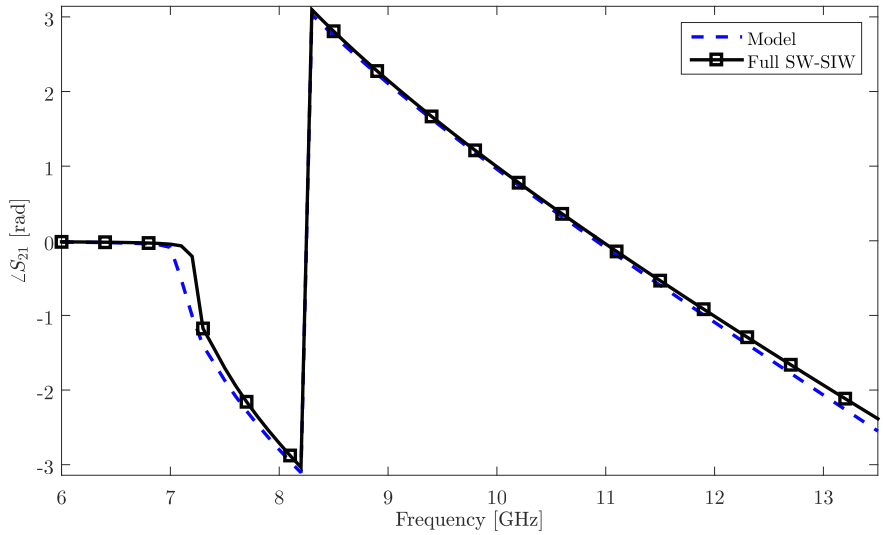

Figure 3.17 – S_{21} phase of a 5.6 mm straight SW-SIW and its equivalent model.

The model provides a relatively good representation of the propagation along the waveguide. The main difference occurs at the cut-off frequency, then the two curves follow a very similar trend. Finally, a maximum deviation of 9.5 degrees is observed at 13.5 GHz over a total electrical length of about 500 degrees.

The main advantage of such a representation of the slow-wave effect is that it provides a very fast simulation tool. This is even more true for electrically large devices such as couplers. This point will be illustrated in the following sections.

3.2.3.2 Coupler design

In order to apply the design method used in the context of SIW, the equivalent free-space wavenumber k_{sw} defined by equation (3.9) is introduced along with the effective relative permittivity.

$$k_{sw} = \frac{\omega}{c_0}\sqrt{\varepsilon_{reff}} \tag{3.9}$$

Then, by applying equations (3.1) and (3.2), cavity width W_{sw} and length L_{sw} were obtained. Obviously, this calculation is equivalent to scaling the SIW coupler dimensions by a factor $1/SWF$, or $\sqrt{\varepsilon_r/\varepsilon_{reff}}$, where $\varepsilon_r = 3.55$, the permittivity of the RO4003 substrate. The initial dimensions given by design equations are $W_{sw} =$ 10.65 mm and $L_{sw} = 6.87$ mm. The same choice of solution order $n = 1$ was done in SW-SIW, the arguments behind that being unchanged. Because of the absence of blind via holes, the optimization process can be very fast. The optimized model dimensions are given in the second row of Table 3.4. A very similar trend as in SIW is observed between the initial values and the optimized solution. Once again, this is because defining the model with an effective relative permittivity corresponds to a simple scaling of the structure.

	W_{sw} [mm]	L_{sw} [mm]	L'_{sw}
Design equations	10.65	6.87	-
Optimized model (ε_{reff})	11.48	8.7	5.12
Optimized real structure	11.45	8.58	5.14

Table 3.4 – Optimized dimensions of the 3-dB coupler in SW-SIW technology.

After optimization using the effective permittivity, the complete SW-SIW simulation was performed. For that, the blind via holes were arranged in the coupling region to fill most of the transverse section. In this case 13 of them were necessary. The full structure is illustrated in Figure 3.18, the top and bottom copper were removed to ease the visualisation. This structure was slightly optimized and final dimensions were obtained, they are listed in the third row of Table 3.4. A very small adjustment was necessary.

Moreover, because of the periodical character of the SW-SIW a strong discontinuity is introduced at the excitation ports. In order to remove its effect and normalise the S-Parameters to the fundamental mode impedance, the same de-embedding approach as described in section 3.2.2.3 was adopted.

Different sets of simulation results are presented in Figure 3.19. The real structure with all the blind via holes is given in black solid line. It is compared with two different models. The first one, in blue dashed line, corresponds to the equivalent coupler with the exact same dimensions but with an effective relative permittivity of 10.45 and no blind via holes. Then, a second simulation result is shown in green dotted line, it is associated with the same structure but with a linearly frequency dependent permittivity. This relative permittivity ranges from 10.2 at 9 GHz to 10.72 at 13 GHz,

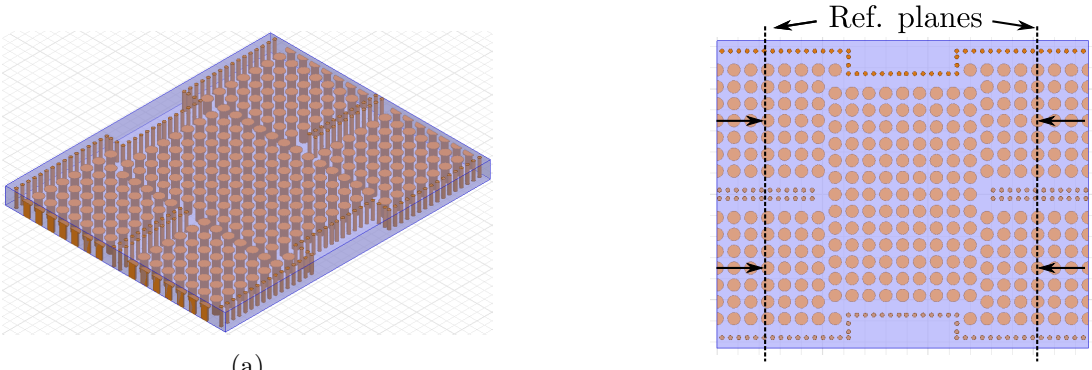

Figure 3.18 – Simulated 3-dB coupler in SW-SIW technology (a) 3D view (b) Top view.

which corresponds to a 2.5% variation of the slow-wave factor SWF. This variation was estimated by Eigenmode simulation, using again the same loaded parallel-plate waveguide configuration.

Between the three sets of results, a good agreement can be observed on the overall response. However, an increasing shift between the two models and the real structure can be noticed as the frequency increases. The shift is about 400 MHz at a maximum for the constant permittivity model, it is approximately divided by two using the variable one.

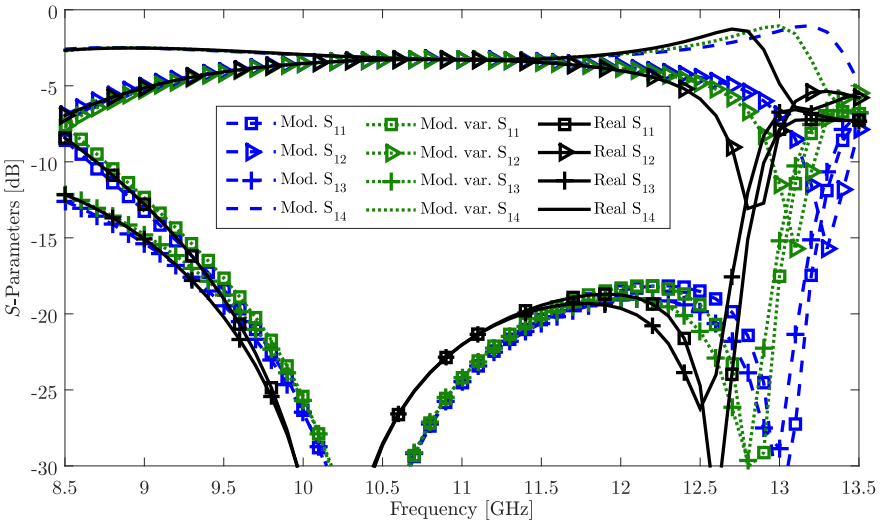

Figure 3.19 – Simulated S-Parameters of the 3-dB coupler in SW-SIW, compared to equivalent models based on an effective permittivity.

Thanks to the use of the equivalent substrate, the optimization process in SW-SIW can be drastically reduced. Because of the good agreement observed with the real structure, most of the optimization can be done without any blind via holes. In

fact, the simulation time for one iteration of the full coupler takes about a minimum of 3 hours, versus less than 10 minutes using the equivalent structure. Furthermore, these 3 hours are only achievable by taking advantage of all symmetries and parallel computing possibilities in the laboratory, as it will be discussed in section 3.2.3.5.

3.2.3.3 Crossover design

The 0-dB coupler design procedure does not differ much from that of the 3-dB version. As the exact same slow-wave factor was targeted an identical equivalent medium was adopted. First, the dedicated design equations (3.5) and (3.6) were used along with the already defined wavenumber k_{sw}. Then, a first optimization using the equivalent substrate was performed. As a very good agreement between the models (with constant and variable effective permittivities) and real structure simulations was observed, no final optimization was needed. The final dimensions are given in Table 3.5 along with those provided by design equations.

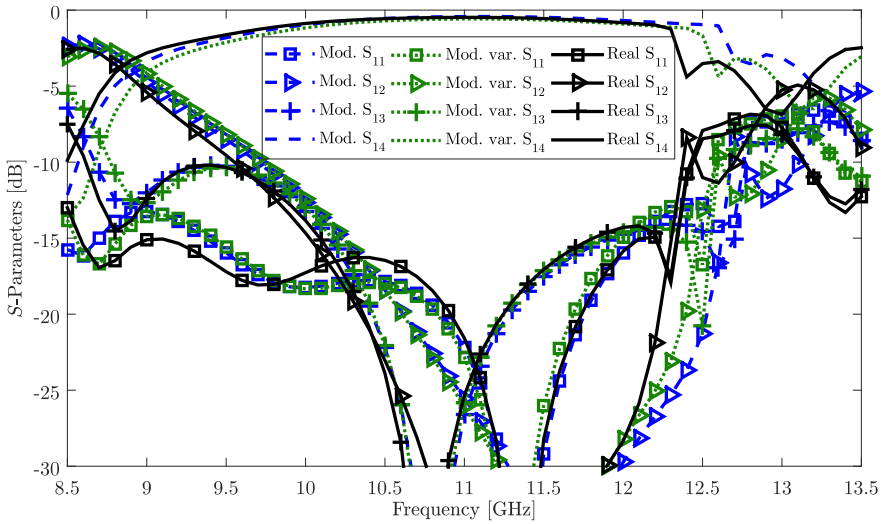

Figure 3.20 – Simulated S-Parameters of the 0-dB coupler in SW-SIW, compared to equivalent models based on an effective permittivity.

	W_{sw} [mm]	L_{sw} [mm]	L'_{sw}
Design equations	11.26	15.93	-
Optimized structure (ε_{reff})	11.34	17.2	12.96

Table 3.5 – Optimized dimensions of the 0-dB coupler in SW-SIW technology.

An illustration of the optimized crossover is given in Figure 3.21. One can notice that a tapered transition to the coupling region was added, this was done in order to improve the return loss.

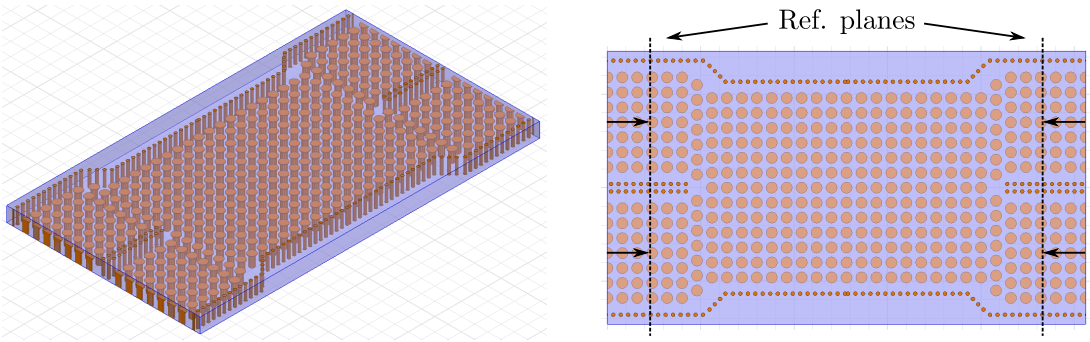

(a) (b)

Figure 3.21 – Simulated 0-dB coupler in SW-SIW technology (a) 3D view (b) Top view.

3.2.3.4 Feeding structures and de-embedding

As for the SIW circuits, broadband transitions as well as feeding lines were implemented in order to facilitate both measurement and de-embedding. A similar topology as that of transition for SIW couplers was used in SW-SIW. However, the feeding line was modified to improve the matching with the waveguide. As pointed out in [29] in microstrip topology, blind via holes should also be placed below signal strip in order to match the electrical field distribution of the SW-SIW. Similarly, for the G-CPW configuration the center strip was loaded with blind via holes (Loaded G-CPW, LG-CPW) so that most of the electric field lines are confined in the upper layers, as illustrated in Figure 3.22. The geometric parameters of these two configurations are given in Figure 3.23.

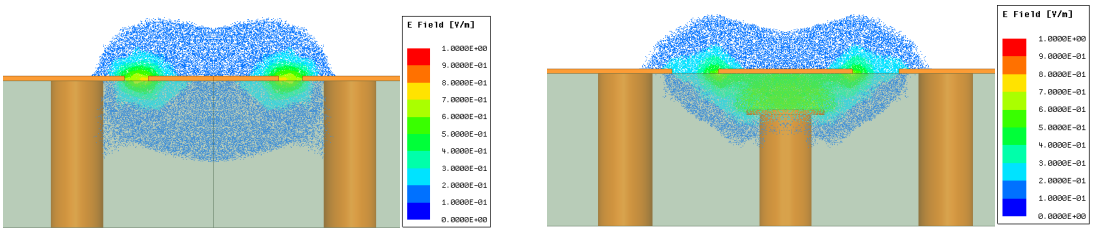

(a) (b)

Figure 3.22 – Electric field amplitude for both (a) G-CPW and (b) LG-CPW.

The dimensions of the LG-CPW which correspond to a characteristic impedance of 50 Ω but also complied with the connectors specifications were determined by full-wave simulation. They are listed in Table 3.6, the blind via holes are the same as the one placed inside the waveguide.

The blind via hole below the signal strip is also adding some capacitance per unit length, thus reducing phase velocity. However, at the frequency of operation the length of a period is about one sixteenth of a guided wavelength. The loading can therefore be considered as distributed.

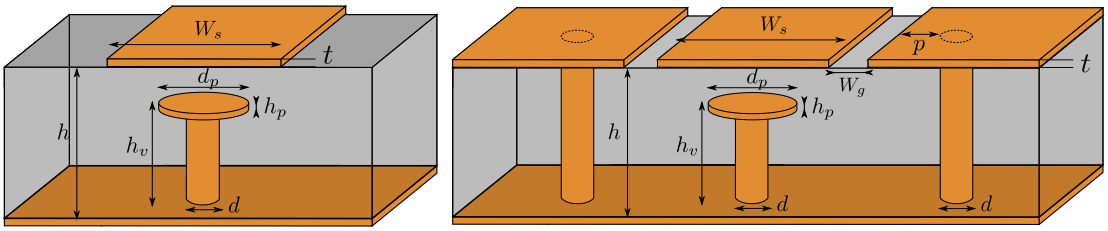

(a) (b)

Figure 3.23 – Loaded feeding lines for SW-SIW in (a) Microstrip and (b) G-CPW configurations.

Parameter	h	W_g	W_s	p	t	d
Value [mm]	1.113	0.34	1	0.14	0.035	0.4

Table 3.6 – Loaded Grounded Coplanar Waveguide (LG-CPW) dimensions for SW-SIW couplers measurement

A transition to the SW-SIW was realised in a similar way as in SIW, with a tapering of the central conductor as depicted in Figure 3.24. In this figure the top view of the transition is represented with the top copper in partial transparency. The initial length of the tapered section L_{taper} was set to a quarter guided wavelength at 11 GHz, which is 3.62 mm. Via-holes were kept along the slot as for the feeding line, following the tapered shape. Then, full-wave simulations were performed in order to minimise return loss around the operating frequency. The final dimensions are $L_{taper} = 4.18$ mm and $\theta_{taper} = 32$ degrees.

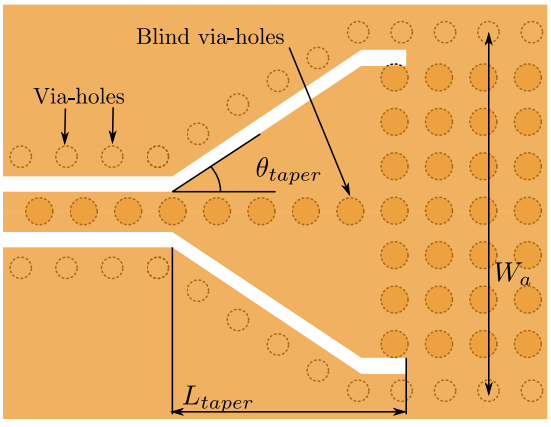

Figure 3.24 – Transition from LG-CPW to SW-SIW geometry.

The same de-embedding strategy was used for the SW-SIW couplers, placing the reference planes at a quarter-wavelength from the coupling region.

3.2.3.5 Simulation method for reduced simulation time

Because of the high complexity of the slow-wave structure, simulations of large circuits such as these four-port devices require a large amount of memory as well as computing power. In the laboratory, simulations were performed using a sixteen-core processor along with 48 GB of RAM. Even if most of the optimization is done with the equivalent model, the last simulations require the full model to be taken into account.

In order to reduce the simulation time for the complete structure we tried to take advantage of all geometrical symmetries. As depicted in Figure 3.25, two orthogonal symmetry planes can be defined. However, from the electromagnetic field point of view these two planes cannot be considered as either electric or magnetic symmetries. The plane P1 is a magnetic symmetry plane for the TE_{10}, but instead is an electric symmetry plane for the TE_{20}. Because these two modes are excited in the center coupling region it is not possible to consider either of the symmetry types. The plane P2 does not exhibit any specific field symmetry because it is orthogonal to the direction of propagation.

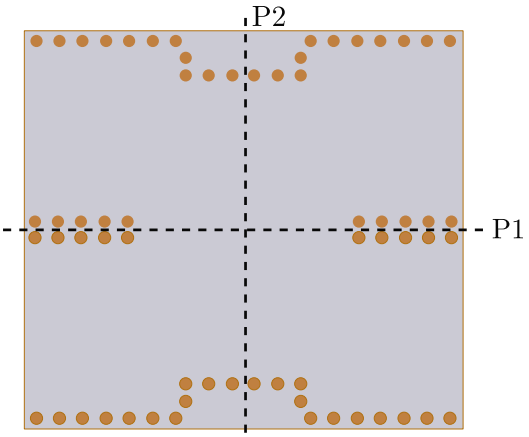

Figure 3.25 – Symmetry planes for the coupler design.

That being said, because of the geometrical symmetries the even-odd mode analysis given in [30] can still be applied to calculate the four-port scattering matrix. The idea is to apply this decomposition in the two planes consecutively, thus resulting in four simulations. As an example, a magnetic symmetry condition is applied on P1 while P2 is successively considered as an electric and then magnetic symmetry condition. Then, the operation is repeated with an electric condition on P1. In each simulation, only one port is used so that the final result consists of four reflection parameters S_{11}: S_{11}^{oo}, S_{11}^{oe}, S_{11}^{eo} and S_{11}^{ee}. The two types of symmetries, "e" for even (magnetic) and "o" for odd (electric), assigned to P1 and P2 are written in that order, respectively.

To obtain the four port S-Parameters, the first step is to calculate two separate two-port matrices corresponding to even and odd mode relatively to P1. These two matrices are symmetric and reciprocal so that only two coefficients (reflection and transmission) need to be specified. The reflection coefficients are denoted S_{11}^{e} and S_{11}^{o} for the even- and odd-modes, respectively. A similar formalism is used for the

transmission. These four coefficients are given by equations (3.10)-(3.13).

$$S_{11}^{e} = \frac{1}{2}\left(S_{11}^{ee} + S_{11}^{eo}\right) \tag{3.10}$$

$$S_{11}^{o} = \frac{1}{2}\left(S_{11}^{oe} + S_{11}^{oo}\right) \tag{3.11}$$

$$S_{21}^{e} = \frac{1}{2}\left(S_{11}^{ee} - S_{11}^{eo}\right) \tag{3.12}$$

$$S_{21}^{o} = \frac{1}{2}\left(S_{11}^{oe} - S_{11}^{oo}\right) \tag{3.13}$$

At the end, the coupler S-Parameters can be calculated by considering the second symmetry. Equations (3.14)-(3.17) were used to obtain the final results.

$$S_{11} = \frac{1}{2}\left(S_{11}^{e} + S_{11}^{o}\right) \tag{3.14}$$

$$S_{21} = \frac{1}{2}\left(S_{21}^{e} + S_{21}^{o}\right) \tag{3.15}$$

$$S_{31} = \frac{1}{2}\left(S_{11}^{e} - S_{11}^{o}\right) \tag{3.16}$$

$$S_{41} = \frac{1}{2}\left(S_{21}^{e} - S_{21}^{o}\right) \tag{3.17}$$

Regarding the practical implementation of this methodology, a script was written in MATLAB in order to automatically assign the symmetries, simulate each configuration and retrieve the output S-Parameters. As an example, the simulation times for the 3-dB coupler with and without the use of symmetries are given in Table 3.7. The total time includes both adaptive passes and a discrete frequency sweep of 61 points calculated separately (Discrete Sweep in HFSS). The convergence criteria was fixed to a 1% maximum variation of the S-Parameters. The total simulation time was divided more than 5 thanks to the use of symmetries and parallel computing.

	ΔS [%]	Freq. Points	Parallel tasks	Total time
Initial	1	61	1	20h38
With symmetries	1	61	1	10h37
With symmetries & Parallel computation	1	61	4	3h49

Table 3.7 – Simulation time obtained for the 3-dB coupler with different configurations.

In fact, because of the structure complexity, an important memory capacity is required. Therefore, the frequency points calculation cannot be distributed among the 16 cores in the initial configuration. However, thanks to the use of symmetries the complexity is drastically reduced and a parallel computation can be considered (four tasks on four cores each).

3.3 Measurement results and retro-simulations

3.3.1 Measurement results

3.3.1.1 3-dB couplers in SIW and SW-SIW technologies

All fabricated devices were measured using the Anritsu VectorStar MS4647B four ports network analyser along with end-launch connectors. The fabricated 3-dB couplers in both SIW and SW-SIW technologies are illustrated in Figure 3.26.

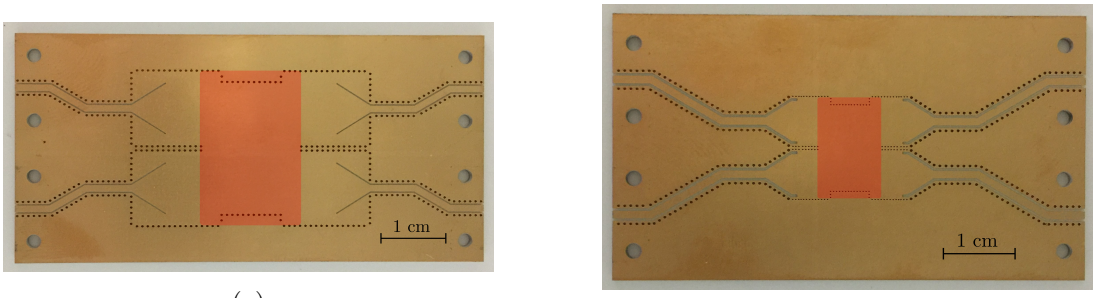

(a) (b)

Figure 3.26 – Realised 3-dB couplers in (a) SIW and (b) SW-SIW technologies.

The main constraint on the layout was the important connectors dimension, therefore the total size of circuits (bended feeding lines, transitions, waveguide access and coupler) is similar for the two technologies. For this reason, the coupling region size is highlighted in red to illustrate the actual miniaturization. This region occupies a surface of 336 mm^2 in SIW, it is reduced to 113 mm^2 for the SW-SIW version, which is nearly 3 times smaller.

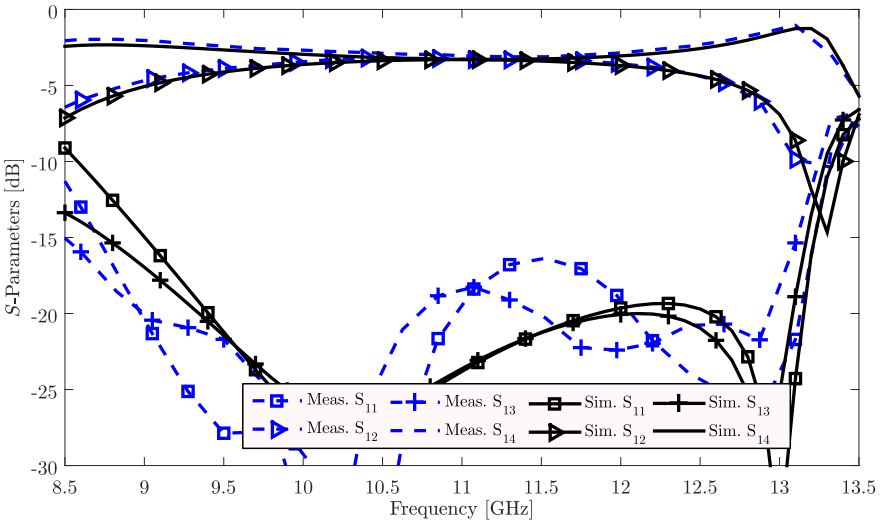

Figure 3.27 – Comparison between simulated and measured S-Parameters for the 3-dB coupler in SIW technology.

A comparison between measured and simulated S-Parameters for the SIW coupler is illustrated in Figure 3.27, as well as the corresponding amplitude/phase imbalance in Figure 3.28.

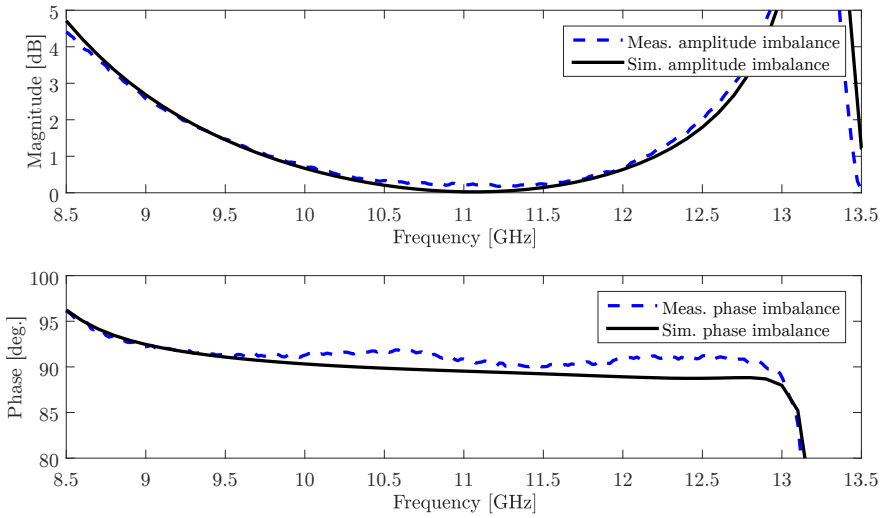

Figure 3.28 – Compared amplitude and phase imbalance between simulation and measurement for the 3-dB coupler in SIW technology.

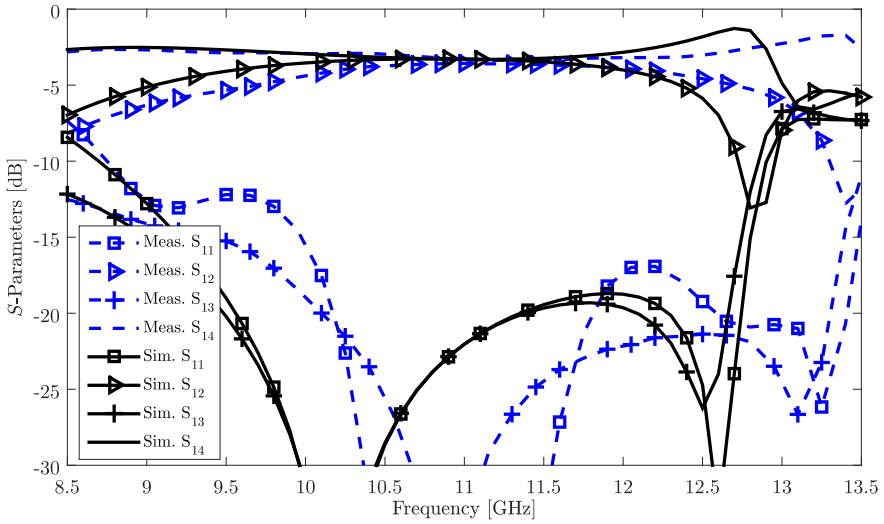

Figure 3.29 – Comparison between simulated and measured S-Parameters for the 3-dB coupler in SW-SIW technology.

The measured coupler operates around the frequency of 11 GHz, with a return loss better than 10 dB in a 43% relative bandwidth. Also, the amplitude imbalance is lower than 1 dB between 9.8 and 12.14 GHz, which corresponds to a 21% range around 11 GHz. In this same frequency interval, the phase imbalance lies between 0

and 1.6 degrees. Finally, measured insertion loss is 3.1 dB at the center frequency on each output port.

Regarding the SW-SIW version, the comparison between measured and simulated S-Parameters is illustrated in Figure 3.29.

First of all, a shift toward the higher frequencies is observed, as the center frequency defined by the optimal coupling is moved from 11 GHz to 11.15 GHz. Dealing with return loss and isolation this shift is even greater, about 500 MHz depending on the selected parameter. However, the overall behaviour of the coupler is maintained, with a return loss better than 10 dB between 8.7 and 13.55 GHz, which represents a 42% relative bandwidth compared to 39% in simulation. Finally, measured insertion loss is 3.36 dB and 3.6 dB for both transmission parameters at 11.15 GHz, versus 3.3 dB in simulation. Phase and amplitude imbalances are discussed along with retro-simulation results, in section 3.3.2.

3.3.1.2 0-dB couplers in SIW and SW-SIW technologies

The fabricated 0-dB couplers in both SIW and SW-SIW technologies are illustrated in Figure 3.30. The exact same feeding structures were used for these devices as for the 3-dB couplers. Thanks to the slow-wave effect, the coupling region area is reduced from 667 to 231 mm^2, which represents a miniaturization by a factor 2.46.

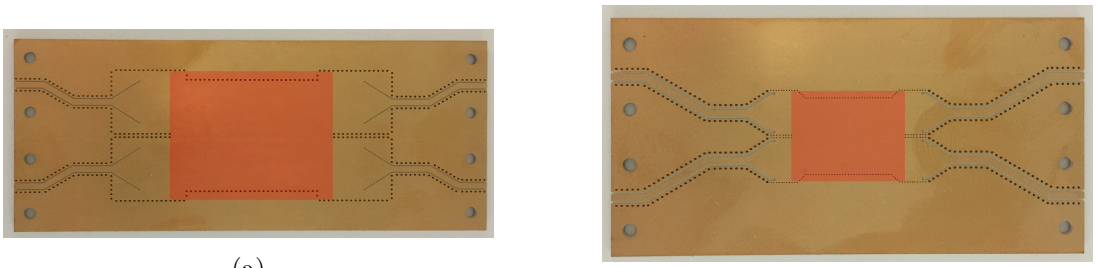

(a) (b)

Figure 3.30 – Fabricated 0-dB couplers in (a) SIW and (b) SW-SIW technologies.

Simulation results are compared to the measurement in Figure 3.31 for the SIW technology. A very good agreement is obtained. Measured insertion loss is 0.46 dB at 11 GHz, while simulated one is 0.39 dB at the same frequency. Return loss as well as isolation of ports 2 and 3 are better than 10 dB from 9.4 to 12.6 GHz. This represents a relative bandwidth of 29%.

Finally, the comparison for the 0-dB coupler in SW-SIW technology is given in Figure 3.32. Once again a shift in frequency was observed, of about 400 MHz. Measured insertion loss is 0.58 dB, which is relatively close to the 0.47 obtained in simulation. That being said, the 0-dB coupling function is maintained, with both return loss and isolation better than 10 dB between 9.9 and 12.9 GHz, which corresponds to a 26% relative bandwidth.

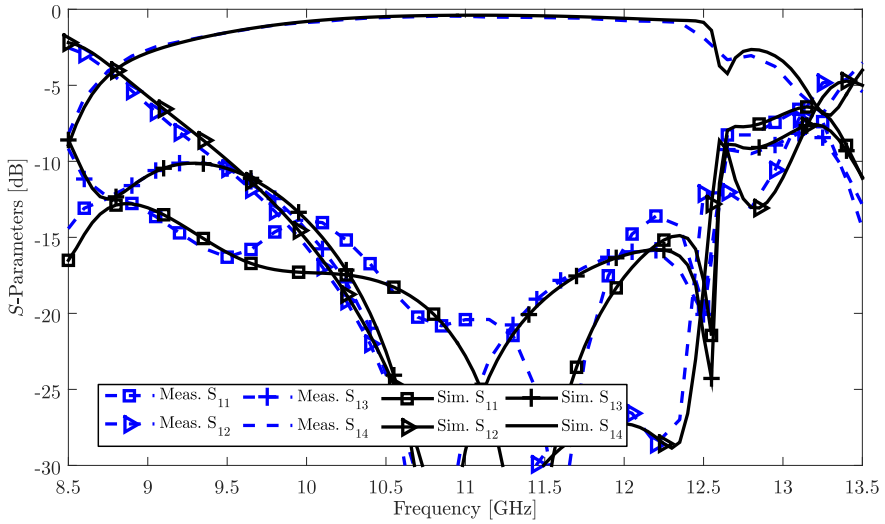

Figure 3.31 – Comparison between simulated and measured S-Parameters for the 0-dB coupler in SIW technology.

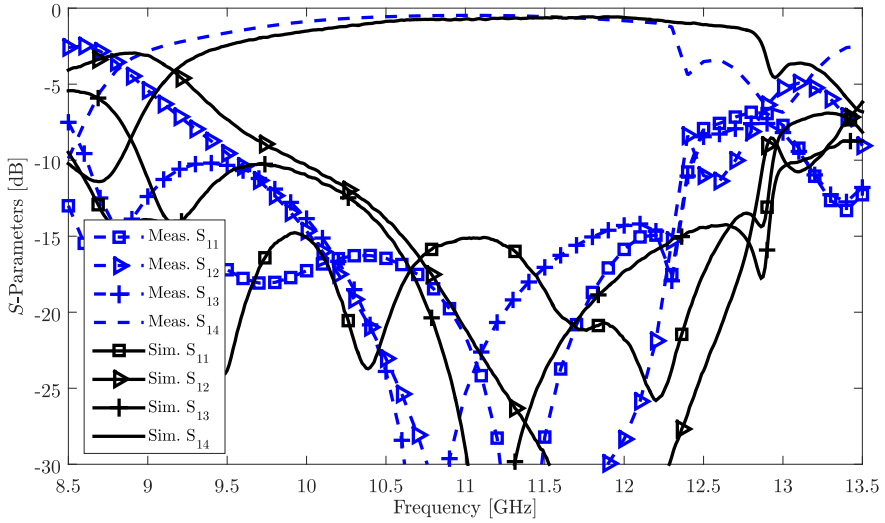

Figure 3.32 – Comparison between simulated and measured S-Parameters for the 0-dB coupler in SW-SIW technology.

3.3.2 Fabrication process variations and retro-simulations

In order to verify that all dimensions were correctly respected during the fabrication, cross-sections were realised by mechanical polishing and then analysed under microscope. A photograph of a 400 µm blind via diameter via hole is illustrated in Figure 3.33. A dozen of via hole were measured, with a specific attention on the copper land diameter d_p, thickness h_p, and via diameter d. Geometrical parameters such as W and s did not exhibit any variation, as well as all substrate thickness's. Because of optics limitation and copper surface roughness a variation of plus or minus 5 µm can

be expected in the measured values.

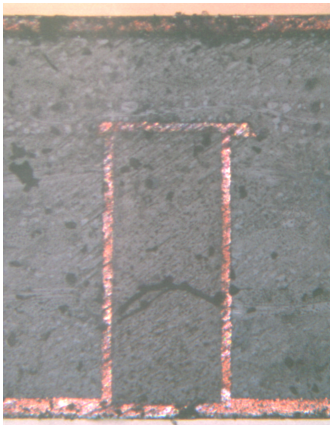

Figure 3.33 – Cross-sectional photograph of a blind via hole of diameter 400 µm used for couplers in SW-SIW.

An average of the measured dimensions was performed and compared with the initial values used for the simulation. All of them are listed in Table 3.8.

	d	d_p	h_p
Initial	400	600	35
Measured (averaged, ±5 µm)	400	500	46

Table 3.8 – Measured versus simulated dimensions of the 400 µm diameter via holes.

Two main variations can be observed, first the copper-land diameter d_p is reduced by 100 µm. Secondly, its thickness is also greater than the expected value by an estimated 11 µm, corresponding to a 31% increase. These two variations have an impact on the slow-wave factor, thus shifting the operating frequencies. In addition, a non negligible surface roughness was noticed on the via holes, with at least 5 µm of maximum deviation. The Groisse model implemented in HFSS was used to take the roughness into account.

These updated geometric and physical parameters were inserted in the simulations of both 0-dB and 3-dB couplers. First, the retro-simulated S-Parameters for the 3-dB coupler are compared with the measured ones in Figure 3.34. Both amplitude and phase imbalance are also illustrated in Figure 3.35. By considering the updated dimensions the shift in frequency is nearly fully recovered. However, degraded phase and amplitude imbalance between output ports were observed. The amplitude imbalance reaches a minimum of 0.2 dB at 11.15 GHz and remains below 1 dB in a 18% relative bandwidth. Over the same frequency range, the phase variation is ± 1.5 degrees. Finally, retro-simulated insertion loss is 3.38 dB, which is very close to the measured values of 3.36 and 3.6 dB.

The same geometric parameters are applied to the 0-dB coupler simulation and compared with its measurement. The S-Parameters are compared in Figure 3.36.

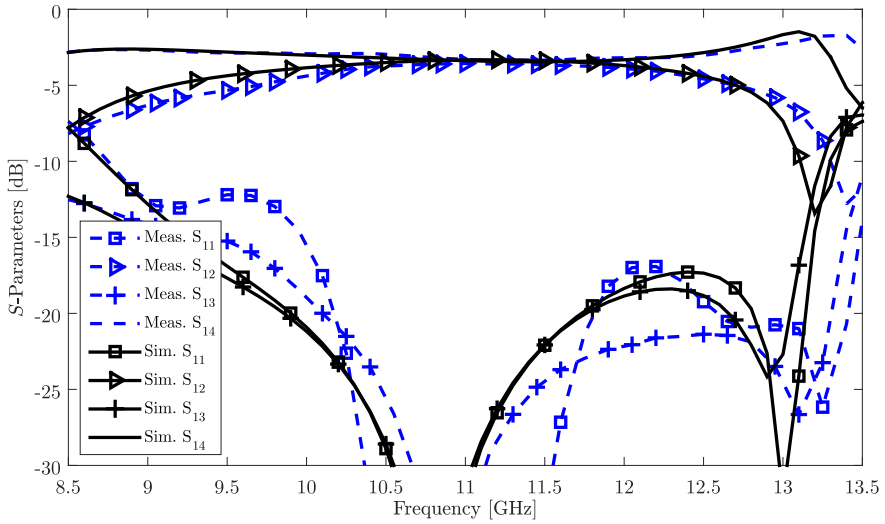

Figure 3.34 – Comparison between retro-simulated and measured S-Parameters for the 3-dB coupler in SW-SIW technology.

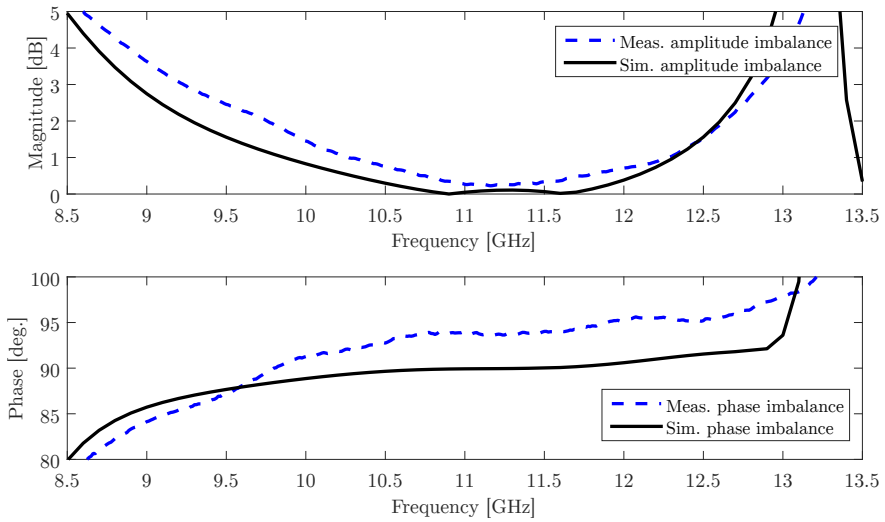

Figure 3.35 – Compared amplitude and phase imbalance between retro-simulation and measurement for the 3-dB coupler in SW-SIW technology.

Here again, in comparison with the first simulations the agreement is significantly improved. A slight frequency shift can be noticed only when considering the transmission parameter. A minimum insertion loss of 0.6 dB was found in simulation, which is very close to the 0.58 dB obtained in measurement. In comparison with the initial simulation, taking into account the surface roughness led to an increase of the insertion loss of about 0.1 dB.

Altogether, by considering fabrication process variations a good agreement can be obtained between simulation and measurement results. These results also confirm that

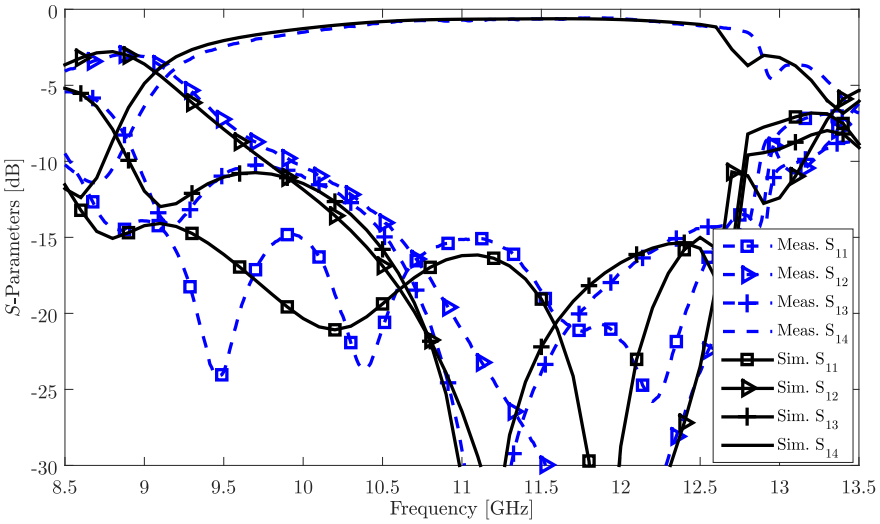

Figure 3.36 – Comparison between retro-simulated and measured S-Parameters for the 0-dB coupler in SW-SIW technology.

the blind-via dimensions are critical to the slow-wave effect, more precisely a precise control of both copper land thickness and diameter is the key to obtain satisfying results. In addition, a better estimation of insertion can be obtained if surface roughness is taken into account.

To summarize, all four realised circuits are compared in Table 3.9 in terms of electrical performance and normalised occupied area. The normalisation was performed relatively to the free-space wavelength at the operating frequency, in the considered relative permittivity of 3.55. The operating frequency of each coupler f_0 was defined by the optimum coupling. Two different relative bandwidth are compared. The first one was defined by a return loss better than 10 dB and written BW_{RL}. A second one corresponds to the frequency range in which the amplitude imbalance is less than 1 dB, it is denoted BW_{1dB}. The phase imbalance variation inside this frequency range $\Delta\Phi$ is also given. Finally, the normalised occupied area of the coupling region is compared, the normalisation factor being the free-space wavelength at f_0.

Circuit	f_0 [GHz]	BW_{RL} [%]	IL [dB]	BW_{1dB} [%]	$\Delta\Phi$ [deg]	$Area/\lambda_0^2$
3-dB SIW	11	43	3.1	21	± 0.8	1.6
3-dB SW-SIW	11.15	42	3.36-3.6	18	± 1.5	0.55
0-dB SIW	11	29	0.46	27	–	3.17
0-dB SW-SIW	11.4	26	0.58	25	–	1.18

Table 3.9 – Summary of electrical performance and dimensions of the 4-port circuits in SIW and SW-SIW.

As already mentioned, the area reduction factor is close to 3, more precisely 2.9 for the 3-dB version and 2.7 for the 0-dB one. Concerning the relative bandwidths,

the slow-wave and classical circuits exhibit similar performance. The most significant difference was observed for BW_{1dB} for the 3-dB couplers, with a reduction from 21 to 18%. This difference is mainly due to the fact that the amplitude imbalance in SW-SIW does not reach 0 dB at the center frequency. As to insertion loss, an additional 0.4 dB and 0.1 dB was observed for the 3 dB and 0-dB couplers, respectively. Finally, phase imbalance is ± 1.5 degrees in SW-SIW, versus ± 0.8 degrees in SIW.

Finally, the SW-SIW 3-dB realization is compared to the state-of-the-art short-slot 3-dB couplers in terms of miniaturization. The comparison is realised with the already mentioned half-mode SIW coupler from [10] along with the ridge half-mode version from [11]. All the results are listed in Table 3.10. First, the return loss defined bandwidths are very similar for all technologies. Also, insertion loss is very close between the SW-SIW and HM-SIW versions. On the contrary, a very high value of 4.28 dB was obtained for the ridge version. This last solutions also exhibited poor amplitude imbalance, which is lower than 1 dB in a fractional bandwidth of only 7%. Finally, close miniaturization factors were obtained in both SW-SIW and RHM-SIW versions, which is about half that of the HM-SIW version.

Tech.	f_0 [GHz]	BW_{RL} [%]	IL [dB]	BW_{1dB} [%]	$\Delta\Phi$ [deg]	$Area/\lambda_0^2$
SIW	11	43	3.1	21	± 0.8	1.6
SW-SIW	11.15	42	3.36-3.6	18	± 1.5	0.55
HM-SIW [10]	12	> 40	3.5	21	± 2	1.07
RHM-SIW [11]	7	43	4.28	7.1	± 1	0.47

Table 3.10 – Comparison of the SW-SIW 3-dB coupler with the state-of-the-art short-slot coupler.

Very recently, a new topology of slow-wave SIW was introduced based on a polyline loading of the SIW [31]. It was combined with the half-mode principle and applied to the design of a coupler in [32]. The adopted topology is not based on short-slot coupling, but rather on proximity coupling between adjacent waveguides. It is compared with the work presented here in Table 3.11. Significant differences can be observed because of the different operating principles. The relative bandwidths are much larger in [32], with a return loss better than 10 dB in a 72% fraction of the center frequency. Insertion loss and phase imbalance are very reasonable, the only drawback is the major surface occupation of $2.1\lambda_0^2$, which is nearly five times that of our coupler.

Tech.	f_0 [GHz]	BW_{RL} [%]	IL [dB]	BW_{1dB} [%]	$\Delta\Phi$ [deg]	$Area/\lambda_0^2$
SW-SIW	11.15	42	3.36-3.6	18	± 1.5	0.55
SW-SIW [32]	14.1	72	3.3	41	± 2.5	2.6

Table 3.11 – Comparison of the SW-SIW 3-dB coupler with a different slow-wave coupler from [32].

3.4 Conclusion

In this chapter, the first concrete realizations in SW-SIW have been presented along with their SIW counterparts. More precisely, the slow-wave concept was applied to the design of 0-dB and 3-dB couplers based on the short-slot topology. Without any change in the principle of operation, a miniaturization of more than 65% was demonstrated while maintaining reasonable insertion loss. This miniaturization factor is very close to what was obtained in the state-of-the-art by combining the half-mode topology with the ridge waveguide. Therefore, an even greater miniaturization could be achieved by using an half-mode slow-wave waveguide, as in [32].

Furthermore, for these kind of non-resonant circuits, a uniform distribution of blind via holes was adopted. Thanks to the quasi-distributed effect induced by this arrangement, an equivalent homogeneous medium was used to model the slow-wave effect. This equivalent model was solely defined by an increased permittivity, which took the value of the effective permittivity introduced to model the velocity reduction. Interestingly enough, a very good agreement was obtained between the full simulations including all the blind via holes, and the equivalent coupler. Therefore, a very fast optimization process was followed. Nevertheless, a script was developed to reduce the simulation time by considering all available symmetries.

Finally, measurement and simulations are in good agreement, once fabrication variations were taken into account.

References

[1] T. Djerafi, N. J. G. Fonseca, and K. Wu, "Planar ku-band 4x4 nolen matrix in siw technology," *IEEE Transactions on Microwave Theory and Techniques*, vol. 58, no. 2, pp. 259–266, Feb. 2010.

[2] A. Ali, N. Fonseca, F. Coccetti, and H. Aubert, "Novel two-layer 4x4 siw nolen matrix for multi-beam antenna application in ku band," in *Proc. 2009 3rd European Conference on Antennas and Propagation*, Berlin, Germany, March 2009, pp. 241–243.

[3] T. Djerafi and K. Wu, "A low-cost wideband 77-ghz planar butler matrix in siw technology," *IEEE Transactions on Antennas and Propagation*, vol. 60, no. 10, pp. 4949–4954, Oct. 2012.

[4] S. Karamzadeh, V. Rafii, M. Kartal, and B. S. Virdee, "Compact and broadband 4x4 siw butler matrix with phase and magnitude error reduction," *IEEE Microwave and Wireless Components Letters*, vol. 25, no. 12, pp. 772–774, Dec. 2015.

[5] A. A. M. Ali, N. J. G. Fonseca, F. Coccetti, and H. Aubert, "Design and implementation of two-layer compact wideband butler matrices in siw technology for ku-band applications," *IEEE Transactions on Antennas and Propagation*, vol. 59, no. 2, pp. 503–512, Feb. 2011.

[6] C.-J. Chen and T.-H. Chu, "Design of a 60-GHz substrate integrated waveguide butler matrix: A systematic approach," *IEEE Transactions on Microwave Theory and Techniques*, vol. 58, no. 7, pp. 1724–1733, June 2010.

[7] W. Che, K. Deng, E. K. N. Yung, and K. Wu, "H-plane 3-db hybrid ring of high isolation in substrate-integrated rectangular waveguide (sirw)," *Microwave and Optical Technology Letters*, vol. 48, no. 3, pp. 502–505, Jan. 2006.

[8] W. A. Tyrrell, "Hybrid circuits for microwaves," *Proceedings of the IRE*, vol. 35, no. 11, pp. 1294–1306, Nov. 1947.

[9] A. A. M. Ali, H. B. El-Shaarawy, and H. Aubert, "Compact wideband double-layer half-mode substrate integrated waveguide 90 deg coupler," *Electronics Letters*, vol. 47, no. 10, pp. 598–599, May 2011.

[10] B. Liu, W. Hong, Y. Q. Wang, Q. H. Lai, and K. Wu, "Half mode substrate integrated waveguide (hmsiw) 3-db coupler," *IEEE Microwave and Wireless Components Letters*, vol. 17, no. 1, pp. 22–24, Jan. 2007.

[11] T. R. Jones and M. Daneshmand, "The characterization of a ridged half-mode substrate-integrated waveguide and its application in coupler design," *IEEE Transactions on Microwave Theory and Techniques*, vol. 64, no. 11, pp. 3580–3591, Nov. 2016.

[12] Y. Ding and K. Wu, "Miniaturized hybrid ring circuits using t-type folded substrate integrated waveguide (tfsiw)," in *2009 IEEE MTT-S International Microwave Symposium Digest*, Boston, MA, June 2009, pp. 705–708.

[13] A. A. M. Ali, H. B. El-Shaarawy, and H. Aubert, "Miniaturized hybrid ring coupler using electromagnetic bandgap loaded ridge substrate integrated waveguide," *IEEE Microwave and Wireless Components Letters*, vol. 21, no. 9, pp. 471–473, Sept. 2011.

[14] H. J. Riblet, "The short-slot hybrid junction," *Proceedings of the IRE*, vol. 40, no. 2, pp. 180–184, Feb. 1952.

[15] R. Levy, "Directional couplers," in *Advances in microwaves*, L. Young, Ed. Academic press inc., London, 1966, vol. 1.

[16] S.-i. Yamamoto and J. Hirokawa, "A half-sized post-wall short-slot directional coupler with hollow rectangular holes in a dielectric substrate," *IEICE transactions on electronics*, vol. 88, no. 7, pp. 1387–1394, July 2005.

[17] J.-X. Chen, W. Hong, Z.-C. Hao, H. Li, and K. Wu, "Development of a low cost microwave mixer using a broad-band substrate integrated waveguide (SIW) coupler," *IEEE Microwave and Wireless Components Letters*, vol. 16, no. 2, pp. 84–86, Feb. 2006.

[18] E. Moldovan, R. Bosisio, and K. Wu, "W-band multiport substrate-integrated waveguide circuits," *IEEE Transactions on Microwave Theory and Techniques*, vol. 54, no. 2, pp. 625–632, Feb. 2006.

[19] Z. Hao, W. Hong, J. Chen, H. Zhou, and K. Wu, "Single-layer substrate integrated waveguide directional couplers," *Microwaves, Antennas and Propagation, IEE Proceedings*, vol. 153, no. 5, pp. 426–431, Oct. 2006.

[20] A. Doghri, T. Djerafi, A. Ghiotto, and K. Wu, "Substrate integrated waveguide directional couplers for compact three-dimensional integrated circuits," *IEEE Transactions on Microwave Theory and Techniques*, vol. 63, no. 1, pp. 209–221, Jan. 2015.

[21] R. Levy, "Determination of simple equivalent circuits of interacting discontinuities in waveguides or transmission lines," *IEEE Transactions on Microwave Theory and Techniques*, vol. 48, no. 10, pp. 1712–1716, Oct. 2000.

[22] L. W. Hendrick and R. Levy, "Design of waveguide narrow-wall short-slot couplers," *IEEE Transactions on Microwave Theory and Techniques*, vol. 48, no. 10, pp. 1771–1774, Oct. 2000.

[23] Southwest company. [Online]. Available: http://mpd.southwestmicrowave.com/

[24] C.-Y. Lee and T. Itoh, "The effect of air-bridges on the mode suppression of asymmetrical cpw-fed slot antennas," in *IEEE Antennas and Propagation Society International Symposium Digest*, vol. 1, Newport Beach, CA, June 1995, pp. 338–341.

[25] D. Deslandes, "Etude et developpement du guide d'ondes integre au substrat pour la conception de systemes en ondes millimetriques," Ph.D. dissertation, Ecole Polytechnique, Montreal, 2005.

[26] M. Wojnowski, V. Issakov, G. Sommer, and R. Weigel, "Multimode trl calibration technique for characterization of differential devices," *IEEE Transactions on Microwave Theory and Techniques*, vol. 60, no. 7, pp. 2220–2247, July 2012.

[27] P. Souzangar and M. Shahabadi, "Numerical multimode thru-line (tl) calibration technique for substrate integrated waveguide circuits," *Journal of Electromagnetic Waves and Applications*, vol. 23, no. 13, pp. 1785–1793, Sep. 2009.

[28] G. F. Engen and C. A. Hoer, "Thru-reflect-line: An improved technique for calibrating the dual six-port automatic network analyzer," *IEEE Transactions on Microwave Theory and Techniques*, vol. 27, no. 12, pp. 987–993, Dec. 1979.

[29] A. Niembro-Martin, V. Nasserddine, E. Pistono, H. Issa, A. L. Franc, T. P. Vuong, and P. Ferrari, "Slow-wave substrate integrated waveguide," *IEEE Transactions on Microwave Theory and Techniques*, vol. 62, no. 8, pp. 1625–1633, Aug. 2014.

[30] J. Hong and M. Lancaster, *Microstrip Filters for RF / Microwave Applications*. Wiley, 2004.

[31] H. Jin, K. Wang, J. Guo, S. Ding, and K. Wu, "Slow-wave effect of substrate integrated waveguide patterned with microstrip polyline," *IEEE Transactions on Microwave Theory and Techniques*, vol. 64, no. 6, pp. 1717–1726, June 2016.

References

[32] H. Jin, Y. Zhou, Y. M. Huang, S. Ding, and K. Wu, "Miniaturized broadband coupler made of slow-wave half-mode substrate integrated waveguide," *IEEE Microwave and Wireless Components Letters*, vol. 27, no. 2, pp. 132–134, Feb. 2017.

Chapter 4

Miniaturization of resonant circuits in X-band

Contents

4.1 Introduction 108

4.1.1 Overview of SIW filter technologies 108

4.1.2 Slow-wave topology for the miniaturization of SIW filters 111

4.2 Implementation of a synthesis method in SIW technology . . . 112

4.2.1 Global description 112

4.2.2 Implementation and verification 117

4.3 Development of the synthesis method in SW-SIW technology 123

4.3.1 Application of the classical synthesis method 123

4.3.2 Homogenisation of the blind-via distribution 127

4.3.3 Development of a segmentation algorithm for fast optimization . 131

4.3.4 Algorithmic implementation 139

4.4 Measurement results and perspectives 141

4.4.1 5^{th}-order, 1 GHz bandwidth filter in SW-SIW technology 141

4.4.2 5^{th}-order, 0.5 GHz bandwidth filter in SW-SIW technology . . . 142

4.4.3 3-rd order, 1 GHz bandwidth filter in HM-SW-SIW technology . 143

4.4.4 Retro-simulation based on fabrication issues and perspectives . . 144

4.5 Conclusion 147

References 148

4.1 Introduction

Since the rapid development of the SIW technology, filters in particular have attracted a lot of attention. That is mainly because the theoretical backgrounds and synthesis methods in rectangular waveguide had been extensively studied during the previous decades for high-power, often space-oriented applications. Based on this historical legacy, the development of filters in the integrated technology has been very fast.

Also, one of the advantage of integrated waveguide is that it offers a lot of new possibilities in terms of miniaturization. Synthesis methods have been developed but still often needs to be adapted for specific geometries of miniaturised waveguides. In this context, this chapter aims at providing some insight on the work conducted for the synthesis of filters in the slow-wave technology previously introduced.

More precisely, the well-known ladder topology synthesis method was first implemented in the general context of SIW (see 4.2.1), then it was adapted to the slow-wave waveguide (see 4.3). Also, some details about the algorithmic implementation are given in section 4.3.4. Finally, simulation and measurement results will be presented in section 4.4.

4.1.1 Overview of SIW filter technologies

Let's illustrate these developments with a few examples in the microwave frequency band.

Many innovative filters topologies have been successfully developed in the last years, taking advantage of the high quality factor Q and low cost fabrication processes of the SIW. Several journal papers have presented some overviews of the existing topologies, as [1] or [2]. In fact, it is now more and more complex to have an extensive overview of filter recent design methods and realizations, mainly because of the increasing number of publications dedicated to this specific topic as illustrated in Figure 4.1.

Four popular topologies are illustrated in Figure 4.2, namely the symmetric or asymmetric inductive posts structures, coupled circular cavities or cross-coupled rectangular cavities. The associated synthesis method is usually based on the conventional waveguide theory but more and more development led to specific SIW modelling, that of inductive via holes for example [3]. Thanks to the simplicity of the SIWs fabrication process, alternative cavity shapes can also be realised like circular [4] or triangular [5].

In addition, existing topologies also include 3D designs with vertical coupling ([6],[7]). More complex functions such as multi-band ([8]-[9]), tunable ([10]-[11]) and balanced filters ([12]-[13]) were also demonstrated. These realizations have demonstrated the potential of SIW to achieve narrow-band filters at microwave and even mm-wave frequencies, also providing fully shielded topologies reducing the coupling and interferences between adjacent waveguides.

4.1.1.1 Miniaturisation of SIW filters

Most of the work related to the miniaturization of filters is carried out for frequencies below 15 GHz. Obviously, this is because SIW suffers from a frequency dependant size which is hardly comparable to that of planar microstrip or CPW structures in this

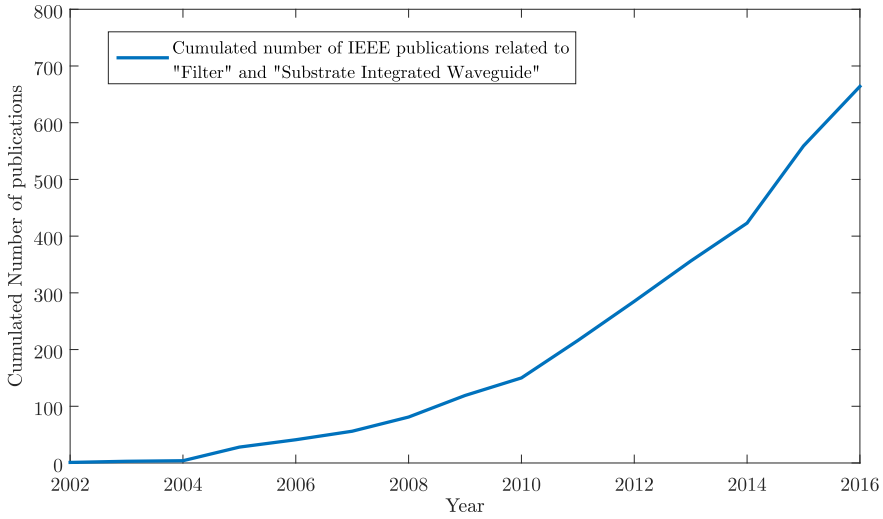

Figure 4.1 – Cumulated number of publications in *IEEE Xplore* dedicated to filters in SIW technology.

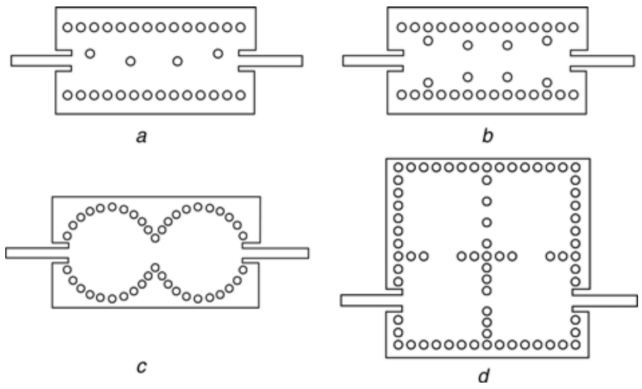

Figure 4.2 – Some of the SIW filter topologies: (a) Filter with asymmetric inductive posts, (b) Filter with symmetric inductive posts, (c) Filter with circular cavities, and (d) Filter with rectangular cavities and cross-coupling [1].

range of frequencies. As already presented in the first chapter, several miniaturization techniques have been developed to reduce SIW filters dimensions.

First of all, if a single layer substrate is required for cost reasons, several techniques can provide significant size reduction. In order to maintain a reasonable quality factor the magnetic symmetry planes can be replaced by open circuit conditions to reduce drastically the dimensions. Because of the initial symmetries, the field distributions are not really affected for thin layers, however radiation has to be carefully considered for thicker substrates. This is the objective of partial modes solutions such as half-mode [14] or quarter-mode topologies [14][15] reducing by a factor of two and four the resonator dimensions, respectively (see Figure 4.3).

Alternatively, instead of limiting the occupied area by the resonant mode a differ-

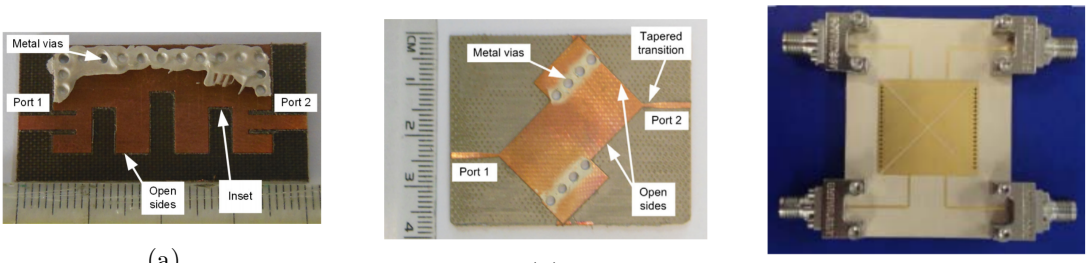

(a) (b) (c)

Figure 4.3 – Some partial modes filter topologies: (a) Half-mode [14], (b)(c) quarter mode [14][15].

ent approach consists in extending the number of modes resonating within the same area [16][17]. More precisely, oversized cavities compared to the operating frequencies can exhibit several resonant modes, providing either poles or transmission zeros [18] depending on the coupling schemes.

On the other hand, the integration of coaxial waveguide resonators also provided an interesting miniaturization capability [19]. Because of the localised capacitive effect on the top of the cavities this solution also demonstrated its potential for tunability thanks to the use of varactors [20][21] (see Figure 4.4).

(a) (b)

Figure 4.4 – Combline tunable filters in SIW technology : (a)[20], (b)[21].

Finally, the miniaturization of filters was demonstrated with loaded cavities (see Figure 4.5). Indeed, many solutions rely on complementary split ring resonators (CSRR) [22][23][24] which lower the resonance frequencies. Stub-loading of SIW cavities has also been used in [25].

Further reductions of filters dimensions can be achieved through more complex structures relying on multilayer substrates. The first solution which naturally derives from the planar solution is the vertical coupling of cavities. By vertically stacking several resonant structures a good compactness was demonstrated in both PCB [26] and LTCC [27][28] technologies (see Figure 4.6), however the latter remains a relatively costly solution.

Inherently based on the multilayer structure, several folded configurations were also applied to filter design as in[29][30][31]. The reduction of occupied area in this last solution is directly linked to the number of layers comprising each cavity.

Finally, the insertion of blind via holes in a layered structure was also used to create

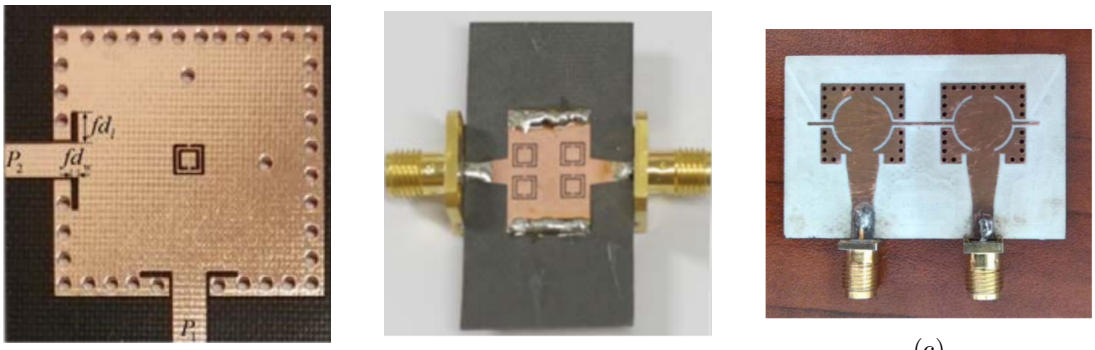

(a) (b) (c)

Figure 4.5 – Loaded SIW cavity filters: (a)(b) with CSRR [22][23], (c) with stub [25].

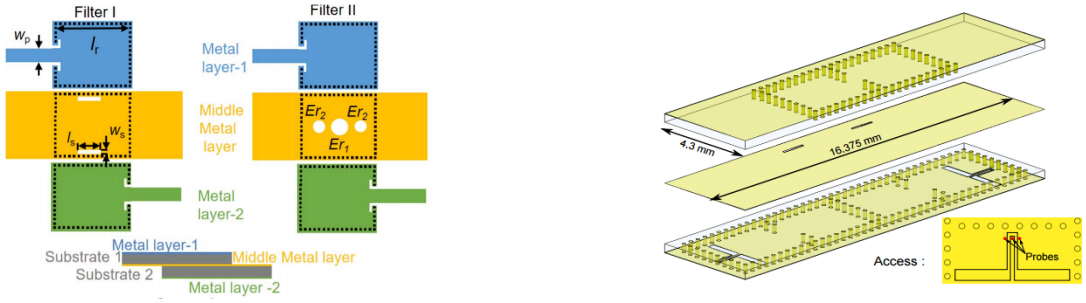

(a) (b)

Figure 4.6 – Vertical stacking of cavities in (a) PCB [26] and (b) LTCC [27] technologies.

miniaturised resonators such as in [32]. In this last realization, the use of asymmetric mushrooms shaped resonators provided interesting features besides miniaturization, such as the control of finite transmission zeros.

4.1.2 Slow-wave topology for the miniaturization of SIW filters

As already shown in the previous chapter, the slow-wave technology can constitute an interesting solution for reducing the occupied area of passive components in SIW. More precisely, it was demonstrated that a distributed slow-wave effect can be directly inserted in existing SIW topologies in order to reduce dimensions without changing the principle of operation.

For non-resonant structures such as power-dividers, couplers or cross-overs which exhibit low insertion loss in the conventional topologies, the use of an homogeneous distribution of blind via holes is motivated by the idea of using an equivalent medium. Yet, the placement of blind via holes in the whole transverse section resulted in increased losses but they remained low when dealing with non resonant circuits. In addition, the simulation time was significantly reduced thanks to the equivalent medium.

For filter design, insertion loss can be already important in conventional topologies, mainly related to substrate dielectric losses and waveguide thickness. The slow-wave

property will provide strong miniaturization of these structures, however it will also increase insertion loss. It is therefore reasonable to try to limit the additional losses caused by the insertion of blind via holes. This can be already done by removing the via holes which are in the low electric field regions, as they do not really contribute to the slow-wave effect. Only the ones in the center of the waveguide should therefore be maintained.

Of course, this topology modification will remove the possibility of using an equivalent medium filling all the transverse section. However, the need for an equivalent medium is much less relevant because the filter synthesis methods would require an extreme precision on the electrical model of the waveguide, which is hardly defined in SW-SIW. In fact, the quasi-distributed character of the SW-SIW makes each coupling or resonator structure potentially sensitive to the blind via holes placement, thus making the idea of an equivalent homogeneous waveguide useless.

First of all, the classical synthesis method will be described and applied to the SIW in 4.4.4. Then, the exact topology used for the synthesis of filters in SW-SIW technology will be described for the X band in section 4.3.

4.2 Implementation of a synthesis method in SIW technology

4.2.1 Global description

In this chapter, the design method of coupled cavity filters is described. The ladder topology was chosen as a first step toward the design of more complex miniature slow-wave filters. In fact, as the slow-wave topology brings extra complexity to the classical method, it was therefore decided to tackle this complexity in the simplest cases first. The studied topology is that of a ladder of coupled resonators which interact with their adjacent neighbours only. From the coupling matrix point of view this would mean that all extra-diagonal terms are null. In practice, non-adjacent coupling are neglected. A representation of this topology is given in Figure 4.7, where n resonators placed between the source S and the load L are coupled through coupling coefficients $\{k_{ij}\}, i = 0..n+1$.

Figure 4.7 – Schematic description of a coupled resonator filter in ladder topology.

In the schematic representation given above, each resonator refers to a single-mode resonant cavities. All these cavities will be realized in SIW, SW-SIW and HM-SW-SIW technologies. The goal of the design method is the definition of all physical dimensions of the filter based on the specifications given by the targeted application. The main geometrical parameters are the cavities dimensions and the size of inter-cavity coupling

structures.

The global procedure will first be presented and applied in SIW technology, in addition some algorithmic implementation elements will also be given. Then, this method will be adapted and applied to the SW-SIW technology. Finally, it will be applied to the HM-SW-SIW technology. The basis of this work, especially the conventional method steps are well-documented in most of the microwave engineering books [33]-[34], a clear description being given in [35] as well.

4.2.1.1 Synthesis objectives

The first step of the synthesis is the definition of the frequency response of the filter, defined by the parameters listed in Table 4.1. A schematic view of the general procedure applied in this chapter is given in Figure 4.8.

Parameter	Unit	Description
f_0	[Hz]	Center frequency
BW	[%]	Bandwidth
L_{Ar}	[dB]	Attenuation level in the selected band
L_{As}	[dB]	Attenuation level in the rejected band
f_s	[Hz]	Frequency at which the attenuation must reach L_{As}

Table 4.1 – Filter frequency response parameters.

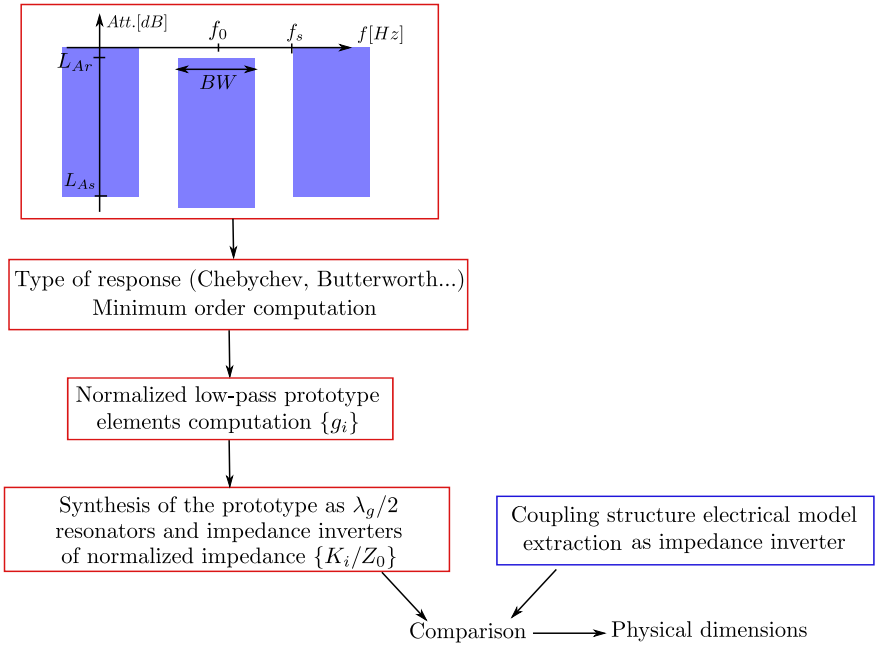

Figure 4.8 – Schematic description of the synthesis method.

Starting from the specifications and polynomial approximation chosen by the designer (Tchebychev, Butterworth, Elliptic etc...), the theoretical minimum order N_{min} can be calculated. As an example, the equations leading to this minimum order for a Tchebychev approximation are given in (4.1)-(4.3). In (4.1), λ^l and λ^h are the guided wavelengths at the low and high cut-off frequency $f_l = f_0 - BW/2$ and $f_h = f_0 + BW/2$, respectively

$$B = \left(\frac{\lambda^l - \lambda^h}{\lambda^0} \right)^{-1} \tag{4.1}$$

$$\Omega_s = B \left(\frac{f_s}{f_0} - \frac{f_0}{f_s} \right) \tag{4.2}$$

$$N_{min} = \frac{\operatorname{acosh}\left[\sqrt{\dfrac{10^{L_{As}/10} - 1}{10^{L_{Ar}/10} - 1}} \right]}{\operatorname{acosh}\left(\Omega_s\right)} \tag{4.3}$$

Once the order of the filter is calculated, the elements of the normalized low-pass prototype $\{g_i\}$ can be obtained depending on the chosen polynomial approximation [34].

Then, the implementation of the theoretical prototype into a specific circuit topology made of coupled resonators can be performed. First, the low-pass prototype must be transformed into its bandpass equivalent, then it is synthesized in terms of half-wavelength resonators coupled via apertures modelled as impedance inverters. This overall topology is illustrated in Figure 4.9. The calculation steps which are behind these transformations are not developed here as the literature thoroughly deals with the subject [34, 36–39].

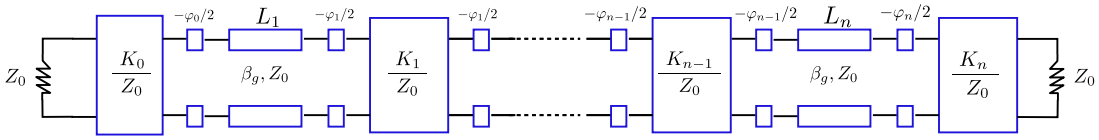

Figure 4.9 – Topology of the pass-band filter synthesized in terms of real impedance inverters and half-wavelength resonators.

The synthesis can be divided into two distinct steps. On one hand, theoretical impedance inverters have to be matched to real coupling structures whose dimensions need to be fixed, in this case we used inductive slots. On the other hand, the dimensions of coupling cavities between these inverters must be determined. The following sections 4.2.1.2 and 4.2.1.3 are dedicated to these two distinct steps.

4.2.1.2 Equivalence between impedance inverters and coupling structures

The underlying idea providing the link between the impedance inverter function and any coupling structure was demonstrated by Ralph Levy in the 1970's [40]. The

demonstration relies on the ABCD matrix formalism and established that any lossless reciprocal passive quadripole can be assimilated to an ideal impedance inverter or generalized impedance K, providing the reference planes are moved away by an electrical length φ. In order to obtain these two parameters, two calculation methods are presented here. The first one is directly that of R. Levy, the second one is based on modelling the coupling structure as a T-shaped circuit [41].

The principle of the first method is illustrated in Figure 4.10. Equations (4.5)-(4.6) can be used to calculate the normalized impedance $\tilde{K}$ and φ as function of the elements of the input matrix $[A, jB; jC, D]$, where $[a, jb; jc, d]$ represents the same matrix normalized to the impedance Z_0.

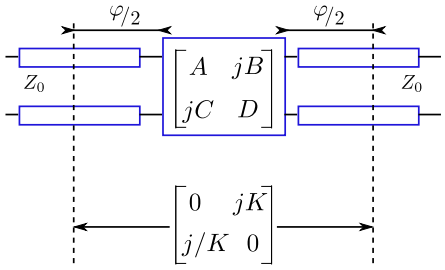

Figure 4.10 – Position of reference planes providing the equivalence between any lossless reciprocal passive quadripole and an ideal impedance inverter.

$$L = 1 + \frac{1}{4}(a-d)^2 + \frac{1}{4}(b-c)^2 \tag{4.4}$$

$$\tilde{K} = \frac{K}{Z_0} = \sqrt{L} - \sqrt{L-1} \tag{4.5}$$

$$tan\,(\varphi) = \frac{2\,(db-ac)}{a^2 - d^2 + b^2 - c^2} \tag{4.6}$$

The electrical length φ is directly the one given in Figure 4.9, that is because the equivalence can be seen in the reversed way. Indeed, if the slot can be interpreted as an ideal inverter when the reference plane is placed at an electrical length φ from it, therefore this same slot is equivalent to an ideal inverter with artificial negative electrical length $-\varphi/2$ on both sides.

The second method [41] relies on the same principle but uses a serie impedance jX_s along with an inductance in parallel X_p. Because of the symmetry it is possible to have identical impedances X_s on each side of the inductance for the calculation. The equivalent compensated inverter model can be calculated by equations (4.7)-(4.8) and (4.9)-(4.10) starting from the simulated scattering matrix S. The principle is illustrated in Figure 4.11.

$$\frac{jX_p}{Z_0} = \frac{2S_{21}}{(1-S_{11})^2 - S_{21}^2} \tag{4.7}$$

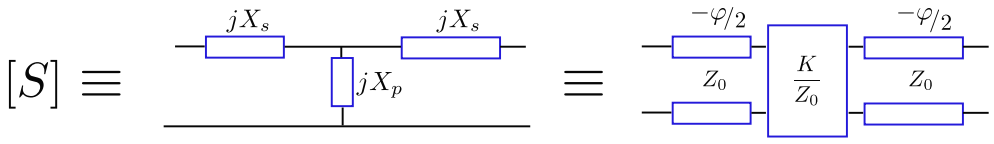

Figure 4.11 – Equivalent T circuit of the coupling structure.

$$\frac{jX_s}{Z_0} = \frac{1 + S_{11} - S_{21}}{1 - S_{11} + S_{21}} \tag{4.8}$$

$$\varphi = atan\left(\frac{2X_p}{Z_0} + \frac{X_s}{Z_0}\right) - atan\left(\frac{X_s}{Z_0}\right) \tag{4.9}$$

$$\tilde{K} = \frac{K}{Z_0} = |tan\left(\frac{\varphi}{2} + atan\left(\frac{X_s}{Z_0}\right)\right)| \tag{4.10}$$

For these two methods, the important point is to realize all computations based one the S matrix of the slot only, normalized to the fundamental mode impedance of the access waveguides. In the non-TEM waveguide topology, this impedance might have several definitions because of the ambiguity in the definition of equivalent currents and voltages. However, the knowledge of the absolute value of this impedance is not required here, only the proper normalization of the S-matrix to this impedance must be achieved.

In the general case, in order to realize this normalization a de-embedding procedure is implemented. If the structure is uniform along the propagation axis one can directly use the port de-embedding function in HFSS. Otherwise, a proper de-embedding algorithm has to be used. In this work, a two line method called "Thru-Line" was implemented in MATLAB for this purpose [42]. Finally, a very strict convergence criteria must be imposed on all simulations. This is necessary because the filter response will strongly depend on the extracted model accuracy. In this work, a convergence criteria imposed on the maximum variation of the S-Parameters was fixed at 0.1% instead of the default 2%.

As mentioned previously, the goal of this extraction is to obtain the slot model for several geometrical configurations, so that these configurations can be matched to the value required by the filter theoretical values. In this work, inductive slots were chosen as coupling structures, the main geometrical parameter being its aperture W_s. In order to calculate the dimension which corresponds to a desired value of inverter impedance a polynomial fitting was realized using MATLAB [43] and Ezyfit toolbox.

As it will be shown later, the variations of φ and $\tilde{K}$ versus W_s are relatively regular, therefore polynomials of fifth order are usually used. Also, in order to facilitate the synthesis, the fitting is first calculated for W_s as a function of $\tilde{K}$. Thus, the physical apertures W_s can be directly obtained by evaluating the computed function at the desired values of $\tilde{K}$. Then, the resulting electrical length to be compensated φ is given by the evaluation of the polynomial which maps φ as a function of W_s.

4.2.1.3 Equivalence between resonators and waveguide sections

Half-wavelength sections of waveguides are used to realize the resonators. The goal is therefore to set their electrical length to π at the center frequency of the passband f_0. At the beginning of the synthesis all resonators are identical. However, the electrical lengths induced by the coupling structures have to be taken into account and compensated in these resonators. As a result, each cavity must take into consideration the influence of the slot on both sides. This compensation is expressed by equation (4.11), where i stands for the cavity index, and φ_i for the electrical length of the i-th slot. Next, the guided wavelength at the center frequency λ^0 is given by the de-embedding algorithm used in the slot extraction.

$$L_i = \frac{\lambda^0}{2}\left(1 + \frac{1}{2\pi}\left(\varphi_{i-1} + \varphi_i\right)\right) \quad , i = 1..n \tag{4.11}$$

4.2.2 Implementation and verification

In this first application part, the method described previously will be followed for a filter design in SIW technology. The relatively good equivalence between SIW and rectangular waveguide makes it a good candidate to validate the design method. Additional complexity will be dealt with in the case of SW-SIW and HM-SW-SIW.

Once again, the technology stack-up is identical to the one introduced in Figure 2.5. As detailed later, the filter center frequency was chosen at 11 GHz, which gives a guided wavelength of about 1.5 cm. Concerning the lateral via holes a standard drilling diameter d_{ext} of 400 µm with a spacing s of 800 µm was considered. These dimensions satisfy the conditions given in [35] for proper field confinement and avoidance of periodic effects.

4.2.2.1 Specifications and first calculations

The goal is to design a bandpass filter centered at 11 GHz with an absolute bandwidth of 1 GHz. The oscillation in the passband L_{Ar} is set to 0.04 dB, which is equivalent to a return loss level of -20 dB in the lossless case. The out-of-band rejection is set to 40 dB for a frequency f_s of 14.5 GHz. By application of the equations given in 4.2.1.1 the minimum order for a Tchebychev approximation can be calculated, it is found to be 4. However, the use of Tchebychev approximation with even orders requires non-symmetric access ($g_0 = 1$, $g_{n+1} \neq 1$), which translates into the impossibility to connect directly the same waveguide as input and output of the filter. An order of 5 is thus selected. In all the synthesis presented in this chapter, the Tchebychev approximation is considered.

The waveguide cut-off frequency is fixed at 7.5 GHz so that the filter will approximately operate in the middle of the mono-mode frequency band. In order to obtain this cut-off frequency, the width W is fixed at 10.8 mm. This value is obtained by using an intermediate effective width W_{eff} in the classical formula (4.12). This effective width is introduced to take into account the via hole diameters and spacing, once it is calculated W can be obtained by (4.13) [35].

$$f_c = \frac{c_0}{2W_{eff}\sqrt{\varepsilon_r}} \tag{4.12}$$

$$W_{eff} = W - \frac{d_{ext}^2}{0.95s} \tag{4.13}$$

4.2.2.2 Impedance inverter model extraction

Because of the periodicity of SIW along the propagation direction, a de-embedding based on excitation ports data in HFSS cannot be used. In fact the waveguide cannot rigorously be considered as uniform along the propagation axis. Therefore, it is necessary to perform a de-embedding based on two different sections of waveguides in order to set the reference planes and normalize the S-Parameters to the fundamental mode impedance. The de-embedding features used for the extraction of the inductive slot model as a function of its width W_s are illustrated in Figure 4.12. From left to right, one can see the short waveguide section "Thru", the longer waveguide "Line" and the so-called "Device-Under-Test" (DUT), in that case the inductive slot. Thanks to this de-embedding, reference planes are positioned right next to the slot, as shown in Figure 4.13.

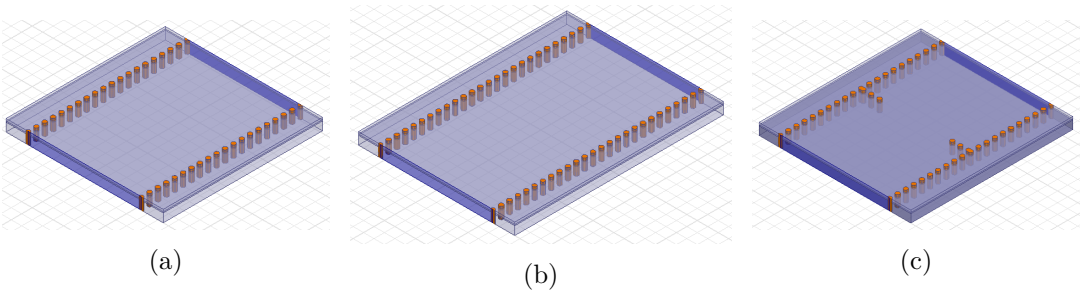

(a) (b) (c)

Figure 4.12 – Extraction of the inductive slot model: (a) Thru, (b) Line and (c) DUT.

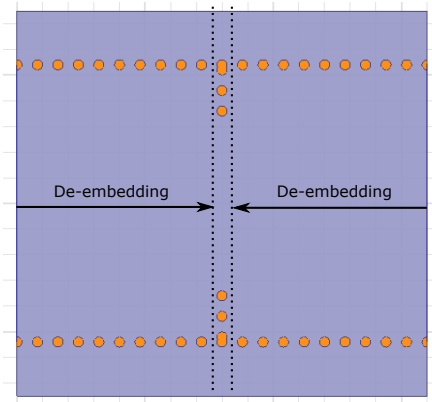

Figure 4.13 – Position of reference planes for the extraction of inductive slot model.

The extraction is performed at the center frequency of 11 GHz. The extracted $\tilde{K}$ and φ are presented as function of the normalized width W_s/W in Figure 4.14 along with the two polynomials regressions in Figure 4.15. In this particular case, an order of five was sufficient for imitating accurately the extracted parameters variations. As stated before, the polynomials regressions are used to provide an empirical model which can then be used in the synthesis.

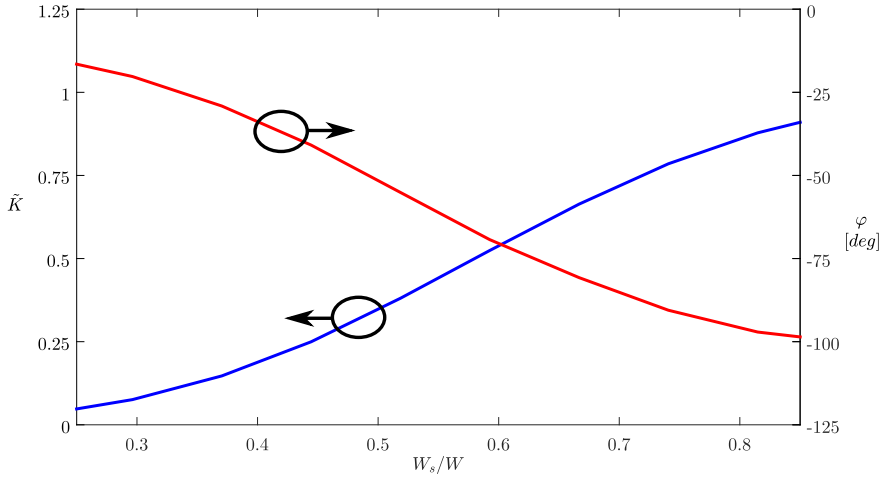

Figure 4.14 – Extracted inverter model of the inductive slot in SIW technology.

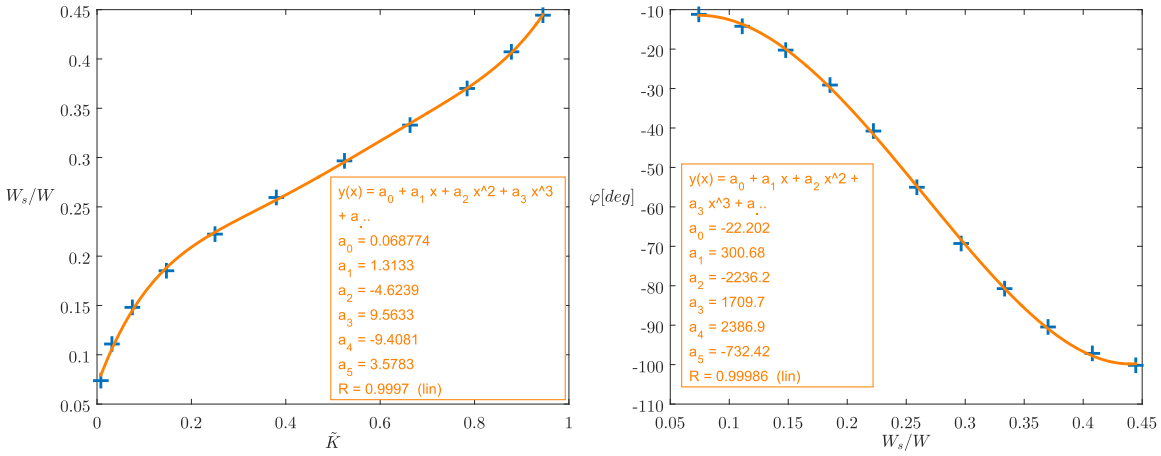

Figure 4.15 – 5-th order polynomial fittings for the inductive slot parameters.

First, for low values of W_s/W the aperture is close to a short-circuit condition. From the extracted model point of view it is interpreted as small values of $\tilde{K}$ and small negative values of φ. By neglecting the influence of the small electrical phase shift $\varphi/2$ one obtains the equivalent circuit of an ideal quarter-wavelength inverter with a transformer of infinite factor as illustrated in Figure 4.16. This is then equivalent to a quarter-wavelength open-ended stub, which brings back in the reference plane of both sides a short-circuit condition.

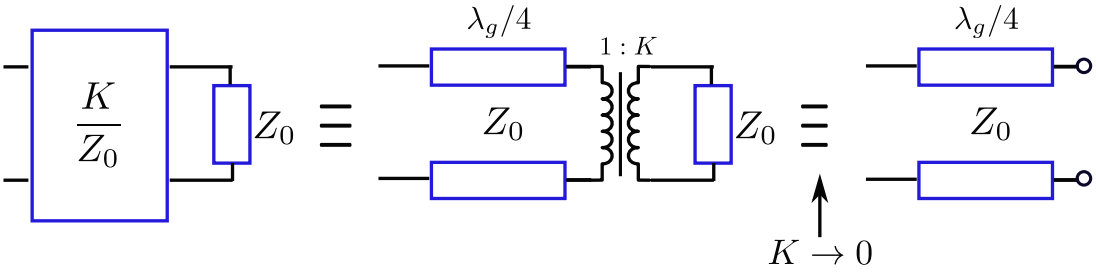

Figure 4.16 – Equivalent circuit for small apertures of the inductive slot.

The other side of the graph shows that for large apertures - which means no discontinuity along propagation path - the inverter impedance tends to one while the phase shift on each side of it tends to approximately $90/2 = 45$ degrees. In this case the two electrical phase shifts will compensate the 90 degrees introduced by the ideal inverter. Besides, the unity factor in the inverter will just cancel and the equivalent circuit reduces to nothing.

4.2.2.3 Filter synthesis

Once the extraction of the physical model of coupling slots is done, the synthesis can now be performed. In this step, the elements of the low-pass prototype are calculated according to the specifications and provide the starting point for the definition of the inverters impedances. By considering a Tchebychev approximation, the low-pass prototype elements $\{g_i\}_{i=0..n+1}$ are calculated as in [34], they are listed in Table 4.2. Then, the normalized inverter impedances $\{\tilde{K}_i\}_{i=0..n}$ are calculated using equations (4.14)-(4.16). Finally, polynomials fittings are used to find the physical aperture width $\{W_{si}\}_{i=1..n+1}$ which realizes these impedances, as well as the corresponding electrical length $\{\varphi_i\}_{i=1..n+1}$. The numerical values for all calculated parameters are listed in Table 4.3.

$$\tilde{K_0} = \sqrt{\frac{\pi}{2B}\frac{1}{g_0 g_1}} \tag{4.14}$$

$$\tilde{K_i} = \frac{\pi}{2B}\sqrt{\frac{1}{g_i g_{i+1}}} \quad , i = 1..n-1 \tag{4.15}$$

$$\tilde{K_n} = \sqrt{\frac{\pi}{2B}\frac{1}{g_n g_{n+1}}} \tag{4.16}$$

i	**0**	**1**	**2**	**3**	**4**	**5**	**6**
g_i	1	0.9576	1.3704	1.7850	1.3704	0.9576	1

Table 4.2 – Low-pass prototype elements given by the filter specifications in SIW technology.

i	**1**	**2**	**3**	**4**	**5**	**6**
$\tilde{K_i}$	0.538	0.242	0.177	0.177	0.242	0.538
W_{si} **[mm]**	3.22	2.39	2.16	2.16	2.39	3.22
φ_i **[deg]**	-69	-41.3	-34.3	-34.3	-41.3	-69

Table 4.3 – Synthesized coupling parameters for the filter in SIW technology.

Then, cavity length $\{L_i\}_{i=1..n}$ can be calculated from (4.11) by taking into consideration the synthesized electrical lengths $\{\varphi_i\}_{i=1..n+1}$ and guided wavelength from the de-embedding algorithm. The calculated cavity lengths are listed in Table 4.4.

i	**1**	**2**	**3**	**4**	**5**
L_i	6.94	7.91	8.1	7.91	6.94

Table 4.4 – Physical length of resonators in SIW technology.

4.2.2.4 Simulation results

The geometry of the filter simulated in HFSS is illustrated in Figure 4.17. Both the structure and the excitation are symmetric along the vertical longitudinal plane, it is therefore possible to reduce the simulation time by assigning a symmetry condition on this plane (magnetic). The S-Parameters presented here are normalized to the impedance of the waveguide access.

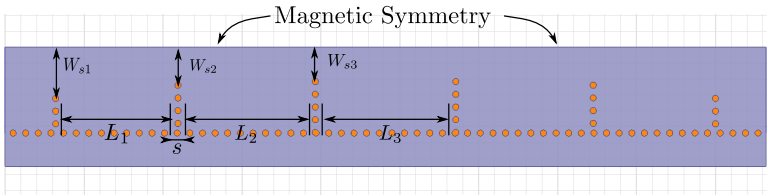

Figure 4.17 – 3D structure of the simulated SIW filter in HFSS.

The simulated S-Parameters obtained right after synthesis are plotted in Figure 4.18. Four poles can be seen in the passband and the simulated frequency bandwidth is 1.06 GHz, which is very close to the targeted 1 GHz. This first result can therefore be used as a good starting point for the optimization procedure.

In order to accelerate the optimization phase, lateral via holes walls can be replaced by equivalent metallic walls, using the equivalent width already mentioned in (4.13). Hence, each simulation takes about 1.5 minutes (including adaptive passes with a maximum S matrix variation of 2%). Also, the interpolation algorithm "fast" is used as it is highly efficient for resonant structures. The dimensions after optimization are compared with those of the synthesis in Table 4.5, in addition only half of the dimensions are shown as the symmetry is kept.

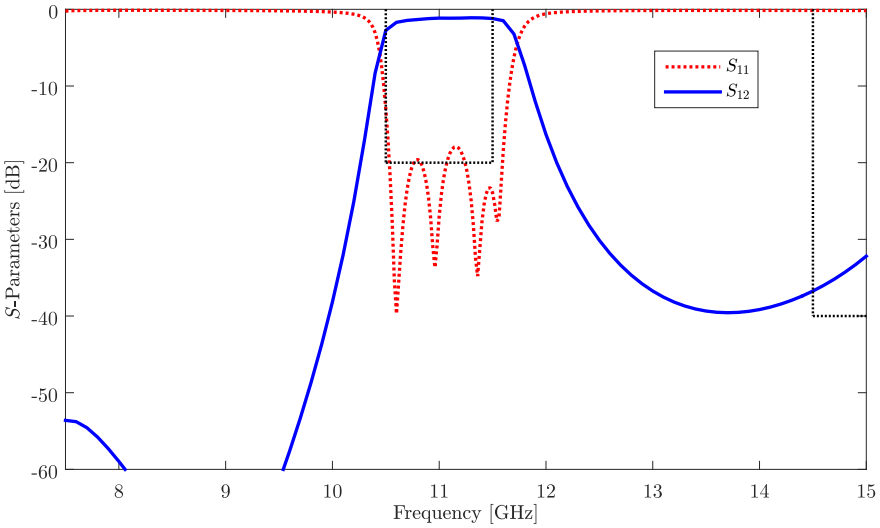

Figure 4.18 – S-Parameters of the simulated SIW filter in HFSS.

	W_{s1}	W_{s2}	W_{s3}	L_1	L_2	L_3
Synthesis	3.22	2.39	2.16	6.94	7.91	8.1
Optimization	3.24	2.38	2.16	6.92	7.94	8.165
Relative variation	0.6%	0.4%	0%	0.3%	0.3%	0.7%

Table 4.5 – SIW filter dimensions, before and after optimization.

A maximum variation of 0.6% is necessary to obtain the final response, thus confirming the reliability of the implemented extraction procedure and synthesis. The final optimized S-Parameters are illustrated in Figure 4.19 along with the initial ones.

4.2.2.5 Some details about the simulation method

The results presented here are obtained in the frequency domain, which is the default solver implemented in HFSS. This computation is made of two steps, first the structure is meshed with an increasing precision until a convergence criteria is satisfied, in this case it is a maximum variation of the S-Parameters amplitude. Secondly, a variation in frequency is performed around the frequency at which the first step was completed in order to obtain the full S-Parameters.

As already mentioned, during this second step an algorithm called "Fast" is used to accelerate the optimization procedure. However, one has to use a discrete sweep (without interpolation) for the broadband results because the "Fast" algorithm relies on the field solution at the resonant frequency, making it obsolete for producing broadband computation.

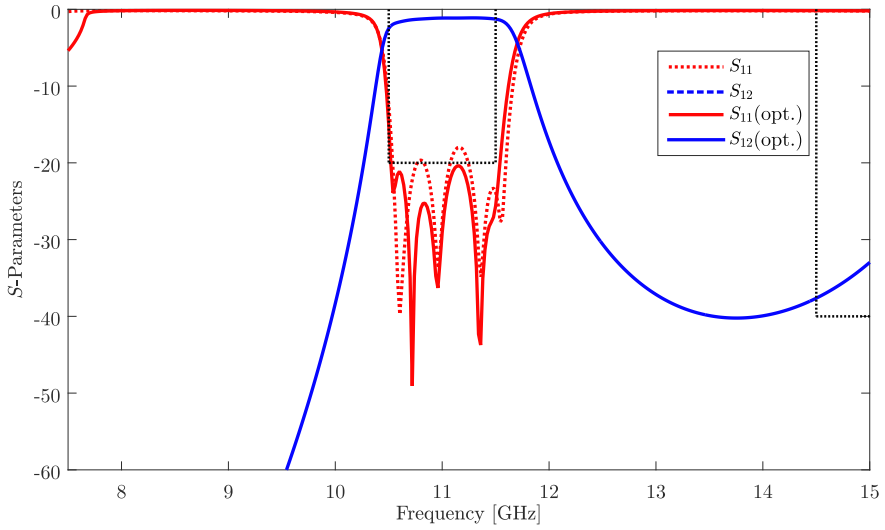

Figure 4.19 – Simulated S-Parameters of the optimized SIW filter in HFSS.

4.3 Development of the synthesis method in SW-SIW technology

In this second part, the developed methodology will be applied to the slow-wave technology in order to fabricate more compact filters.

4.3.1 Application of the classical synthesis method

4.3.1.1 Technology description

A transverse view of the SW-SIW used in this part is illustrated in Figure 4.20. For simplicity, blind and through-via holes are distributed with the same spacing s, this spacing being kept also in the transverse plane for the blind via holes. The diameter of all via holes is $d_v = 0.4$ mm, and the blind ones are covered with copper land of diameter $d_p = 0.6$ mm and thickness $h_p = 0.035$ mm.

In order to minimize insertion loss in the cavities, the number of via holes is limited to five. This configuration provides the required energy separation for reducing the phase velocity without increase to much the ohmic losses. The lateral size of the waveguide W is set to 6 mm, which corresponds to a cut-off frequency of 7.7 GHz for the fundamental mode, similar to that of de SIW waveguide studied in the previous section.

4.3.1.2 Impedance inverter model extraction

The simulation of the slow-wave topology requires more memory and computation resources than the conventional SIW due to the blind via holes. Therefore, in order to gain some time in each step of the procedure the lateral via holes are replaced by full metallic walls from the beginning. Starting from equation (4.13) an approximate

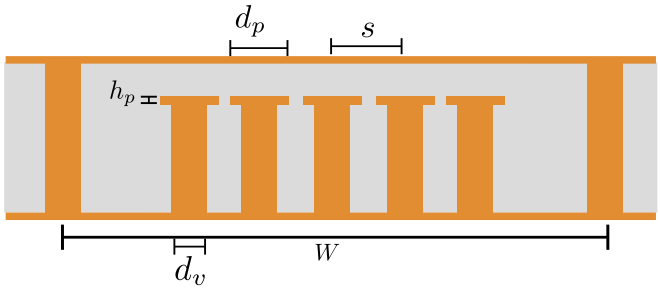

Figure 4.20 – Technology transverse view for the design of filters in SW-SIW technology.

value of 5.79 mm is obtained for the waveguide effective width W_{eff}, then this value is lowered to 5.72 mm by matching simulations of real and equivalent waveguides. The de-embedding structures used for the extraction of the inductive slot equivalent model are illustrated on Figure 4.21. In addition, the magnetic symmetry is used to reduce the size of the volume by two (see 4.23)

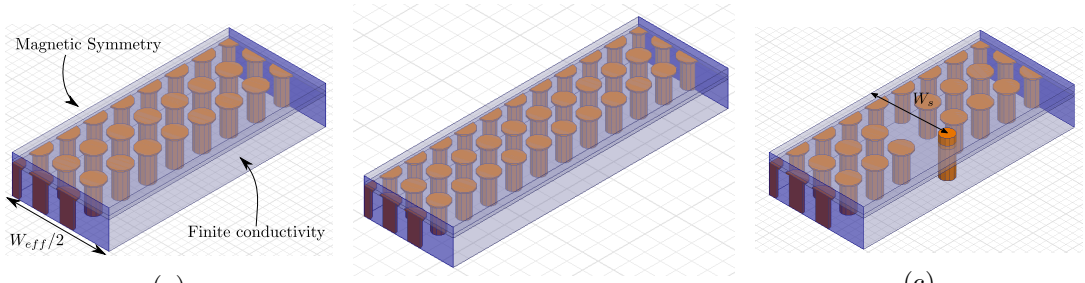

(a) (b) (c)

Figure 4.21 – Extraction of the inductive slot model in SW-SIW: (a) Thru, (b) Line and (c) DUT.

As shown in Figure 4.21(c), in order to simplify the slot topology only one via hole is placed in its center for any width W_s. This is an arbitrary choice, it could be done without any blind via in the slot for example.

Finally, the reference planes are placed right next to the slot (as previously), more precisely at a distance of $s/2$ from it. The extraction is realized at the same center frequency of 11 GHz by the same methodology as previously described. The extracted impedance inverter parameters are presented in dashed line in Figure 4.22 along with those obtained for the SIW configuration in 4.2.2.2. A very similar evolution is observed between the two technologies, only a slight shift in the electrical length can be noticed as well as a slower increase of $\tilde{K}$ as function of the normalised aperture width. In fact, the impedances values obtained for large apertures are lower for the slow-wave case. In the extreme case of an aperture as large as the waveguide, the slot does not reduce to nothing as for the SIW. Indeed, a discontinuity is still affecting the propagation, as only one blind via hole stands in the transverse section. It would therefore be surprising if the equivalent circuit was the same as in the SIW configuration.

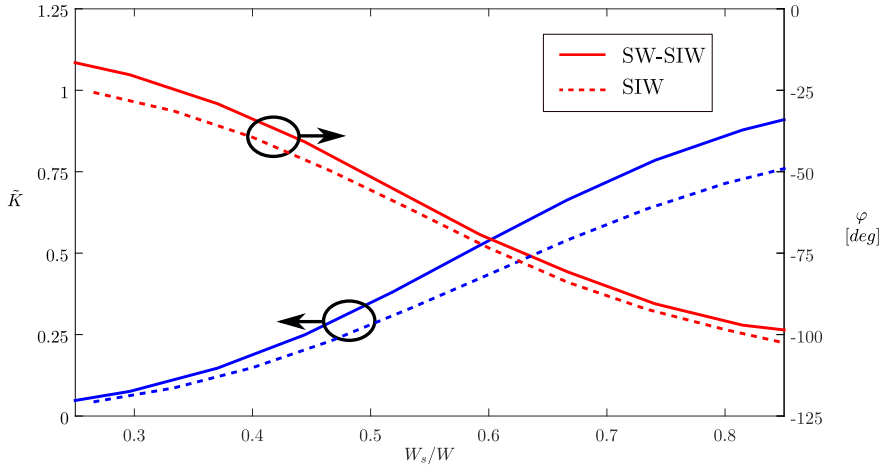

Figure 4.22 – Extracted inverter model of the inductive slot in both SIW and SW-SIW technologies.

4.3.1.3 Synthesis in SW-SIW technology

The filter dimensions are calculated in the same way previously described in SIW technology, the synthesised values are given in Table 4.6. Once again the center symmetry is kept so that half of the dimensions are listed here.

Parameter	W_{s1}	W_{s2}	W_{s3}	L_1	L_2	L_3
Value [mm]	2.02	1.46	1.3	4.4	5.05	5.18

Table 4.6 – Synthesized dimensions for the filter in SW-SIW technology.

An illustration of the simulated structure is given in Figure 4.23. For the simulation in SW-SIW technology,lateral via holes do not constitute significant discontinuities at the excitation port because of their position at the waveguide edges. By contrast, the blind via holes placed in the middle of the transverse section can lead to strong discrepancies in the computed S-Parameters if not properly handled. First, in order to minimize the return loss at the excitation port the excited electrical field should be confined in the higher layers of the substrate. Obviously, the excited mode will not perfectly match the SW-SIW field distribution but it is possible to limit the errors by placing blind via holes directly in the port. Secondly, a de-embedding with longer access waveguides can be used to obtain more rigorous final results. Another argument for the implementation of the blind via holes in the excitation port is the fact that it reduces the cut-off frequency of the excited mode close to that of the fundamental SW-SIW mode. Without these via holes, the excited mode would be the TE_{10} in the uniform rectangular waveguide, which is evanescent at this frequency of operation (for a width W of 6 mm).

In this first version, the spacing s between the blind via holes is fixed at its initial value of 0.8 mm in order to maintain the expected slow-wave effect, and thus the guided

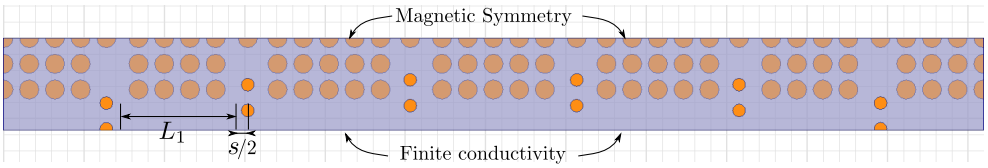

Figure 4.23 – Simulated structure for the SW-SIW filter in HFSS.

wavelength value. These via holes were arbitrary placed in each cavity starting from the center. For instance the first cavity, of length $L_1 = 4.4$ mm is filled with four rows. Obviously, this configuration introduces discontinuities at the coupling slots. These discontinuities are not taken into account in the synthesis, degraded results should therefore be expected.

4.3.1.4 First simulation results

The simulated S-Parameters of the synthesised filter presented in Figure 4.23 are illustrated on 4.24. As explained previously, the use of blind via holes in the ports provides a strong reduction of artificial return loss. In this simulation, no de-embedding was performed and the S-Parameters are re-normalized to the fixed impedance $Z_{ref} = 34\ \Omega$. This impedance is chosen because it provides low return loss in the simulations of slow-wave waveguides in this technology around 11 GHz. Of course, because of the ambiguity in impedance definition for non-TEM propagation, this numerical value depends on the definition adopted in HFSS, it is also not suitable for wide band simulation as dispersion is very strong for these kind of guided waves. During the optimization phase the approximation of a fixed impedance value in the selected frequency band is done for simplicity. The final results will however be obtained after a rigorous de-embedding.

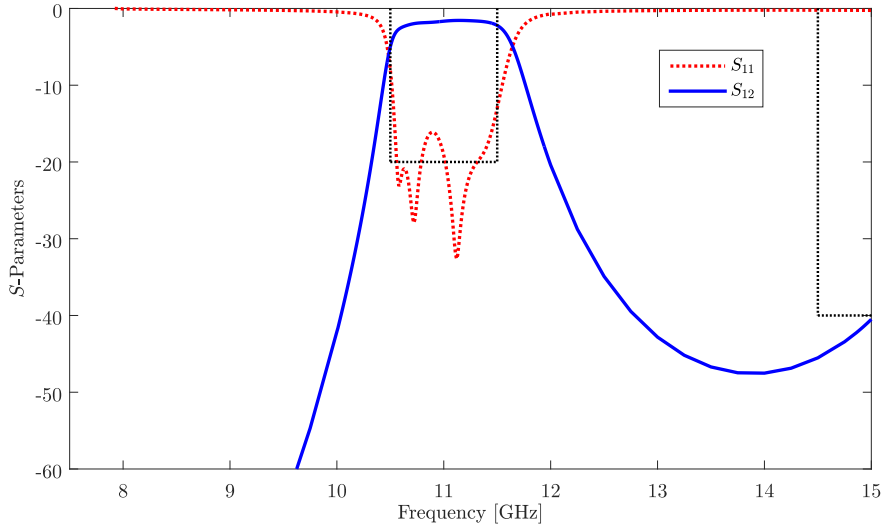

Figure 4.24 – S-Parameters of the simulated SW-SIW filter in HFSS.

The filter center frequency is close to the expected frequency of 11 GHz, 11.05 GHz more precisely. The bandwidth is reduced to 740 MHz compared to the expected 1 GHz, while an increased return loss is observed around 11.3 GHz. Finally, the five poles are not all visible, but the shape of transmission coefficient S_{21} seems to advocate that they are all in the passband.

The optimization procedure could start from this geometrical parameters, however it is highly possible that an important number of iterations would be needed. In order to design a first version closer to the optimum, the synthesis will be modified in the following section.

4.3.2 Homogenisation of the blind-via distribution

The filter is made of resonant cavities coupled by apertures. These cavities lengths, which are given by (4.11), are exactly half of the guided wavelength taking into account the apertures equivalent electrical lengths. In order to obtain the required length it is therefore necessary that between each aperture lies a uniform waveguide which supports a guided mode of phase constant β.

In the specific case of SW-SIW however, this phase constant is fixed at the very beginning of the synthesis by the spacing s between the blind via holes. Moreover, the computation of the cavity length assumes that it can be continuously arranged without taking care of the discrete loading of the cavity. Consequently, the calculated lengths have no reason to be an integer number of spacing s. Unless this spacing is changed, an extra discontinuity will automatically emerge at each slot proximity. For instance, the arrangement chosen for the first cavity of the previous filter is shown in Figure 4.25. The discontinuity in the longitudinal direction is clearly visible, with a distance of 1 mm between the slot and the first column of via holes, instead of 0.8 mm.

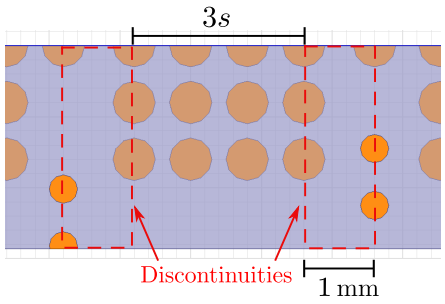

Figure 4.25 – First arrangement of blind via holes in the second cavity of the SW-SIW filter.

The introduction of these discontinuities do affect the filter response as they are not taken into account during the synthesis. First, the equivalent electrical length of each cavity is modified as the phase constant is not preserved from one slot to the other. Secondly, the structure of the electromagnetic field near the aperture is modified compared to that used in the extraction, potentially affecting the coupling

phenomenon and thus the bandwidth. In order to avoid these issues, a new method must be introduced which aims at satisfying the two following conditions:

- Minimise all discontinuities along the longitudinal path
- Maintain the proper resonance frequency of each cavity

To satisfy the first condition, it is necessary to distribute uniformly the blind via holes between the slots. The direct implication of this change is the necessary modification of the spacing s, and thus of the guided phase constant β. The second condition translated in terms of electrical length will provide for each cavity i the relationship between the new spacing s'_i, the phase constant $\beta(s'_i)$ and the number or columns of via holes N_i. This last condition is expressed by equation (4.17).

$$\beta(s'_i)(N_i+1)s'_i = \pi + \frac{1}{2}(\varphi_i + \varphi_{i+1}) \quad , i = 1..5 \tag{4.17}$$

In this equation, the physical length taken into account for each cavity is defined from one slot to the other, the reference planes for the extraction of the electrical length $\{\varphi_i\}$ are therefore positioned at the center of each slot. The reason for that is to minimise the variations of s, simply because the greater the length which will be affected by the change in β the smaller the change will be for a fixed electrical length target. The new goal is to find a solution to this equation while also satisfying fabrication constraints, especially the minimum spacings between via holes. In particular, the minimum spacing corresponds is defined by the distance between the copper lands, which cannot be lower than 100 µm (see Figure 4.26). Since this copper land radius is 200 µm larger than the hole diameter d_v = 400 µm, the minimum spacing s_{min} becomes 700 µm.

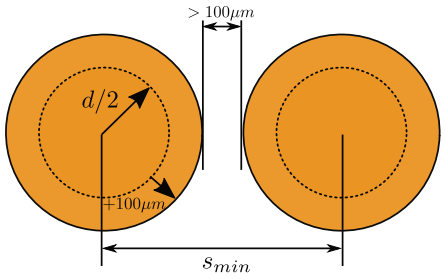

Figure 4.26 – Fabrication constraints regarding the blind via holes arrangement.

First, the phase constant β has to be precisely known for different values of s. A de-embedding algorithm with different sections of waveguides could be used to extract this variation but it would imply a large number of simulations. Furthermore, the accuracy of the phase determination in HFSS for complex structures is relatively low compared to amplitudes. The convergence criteria should thus be very strict. This accuracy could be increased by simulating very long waveguides but then it would once again become extensively time-consuming.

To obtain the phase constant rapidly with a good accuracy the "eigen-mode" solver is preferred. Based on the periodicity of the waveguide, only a single equivalent resonant unit cell needs to be simulated as in Figure 4.27. Additionally, to obtain sufficient variations of β the spacing s is simultaneously modified in the longitudinal and transverse directions.

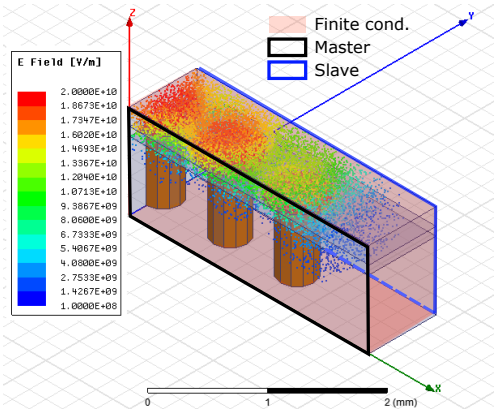

Figure 4.27 – Eigenmode simulation of a SW-SIW unit cell for the extraction of β.

Let's consider equation (4.17), the synthesis provides the phase term on the right, the idea is now to plot the term on the left as a function of s' and look for the intersections. A solution is defined by a pair of variables (N_i, s'_i), while $N_i \in \mathbb{N}$ and $s'_i \geq 700$ µm, where i stands for the cavity index. As the structure is symmetric, we will consider for this case $i \in [1;3]$. Finally, the spacing s is limited by the upper value of 900 µm in order to stay close to the initial value of 800 µm.

After extraction of β, the numerical resolution can be done, the obtained variations are illustrated in Figure 4.28.

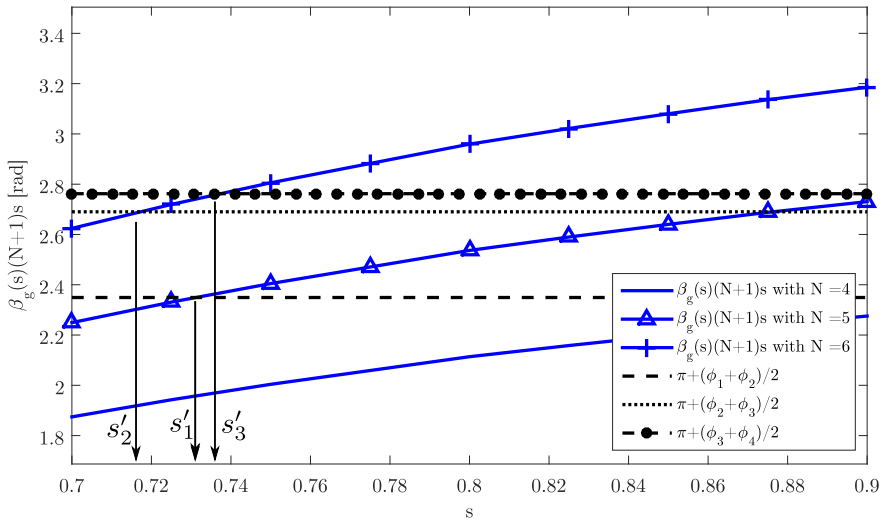

Figure 4.28 – Numerical resolution of the homogenisation procedure.

The obtained filter dimensions after homogenisation are listed in Table 4.7. It is important to notice that only the cavity parameters have changed during the homogenisation procedure (see Table 4.6), the slots are not affected.

Parameter	W_{s1}	W_{s2}	W_{s3}	L_1	L_2	L_3
Value [mm]	2.02	1.46	1.3	4.386 (6 x 0.731)	5.019 (7 x 0.717)	5.159 (7 x 0.737)

Table 4.7 – Synthesized dimensions for the filter in SW-SIW technology after homogenisation.

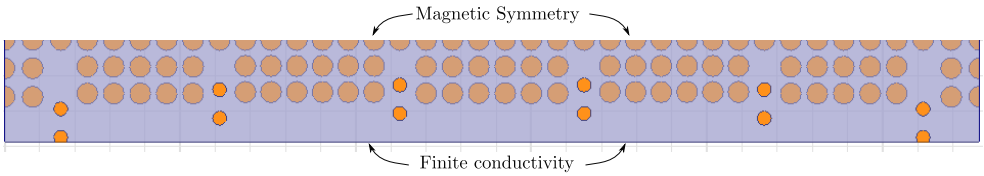

Figure 4.29 – Simulated SW-SIW filter after homogenisation.

Once all the new dimensions have been obtained, a complete simulation is realised with the geometry presented in Figure 4.29.

The simulated S-Parameters are shown in Figure 4.30. The center frequency is very close to 11 GHz. Regarding the bandwidth, the higher limit is perfectly matching the specification, the lower one if slightly shifted toward higher frequencies but a pole can be distinguished in this same region so after optimization it should be possible to have the good response.

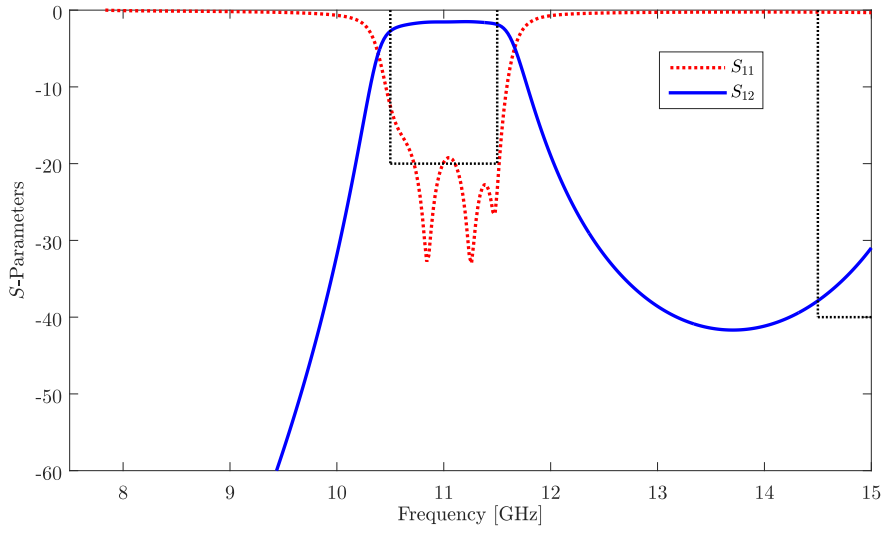

Figure 4.30 – S-Parameters of the simulated SW-SIW filter in HFSS after homogenisation.

4.3.2.1 Discussion on the homogenisation method

The core issue here is that because of the introduced relation between phase constant and via spacing, a degree of freedom is removed compared to the uniform waveguide case where cavity lengths and coupling can be adjusted separately. As a consequence, there is no certainty that a certain configuration will satisfy the specifications with a given via hole geometric configuration (diameter and spacing).

The method developed here removes the ambiguity of the number of via holes to place in each cavity depending on fabrication constraints. It also highlights the impact of the discretization. Indeed, the smaller s compared to the guided wavelength the less sensitive will be the synthesis to the number of via holes in the cavity. The mathematical term which translates this homogeneity is the electrical length of a single row of blind via holes. On the plot of Figure 4.28, this term is exactly the offset from one curve to the other (see (4.18)). Graphically, the smaller this phase shift the higher the probability that one curve crosses the targeted phase shift around the initial value of s. From the geometric point of view the good electrical length would thus be easily obtained by a very small variation of the spacing s.

$$\beta(s)Ns - \beta(s)(N-1)s = \beta s \tag{4.18}$$

One of the straight solution would then to set from the beginning a very small spacing compared to the guided wavelength. However, that would require thin via holes which are not always possible to fabricate. A trade-off has thus to be found between insertion loss, fabrication constraints, and specifications satisfaction.

In addition, in this method the mode impedance is slightly modified by the variation of s, and that is not taken into account. We assumed that the impedance variations were negligible for small variations of s. Furthermore, the overall synthesis would be much more complex if the impedance variations were taken into account, a trade-off between electrical length and impedance value would need to be found with probably a recursive procedure.

Finally, the developed homogenisation is not strictly limited to the SW-SIW structure. In fact, we believe it to be of interest for any coupled resonators topology which would be based on a periodical waveguide or transmission line in the limit of the distributed model.

4.3.3 Development of a segmentation algorithm for fast optimization

4.3.3.1 Motivations and general formulation

The two synthesis procedures described in sections 4.2.2 and 4.3 have for objective the definition of the filter geometrical dimensions which provide the closest response to the specifications. However, it is most of the time necessary to perform some iterative optimization to obtain the desired results. This last step of optimization can be time consuming, especially for higher order filters. Consequently, it seems interesting to implement a faster method for this task. We propose to use a segmentation of the problem using cascaded matrices. Obviously, such a method is especially useful for complex waveguides, such as the SW-SIW, this is why it is presented in this section.

A segmentation method has already shown great results in [44] but is was based on generalized scattering matrices.

The core of this method is the assumption that the full cascaded matrix of the filter can be accurately obtained by cascading elementary quadripole matrices which have previously been obtained. The ABCD matrix formalism will be used to translate this cascading operation. The segmentation strategy follows the decomposition used for the homogenisation, once again in order to minimise the variation of spacing between the via holes the reference planes are positioned exactly at the center of each slot. This decomposition is illustrated in Figure 4.31 for the SW-SIW filter.

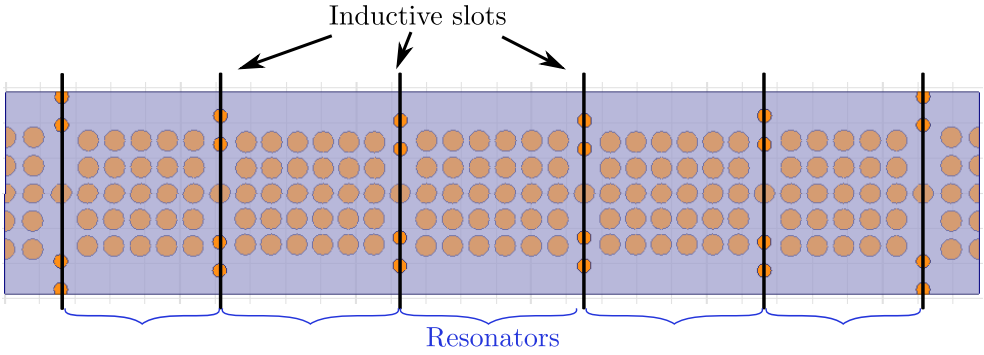

Figure 4.31 – Proposed segmentation of the SW-SIW filter.

The usefulness of this segmentation will depend both on the accuracy and speed at which the estimated filter ABCD matrix T_{est} can be obtained for a set of geometrical parameters (aperture widths and cavity lengths). If both speed and accuracy are realized, then a great number of parameter combinations can be tested and the optimum reached within a limited time.

Based on the cascading of ABCD matrices, the filter matrix T_{est} can be written as in (4.19). The aperture matrices are written A_i, where i varies from 1 to $n+1$ and are functions of the spacing on each side as well as the aperture width W_{si}. The resonators matrices are denoted R_i, where i runs from 1 to n, they are functions of the spacing s'_i as well as the number of via holes rows N_i. All of these dependences are not always written in order to reduce the amount of notations, this is also the case of the frequency dependence which affects all matrices.

$$T_{est}(W_0, ..W_n, s'_1, ..s'_n, N_1, ..N_n) = A_1 R_1 A_2 ... R_n A_{n+1} \tag{4.19}$$

The decomposition of T_{est} into the product of several matrices reduces the problem complexity because it distributes the geometric dependences on several blocks which can be computed more quickly. The idea is now to apply parametric variations on each of these blocks to obtain a massive number of filter response T_{est} in a short period of time. In order to obtain all of these blocks matrices, the straightforward method makes use of a de-embedding algorithm which would isolate the features of interest, namely slots or resonators. However, it will be shown in the following sections that more efficient methods can be applied.

4.3.3.2 Half-wavelength resonators

The resonators matrices will be extracted by a method which offers more flexibility than a straight de-embedding of all possible configurations but which tries to take advantage of the previously realized simulations during the synthesis.

First of all, let's precise the objective. By assuming that the periodical loading by blind via holes can be seen as distributed, each resonator can be considered as an homogeneous waveguide of length $(N_i + 1)s'_i$, propagation constant $\gamma(\omega, s'_i)$ and characteristic impedance $Z_0(\omega, s'_i)$ (see (4.20)). Consequently, the matrix computation for any combination of spacing and number of via holes only relies on the extraction of $\gamma(\omega, s'_i)$ and $Z_0(\omega, s'_i)$.

$$[R_i] = \begin{bmatrix} cosh\left(\gamma(N_i+1)s'_i\right) & Z_0 sinh\left(\gamma(N_i+1)s'_i\right) \\ \frac{1}{Z_0} sinh\left(\gamma(N_i+1)s'_i\right) & cosh\left(\gamma(N_i+1)s'_i\right) \end{bmatrix} \tag{4.20}$$

First, thanks to all previous simulations it is possible to avoid additional simulation for the extraction of $\gamma = \alpha + j\beta$. In fact, during the homogenisation procedure the variation of β as function of s was already extracted through parametric eigenmode simulations (see 4.27). The real part α of the propagation constant was set to 0.01 dB per millimeter taking into account the insertion loss obtained in the Thru and Line simulations.

Secondly, as already mentioned the characteristic impedance definition is ambiguous for non-TEM waveguides, this is not really an issue here as only relative variations compared to the access impedance are pertinent. For example, we can arbitrary assume that the access waveguides characteristic impedance is $Z_a = 50\Omega$ with a fixed spacing s_a, then by choosing one of the impedance calculation method the waveguide impedance for a given value of s'_i can be calculated by (4.21).

$$Z_0 = Z_a \frac{Z_0^{calc}(s'_i)}{Z_0^{calc}(s_a)} \tag{4.21}$$

The calculation method applied in this work was the average volumetric wave impedance Z_{vol} on the unit cell defined by (4.22), where V is the total considered volume. This definition was directly implemented in HFSS using the Field Calculator module and exported for each frequency and spacing values.

$$Z_0^{calc} = Z_{vol} = \frac{1}{V} \int_V \frac{|\boldsymbol{E}|}{|\boldsymbol{H}|} \tag{4.22}$$

Finally, in order to facilitate the evaluation of the resonator matrix for a given value of spacing s, polynomials fitting functions were used as approximations of Z_0 and β.

4.3.3.3 Coupling structures

The apertures matrices could as well be extracted by de-embedding of feeding waveguides. This technique was first implemented, however for reducing simulations time, a curve fitting approach was once again applied. In fact, during the synthesis procedure,

the extraction of the apertures as impedance inverters with electrical length compensation was already performed, thus it was decided to use the exact same data for the segmentation strategy.

In order to know the $[ABCD]$ matrix for a given aperture width W_s without having to simulate this specific value, polynomial functions of W_s, $\tilde{K}_p$ and φ_p were used to match the evolution of $\tilde{K}$ and φ. The polynomials expansion used in this process are not directly that of the synthesis. Indeed, for a better accuracy, these fitting functions were calculated in the vicinity of every value given by the synthesis, as only small variations are to be expected during the optimization.

Finally, the impedance of the compensation lines of electrical length $\varphi/2$ was assumed to be that of reference, ie. that of the access waveguides, arbitrary set to $Z_a = 50\Omega$. The estimated $[ABCD]$ matrix of a slot section can therefore be written as in (4.23).

$$[A_i] = \begin{bmatrix} cosh\left(j\frac{\varphi_p(W_{si})}{2}\right) & Z_a sinh\left(j\frac{\varphi_p(W_{si})}{2}\right) \\ \frac{1}{Z_a} sinh\left(j\frac{\varphi_p(W_{si})}{2}\right) & cosh\left(j\frac{\varphi_p(W_{si})}{2}\right) \end{bmatrix} \begin{bmatrix} 0 & j\tilde{K}_p(W_{si})Z_a \\ \frac{j}{\tilde{K}_p(W_{si})Z_a} & 0 \end{bmatrix} \begin{bmatrix} cosh\left(j\frac{\varphi_p(W_{si})}{2}\right) & Z_a sinh\left(j\frac{\varphi_p(W_{si})}{2}\right) \\ \frac{1}{Z_a} sinh\left(j\frac{\varphi_p(W_{si})}{2}\right) & cosh\left(j\frac{\varphi_p(W_{si})}{2}\right) \end{bmatrix} \tag{4.23}$$

4.3.3.4 Optimum determination

Starting from the value obtained by synthesis with homogenisation, each parameter was swept by a few percent resulting in several hundred thousands of filter response which have to be sorted out. After transferring the $[ABCD]$ matrices into their equivalent S-Parameters, the following strategy was adopted to efficiently select the solutions:

- Evaluation of the filter response on a limited (about 10) frequency points within the band of interest.
- Storage in a text file of the reflection coefficient S_{11} only in decibels (more than 100 Mo)
- Reading of all solutions and assignment of a cost function value for each one
- Selection of the optimum solution thanks to cost function minimum value determination

Before assigning the cost function value to any solution, a prior test for removing the response which does not have the proper bandwidth was done. This criteria is written as (4.24) and (4.25), where f_L and f_H stands for the lower and upper cut-off frequencies, respectively.

$$\left| dB\left(S_{11}^{opt}(f_L)\right) + 20 \right| \leq 1 \tag{4.24}$$

$$\left| dB\left(S_{11}^{opt}(f_H)\right) + 20 \right| \leq 1 \tag{4.25}$$

Once this first selection is done, the cost function is simply defined as the maximum return loss in the pass-band:

$$Cost(W_{01}, .., W_{23}, s'_1, .., s'_3) = \max_{f \in BW} dB(S_{11}) \tag{4.26}$$

Finally, the optimum parameters configuration is obtained for the response which minimise this cost (see (4.27)):

$$Cost([W_{01}, .., W_{23}, s'_1, .., s'_3]^{opt}) = \min(Cost) \tag{4.27}$$

Another criteria can be applied in order to avoid particular cases were one pole moved out of the band. If the pole is still at proximity of the cut-off frequencies it will lead to a change in the reflection coefficient slope. More precisely, two necessary conditions for the response to be validated are that the reflection coefficient must be a strictly decreasing function around f_L and strictly increasing one around f_H. As an example, the equation (4.28) can be implemented for the lower cut-off frequency, where Δf stands for the frequency step.

$$S_{11}^{opt}(f_L - \Delta f) > S_{11}^{opt}(f_L) > S_{11}^{opt}(f_L + \Delta f) \tag{4.28}$$

Obviously, other criteria could be used, as the number of visible poles in the selected band. One must however keep in mind that the most complex the criteria the more frequency points need generally to be used, especially for the poles detection as local minimums.

4.3.3.5 Results

The strategy described for the segmentation of the SW-SIW filter was applied after the homogenisation. The optimum combination of parameters is compared to that of the synthesis in Table 4.8. The relative variation does not exceed 2.7% and is lower than 1% for all parameters except one.

Parameter	W_{s1}	W_{s2}	W_{s3}	s'_1	s'_2	s'_3
After homogenisation [mm]	2.02	1.46	1.3	0.731	0.717	0.737
After optimization [mm]	2.01	1.42	1.29	0.724	0.720	0.742
Relative variation [%]	0.5	2.7	0.8	1	0.4	0.7

Table 4.8 – Comparison between synthesized and optimized dimensions for the filter in SW-SIW technology.

The optimized filter simulated S-Parameters in SW-SIW technology are illustrated in Figure 4.32. The calculated results obtained in MATLAB by segmentation are also depicted on the same plot. First of all, a good agreement between the two simulations is observed, which confirms the validity of the developed method. Also, the bandwidth

is very close to the one fixed in the specifications, with four clearly visible poles. A good matching is realised around 11 GHz with a maximum return loss of -24 dB. The slight difference between the segmentation and the full electromagnetic simulation is probably related to the uncertainty affecting all extractions performed for the segmentation. However, this method provides a non negligible gain in optimization time, even if some additional manual adjustment is required after that. Furthermore, the segmentation algorithm could also be used as a sensitivity analysis tool that could be used to visualize very quickly the influence of each physical parameter on the filter response.

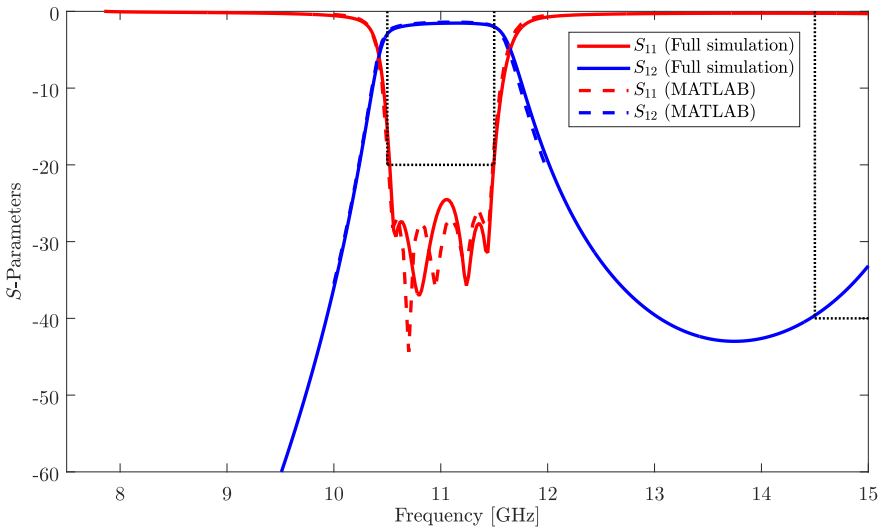

Figure 4.32 – Simulated S-Parameters of the filter in SW-SIW technology after optimization.

Finally, a last simulation with real lateral walls made of conductive via holes was performed to ensure the proper behaviour of the filter before fabrication. For this last step, the same de-embedding as previously was applied in order to obtain the good normalisation taking into account the impedance dispersion. The simulated structure along with the obtained S-Parameters are illustrated in Figure 4.33 and Figure 4.34, respectively. The intersection between the lateral via holes than can be observed was just authorized in HFSS for simplifying the geometry, it had no influence on the results. As one can see the replacement of the lateral walls by their concrete realization has no significant impact on the response, as the response is very close to that of the filter with lateral finite conductivity walls.

4.3.3.6 An alternative segmentation strategy for narrow-band filters

The segmentation strategy presented in the previous sections can be adopted for different topologies. However, for reduced bandwidth it was observed that this segmentation can lead to unsatisfying results. More precisely, the agreement between the segmented calculation and the full simulation was poor for a filter centered at the same frequency but with a reduced bandwidth of 500 MHz instead of 1 GHz. The resolution of this

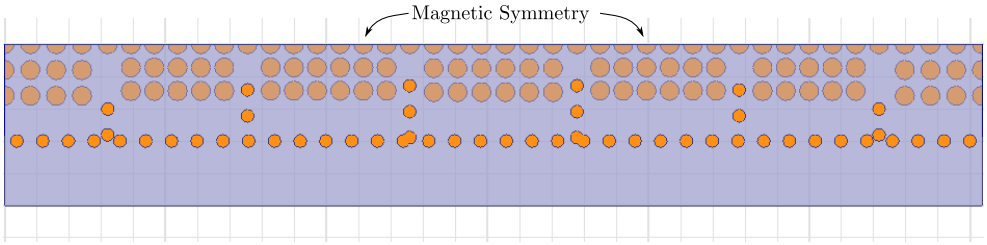

Figure 4.33 – Simulated final filter in SW-SIW technology.

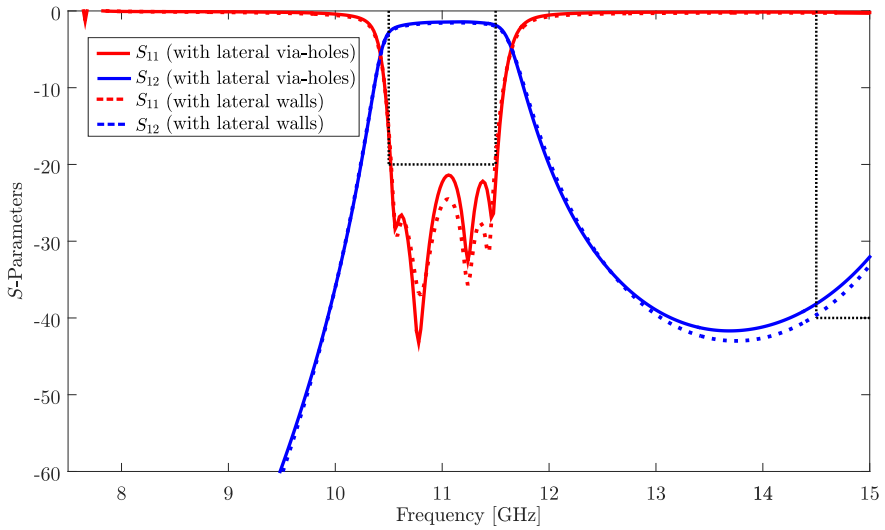

Figure 4.34 – Simulated S-Parameters of the filter in SW-SIW technology after optimization with real lateral walls.

issue with an improved segmentation method will be shortly detailed here.

In fact, before the optimization step the segmentation already does not provide an accurate representation of the full simulation, thus making the optimization step useless. The different S-Parameters obtained with full simulations and two different segmentation approaches are illustrated in Figure 4.35. These results show that the first version of the segmentation does not represent the return loss very well in the pass-band, especially its critical maximum value around 10.9 GHz. The second version of the segmented response is more accurate. The following paragraph will detail the new segmentation approach.

Several ideas were investigated concerning the reasons for this mismatch (precision of the extractions, misalignment of the reference planes etc...). It was found that a critical point is actually the context in which every slot has to be extracted. More precisely, in the previously described method the extraction of the slots model for the segmentation assumes that the slots are surrounded on each side by via holes positioned at an equal distance of 0.8 mm. In fact, this is not the case after homogenisation, because the via holes spacings are modified separately in each cavity, so the actual

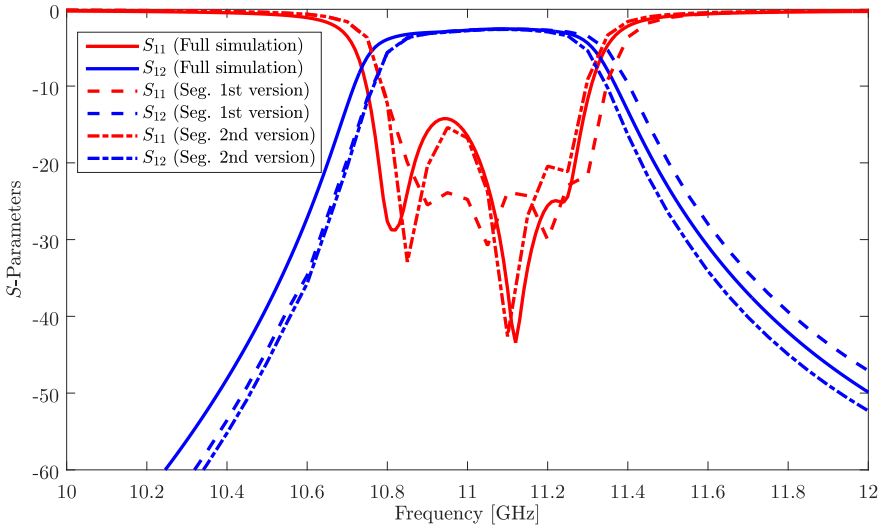

Figure 4.35 – Compared S-Parameters obtained for a 0.5 GHz bandwidth filter with the full-wave simulation, first and second segmentation methods.

coupling structure is asymmetric like the one given in Figure 4.36. For the 1 GHz filter, this had no critical influence on the overall response probably because of compensating errors.

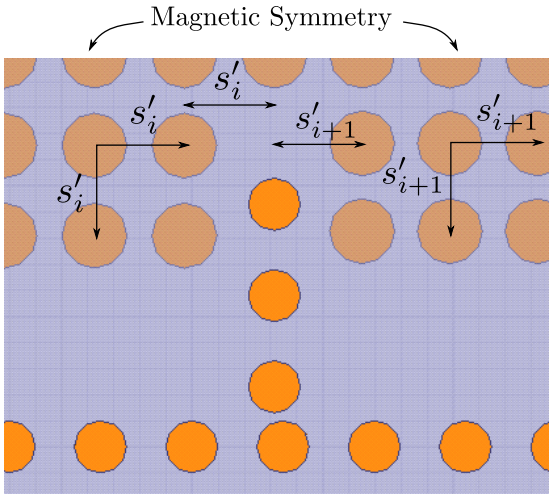

Figure 4.36 – Asymmetry of the inductive apertures after homogenisation.

By taking into consideration this asymmetry in the segmentation, the agreement with the full electromagnetic simulations is directly improved (see second version in Figure 4.35). Only the extraction of the slots is thus modified, by moving the reference planes further from the center, as depicted in Figure 4.37. That being said, the resonators matrix reconstitution can be very easily modified by reducing the length that has to be considered.

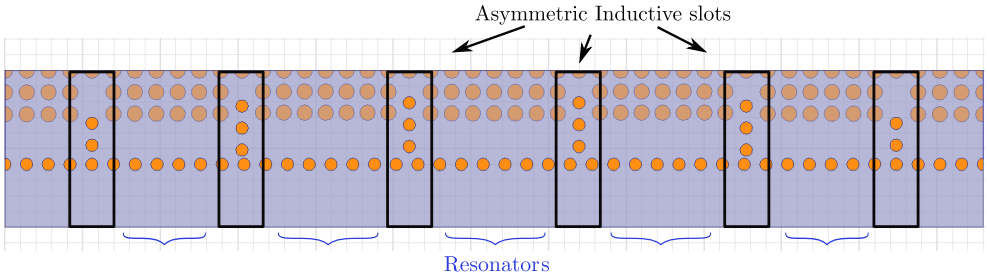

Figure 4.37 – Second version of the segmentation procedure taking into account the asymmetry of the coupling apertures.

Moreover, in order to avoid increasing dramatically the number of parametric simulations to be performed, the slot distance to the first row of blind via holes is not modified during the optimization, it is fixed to the value given by the homogenisation and the variation is only applied on the remaining rows. At the end of the synthesis, each cavity will therefore be defined by the initial spacing s'_i for the outer rows, and a modified spacing s''_i for the inner ones, as illustrated on Figure 4.38.

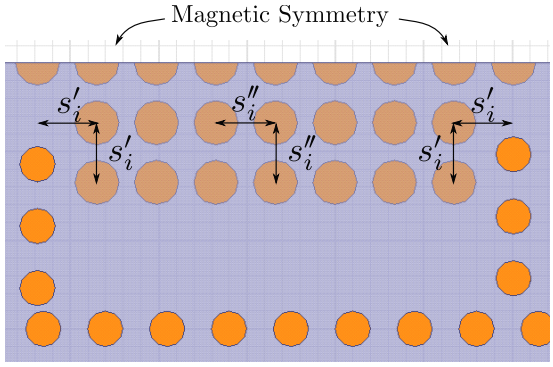

Figure 4.38 – Final parameters of the i-th cavity.

4.3.4 Algorithmic implementation

As already mentioned in the previous sections, the implementation of the filter design procedure was performed in the MATLAB environment. Also, several scripts were developed in order to interface MATLAB with HFSS for accelerating the procedure. Practically (see Figure 4.39), MATLAB is first used to write Visual Basic scripts which are then executed by Windows in order to execute commands in HFSS, it also provides the environment for the post-processing and related calculations. As a result, most of the work is done in MATLAB, only the geometry is at the beginning defined in HFSS. The simulation results (S matrices, field calculator numerical values, phase constant etc...) are transferred from HFSS to MATLAB via touchstones files (.SnP) or comma-separated-files (.csv) depending on the data type.

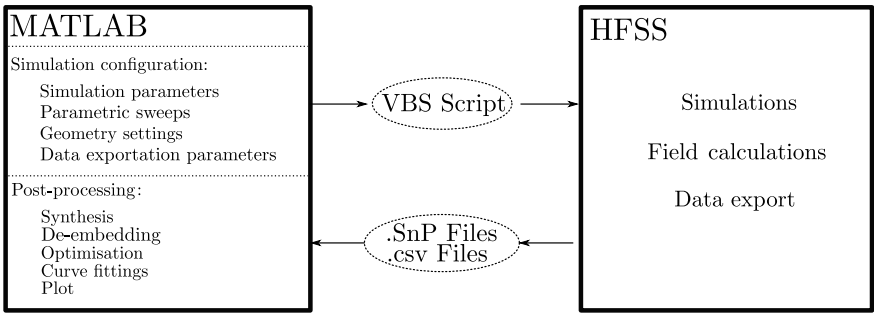

Figure 4.39 – General operation principle for the interface between MATLAB and HFSS.

For the synthesis procedure, we tried to minimise as possible the number of simulations to be run before obtaining the optimized response. Therefore, curve fitting techniques were used for most of the pertinent physical and model parameters. The synthesis in SW-SIW can be summarised by steps illustrated in Figure 4.40.

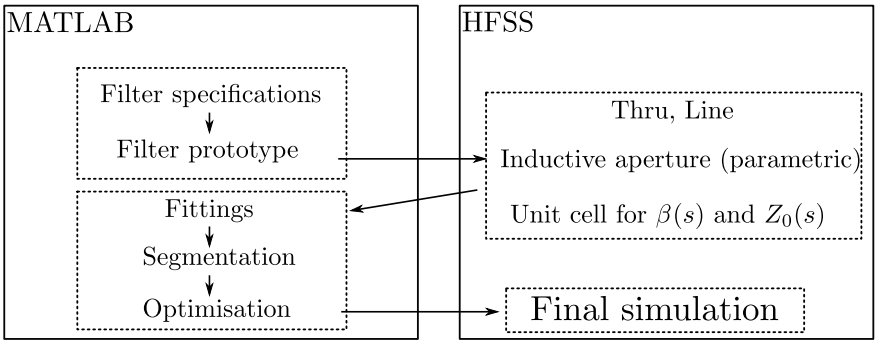

Figure 4.40 – General procedure for the full synthesis of the filter in SW-SIW technology.

First of all, the filter specifications have to be defined in MATLAB. Then, by applying the well-known filter theory, the filter prototype is then calculated and compared with simulations of physical structures in order to realise the synthesis. Two types of simulations have to be defined. On one hand Driven Modal solver is selected along with a de-embedding procedure for the extraction of the aperture model. In addition, the de-embedding provides the variations of the phase constant β which can be used for calculating the resonator lengths. On the second hand, a parametric Eigenmode simulation is performed on a single unit cell of waveguide for the segmentation and optimization procedure. For this last simulation, an equivalent impedance calculation is also implemented in the Field Calculator. Finally, the final filter can be simulated in HFSS.

4.4 Measurement results and perspectives

Several filters centered at 11 GHz were realised based on the developed synthesis approach. The specifications of these filters are listed in Table 4.9. In order to show different slot topologies, a second filter with a 0.5 GHz bandwidth was realised using slots without blind via holes. Also, the via holes dimensions for the 500 MHz bandwidth filters were reduced to $d_v = 0.3$ mm, $d_p = 0.5$ mm and $s = 0.7$ mm in order to be able to achieve a good return loss after homogenisation. The simulated and measured S-Parameters will be detailed in the following subsections.

Tech.	f_0 [GHz]	BW [GHz]	Order	L_{Ar} [dB]	L_{As} [dB]	f_s [GHz]
SW-SIW	11	1	5	0.04	-40	14.5
SW-SIW	11	0.5	5	0.04	-40	12.5
HM-SW-SIW	11	1	3	0.04	-30	15.5

Table 4.9 – Fabricated filters in SW-SIW technology.

All of these filters were measured using a two-port vector network analyzer Anritsu [45] 37369A with end-launch connectors. A Through-Reflect-Line calibration method was performed to set the reference planes at the input/output coupling structure. Also, broadband transitions were added between TEM access lines and integrated waveguides.

As it will be shown by the measurement results, a frequency shift was observed for all filters in SW-SIW technology. The analysis of the possible reasons for this frequency shift presented in the previous chapter also applies to this case and will thus not be presented here a second time. However, retro-simulations based on updated dimensions will be presented in section 4.4.4 in order to explain the observed shift.

4.4.1 5^{th}-order, 1 GHz bandwidth filter in SW-SIW technology

This first filter is the one that was introduced previously as example for the synthesis method in SW-SIW technology. The full fabricated structure is illustrated in Figure 4.41. The same kind of broadband transitions from G-CPW access lines to SW-SIW as for the couplers in Chapter 3 were used. After de-embedding, reference planes are positioned next to the first aperture.

Simulated S-parameters are compared with measured ones in Figure 4.42. The first observation is that the center-frequency is shifted toward the higher frequencies, it is indeed 11.24 GHz instead of 11 GHz in simulation. That being said, a very good correspondence is observed for the bandwidth, with 1.06 GHz versus 1.02 GHz in simulation. Concerning the matching, measured return loss is better than 15.5 dB between 10.7 and 11.75 GHz. Finally, insertion loss reaches a minimum of 1.9 dB while 1.55 dB was expected in simulation. The broadband response follows that predicted by the simulation.

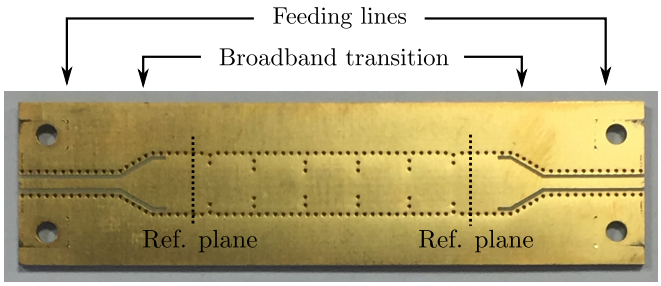

Figure 4.41 – Realised filter of 1 GHz bandwidth in SW-SIW technology.

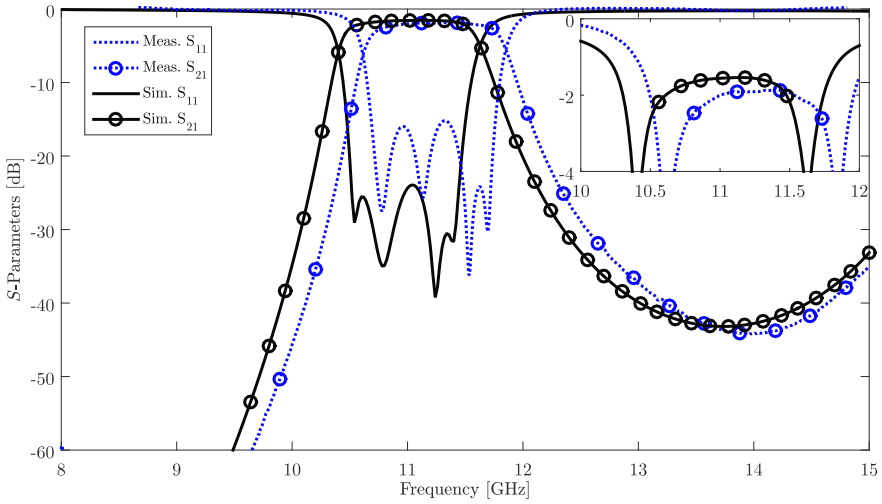

Figure 4.42 – Comparison between measurement and simulation for the 1 GHz bandwidth filter in SW-SIW technology.

4.4.2 5^{th}-order, 0.5 GHz bandwidth filter in SW-SIW technology

A second filter in SW-SIW technology is presented here. Compared to the previous one, the frequency bandwidth is reduced to 0.5 GHz with a rejection level more strict of -40 dB at 12.5 GHz. The photograph of the filter is not shown here as it is very similar to the first one. In order to achieve a good return loss within the passband, the blind via holes pitch s was reduced to 0.7 mm, thus providing more flexibility during the homogenisation procedure. Simultaneously, their diameter d was fixed at 0.3 mm alongside 0.5 mm copper lands. Simulated and measured S-Parameters are illustrated in Figure 4.43.

For this second filter, an asymmetry as well as a shift toward the higher frequencies are observed. However, a good return loss was achieved, it remains higher than 17 dB in the passband. A bandwidth of about 480 MHz centered at 11.38 GHz was obtained in comparison to the expected 500 MHz centered at 11 GHz. Finally, measured insertion loss is equal to -3.6 dB, which is 0.8 dB more than expected in simulation. The connectors were changed and precisely positioned but the symmetry was not recovered,

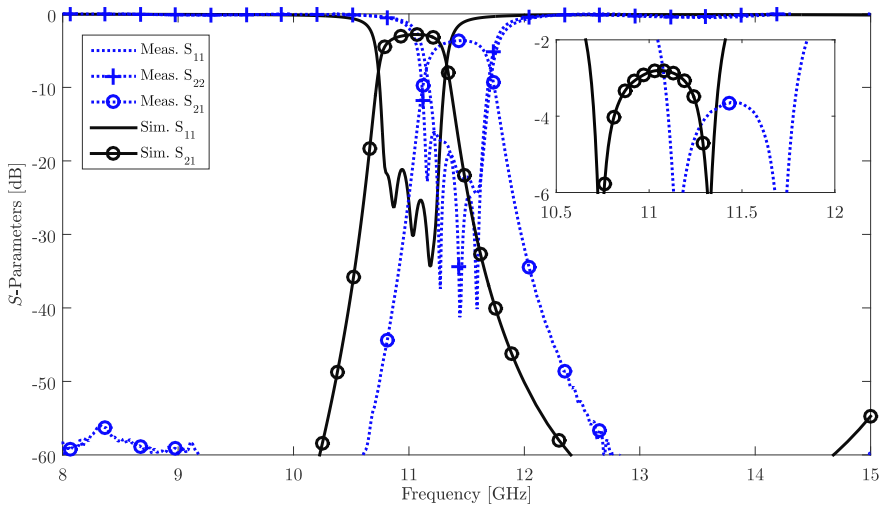

Figure 4.43 – Comparison between measurement and simulation for the 0.5 GHz bandwidth filter in SW-SIW technology.

the symmetry is therefore related to a fabrication issue.

4.4.3 3-rd order, 1 GHz bandwidth filter in HM-SW-SIW technology

This last filter is implemented in a different technology as the two previous ones. In order to show an even further miniaturization compared to the SIW technology, the half-mode principle was applied to the slow-wave technology. This is only possible because the fundamental mode of the SW-SIW exhibits the same magnetic symmetry as the quasi-TE_{10}, thus allowing the imitation of this magnetic wall by an open-circuit boundary.

The realised filter is illustrated in Figure 4.44, as for the SW-SIW technology broadband transitions were inserted in order to set the reference planes just next to the filter. A microstrip feeding line was preferred to the coplanar waveguide in this case.

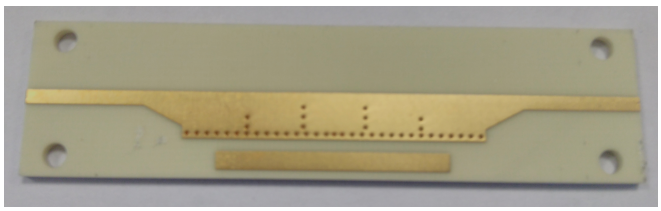

Figure 4.44 – Realised filter in half-mode SW-SIW technology.

Both simulated and measured S-Parameters are illustrated in Figure 4.45. Unfortunately, the de-embedding did not give any reliable results because of non negligible radiation losses of the Thru and Line devices. The measured and simulated S-Parameters presented here include feeding lines and transitions, as well as connec-

tors for the measured ones. The only difference between the two sets of results is therefore the influence of the end-launch connectors in the measurement. Insertion loss related to these connectors was estimated to about .6 dB by comparison with previous measurement results.

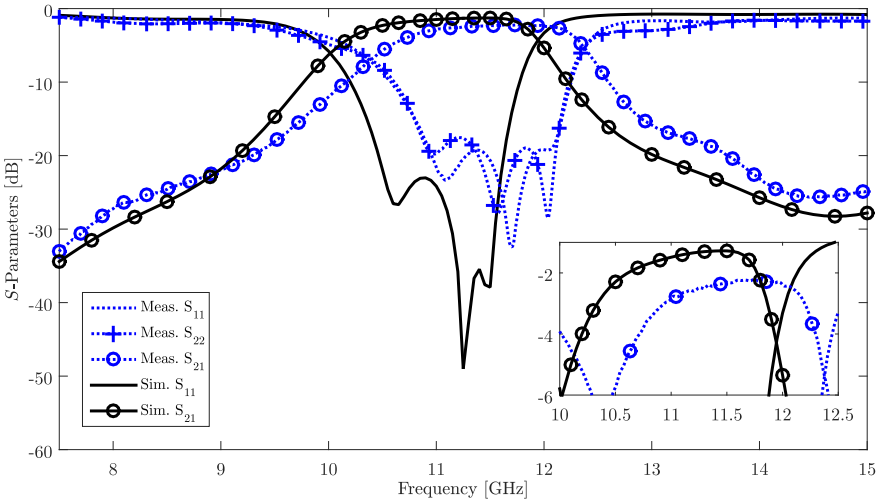

Figure 4.45 – Comparison between measurement and simulation for the 0.5 GHz bandwidth filter in SW-SIW technology.

It seems that the radiation is really affecting the filter response, with unexpected fluctuations below and above the passband. Also, a frequency shift is still observed. The fabricated filter is centered at 11.5 GHz with an absolute bandwidth of 1.22 GHz, instead of the simulated 1 GHz centered at 11 GHz. However, even if the filter response is shifted, the matching is very good with a minimum return loss of of 17.5 dB return loss within the passband. Finally, measured insertion loss reaches a minimum of 2.2 dB versus 1.3 dB in simulation. Considering the insertion loss related to the connectors a remaining .3 dB of difference is observed.

4.4.4 Retro-simulation based on fabrication issues and perspectives

All of the previous measurement results exhibited the same kind of variations compared to the simulation. First, the center frequency is systematically increased by 2 to 3.5%, with the largest shift observed for the most selective filters. Secondly, insertion loss is generally higher in measurement, especially for the full-mode filters (1 dB in excess).

The analysis of the process variation which was done for the couplers (see Table 3.8) is still valid in this context as all these circuits were fabricated at the same time. However, only the dimensions of the 400 µm via holes were studied in Chapter 3. The measured dimensions of the 300 µm used for the 0.5 GHz bandwidth filter are listed in Table 4.10. The same king of variations were observed as for the larger via holes, ie. both a significant diameter decrease and copper land increase.

All of these new geometric parameters were inserted in the simulations of the previously realised filters. The comparison for the 1 GHz bandwidth filter in SW-

	d_v	d_p	h_p
Initial	300	500	35
Measured (averaged, ±5 µm)	310	386	54

Table 4.10 – Measured versus simulated dimensions of the 300 µm diameter via holes.

SIW technology between the retro-simulation and the measurement is illustrated in Figure 4.46. This configuration of new geometric and physical parameters seems to provide a good explanation for the shift in frequency. Also, insertion loss difference is reduced to 0.2 dB by considering an increased copper surface roughness only.

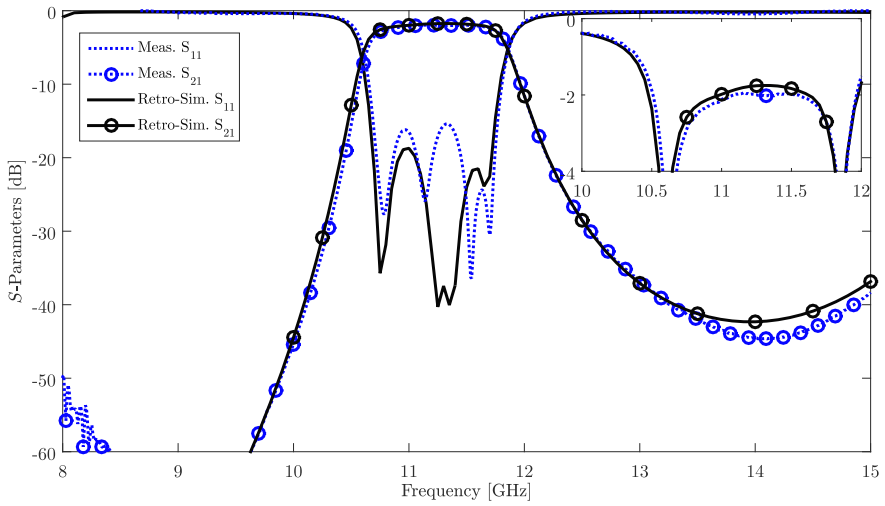

Figure 4.46 – Comparison between measurement and retro-simulation for the 1 GHz bandwidth filter in SW-SIW technology.

The results are compared in Figure 4.47 for the 0.5 GHz bandwidth filter, with reduced via diameter. The shift that was observed for this narrower filter is nearly completely recovered, especially in the higher part of the passband. In this case, the reduction of copper land diameter led to a higher resonant frequency via a lower slow-wave effect. Despite its thickness increase, the overall result is a reduction of the slow-wave effect.

Insertion loss difference is not fully explained by the surface roughness of the blind via, as a remaining .6 dB difference is observed. Finally, a good agreement is observed between the slopes of the transmission coefficient on each side of the selected frequency band.

Concerning the half-mode configuration, the frequency shift is nearly totally compensated if we look at the transmission coefficient. The reflection is still shifted of about 120 MHz. With the updated set of parameters, the minimum insertion loss is -1.4 dB is obtained at 11.9 GHz which is 0.2 dB lower than the expected value taking the connectors into consideration.

To summarize, a rather good agreement is observed for the center frequency in two

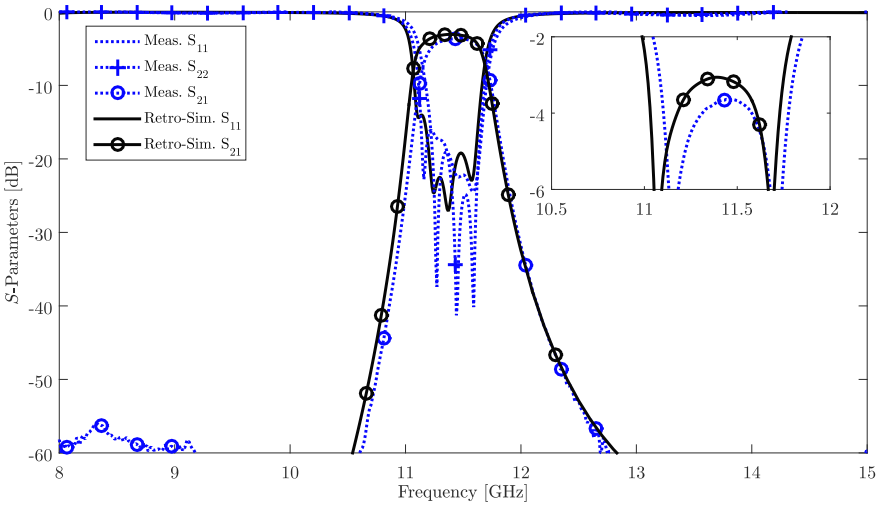

Figure 4.47 – Comparison between measurement and retro-simulation for the 0.5 GHz bandwidth filter in SW-SIW technology.

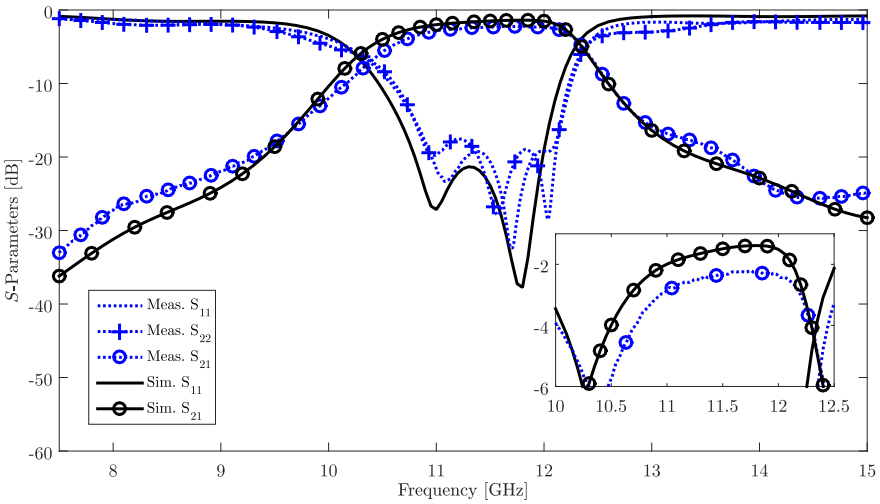

Figure 4.48 – Comparison between measurement and retro-simulation for the 1 GHz bandwidth filter in HM-SW-SIW technology.

of the three realised filters (1 and 3). A further reduction of d_p could actually be tried in order to reach the measured center frequency for the second filter with 0.5 GHz bandwidth. However because the initial frequency shift is different for the narrower filter a single value would not give the correspondence for all of the three filters. Finally, a correct correspondence for insertion loss was obtained but here again the discrepancy between filter responses is hard to explain with a single set of parameters. Further investigations concerning copper surface roughness might be conducted to improve the understanding of these variations.

To illustrate the miniaturization capability of slow-wave topology, the measured

Tech.	f_0 [GHz]	BW [GHz]	$Order$	IL [dB]	$Area/\lambda_0^2$
SIW (sim.)	11	1	5	1.1	2.15
SW-SIW(meas.)	11	1	5	1.9	0.68

Table 4.11 – Comparison between SIW and SW-SIW technologies for the 1 GHz bandwidth filter.

filter with a 1 GHz bandwidth was compared to its simulated SIW counterpart from section . For these two filters, the exact same specifications were targeted. The comparison results are given in Table 4.11. The slow-wave technology provides a division by 3 of the occupied surface, at the cost of a .8 dB increase in insertion loss. Further miniaturization could be achieved by using more complex filtering topologies, yet this work intends to demonstrate the area reduction obtained by only considering an additional slow-wave effect.

4.5 Conclusion

In this chapter, a novel design method for compact SW-SIW filters in ladder topology was presented. This design method was implemented in MATLAB environment along with the classical method for SIW. In particular, this design method aims at reducing both design time and complexity related to the periodicity of the waveguide. To do so, curve fitting techniques were used for the relevant parameters evolution as well as a segmentation strategy. An alternative design approach to reduce the impact of the periodicity was also developed, which could be extended to other waveguides having similar geometrical constraints.

To illustrate the design method, several passband filters were fabricated in X-band. Measurement results showed a good agreement with the simulation after taking into consideration fabrication variations.

Hence, the SW-SIW topology exhibits interesting miniaturization factor for resonant structures such as cavity filters. Future works could provide extension of this methodology to more complex coupling mechanisms with the use of coupling matrix for example.

References

[1] M. Bozzi, A. Georgiadis, and K. Wu, "Review of substrate-integrated waveguide circuits and antennas," *IET Microwaves, Antennas Propagation*, vol. 5, no. 8, pp. 909–920, June 2011.

[2] X.-P. Chen and K. Wu, "Substrate integrated waveguide filters: Design techniques and structure innovations," *IEEE Microwave Magazine*, vol. 15, no. 6, pp. 121–133, Sep. 2014.

[3] M. Bozzi, L. Perregrini, and K. Wu, "Direct determination of multi-mode equivalent circuit models for discontinuities in substrate integrated waveguide technology," in *IEEE MTT-S International Microwave Symposium Digest*, San Francisco, CA, June 2006, pp. 68–71.

[4] F. Cheng, X. Q. Lin, M. Lancaster, K. Song, and Y. Fan, "A dual-mode substrate integrated waveguide filter with controllable transmission zeros," *IEEE Microwave and Wireless Components Letters*, vol. 25, no. 9, pp. 576–578, Sep. 2015.

[5] M. Li, C. Chen, X. Zhang, and W. Chen, "Multi-mode bandpass filters using triangular half-mode substrate integrated waveguide," in *Proc. Progress in Electromagnetic Research Symposium (PIERS)*, Shanghai, China, Aug. 2016, pp. 3809–3813.

[6] W. Bo, Z. Xu, L. Hao, X. Meijuan, and L. Jiaxuan, "Substrate integrated waveguide cross-coupling filter with multilayer hexagonal cavity," in *Proc. International Workshop on Microwave and Millimeter Wave Circuits and System Technology (MMWCST)*, Chengdu, China, Oct. 2013, pp. 221–224.

[7] D. Jia, Q. Feng, Q. Xiang, and K. Wu, "Multilayer substrate integrated waveguide (SIW) filters with higher-order mode suppression," *IEEE Microwave and Wireless Components Letters*, vol. 26, no. 99, pp. 1–3, Aug. 2016.

[8] X. P. Chen, K. Wu, and Z. L. Li, "Dual-band and triple-band substrate integrated waveguide filters with chebyshev and quasi-elliptic responses," *IEEE Transactions on Microwave Theory and Techniques*, vol. 55, no. 12, pp. 2569–2578, Dec 2007.

[9] M. Pal and R. Ghatak, "A distinctive resonance: Multiband bandpass filter design techniques using multimode resonators," *IEEE Microwave Magazine*, vol. 16, no. 11, pp. 36–55, Dec. 2015.

[10] S. Saeedi, J. Lee, and H. H. Sigmarsson, "Tunable, high-q, substrate-integrated, evanescent-mode cavity bandpass-bandstop filter cascade," *IEEE Microwave and Wireless Components Letters*, vol. 26, no. 4, pp. 240–242, Apr. 2016.

[11] F. Mira, J. Mateu, and C. Collado, "Mechanical tuning of substrate integrated waveguide filters," *IEEE Transactions on Microwave Theory and Techniques*, vol. 63, no. 12, pp. 3939–3946, Dec. 2015.

[12] M.-Y. Chen, W. Hong, and M.-H. Ho, "Balanced BPF design of substrate-integrated waveguide cavity using hybrid microstrip/slot feed for CM suppression," *Electronics Letters*, vol. 50, no. 21, pp. 1533–1534, Oct. 2014.

[13] K. Zhou, W. Kang, and W. Wu, "Compact dual-band balanced bandpass filter based on double-layer SIW structure," *Electronics Letters*, vol. 52, no. 18, pp. 1537–1539, Aug. 2016.

[14] M. Bozzi, C. Tomassoni, and L. Perregrini, "Miniaturization of substrate integrated waveguide cavity filters," in *Proc. IEEE MTT-S International Conference on Numerical Electromagnetic and Multi-physics Modeling and Optimization (NEMO)*, Beijing, China, July 2016, pp. 1–2.

[15] P. Li, H. Chu, and R. S. Chen, "Design of compact bandpass filters using quarter-mode and eighth-mode siw cavities," *IEEE Transactions on Components, Packaging and Manufacturing Technology*, vol. 7, no. 99, pp. 956–963, Mar. 2017.

[16] Z. Liu, G. Xiao, and L. Zhu, "Triple-mode bandpass filters on csrr-loaded substrate integrated waveguide cavities," *IEEE Transactions on Components, Packaging and Manufacturing Technology*, vol. 6, no. 7, pp. 1099–1105, July 2016.

[17] S. Wang, D. Zhang, Y. Zhang, L. Qing, and D. Zhou, "Novel dual-mode bandpass filters based on siw resonators under different boundaries," *IEEE Microwave and Wireless Components Letters*, vol. 27, no. 1, pp. 28–30, Jan. 2017.

[18] U. Naeem and S. Bila, "Compact siw based multimode filters for future generation wireless front-ends," in *Proc. European Microwave Conference (EuMC)*, Paris, France, Sep. 2015, pp. 967–970.

[19] S. Sirci, M. A. Sanchez-Soriano, J. D. Martinez, V. E. Boria, F. Gentili, W. Bosch, and R. Sorrentino, "Design and multiphysics analysis of direct and cross-coupled siw combline filters using electric and magnetic couplings," *IEEE Transactions on Microwave Theory and Techniques*, vol. 63, no. 12, pp. 4341–4354, Dec. 2015.

[20] D. Lu, T. f. Yan, and X. h. Tang, "Compact quasi-elliptic combline filter in single-layered siw technology with two tunable transmission zeros," in *Proc. IEEE 17th Annual Wireless and Microwave Technology Conference (WAMICON)*, Clearwater Beach, FL, Apr. 2016, pp. 1–3.

[21] S. Sirci, J. D. Martinez, M. Taroncher, and V. E. Boria, "Analog tuning of compact varactor-loaded combline filters in substrate integrated waveguide," in *42nd European Microwave Conference*, Amsterdam, Netherlands, Oct. 2012, pp. 257–260.

[22] Z. Liu, G. B. Xiao, and L. Zhu, "A novel method to design triple-mode siw filter based on the complementary split ring resonators (csrrs)," in *Proc. IEEE MTT-S International Microwave Symposium (IMS)*, San Francisco, CA, 2016.

[23] W. Y. Park and S. Lim, "Miniaturized substrate integrated waveguide (siw) bandpass filter loaded with double-sided-complementary split ring resonators (ds-csrrs)," in *Proc. 41st European Microwave Conference*, Manchester, United Kingdom, Oct. 2011, pp. 740–743.

[24] Q. L. Zhang, W. Y. Yin, S. He, and L. S. Wu, "Compact substrate integrated waveguide (siw) bandpass filter with complementary split-ring resonators (csrrs)," *IEEE Microwave and Wireless Components Letters*, vol. 20, no. 8, pp. 426–428, Aug. 2010.

[25] L. Riaz, U. Naeem, and M. F. Shafique, "Miniaturization of SIW cavity filters through stub loading," *IEEE Microwave and Wireless Components Letters*, vol. 26, no. 12, pp. 981–983, Dec. 2016.

[26] D. Jia, Q. Feng, Q. Xiang, and K. Wu, "Multilayer substrate integrated waveguide (siw) filters with higher-order mode suppression," *IEEE Microwave and Wireless Components Letters*, vol. 26, no. 9, pp. 678–680, Sep. 2016.

[27] J. Garreau, B. Potelon, . Rius, J. F. Favennec, C. Quendo, C. Caille, H. Leblond, J. C. Azzara, and L. Raynaud, "Ultra-compact x-band siw filter in ltcc technology using high permittivity substrate for a space application," in *IEEE/MTT-S International Microwave Symposium Digest*, Montreal, QC, Canada, June 2012, pp. 1–3.

[28] T. Y. Huang, T. M. Shen, B. J. Chen, H. Y. Chien, and R. B. Wu, "Design of miniaturized vertically stacked siw filters in ltcc," in *Proc. European Microwave Conference (EuMC)*, Rome, Italy, Sep. 2009, pp. 413–416.

[29] H. Y. Chien, T. M. Shen, T. Y. Huang, W. H. Wang, and R. B. Wu, "Miniaturized bandpass filters with double-folded substrate integrated waveguide resonators in ltcc," *IEEE Transactions on Microwave Theory and Techniques*, vol. 57, no. 7, pp. 1774–1782, July 2009.

[30] R. Moro, S. Moscato, M. Bozzi, and L. Perregrini, "Substrate integrated folded waveguide filter with out-of-band rejection controlled by resonant-mode suppression," *IEEE Microwave and Wireless Components Letters*, vol. 25, no. 4, pp. 214–216, Apr. 2015.

[31] R. Zhang, Z. Wang, B. Yan, and R. Xu, "Fsiw cavity filter and derivative fsiw cavity and its filters with ltcc technology," in *Proc. Asia Pacific Microwave Conference*, Singapore, Singapore, Dec. 2009, pp. 1360–1363.

[32] C. Tomassoni, L. Silvestri, M. Bozzi, and L. Perregrini, "Novel substrate integrated waveguide filter based on mushroom resonators," in *Proc. IEEE 15th Mediterranean Microwave Symposium (MMS)*, Lecce, Italy, Nov. 2015, pp. 1–4.

[33] D. Pozar, *Microwave Engineering, 4th Edition*. Wiley, 2011.

[34] J. Hong and M. Lancaster, *Microstrip Filters for RF / Microwave Applications*. Wiley, 2004.

[35] D. Deslandes, "Etude et developpement du guide d'ondes integre au substrat pour la conception de systemes en ondes millimetriques," Ph.D. dissertation, Ecole Polytechnique, Montreal, 2005.

[36] G. Matthaei, L. Young, and E. Jones, *Microwave filters, impedance-matching networks, and coupling structures*. McGraw-Hill, 1964, vol. 1.

[37] D. Natarajan, *A Practical Design of Lumped, Semi-lumped & Microwave Cavity Filters*, ser. Lecture Notes in Electrical Engineering. Springer Berlin Heidelberg, 2012.

[38] I. Hunter and I. of Electrical Engineers, *Theory and Design of Microwave Filters*, ser. Electromagnetics and Radar Series. Institution of Engineering and Technology, 2001.

[39] R. Cameron, R. Mansour, and C. Kudsia, *Microwave Filters for Communication Systems: Fundamentals, Design and Applications*. Wiley, 2007.

[40] R. Levy, "A generalized design technique for practical distributed reciprocal ladder networks," *IEEE Transactions on Microwave Theory and Techniques*, vol. 21, no. 8, pp. 519–526, Aug. 1973.

[41] S. S. Park, S. T. Han, Y. M. Cho, D. H. Je, K. D. Kim, and D. C. Park, "Design of 40 ghz-band iris-type waveguide bandpass filter," *International Journal of Infrared and Millimeter Waves*, vol. 24, no. 6, pp. 941–951, June 2003.

[42] P. Souzangar and M. Shahabadi, "Numerical multimode thru-line (tl) calibration technique for substrate integrated waveguide circuits," *Journal of Electromagnetic Waves and Applications*, vol. 23, no. 13, pp. 1785–1793, Sep. 2009.

[43] MATLAB and E. Toolbox, *version 8.5.0 (R2015a)*. Natick, Massachusetts: The MathWorks Inc., 2015.

[44] J. A. Martinez, A. Belenguer, H. Esteban, and V. E. Boria, "Segmentation strategy for the efficient analysis and design of substrate integrated waveguide directly coupled cavity filters," *IET Microwaves, Antennas Propagation*, vol. 10, no. 3, pp. 283–287, Feb. 2016.

[45] Anritsu company. [Online]. Available: https://www.anritsu.com/en-GB/

Chapter 5

Integration of waveguides in advanced technologies for millimeter-wave frequencies

Contents

5.1 Introduction . . . 152

5.2 Analytical modelling of inhomogeneous integrated waveguides and numerical resolution . . . 153

5.2.1 The solution of Maxwell's equations in inhomogeneous rectangular waveguides . . . 154

5.2.2 Numerical resolution strategy and algorithm definition . . . 156

5.3 Validation of the implemented resolution . . . 162

5.3.1 The IHP HR-Si interposer technology . . . 162

5.3.2 The MnM interposer technology . . . 167

5.4 Design of test features on IHP interposer . . . 169

5.4.1 Broadband transitions from G-CPW to integrated waveguide . . . 169

5.4.2 0-dB and 3-dB Couplers . . . 173

5.5 Design of test features on the Nano-porous Alumina Membrane interposer as an alternative to the TSV process . . . 176

5.5.1 Broadband transition from G-CPW to integrate waveguide . . . 177

5.5.2 Other passive circuits . . . 178

5.5.3 Measurement results . . . 179

5.6 Prospects and conclusion . . . 185

References . . . 186

5.1 Introduction

Implementation of slow-wave integrated waveguides in advanced technologies such as silicon, glass, ceramic or even alumina membrane as we will see could be of high interest for the design of compact antenna arrays (including feeding network) or filters and diplexers at mm-wave frequencies. However, the integration of rectangular waveguides at mm-waves is still a subject of research and development with a limited number of realizations. Very recently, a metal surface roughness analysis was presented in D-band [1]. Also, an IC compatible silicon filled waveguide was introduced for operating frequencies around 35 and 77 GHz in [2]. The same team further developed antennas at 94 GHz [3]. Finally a air-filled cavity resonator was also fabricated at 36 and 66 GHz in [4]. Yet, as one can observe these proposed solutions do not rely on conventional technologies but are rather extensions above IC.

The main reason for that is the fact that integrating waveguides in conventional technologies back-end-of-line (BEOL) requires very large areas even above 100 GHz, resulting in costly solutions. Also, from the geometrical point of view material thickness's were chosen to provide a trade-off between cost and performance for integrated transmission lines such as microstrip, resulting in BEOL thickness from 5 to 10 µm for current advances CMOS/BiCMOS technologies. On the other hand, waveguide thickness is the key parameter for achieving low-loss waveguides, especially in the higher frequencies where dielectric losses are more and more negligible, 5 to 10 µm is clearly not sufficient to achieve high performance.

The interposer technology addresses both thickness and surface limitations. It would by construction provide thicker dielectrics with larger areas, thus paving the way for integrated waveguides. On the other hand, if occupied surface still needs to be reduced, slow-wave principles could be once again applied as at lower frequencies. However, if one considers blind metallic via holes as in PCB technology, reasonable losses could only be achieved with thick multi-layers structures. In that case the introduced slow-wave factor remains in the same order of magnitude. This kind of stack could probably be realized in the future using benzocyclobutene polymers (BCB), or even air-filled technologies.

Meanwhile, development of integrated waveguides on interposer is to our best knowledge still to be demonstrated. Also, as we will see integrated technologies fabrication processes often requires the use of different materials such as semi-conductors and oxide resulting in non-homogeneous structures. A theoretical analysis of this non-homogeneity consequences is therefore carried-out to provide a better understanding for the future developments. A numerical method is developed for the analysis of such waveguides in section 5.2. Then, this method is verified in section 5.3 for two different interposer technologies. In order to measure these waveguides, test features are designed for the mm-wave frequency bands in sections 5.4 and 5.5.

5.2 Analytical modelling of inhomogeneous integrated waveguides and numerical resolution

The relevance of integrating closed waveguides inside the interposers for mm-wave applications was established previously. In practice, for most interposers currently in use, the process mechanisms but also the electrical behaviour require that different materials are stacked together to form the substrate. As an example the Metal to Semiconductor interface is often avoided thanks to the insertion of an insulator layer (SiO_2, SiN etc...). Such a precaution is necessary to reduce the flow of DC current leakage through the substrate. However, as already observed for the coplanar waveguide, this configuration can have a significant impact on the high-frequency losses [5][6].

In the specific case of SIW in PCB, these modifications are not required as the dielectrics are rightly considered as perfect insulators. Therefore, homogeneous modelling of SIW prevailed in the last decade publications except for specific cases. However, the work presented in this chapter deals with integrated technologies, and therefore a multi-layer configuration must be considered.

The two configurations studied during this thesis will be more extensively described and analysed in sections 5.3.1 and 5.3.2. However in order to put the following analysis into context they are respectively illustrated in Figure 5.1 and Figure 5.2, namely the IHP High-Resistivity Silicon (HR-Si) interposer and the metallic-nano-wire-filled-membrane (MnM) substrate technologies.

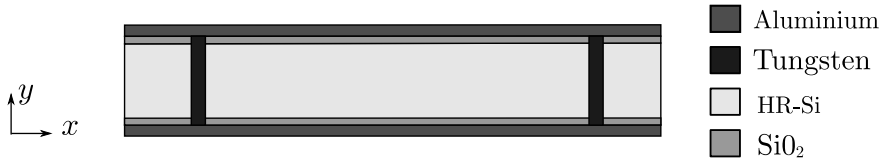

Figure 5.1 – Cross-sectional view of the IHP interposer technology for integrated waveguides.

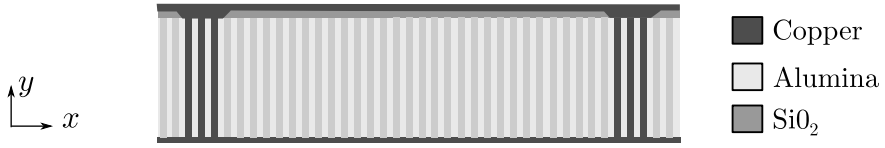

Figure 5.2 – Cross-sectional view of the MnM interposer technology for integrated waveguides.

For the two illustrated configurations, the waveguide is made of two horizontal copper or aluminum foils, vertically connected by Through-Silicon-Vias (TSV) or copper nano-wires. Furthermore, the waveguides filling materials are essentially silicon or alumina, but thin layers of silicon dioxide are used to isolate the metal from the former. For different process the requirements in terms of insulating materials can vary, therefore an interposer is generally made of other insulators as SiN for example.

The thickness's ratios involved in the interposers are quite large, as an example the silicon dioxide layers typical thickness is about 3 µm, while the total thickness is close to 70 µm. As a first approximation, one could assume that the induced variation of dispersion and field distribution can be neglected. Actually, because of new electromagnetic conditions that must be satisfied at the interface between the two different materials the solution to the Maxwell equations is strongly affected. As a consequence, we will see that the energy distribution is significantly different than that of the homogeneous waveguide.

5.2.1 The solution of Maxwell's equations in inhomogeneous rectangular waveguides

5.2.1.1 Context and currently used methods

The context of the following analysis is that of a rectangular waveguide made of perfectly conducting walls. The inner structure is made of an integer number of layers n, each one defined by its dielectric permittivity $\varepsilon_i = \varepsilon_{ri}\varepsilon_0$, where ε_0 stands for the dielectric permittivity of vacuum. We also assume that the dielectric losses are negligible, therefore taking ε_i to be a real number for each layer. The geometrical dimensions are given by the width of the waveguide W and the thickness's $(h_1, .., h_n)$. A schematic view of the waveguide is illustrated in Figure 5.3, the axis are defined in such a way that the interfaces lie in $y = C^{te}$ planes.

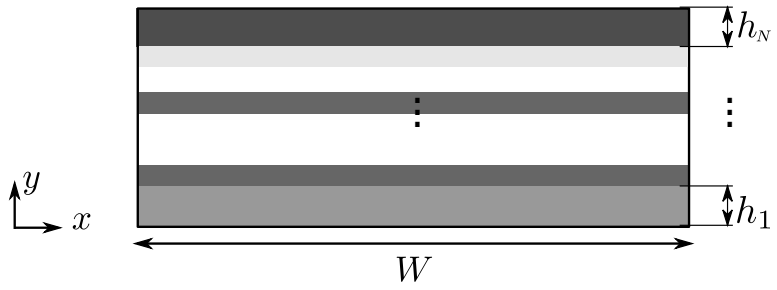

Figure 5.3 – Cross-sectional view of the numerical analysis context.

One can find several methods in the literature dedicated to the numerical resolution of waveguide having one or several dielectric slabs in it. In fact, the resolution of Maxwell equations in the case of inhomogeneous waveguide started in the 1950's [7]. Namely, one can classify the different methods in two categories. The first category is that of adapting dedicated methods that are commonly used in electromagnetism solvers to this specific topology. These methods are based on a proper meshing defining a set of spatial points at which a specific set of equations is solved by matrix computation. In that category lies a number of methods, among them the well-known Finite-Element-Method (FEM) [8] but also modal approximation technique [9].

On the other hand, some analytical work related to this topology has been done, it is well documented in [10]. In the case described in Figure 5.3, there is no need to introduce purely numerical analysis with a strong mesh dependant calculation. Indeed,

some theoretical considerations along with the use of a specific vector potential can reduce drastically the computation effort. In order to explain the solution to this problem, we should first define the set of modes.

5.2.1.2 Definition of the set of modes

First of all, this waveguide supports an infinite number of propagating modes as do all uniform waveguides. However, these modes do not exactly fit into the Transverse-Electric (TE) Transverse-Magnetic (TM) description often used in the homogeneous context. These modes can be somehow seen as a combination of TE and TM modes defined in each layers. Let's introduce an analogy to understand the new modes which will be introduced. Considering a loaded waveguide as in Figure 5.4, it can be demonstrated that the continuity condition at the interface between the hollow-waveguide and the dielectric part can be satisfied with TE only or TM only [10].

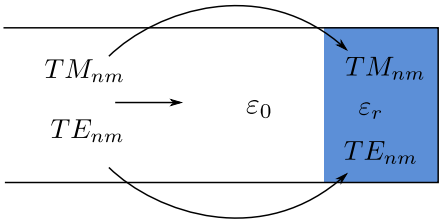

Figure 5.4 – Hollow waveguide loaded with a dielectric termination.

In the context of the inhomogeneous waveguide, it appears that the modes - which obviously satisfy all the interface conditions - can be defined as combinations of either TE or TM in each region, defined accordingly to the normal direction to the interface. A first set of modes is called Longitudinal-Section-Electric (LSE), as they are TE relatively to the interfaces. A second set of modes is called Longitudinal-Section-Magnetic (LSM), as they are TM relatively to the interfaces. For each of these kind of modes, an infinite number of solutions exists. As in the literature, they are designated thanks to integer indexes n and m to represent the order of variation along x and y-axis, respectively. The full set of modes is therefore represented by the LSM_{nm} and LSE_{nm}.

5.2.1.3 Introducing Hertz vector potential

The previously defined categories are therefore not TE or TM modes, as they might have non-zero component of both electric and magnetic field in the longitudinal direction. However, the modes can be considered as TE or TM modes in each layer considering the normal direction to the interface. This property is of great advantage, as the TE and TM modes can be deduced from Hertz potentials oriented in this same normal direction [10]. More precisely the TE modes are derived from the magnetic hertz potential $\mathbf{\Pi_m}$ and TM modes from the electric hertz potential $\mathbf{\Pi_e}$, respectively.

To summarize, the LSE modes are a combination of TE modes, obtained through the intermediate quantity $\mathbf{\Pi_m}$ oriented in the normal direction to the interface ((5.1)).

$$\boldsymbol{\Pi_m} = \phi_m \boldsymbol{e_y} \tag{5.1}$$

On the other hand, the LSM modes are a combination of TM modes in each layer, which can be obtained through the intermediate quantity $\boldsymbol{\Pi_e}$ oriented in the normal direction to the interface (see (5.2)).

$$\boldsymbol{\Pi_e} = \phi_e \boldsymbol{e_y} \tag{5.2}$$

The advantage of using such potential vectors relies mainly on two points. First, these vectors are one dimensional and therefore easier to manipulate than the complete $\boldsymbol{E}$ and $\boldsymbol{H}$ vectors. Secondly, these potentials are solution of the scalar Helmholtz equation in each region, which restricts dramatically the space of solutions as we will see below. Once these vectors are fully determined, the complete electromagnetic field can be retrieved through equations (5.3)-(5.4) for the LSE modes, and (5.5)-(5.6) for the LSM modes.

$$\boldsymbol{E} = -j\omega\mu_0 \nabla \times \boldsymbol{\Pi_m} \tag{5.3}$$

$$\boldsymbol{H} = \nabla \times \nabla \times \boldsymbol{\Pi_m} \tag{5.4}$$

$$\boldsymbol{E} = \nabla \times \nabla \times \boldsymbol{\Pi_e} \tag{5.5}$$

$$\boldsymbol{H} = j\omega\varepsilon(y) \nabla \times \boldsymbol{\Pi_e} \tag{5.6}$$

5.2.2 Numerical resolution strategy and algorithm definition

The overall strategy of the algorithm is illustrated in Figure 5.5. First of all both geometric and analysis parameters are specified by the user as input data. The former is made of W, h_1,...,h_n and the relative permittivities ε_{r1},...,ε_{rn}, it also contains the discretization grid number along the three axis N_x, N_y and N_z. Also, the the maximum targeted wave-number β along the propagation axis should be mentioned as well as a sequence of frequency points at which the fields should be stored in memory for further analysis. The dispersion diagram analysis is multi-modal, however the field computation is implemented for the first propagating mode only as the interposer technology would first be used in its mono-mode operation band for power transmission between the chips, antennas or any other passive component.

The first calculation step is that of the dispersion diagram (ω, β) through the Transverse Resonance Method (TRM) [11], which will be developed in 5.2.2.1. This computed values are then used as input for a second step which aims at defining the value of Hertz vector potentials at each grid points using the interface continuity conditions. Finally, the complex $\boldsymbol{E}$ and $\boldsymbol{H}$ fields are retrieved, Poynting vector $\boldsymbol{\Pi}$ is calculated as well as other derived quantities. If necessary, a normalisation in total transmitted power or peak electrical field value can be also performed.

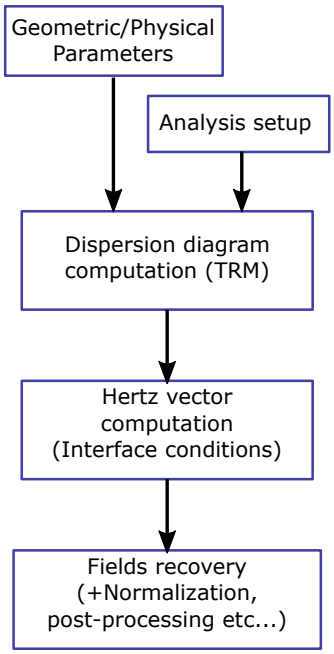

Figure 5.5 – SChematic view of the algorithm operation.

5.2.2.1 Dispersion diagram through the Transverse-Resonance-Method

The first step of the algorithm is the precise determination of the dispersion relation (ω, β), with β standing for phase constant along the longitudinal z-axis. The well established TRM method [11]- [12] was applied for its simple formulation and straightforward generalization to n layers. This method has been used prior to 1950's [13]. Its basis principle relies on the definition of a resonance condition expressed in the orthogonal direction to the power flow.

First of all, an equivalent transmission line transverse section is defined from the actual waveguide. Considering the i^{th} layer, the propagation constant along x and y-axis are written p_i and l_i, respectively. Also, wave impedances are denoted η^i_{te} and η^i_{tm}, for LSE and LSM modes, respectively. They are defined as $\eta^i_{te} = \omega\mu_0/l_i$ and $\eta^i_{tm} = l_i/(\omega\varepsilon)$. With all these notations, one can obtain the equivalent circuit given in Figure 5.6 as an example for the LSM propagation.

The resonance condition can be expressed as follows: the short circuit zero-value impedance at one end should be transformed to the same short circuit impedance value at the opposite end of the transverse section. That said, this impedance can be readily obtained numerically by applying well-known circuit theory [14]. Considering the impedance seen from the bottom short circuit condition Z_1, one can notice that its expression is dependent on a lot of physical and geometrical parameters: For this reason, a numerical evaluation is preferred.

$$Z_1 = Z_1(\omega, \beta, h_1, ..., h_N, l_1, ..., l_n) \tag{5.7}$$

If the resonance condition is satisfied, the impedance value, which is expressed by

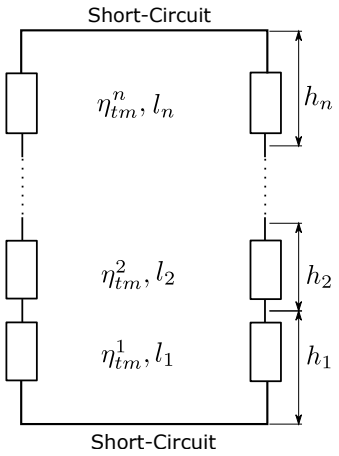

Figure 5.6 – Schematic view of the algorithm operation.

transforming the short-circuit from one end to the other through all the layers should be zero. Therefore, the resonance condition can be expressed as (5.8), with F being called the characteristic function, in that case we have chosen $F = Z_1$.

$$F(\omega, \beta, h_1, ..., h_n, l_1, ..., l_n) = 0 \tag{5.8}$$

One can further simplify this expression by using the wave-number space separation in each layer (see (5.9)). Furthermore, in the x-direction the wave-number p_i should be independent of i and identical to $m\pi/W$ to satisfy the boundary conditions at $x = 0$ and $x = W$, m being a strictly positive integer. This last property can be deduced from the boundary condition applied to the electric field vector $\boldsymbol{E}$ on lateral walls. For simplicity we will therefore write p instead of p_i.

$$\varepsilon_{ri}\left(\frac{\omega}{c_0}\right)^2 - \beta^2 = {p_i}^2 + {l_i}^2 \tag{5.9}$$

Together with these simplifications the resonance condition can therefore be expressed as (5.10).

$$F(\omega, \beta, h_1, ..., h_N, \varepsilon_{r1}, ..., \varepsilon_{rN}, m, W) = 0 \tag{5.10}$$

This last expression is finally a relation between ω and β only, considering all geometrical and physical parameters to be fixed, as well as m, which takes integer values only. The following iterative procedure is applied to solve numerically this problem:

- The phase constant β is set to 0 and characteristic function F is evaluated in order to find the first zero giving the cut-off angular frequency ω_c.
- $\beta \leftarrow \beta + \Delta\beta$ and the corresponding solution ω is found in the upper vicinity of the previous solution.
- The previous step is repeated until the specified maximum value of β is reached.

At the end of this procedure, the dispersion diagram is fully calculated for a given structure, considering a certain number of variations on the x-axis (m) and a specific type of mode, namely LSE or LSM. The higher order modes related to an increase in the variation along the y-axis can be obtained through the same procedure by ignoring the lower order solutions. Once the dispersion diagram is obtained, it can be used in the determination of the Hertz vector potentials.

5.2.2.2 Matrix resolution of the interfaces continuity conditions, the LSM case

We consider the LSM case for this part, since it will be shown later that the LSM_{11} is the first mode to propagate in the fabricated structures. Consequently, the calculation is based on an electric Hertz vector potential $\mathbf{\Pi_e}$, which is related to the fields through equations (5.5) and (5.6), respectively.

Considering a propagating wave along the longitudinal z-axis one can define this vector potential as given by (5.11), where ϕ_e defines the variations related to the transverse coordinates x and y.

$$\mathbf{\Pi_e} = \phi_e(x, y)e^{-j\beta z}\boldsymbol{e_y} \tag{5.11}$$

Also, as previously stated in 5.2.1.3, Hertz potential vectors are solutions of the Helmholtz vector equation (5.12), so that after variable separation one can give a more explicit form for ϕ_e in each region (see (5.13)).

$$\Big(\nabla^2 + k^2)\mathbf{\Pi_e} = 0 \tag{5.12}$$

$$\phi_e(x, y) = \Big[A_i \cos(l_i y) + B_i \sin(l_i y)\Big]\Big[C_i \cos(px) + D_i \sin(px)\Big] \tag{5.13}$$

Using the relation (5.5) one can readily show that $C_i = 0$ in order to satisfy the lateral metallic boundary condition. Then, by incorporating the arbitrary remaining constant D_i into the first term one can write ϕ_e as (5.14).

$$\phi_e(x, y) = \Big[A_i \cos(l_i y) + B_i \sin(l_i y)\Big] \sin(px) \tag{5.14}$$

Finally, in order to simplify the matrix resolution of the interface continuity conditions, this expression is arranged for each layer considering its specific location. First of all the sine variation along y is removed for the outer layer considering again the boundary condition in $y = 0$ and $y = H$, where H is the total height of the waveguide. Secondly, we introduce the elevation of each intermediate layer y_i, defined by (5.15). Then, for the potential function in each layer, the y coordinate is shifted by this elevation so that the boundary conditions at each interface are more easily expressed. The final expression for ϕ_e is given by (5.16).

$$y_i = \sum_{k=1}^{i-1} h_k \qquad , i = 2, .., n-1 \tag{5.15}$$

$$\phi_e(x,y) = \begin{cases} A_1 \cos\left(l_1 y\right) \sin\left(\frac{m\pi}{W} x\right) & 0 \leq y \leq h_1 \\ \left[A_i \cos(l_i(y-y_i)) + B_i \sin(l_{i-1}(y-y_i))\right] \sin\left(\frac{m\pi}{W} x\right) & y_i < y \leq y_{i+1} \\ A_n \cos\left(l_N(H-y)\right) \sin\left(\frac{m\pi}{W} x\right) & y_{n-1} < y \leq H \end{cases} \tag{5.16}$$

Now that an explicit form of $\mathbf{\Pi_e}$ has been determined, the interface continuity conditions can be applied to fix all arbitrary constants. Using equations (5.5) and (5.6) one can derive the two following relations (5.17) and (5.18) for the LSM_{nm} modes. The dual equations for the LSE_{nm} could also be readily obtained from (5.3)-(5.4).

$$E_x \propto \frac{\partial \phi_e}{\partial y} \tag{5.17}$$

$$H_z \propto \varepsilon(y) \phi_e \tag{5.18}$$

These two relations can be used to provide enough restriction at each interface to fully determine ϕ_e, and thus $\mathbf{\Pi_e}$. Indeed, from Maxwell equations it is established that both magnetic and electric field tangential components to the interface are continuous. Combining these informations with the two previous relations we now have two continuity relations at each of the $n-1$ interfaces, which is providing $2(n-1)$ linear equations. On the other hand, the number of arbitrary constants to be determined is exactly $2 + 2(n-2) = 2(n-1)$, i.e. 1 for each outer layer and 2 for each inner one.

Let's first consider relation (5.17). By evaluation at the first interface ($y = y_1$) it leads to (5.19), which is a linear equation with constant coefficients, the wave-number l_1 and l_2 being related to the previously calculated dispersion diagram by (5.9).

$$A_1 l_1 \sin(l_1 h_1) + B_2 l_2 = 0 \tag{5.19}$$

The second relation (5.18) leads to (5.20), which is once again a constant coefficient linear equation.

$$A_1 \varepsilon_1 \cos(l_1 h_1) - A_2 \varepsilon_2 = 0 \tag{5.20}$$

This procedure can be applied in the general case, and a much more efficient matrix formulation is introduced. At the end, the application of the continuity conditions reduces to the resolution of equation (5.21), where $[\mathrm{C}]$ is the $2(n-1)$-long column vector of all the unknown coefficients $[C] = \left[A_1, A_2, B_2, ..., A_n\right]$ and $[\mathrm{P}]$ is a complex matrix which sums up all interface conditions.

$$[P]\,[C] = 0 \tag{5.21}$$

The top of the interface conditions matrix was arbitrary chosen to contain the equations related to the continuity of the tangential magnetic field. Either H_x or H_z can be used for that purpose. Then, the second half of $[P]$ is related to the bottom part and describes the continuity of E_x. The analysis of these continuity relations was performed in the general case of n layers, leading to the following expressions. First, the top half of $[P]$ elements are defined in (5.22)-(5.24).

$$\begin{cases} P_{1,1} = \varepsilon_1 \cos(l_1 h_1) \\ P_{1,2} = -\varepsilon_2 \end{cases} \tag{5.22}$$

$$\begin{cases} P_{i,2i-2} = \varepsilon_i \cos(l_i h_i) \\ P_{i,2i-1} = \varepsilon_i \sin(l_i h_i) \quad , 1 < i < n-1 \\ P_{i,2i} = -\varepsilon_{i+1} \end{cases} \tag{5.23}$$

$$\begin{cases} P_{n-1,2n-4} = \varepsilon_{n-1} \cos(l_{n-1} h_{n-1}) \\ P_{n-1,2n-3} = \varepsilon_{n-1} \sin(l_{n-1} h_{n-1}) \\ P_{n-1,2n-2} = -\varepsilon_n \end{cases} \tag{5.24}$$

As stated before, the second half of $[P]$ is related to the continuity of E_x, it is given by (5.25)-(5.27). In order to avoid useless complicated expressions the layer number $j = i - (n-1)$ was introduced in (5.26).

$$\begin{cases} P_{n,1} = l_1 \sin(l_1 h_1) \\ P_{n,3} = l_2 \end{cases} \tag{5.25}$$

$$\begin{cases} P_{i,2j-2} = l_j \sin(l_j h_j) \\ P_{i,2j-1} = -l_j \cos(l_j h_j) \quad , n < i < 2n-1 \\ P_{i,2j+1} = l_{j+1} \end{cases} \tag{5.26}$$

$$\begin{cases} P_{2n-2,2n-4} = l_{n-1} \sin(l_{n-1} h_{n-1}) \\ P_{2n-2,2n-3} = -l_{n-1} \cos(l_{n-1} h_{n-1}) \\ P_{2n-2,2n-2} = -l_n \sin k_n h_n \end{cases} \tag{5.27}$$

As an example the interface matrix is given for a four layer configuration in (5.28). The upper half of the matrix is related to the continuity of H_x, while the bottom part concerns the continuity of E_x.

$$[P] = \begin{bmatrix} \varepsilon_{r1}\cos(l_1h_1) & -\varepsilon_{r2} & 0 & 0 & 0 & 0 \\ 0 & \varepsilon_{r2}\cos(l_2h_2) & \varepsilon_{r2}\sin(l_2h_2) & -\varepsilon_{r3} & 0 & 0 \\ 0 & 0 & 0 & \varepsilon_{r3}\cos(l_3h_3) & \varepsilon_{r3}\sin(l_3h_3) & -\varepsilon_{r4}\cos(l_4h_4) \\ l_1\sin(l_1h_1) & 0 & l_2 & 0 & 0 & 0 \\ 0 & l_2\sin(l_2h_2) & -l_2\cos(l_2h_2) & 0 & l_3 & 0 \\ 0 & 0 & 0 & l_3\sin(l_3h_3) & -l_3\cos(l_3h_3) & l_4\sin(l_4h_4) \end{bmatrix} \tag{5.28}$$

The last step of this procedure is the calculation of $[P]$ kernel (or null-space), this is done numerically through the determination of its smallest eigen-value. A maximum value for this eigen-value is fixed (below 10^{-1} generally) in order to control the accuracy of the calculation. Obviously, the eigen-space associated to this 0 eigenvalue should be of dimension one, therefore all constants can be calculated if one of them is fixed to an arbitrary value. A key parameter for this last calculation to be accurate is the

precision used in the dispersion diagram computation. Indeed, the relation between ω and β is used in the calculation of all the wave-numbers in the y direction through (5.9). If the accuracy in the dispersion diagram is not good enough, the eigen-value will not reach low values, with eigen-space dimension 0 or more than 1.

5.2.2.3 Transmitted power, losses contributions

Finally, the determination of the field quantities can be performed as the Hertz potential is fully known. In this computation, a fine spatial discretization is necessary in order to compute the curl operation in an efficient way. The mesh is therefore not used as the basis of the computation, it only serves for the final differential operations making the link between vector potentials and fields.

Several interesting physical quantities can now be obtained based on the previous results. The following expressions can be found in [15]. First, the time-averaged transmitted power P_t is calculated through the flux computation of Poynting vector in the cross-section, as in (5.29). This information can be used to normalize the field quantities to a certain amount of transmitted power. For that, one needs to divide $\boldsymbol{E}$ and $\boldsymbol{H}$ by the square-root of the computed flux value and then multiply by that of the desired transmitted power.

$$P_t = \iint_S \frac{1}{2} \mathrm{Re}\{\boldsymbol{E} \times \boldsymbol{H}^*\} \boldsymbol{dS} \tag{5.29}$$

Also, by considering low losses the different attenuation contributions can be obtained using the same equations as in Chapter 2 (see 2.2.3). A careful attention should however be given to the proper assignment of permittivity and loss-tangent in each different layers. From the computation point of view it implies that $\varepsilon = \varepsilon(y)$ and $tan\delta = tan\delta(y)$

5.3 Validation of the implemented resolution

Two different technologies will be introduced in the following sections. Obviously these two technologies provide ways to connect both top an bottom metal layers, so that the walls of the integrated waveguide can be realized. That being said, these two different technologies have very different fabrication processes.

5.3.1 The IHP HR-Si interposer technology

This technology is being developed at IHP (Leibniz-Institut für innovative Mikroelektronik), Frankfurt (Oder) in Germany. An existing collaboration with IMEP-LaHC aims at developing innovative solutions for mm-wave interposers. Through the development of integrated waveguides applications such as antenna arrays, feeding networks and filters are targeted.

Let's now introduce the technology itself. A simplified 3D schematic view as well as a detailed cross-sectional view are illustrated in Figure 5.7. The bulk material is a high-resistivity silicon ($h_{Si} = 70\,\mu\mathrm{m}$, $2\,\mathrm{k\Omega.cm} \leq \rho \leq 10\,\mathrm{k\Omega.cm}$, $\varepsilon_r = 11.9$). Two thick aluminum layers, namely TM1 and TM2 can be used for the top metal cover ($2\,\mu\mathrm{m}$ and

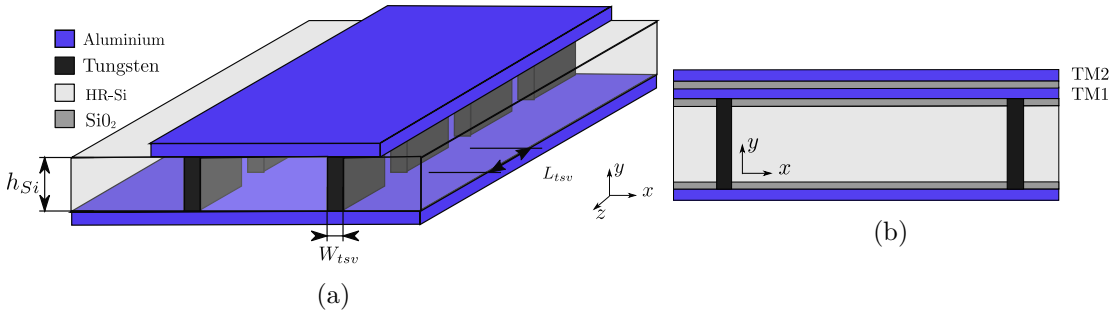

Figure 5.7 – IHP interposer technology: (a) Simplified 3D view, (b) Detailed cross-sectional view.

3 µm resp., $\sigma = 38\,\mathrm{MS.m^{-1}}$). Also, 2 µm of silicon dioxide ($\varepsilon_r = 3.9$, $\tan\delta = 0.0024$) insulates TM1 from the high resistivity silicon as well as TM1 from TM2. The back metal layer is also made of aluminum, it is 3 µm-thick and similarly insulated from the silicon by a dioxide layer of 2 µm.

The metallic walls are realized by tungsten trenches ($\sigma = 18.6\,\mathrm{MS.m^{-1}}$) derivated from the TSV technology. They are insulated from the silicon with a 2.5 µm silicon dioxide barrier. The penetration skin depth at 100 GHz in tungsten reaches 370 nm, these 3 µm are therefore sufficient to keep the conductive losses at a minimum and provide an efficient metallic boundary above this frequency. Finally, trenches dimensions W_{tsv} and L_{tsv} are fixed by the process at 3 and 50 µm, respectively. As a result a fully closed structure can be realized.

The conductivity of the high-resistivity silicon is interpreted as a frequency-dependant loss tangent given by (5.30) [15]. As an example estimated loss tangents are given in Table 5.1 versus frequency for a conductivity of 5 kΩ.cm.

$$\tan\delta = \frac{\sigma}{\omega\varepsilon_0\varepsilon_r} \tag{5.30}$$

Freq. [GHz]	50	100	150	200	250	300	350
$\tan\delta(\times 10^{-4})$	6	3	2	1.5	1.2	1	0.9

Table 5.1 – Equivalent loss-tangent for High Resistivity Silicon (σ =5 kΩ.cm)

The first top metal layer was chosen for the top cover of the integrated waveguide. This was made to avoid the presence of metallic dummies inside the waveguide, which would have been necessary for density reasons if TM2 had been used for the top cover. In this configuration, the second metal layer TM2 has not much influence, since TM1 is acting as a shield.

The algorithm developed for inhomogeneous waveguides was applied to this topology. The targeted frequency bands, as well as the design considerations will be detailed in section 5.4, the goal of this first application is to demonstrate the operability of the algorithm for one of the fabricated waveguides. Let's consider an intermediate waveguide band as WR3, i.e. the 220 GHz-325 GHz frequency band. The lateral width

was chosen so that only the first propagating mode would address all these frequencies. Then, assuming a cut-off frequency close to that of the TE_{10} in an homogeneous waveguide made of HR-Si ($\varepsilon_r = 11.9$) it was fixed to $W = 250\,\mu m$, leading to an estimated cut-off frequency of 174 GHz. Finally, is was considered useless to introduce an effective width for this waveguide as the spacing between the TSV is only 5 µm.

First, the dispersion diagram obtained for the six first propagating modes is shown in Figure 5.8. The first propagating mode is the LSM_{11}, having $k_x = \pi/W$ and k_y being associated to the lowest frequency solution found in the transverse resonance method. The reason behind the fact that the LSM modes propagates at lower frequency is that the LSE modes have by definition no electric field component normal to the interface, namely E_y. That being said, the only remaining components E_x and E_z have to vanish on the top and bottom horizontal walls. In this configuration the waveguide is much larger than thick, so assuming close values for propagation velocities in x and y directions the cut-off frequency of the first LSE mode is significantly higher than that of the LSM_{11}.

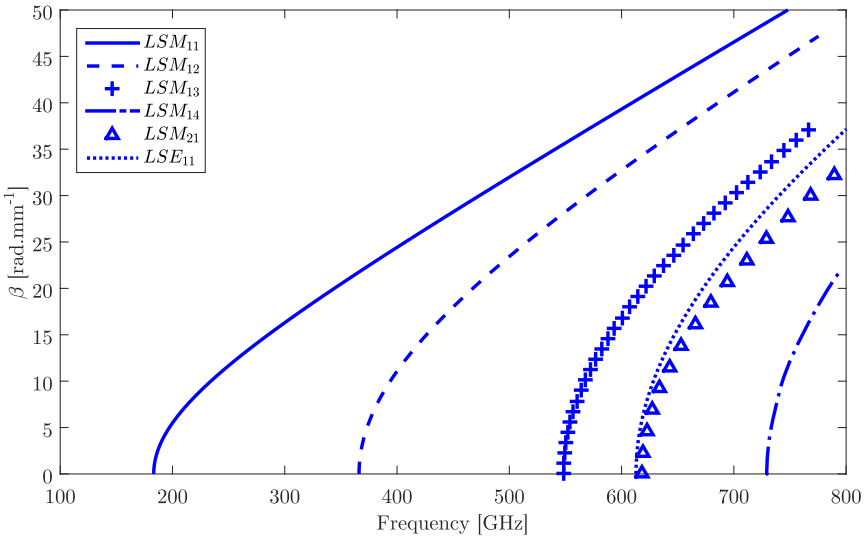

Figure 5.8 – Dispersion diagram for IHP interposer integrated waveguide.

In fact, only LSM_{nm} modes are solutions of the transverse resonance condition until the first LSE_{11} mode starts propagating at about 612 GHz. In reality, the LSE mode would probably not propagate because of the non-uniform metallic boundary on the lateral walls. As already demonstrated for SIW in PCB technologies the longitudinal currents associated with the vertical magnetic field cannot be carried by discrete vertical conductors. These discontinuities produce a strong radiation of the TM modes as mentioned in [16].

Finally, the cut-off frequency of the LSM_{11} was found to be 183.3 GHz, which is slightly higher than the previously calculated one with only silicon considered. It was noticed that a more accurate estimation of the first cut-off frequency can be obtained by considering the weighted geometric average permittivity $\bar{\varepsilon}$ (5.31), in that case it

gives 180.1 GHz. The second order mode cut-off frequency is found to be 366 GHz, which is twice as much as the first one. This leaves a mono-mode bandwidth as great as in homogeneous rectangular waveguides.

$$\bar{\varepsilon} = \left(\prod_{i=1}^{N} \varepsilon_i^{h_i}\right)^{1/\sum_{i=1}^{N} h_i} \tag{5.31}$$

The field component complex magnitudes were obtained after running the algorithm for the first propagating mode, they are illustrated at 270 GHz in Figure 5.9. In this computation, 50 points were used on x-axis and 250 on y-axis, more precisely 230 for the silicon and 10 for each layer on dioxide. With this ratio, the discretization is nearly the same for all the three regions. Also, a unitary power normalization was applied so that the overall transmitted power is 1 Watt.

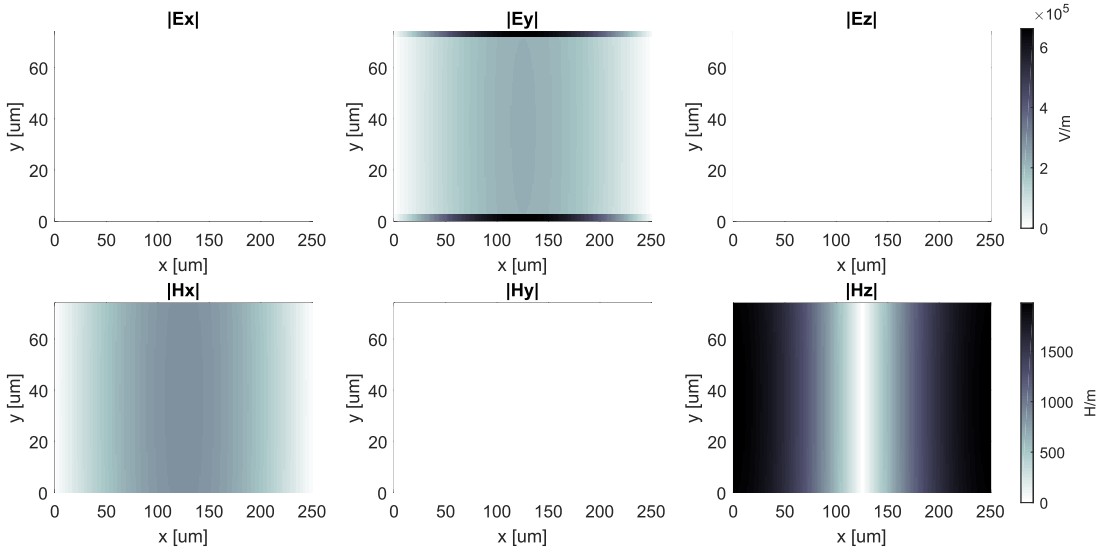

Figure 5.9 – Field magnitudes in IHP technology obtained at 270 GHz.

As one can see in Figure 5.9, field distribution is relatively different from that of the TE_{10} mode that would propagate if only the two thin layers of silicon dioxide were removed. Also, its amplitude is much greater in the lower permittivity layers, i.e. the silicon dioxide layers. The physical reason behind that is the continuity of the normal component of the displacement vector $\boldsymbol{D}$ at any dielectric interface between two regions 1 and 2 (5.32). This relation imposes the ratio between the electric field components on either side of the interfaces to be the inverse of the permittivities ratio. Finally, the main component of electric field is vertical as for the TE_{10}.

$$\varepsilon_1 \boldsymbol{E_1} = \varepsilon_2 \boldsymbol{E_2} \tag{5.32}$$

The magnetic field distribution is very close to that of the TE_{10}, except that a small variation in the vertical direction is noticeable. It is worthwhile noting that the magnetic vector has no component normal to the interface, i.e. $H_y = 0$. This is coherent with the fact that this first propagating mode is of LSM type.

Finally, attenuation and phase constant are compared with the results of a full-wave Finite-Element commercial software for the first mode. Two different solvers are used in HFSS to obtain these results, a conventional "driven-modal" mode which computes S-Parameters and an "Eigen-mode" equivalent cavity calculation [17]. Without re-normalisation, the former provides directly the propagation constant through the insertion loss parameter S_{21} for a given length of waveguide. The latter calculates directly the dispersion relation while the attenuation can then be obtained through the derived group velocity. The results are illustrated in Figure 5.10 for both α and β. The curve obtained with only dielectric losses is also included, it shows that the proportion between the conductive and dielectric losses are well represented by the developed algorithm.

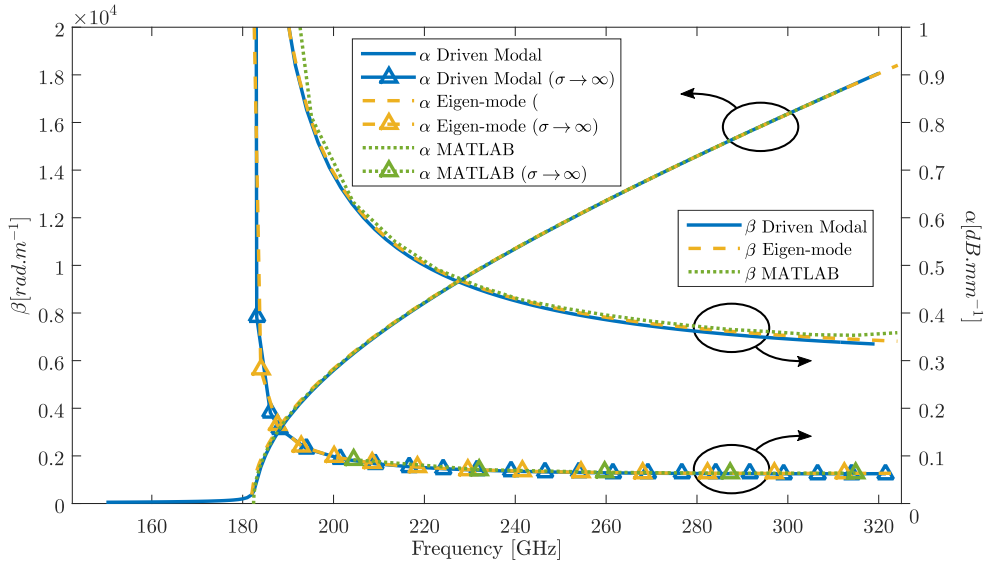

Figure 5.10 – Implemented algorithm versus commercial software for the evaluation of propagation constant in IHP technology.

First of all one can notice the very good correspondence in the phase constant value between all methods. Also, the values of attenuation are very close, in this case, a grid of 200 by 120 by 30 (on x, y and z axis, resp.) in MATLAB is enough to reach a maximum relative error of 5%. The proportion between conductive and dielectric dissipation is also properly represented by the algorithm because the correspondence is maintained with perfect walls ($\sigma \to +\infty$). Interestingly, the attenuation is mainly due to the conductive losses on the metallic walls, in fact for the WR-3 band it represents 80 to 85% of the total. Several reasons can be given for that observation. First the waveguide width is about 3.5 times its height, which is far from being the optimum ratio of 2 for broadband operation [15]. Also, even if the dielectrics are not perfect the contribution of the silicon is a decreasing function of the frequency (5.30) and the silicon dioxide is a relatively low-loss material. In fact, such a conclusion could also be carried out for homogeneous waveguides at these frequencies. Indeed, the inhomogeneity of the cross-section does not change significantly the magnetic field distribution in that

case, so the current distribution is very close to that of a TE_{10}.

5.3.2 The MnM interposer technology

This technology was developed in collaboration with Sao Paulo University, Brazil. The overall idea is to address millimetre-wave transceiver technologies with a new solution for low-cost and high-performance interposer. In fact, the fabrication process differs from that of the conventional silicon interposer in the sense that the bulk material is an already available commercial nano-porous alumina membrane, therefore reducing significantly fabrication costs. Furthermore, the nano-pores can be filled with metal (copper in this case) to provide top to bottom connections. It has already demonstrated good performance for metallic via design [18] but also high quality factor slow-wave transmission lines [19]-[20].

Let's first describe in details this technology, it is illustrated in Figure 5.11. The figure is not to scale, copper nano-wires ($\sigma = 58\,\mathrm{MS.m^{-1}}$) are in reality cylinders of 55 nm diameter, distant from each other by 143 nm. The membrane thickness h_a is 50 µm, it is made of anodic aluminum oxide (AAO), the relative dielectric constant was assumed to be about 7.6 by considering previous results [20]. The loss tangent should be very low in practice as alumina is known for its good dielectric properties [21]. An arbitrary value of 0.001 was chosen for the computation but only experimental results will provide enough information for a more precise value to be determined.

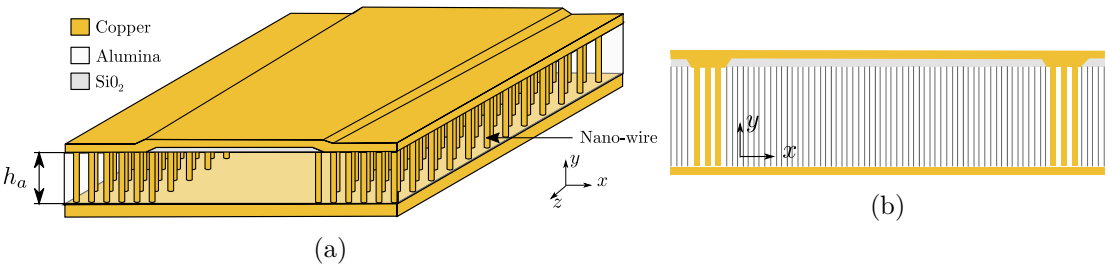

Figure 5.11 – MnM interposer technology: (a) Simplified 3D view, (b) Detailed cross-sectional view.

As one can notice, once again a silicon dioxide layer ($\varepsilon_r = 3.9$, 1 µm) is inserted between the top cover of the waveguide and the alumina membrane. The resulting waveguide will therefore be a two dielectric structure. The fabrication process is made of the following steps [20], it was realised by our partners at Sao Paulo University.

- Cleansing with trichloroethylene, then acetone and at last in isopropyl alcohol.
- Back-side magnetron sputtering of a thin titanium layer and copper.
- Front-side mask deposition (SiO_2, 1 µm) by reactive magnetron sputtering.
- Front-side lithography and buffered oxide etching of the oxide to expose the membrane for selective nano-wires growth.
- Back-side copper thickening by electro-deposition in a cupric sulphate solution.

- Nano-wires growth in the same solution, until copper appears on front-side.
- Front-side mechanical polishing.
- Reactive magnetron sputtering deposition of silicon dioxide.
- Patterning and etching of the silicon dioxide, revealing the nano-wires.
- Front-side deposition thin titanium and copper.
- Thickening of the last copper layer (3 µm), patterning and etching.

The nano-wire density is such that a plane wave propagating in alumina at 300 GHz would "see" more than 2500 nano-wires per wavelength. For this reason the nano-wires were not modelled one by one in the computation, but rather they were considered as equivalent to a conductive copper plane. A specific value for the effective conductivity of these lateral walls could be extracted in the future developments from the measurement results.

Once again the design procedure will be further developed in 5.5, the following results are related to the waveguide dedicated to the W frequency band, i.e. from 75 GHz to 110 GHz. By the same approximation as previously its width was calculated to match the mono-mode frequency band considering a TE_{10} mode, leading to $W = 880\,\mu m$. The dispersion diagram for the six first propagating modes is illustrated in Figure 5.12.

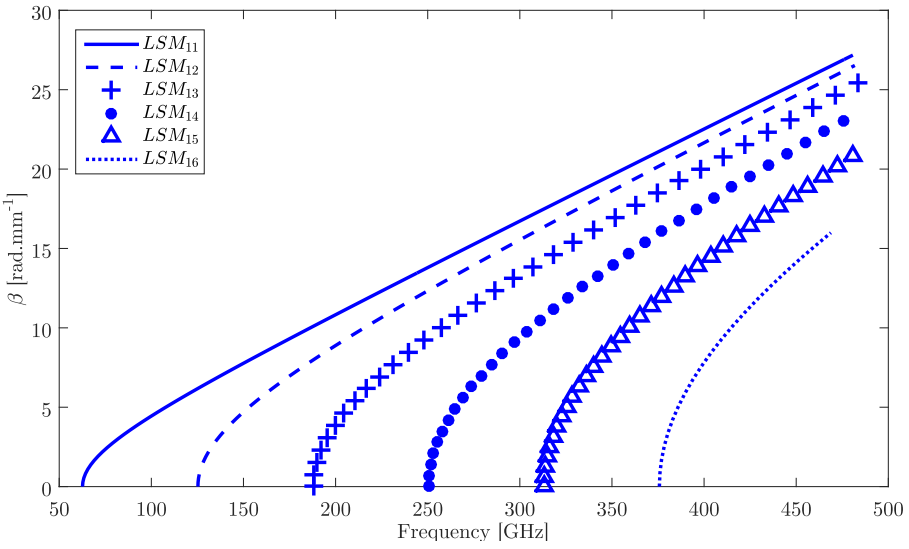

Figure 5.12 – Dispersion diagram for MnM interposer integrated waveguide in W band.

All these modes LSM_{nm} do not have any magnetic component on y-axis by definition, therefore there is no induced current on the lateral walls in the z-axis (see (2.18)). For this reason, the propagation should not be forbidden by the presence of vertical nano-wire, the same way through-via holes forbid TM propagation in SIW as already mentioned [16].

The fields are illustrated for the first propagating mode in the middle of the mono-mode frequency band in Figure 5.13. Once again the continuity of D_y at the interface concentrates the electrical field in the lower permittivity layer. Also, the magnetic field is very similar to that of a TE_{10}, therefore the induced currents will be equally distributed between the top and bottom metallic layers.

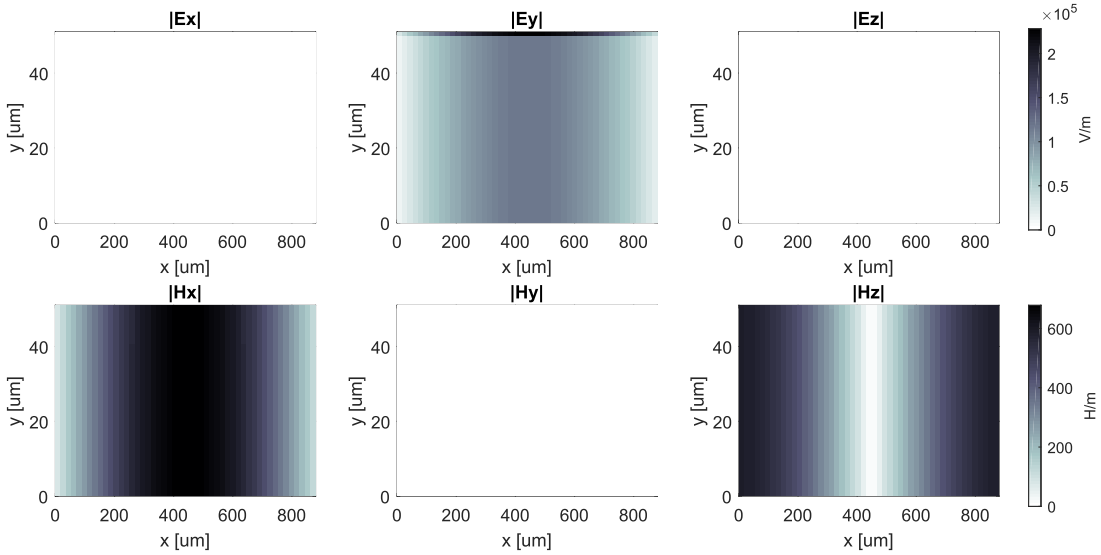

Figure 5.13 – Field amplitudes for MnM technology obtained at 95 GHz.

Finally, a comparison is realized between the algorithm and HFSS, the results are given in Figure 5.14. Once again, the main contribution to the losses is conductive, as the waveguide is in this lower band very large and thin. Also, a good correspondence was obtained between all methods, confirming the validity of the implemented resolution.

5.4 Design of test features on IHP interposer

The IHP interposer was aimed at addressing the upper mm-wave frequency bands (see Table 5.2), that is from D band (110-170 GHz) up to the WR2 band (325-500 GHz). The even higher bands like WR1.5 from 500 GHz to 750 GHz might be addressed later, but already the measurement setup at IHP already provides such possibilities. Also, our laboratory was then able to perform four ports measurement until 140 GHz, therefore another lower band from 90 to 150 GHz was also used for directional coupler design.

5.4.1 Broadband transitions from G-CPW to integrated waveguide

The second step is to design broadband excitation structures so that maximum power can be transmitted in all bands of interest. These excitation structures are then placed in back-to-back configuration to facilitate a two-port measurement, as illustrated in

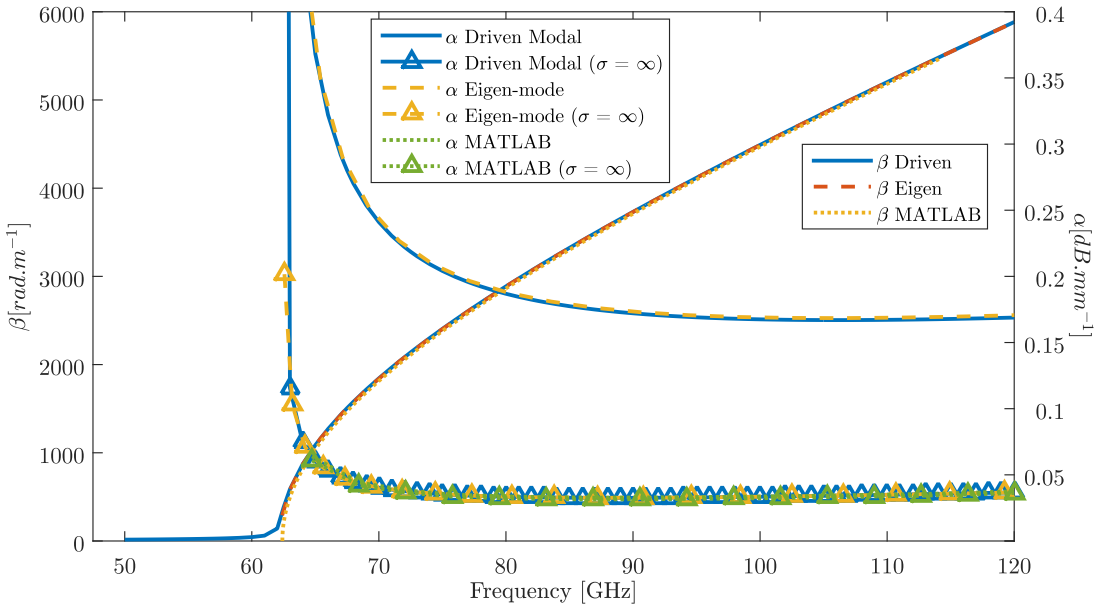

Figure 5.14 – Implemented algorithm versus commercial software for the evaluation of propagation constant in MnM technology.

Freq. Band [GHz]	Name	Cut-off freq. [GHz]	Width W [µm]
90-150		75	580
110-170	WR6	90	480
220-325	WR3	174	250
325-500	WR2	290	150

Table 5.2 – Targeted frequency bands for IHP Interposer fabrication.

Figure 5.15. They are matched to transmission lines which makes the connection to the probe pads.

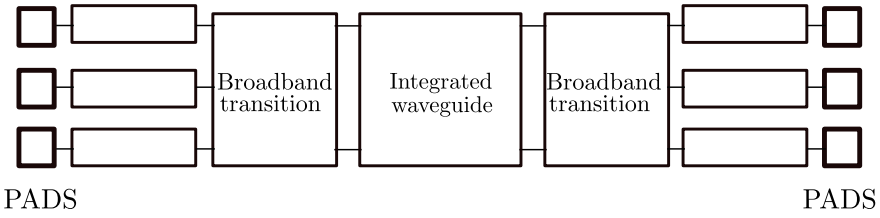

Figure 5.15 – Schematic view of the adopted back-to-back configuration for integrated waveguides measurement.

A similar approach as for the printed-circuit-board technology circuits in Chapter 3 was adopted. In particular, a tapered transition from G-CPW to the waveguide is used.

However, for better results in all frequency bands a slightly more complex geometry was adopted (see Figure 5.16). The slots on the top of the waveguide behave as magnetic dipoles with a vanishing electric field at the end, thus matching the field distribution of the first waveguide mode. Yet, when first introduced by [16], a matching impedance transformer was required to reach the 50 Ω impedance. An improved compactness was achieved by merging the excitation slot with a tapered quarter-wavelength impedance transformer [22]-[23]. This last topology demonstrated especially good performance for thin and high-dielectric substrates because of reduced radiation loss, it was therefore chosen for the test features.

Two angles θ_t and θ_t^i are introduced as well as the taper length l_t. Also, the distance p between the end of the transition and the first TSV is defined. The physical dimensions of the G-CPW are also given: d, W_s and W_{cpw}. The IHP technology is especially interesting because of its flexibility. Indeed, the vertical trenches can be arranged close to the slot because the vertical spacing between them can be very small (5 µm). This topology is of high interest for the proper operation of the transition as mentioned in [23].

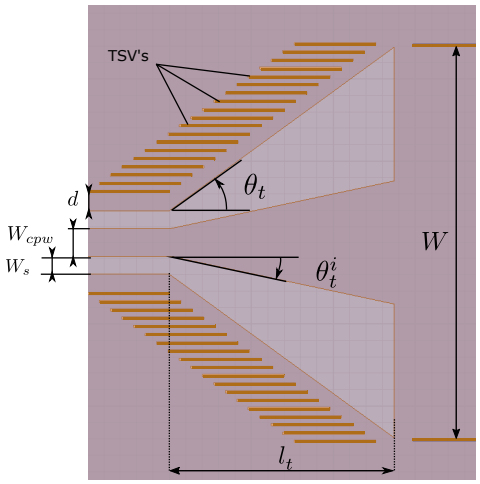

Figure 5.16 – Schematic view of the broadband transition for IHP interposer.

For the starting point l_t should be equal to a quarter-wavelength at the center frequency of the targeted band. This length has to be calculated considering the phase constant of the G-CPW. It was observed that the outer angle θ_t needs to be large, typically around 35 degrees. Also, the typical value for θ_t^i is about 10 degrees. The optimized dimensions of the transitions are given in Table 5.3 for each frequency band along with G-CPW parameters.

As an example, the layout of the transition for the WR6 band is illustrated in Figure 5.17(a), the waveguide being on the right side of the picture.

Concerning the G-CPW dimensions, a 50 Ω characteristic impedance was first obtained and used for the two intermediate bands. Then for the coupler design in the lower band, the spacing d between the TSV's and the ground edge was reduced to keep symmetric transmission lines connected to the 50 µm-pitch GSGSG pads (see

Freq. band [GHz]	Transition			G-CPW		
	l_t [µm]	θ_t [deg]	θ_t^i [deg.]	W_{cpw}[µm]	W_s[µm]	d [µm]
80-150	340	36	12	35	22	9
110-170	280	36	12	35	22	23.5
220-325	140	36	36	35	22	23.5
325-500	97	38	40	32	22	11

Table 5.3 – Optimized dimensions of G-CPW to SIW transition for IHP interposer.

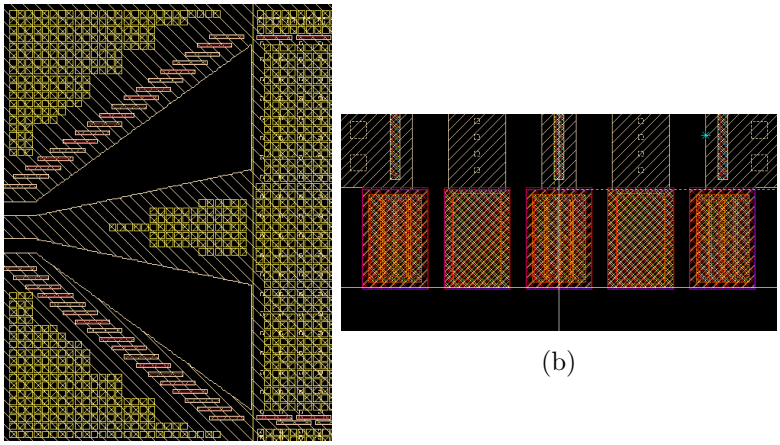

(a) (b)

Figure 5.17 – (a) Layout of the G-CPW to SIW broadband transition for WR6 frequency band and (b) of the GSGSG pads for the coupler at 110 GHz.

Figure 5.17). Finally, this same spacing d was reduced in the highest frequency band to avoid the propagation of the first higher order mode below 500 GHz. Furthermore, signal strip width W_{cpw} was set to 32 µm to correct a slight decrease of the characteristic impedance value.

The extraction of the propagation constant will be performed through a de-embedding algorithm [24] requiring sets of S-parameters for different lengths of waveguides. Ideally, the extraction should be done using two different waveguides whose electrical length differ by 90 degrees at the center frequency [25]. This criteria is applied to avoid the resonances and singularities in the calculation, however for losses estimation a longer phase difference should be necessary to raise the power loss level way above the measurement uncertainty. For these reasons five different lengths were implemented following the rule given by (5.33), where L_0 stands for the waveguide length of the shorter feature ("Thru") and ΔL is close to a quarter of guided wavelength at each band center frequency.

$$L_i = L_0 + i\Delta L \qquad , 0 \leq i \leq 4 \tag{5.33}$$

Therefore, the attenuation constant can be estimated with a better accuracy by comparison of the longest waveguide with the shortest. The dimensions for all bands

are given in Table 5.4 along with the electrical length equivalent to ΔL for each frequency band lower and upper limit.

Freq. band [GHz]	L_0	$\lambda/4$ [µm]	ΔL [µm]	Angular sweep [deg.]
110-170	504	205	224	57-133
220-325	228	105	112	62-127
325-500	224	79	81	49-137

Table 5.4 – Fabricated waveguides parameters for IHP interposer.

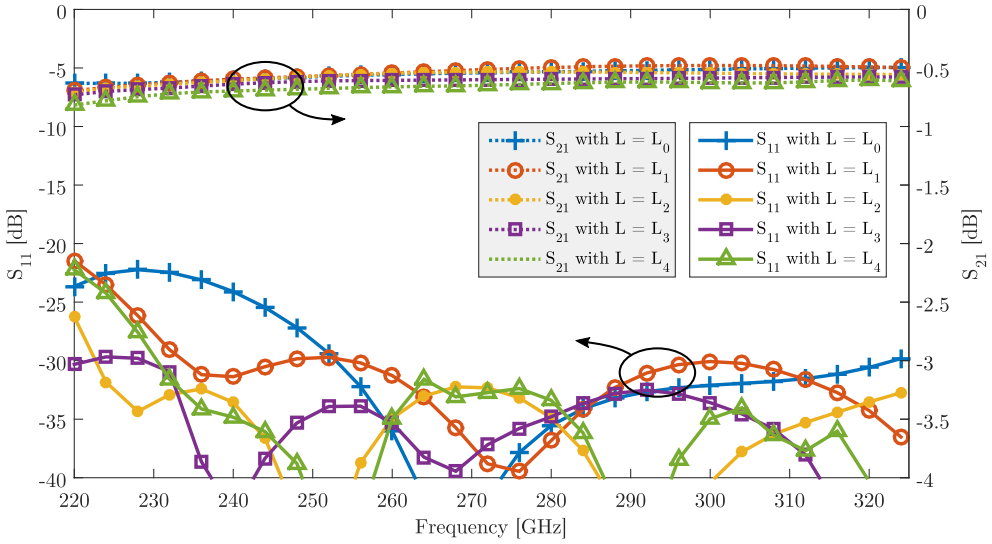

Figure 5.18 – Simulated S-Parameters of the different waveguides with transitions and G-CPW access lines fabricated for the WR-3 frequency band.

For each frequency band, the length of the shortest element was fixed to a certain value above which a low return loss could be achieved. Finally, the extra-length ΔL is not exactly a quarter of wavelength because of layout restrictions related to the length and spacing of the TSV's. Also, this strategy concerns only the waveguide bands WR6, WR3 and WR2, i.e. from 110 GHz to 500 GHz. Only couplers were designed for the lower bandwidth. The optimization of the transitions was performed through full-wave analysis with the commercial software HFSS [26]. As an example the results obtained for the different features in the WR-3 band are illustrated in Figure 5.18.

5.4.2 0-dB and 3-dB Couplers

Finally, as already mentioned a coupler and a crossover were designed in the same technology at 110 GHz, the design procedure followed that of [27]. The simulated S-Parameters of the optimized coupler and crossover are illustrated in Figure 5.19 and Figure 5.20, respectively. These simulation results do not take the influence of the transition from G-CPW to the waveguide into account, a calibration kit will also be

implemented on the interposer to remove their influence. In these simulations the worst case was considered for the bulk silicon conductivity, that is 2 kΩ.cm. The main contribution to the insertion loss is related to the induced currents on the waveguide walls. In reality, insertion loss will probably be higher because of the extrusion in top and bottom layers needed to satisfy density rules.

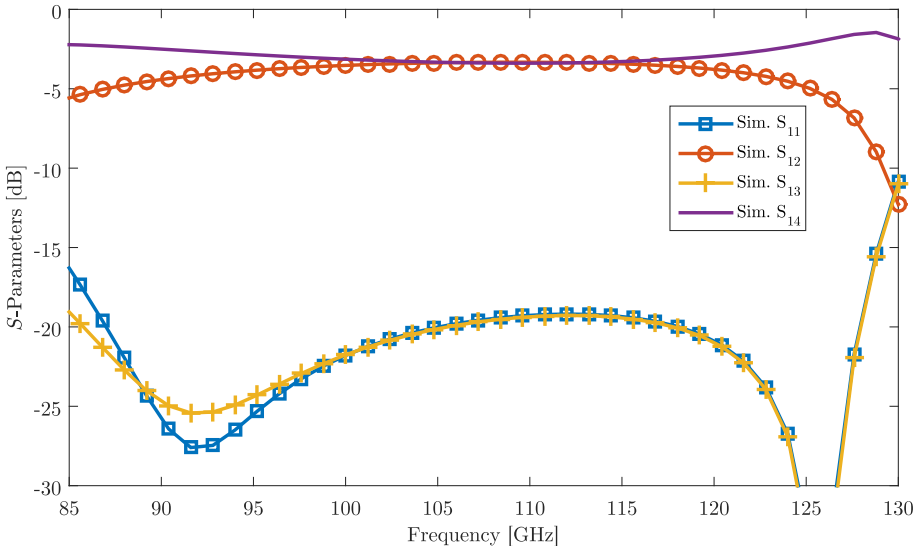

Figure 5.19 – Simulated S-Parameters of the coupler operating at 110 GHz.

The simulated coupler insertion loss at the operating frequency are 3.5 dB. Also, less than 1 dB amplitude imbalance is maintained in a bandwidth of 25 GHz, from 95 to 120 GHz. Within the same interval, return loss remains below 19 dB. The coupling region in itself occupies an area of 1.25 by 0.87 mm^2, which is about 25% of the overall coupler layout considering feeding waveguides, transitions and pads. In fact, all of this additional surface could be drastically reduced in the context of a specific application but are required in the standalone configuration and broadband characterization.

The crossover simulation was realized in the same context, insertion loss is 0.4 dB at 110 GHz and remains below 1.4 dB in a 30 GHz frequency band, between 96 and 126 GHz. On the other hand, all other S-Parameters amplitude are lower than −17 dB between 104 GHz and 126 GHz. The center region size is 1.25 by 1.62 mm^2, which represents 40% of the overall layout.

Top level layouts for all fabricated structures along with overall dimensions are illustrated in Figure 5.21 and Figure 5.22, respectively. The first layout contains all waveguides in back-to-back configuration for the characterization as well as some pads and G-CPW calibration structures. The second one is related to the four port devices in the lower frequency band.

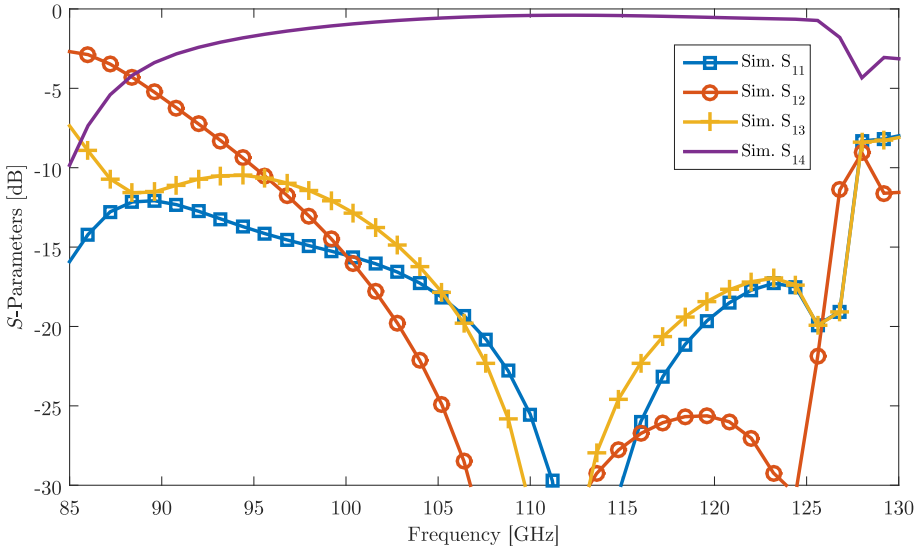

Figure 5.20 – Simulated S-Parameters of the crossover operating at 110 GHz.

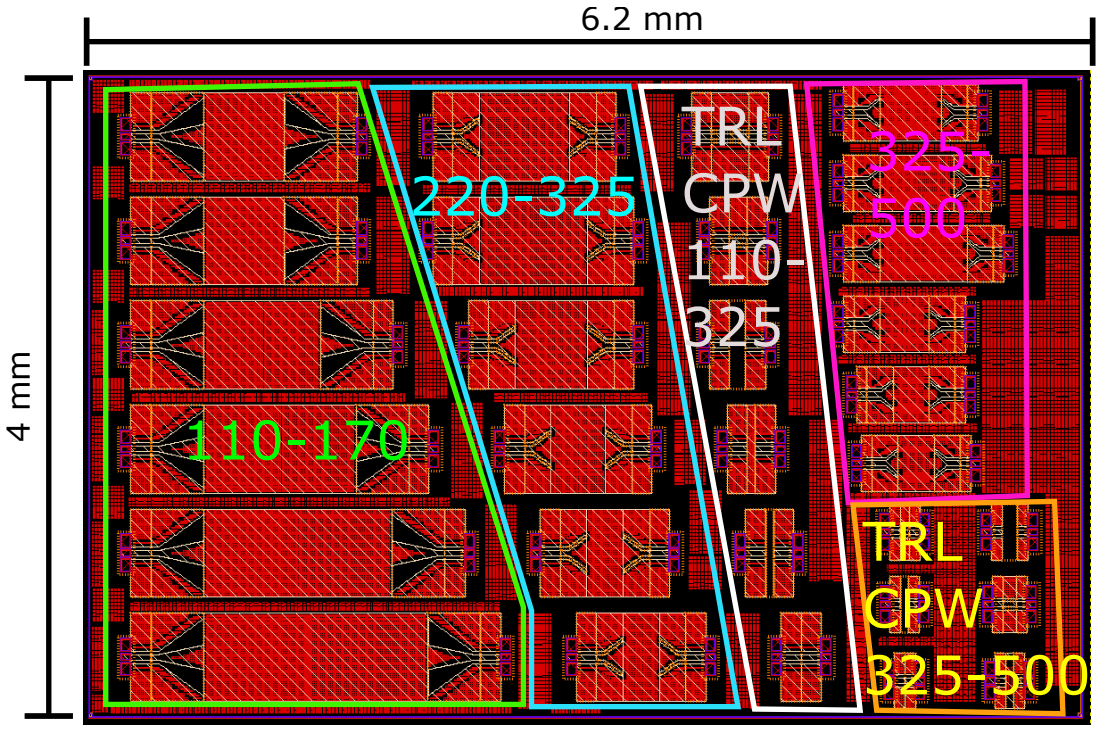

Figure 5.21 – Layout of the waveguides in back-to-back configuration and calibration kits in IHP technology.

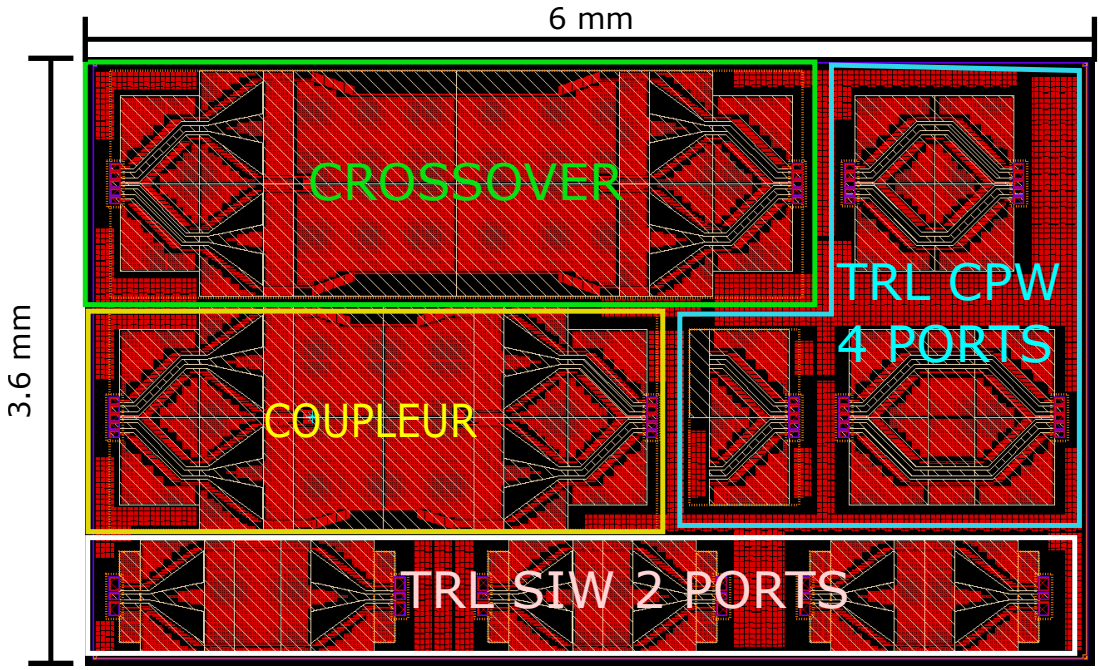

Figure 5.22 – Layout of the coupler, crossover and at 110 GHz along with calibration kits in IHP technology.

5.5 Design of test features on the Nano-porous Alumina Membrane interposer as an alternative to the TSV process

We will now consider the realization of test circuits for the MnM technology. A similar procedure was followed for the extraction of the propagation constant, with broadband transitions from G-CPW to integrated waveguide of different lengths. There is no fundamental difference from the electromagnetic point of view between these two technologies if one considers the nano-wires as equivalent walls. In fact, this second technology is more flexible in one sense because during the fabrication the nano-wires selective growth is only defined by a mask as it would be done for a lithography of any metallic layer. From the layout point of view, the nano-wires are assimilated to a simple metallic layer with very simple design rules.

The targeted frequency bands are given in Table 5.5, most of them are at lower frequencies than that used for IHP realization. This is mainly due to the measurement setup that is available at IMEP-LaHC laboratory. Also, the fabrication process in IHP relies on well established methods and even potentially commercial applications, as this process is still in the development step. Thus, the mask definition and alignment precision are not as accurate as in IHP. For these reasons, the lower frequency bands were chosen in order to reduce the sensitivity to process variations. All of the following results are related to a 50 µm-thick alumina membrane, a similar work was done for a a thickness of 100 µm but are not described here. Basically, a thicker waveguide would

have better performance in terms of losses, however the fabrication process is not yet fully controlled so it was disregarded in this manuscript. Future realizations with this thicker substrate will be done as soon as the process is mature enough.

Freq. Band [GHz]	Name	Cut-off freq. [GHz]	Width W [µm]
50-75	V	41	1330
75-110	W	62	880
90-140	F	75	725
110-170	D	90	600

Table 5.5 – Targeted frequency bands for MnM Interposer fabrication.

5.5.1 Broadband transition from G-CPW to integrate waveguide

Once again, a G-CPW transmission line was adopted and the broadband transition was also designed as for IHP technology. A schematic view of the transition with the geometrical parameters is illustrated in Figure 5.23. As shown on the right, the top copper covers all the nano-wires, they are visible on the left top view only for clarity.

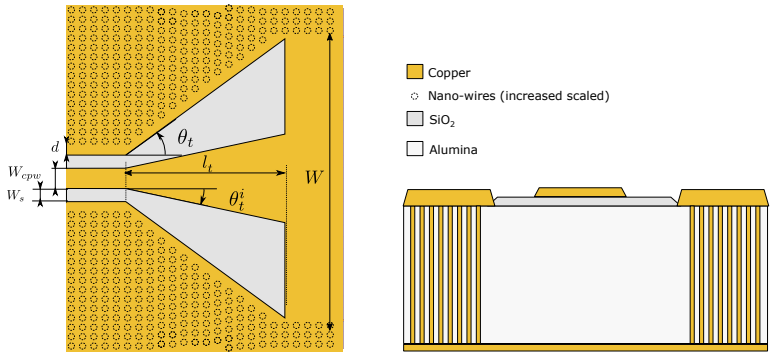

Figure 5.23 – Schematic view of the broadband transition for MnM interposer.

The G-CPW 50 Ω transmission line was defined by $W_{cpw} = 45\,\mu m$, $W_s = 30\,\mu m$ and $d = 30\,\mu m$ for all frequency bands. The optimized dimensions given in Table 5.6 for the transitions were obtained by full-wave simulations, the starting point being $l_t = \lambda_{cpw}/4$.

Freq. Band [GHz]	l_t [µm]	θ_t [deg]	θ_t^i [deg.]
50-75	660	37	13
75-110	570	37	11
90-140	360	37	11.5
110-170	290	36	12

Table 5.6 – Optimized dimensions of G-CPW to SIW transition for MnM interposer.

Also, the same multi-length strategy was adopted for the characterization of the membrane. The different parameters defining the lengths of waveguides as given by relation (5.33) are listed in Table 5.7.

Freq. band [GHz]	L_0	ΔL [µm]	Angular sweep [deg.]
50-75	1190	590	56-122
75-110	810	400	56-120
90-140	695	340	56-133
110-170	530	260	61-138

Table 5.7 – Fabricated waveguides parameters for MnM interposer.

As an example of optimized transition, simulated S-Parameters of the 75-110 GHz W frequency band are illustrated in Figure 5.24.

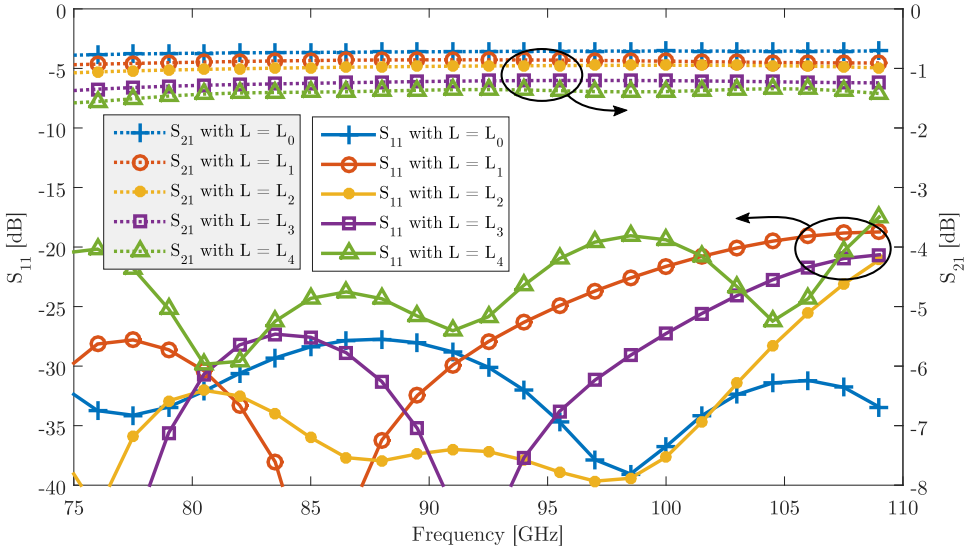

Figure 5.24 – Simulated S-Parameters of the different waveguides with transitions and G-CPW access lines fabricated in MnM technolgy for the W frequency band.

5.5.2 Other passive circuits

In addition, as more space was available in MnM technology some extra passive circuits were designed, namely cavity coupled filters, couplers and adjacent waveguides with different wall thickness to analyse the isolation. For illustration, the simulated S-Parameters of a fifth-order bandpass filter centered at 115 GHz are illustrated on 5.25. The design of this filter was based on the synthesis method developed in the previous chapter.

All these circuits along with the waveguides in back-to-back configuration were drawn in ADS to produce the fabrication masks for two circular wafers of 2.5 cm

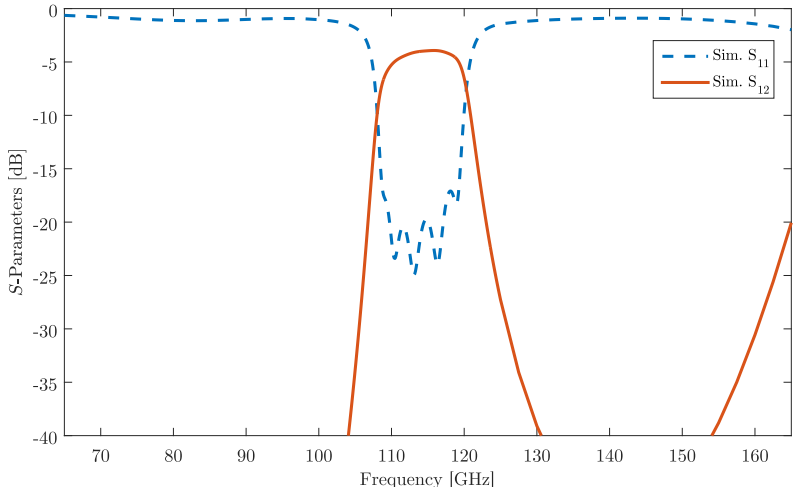

Figure 5.25 – Simulated S-Parameters of the W-band cavity filter in MnM technology.

diameter (see Figure 5.26).

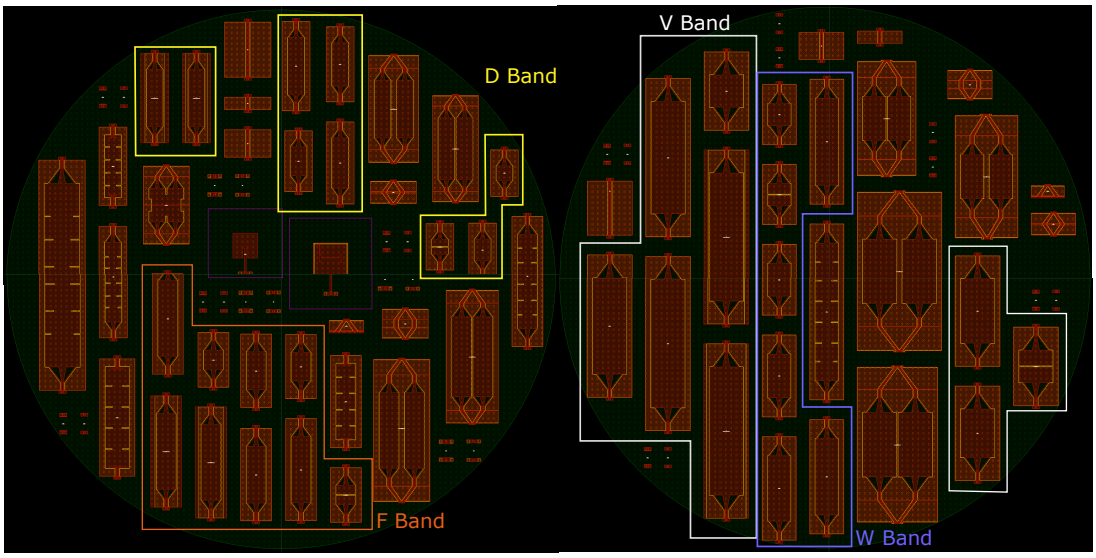

Figure 5.26 – Layout of the all test features on the MnM technology.

5.5.3 Measurement results

After several modifications of the fabrication process the membranes were finally measured. Two photographs of the membrane during the fabrication (after the nano-wire growth) are shown in Figure 5.27. One can notice that the density of nano-wires is such that from a macroscopic view it has the same appearance as a copper layer deposition. Millimeter-wave probes were used along with an Anritsu ME708-C Vector Network Analyser (VNA) and mm-wave extension Anritsu 3742A.

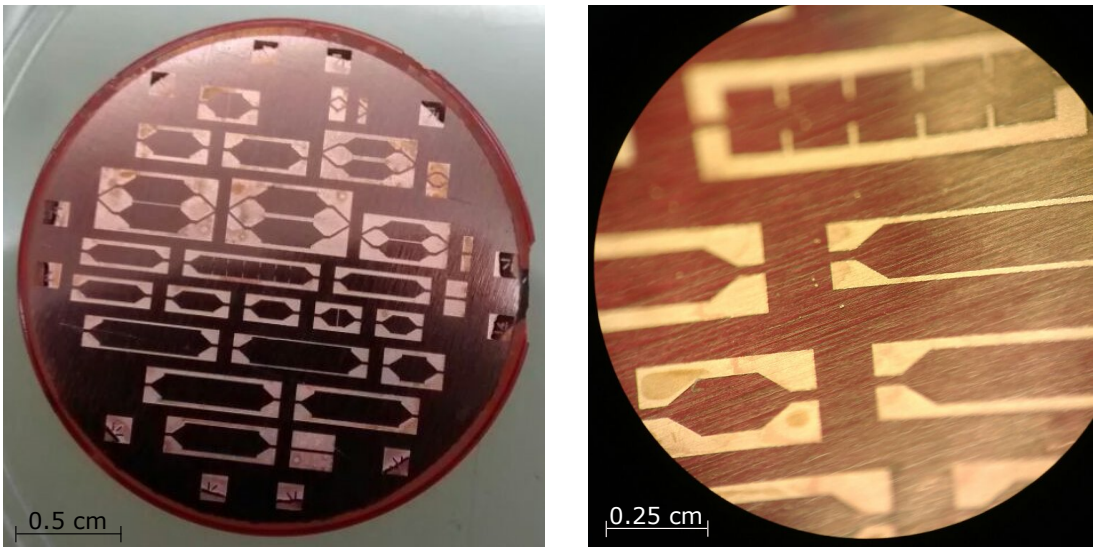

Figure 5.27 – Photographs of the membranes after nano-wire growth.

Unfortunately, a contamination issue during the fabrication caused most of the devices to be completely out of their expected operation. This contamination of the alumina by conductive compound was first observed using the probes directly on the membrane to check its dielectric properties. Surprisingly an inductive behaviour was measured, which leads to the conclusion of non negligible conduction. After investigation in Sao Paulo the reasons for this contamination was found, the process is currently being updated to avoid this to happen again.

Because of these issues, only three of the 20 fabricated wafers provided exploitable results, they are listed in Table 5.8. A measurement is said to be exploitable if it shows reasonable insertion losses compared to the simulation and a sufficient symmetry.

In the lower frequency band V, the wafer S2_2 provided most of the results. Several waveguides with different lengths were measured, as well as two transmission lines and pad open/short. Three different wall thickness's were measured for the longer length of waveguide. Regarding transmission lines, the longer one has an extra 84 degree phase shift compared to the Thru at 62.5 GHz.

Concerning the W frequency band, once again the S2_2 wafer seems to have suffered from less fabrication issues. All waveguides exhibited exploitable results. The phase shift between the two G-CPW lines is 125 degrees at the center frequency of 92.5 GHz. Finally, few measurements were obtained in the higher frequency bands, the shortest waveguide in the F band gave exploitable results on the wafers S1_1 and S1_4. Also, two lines having with a phase difference of 210 degrees at 115 GHz were measured.

From this table, it is obvious that the 2 samples S2_2 and S2_3 have suffered from less fabrication issues. They provide enough data to characterize the guided wave properties in V and W bands.

The analysis was performed for all exploitable results. Yet, only the one con-

Freq. Band [GHz]	Wafer	SIW	G-CPW	Pads
V: 50-75	S2_1	-	Line	Open/Short
	S2_2	L_0 L_1 L_2 L_5 (thin, medium, and thick walls)	Thru (480 µm) Line (1000 µm, +84 deg)	Open/Short
	S2_3	-	Line	Open/Short
W: 75-110	S2_2	L_0 L_1 L_2 L_4 L_5	Thru (480 µm) Line (1000 µm, +125 deg)	Open/Short
	S2_3	L_0 L_3 L_4	Line (1000 µm, +125 deg)	Open/Short
F: 90-140	S1_4	L_0	Thru (455 µm) Line (1000 µm, +210 deg)	-
	S1_1	L_0	-	-
D: 110-170	-	-	-	-

Table 5.8 – List of exploitable measurement results for the first fabrication of SIW in MnM technology.

cerning the W band will be presented here because of the high losses related to the contamination of the alumina. Already, these measurements validates the possibility of manufacturing integrated waveguides, however these results are preliminary and will be completed with the next realization results. The measured S-Parameters amplitude obtained on the S2_2 wafer are illustrated in Figure 5.28 for all available lengths.

First this set of measurement shows that the high-pass behaviour expected from the waveguide is properly obtained. For frequencies below approximately 60 GHz a very smalll quantity of power is transferred from one port to the other. Also, return losses are below −14 dB for all waveguides, taking into account the pads, feeding transmission lines and broadband transitions. This point demonstrates the capability of the transition to match the waveguide impedance to the 50 Ω characteristic impedance of the access. Finally insertion losses are higher for longer waveguides as expected.

A two line algorithm given by [24] was used to extract attenuation and phase constant. The results are presented in Figure 5.29 for several combinations of waveguides, where ΔL is the difference between their lengths. The shortest waveguide is chosen as

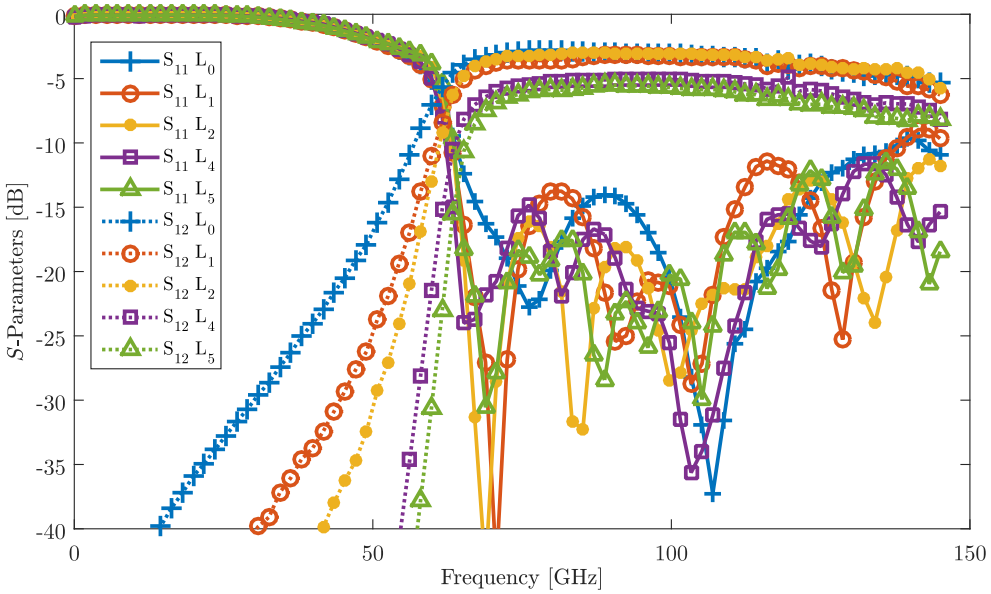

Figure 5.28 – Measured S-Parameters of the different waveguides with transitions and G-CPW access lines fabricated in MnM technology for the W frequency band.

reference ("thru"), all other are compared to this one. The algorithm is a de-embedding procedure which removes all pads parasitics, access lines and transitions. The accuracy of this procedure depends a lot on the symmetry of the measured elements, this property is not always respected, especially at the probe tip. Furthermore, the devices are occupying large area on the wafer so fluctuations in the material properties, thickness's and growth quality can also have influenced the results.

First of all, the cut-off frequencies are relatively close one to each other, however the extracted values of β present non-negligible variations, especially around the cut-off frequency. Higher in frequency the slopes are also close but small shifts at f_c produce strong variation in the absolute value at a given frequency. An interesting point is that the two comparison with the greater length difference exhibit close values. One explanation for that is the way β is calculated as the overall phase shift produced by ΔL divided by this same value, so small variations of phases are smoothed for longer samples.

Concerning the attenuation is was also observed that the longer waveguides give relatively similar values. As already mentioned the extracted attenuation is much more reliable with long waveguides. That is because the overall power loss rises far above the uncertainty of the measurement, also the extracted attenuation is somehow an estimated average per unit length so that the greater the length the greater the accuracy. However for $\Delta L = 400\,\mu\text{m}$ a good matching with the theory is obtained. This could either indicate that no major fabrication issue affected this specific sample, or that the uncertainty led to this correspondence by chance. For the intermediate sample with $\Delta L = 800\,\mu\text{m}$ the attenuation lies in between the other curves with a strong frequency dependence which tends to consider this result as not very reliable.

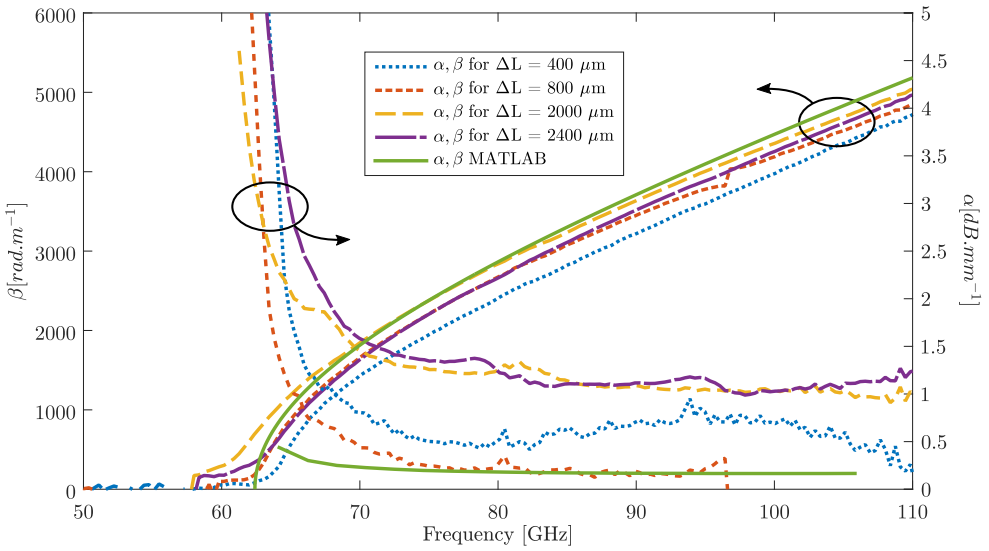

Figure 5.29 – Extracted propagation constant in MnM technology for the W frequency band.

We suppose that at least two fabrication issues affected significantly the performance of the waveguides. One of them is the contamination of the alumina by a conductive compound which increased its conductivity and thus its equivalent loss tangent. The second one is oxidation of the nano-wires at the interface with the top metal layer. This would also have significant impact on the attenuation and propagation characteristic. That being said, the equivalent conductivity of the lateral walls could be lower than that of bulk copper as assumed in simulation, resulting in higher attenuation.

Let's first consider an equivalent conductivity for the lateral walls. In the worst case configuration, this conductivity is the lowest if alumina is not conductive, which might not be the case in reality. As the currents on the lateral walls run along the nano-wires, an equivalent conductivity σ_{eq} based on geometrical considerations is introduced taking into account the filling factor of the membrane given by (5.34), where r_n is the nano-wire radius and s is the spacing between them.

$$\sigma_n = \sigma_{Cu} \frac{\pi r_n^2}{s^2} \tag{5.34}$$

These considerations lead to an approximate reduction of the lateral walls conductivity by a factor of 10. By implementing this new value in the simulation configuration, the attenuation is only increased of 6% at 90 GHz.In fact, induced currents are higher on the edges of the waveguide but they do not contribute significantly to the overall conductive losses because of the short integration path compared to the horizontal copper planes (see (2.19)).

Then, the alumina conductivity was increased to model an hypothetical contamination. For this case the losses might be relatively high so the fields are computed in

MATLAB taking into account the complex permittivity from (5.35).

$$\bar{\varepsilon} = \varepsilon_0 \varepsilon_r (1 - j \tan \delta) \tag{5.35}$$

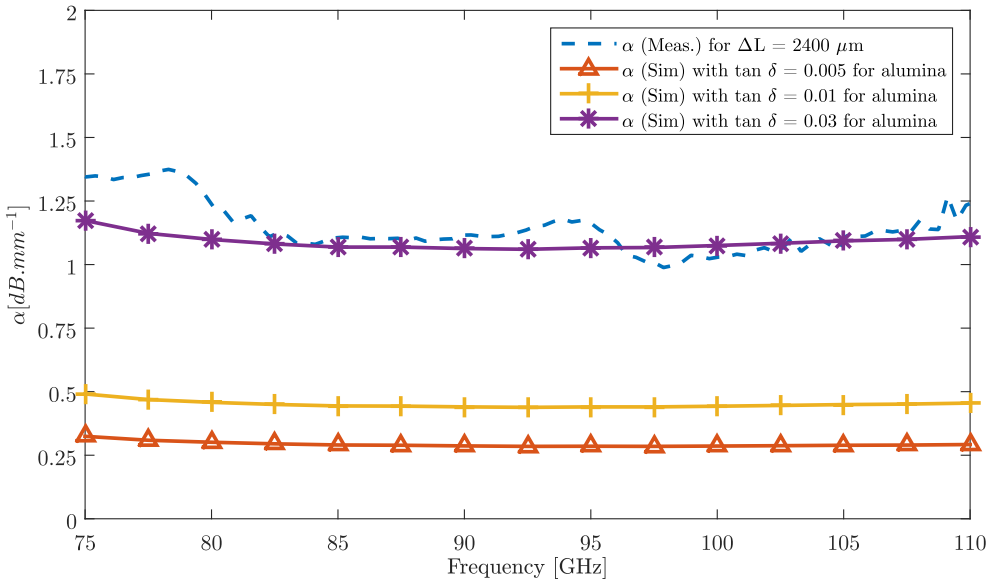

Figure 5.30 – Extracted and simulated attenuation constant in MnM technology for the W frequency band with increased dielectric dissipation.

In order to match the measurement, several values of $tan\delta$ were tested from 0.005 to 0.03, the corresponding attenuations are also illustrated in Figure 5.30. As expected, simulation is able to match the measurement for very large values of $tan\delta$, in this case $tan\delta = 0.03$ is required.

Several issues were detected in the fabricated samples, mainly because the process is developed at the same time as the design of test features. These issues are being corrected, and new measurements will be performed in the coming months.

5.6 Prospects and conclusion

In this chapter, two different technologies were proposed for the realization of integrated waveguides at very high frequencies, namely from 60 GHz up to the sub-THz bands. As mentioned in the introduction, this work intends to constitute a base on which a miniaturization effort will be deployed. Indeed, the development of these two technologies require a step-by-step procedure in which fabrication processes are stabilized and improved. Meanwhile, a theoretical analysis was carried out to provide a better understanding of the propagation characteristics and field distribution in these multilayer configurations.

The first measurement of the alumina based waveguides provided some interesting results, which confirmed the existence of guided modes, but also exhibited very high attenuation. Several fabrication issues, such as alumina contamination by metallic compounds, could explain these results. After investigation these process malfunctions are currently being solved.

The IHP technology based on tungsten trenches is being fabricated now, and future measurement will provide us the first data.

Beyond the integration, miniaturization of these waveguides will be investigated in future works. Also, more complex structures will probably be designed in the near future on both technologies, such as antennas and feeding networks.

References

[1] M. Yi, S. Li, H. Yu, W. Khan, C. Ulusoy, A. Vera-Lopez, J. Papapolymerou, and M. Swaminathan, "Surface roughness modelling of substrate integrated waveguide in d-band," *IEEE Transactions on Microwave Theory and Techniques*, vol. 64, no. 4, pp. 1209–1216, Apr. 2016.

[2] G. Gentile, R. Dekker, P. de Graaf, M. Spirito, L. C. N. de Vreede, and B. Rejaei, "Millimeter-wave integrated waveguides on silicon," in *IEEE 11th Topical Meeting on Silicon Monolithic Integrated Circuits in RF Systems*, Glendale, AZ, Jan. 2011, pp. 37–40.

[3] G. Gentile, V. Jovanovic, M. J. Pelk, L. Jiang, R. Dekker, P. de Graaf, B. Rejaei, L. C. N. de Vreede, L. K. Nanver, and M. Spirito, "Silicon-filled rectangular waveguides and frequency scanning antennas for mm-wave integrated systems," *IEEE Transactions on Antennas and Propagation*, vol. 61, no. 12, pp. 5893–5901, Dec. 2013.

[4] Y. Tian, H. Wang, K. Lee, and K. Ang, "On-chip air-gapped cavity resonators and filters for mm-wave ic applications," *IEEE Transactions on Components, Packaging and Manufacturing Technology*, vol. 6, no. 10, pp. 1549–1554, Oct. 2016.

[5] Y. Wu, S. Gamble, B. M. Armstrong, V. F. Fusco, and J. A. C. Stewart, "Sio2 interface layer effects on microwave loss of high-resistivity cpw line," *IEEE Microwave and Guided Wave Letters*, vol. 9, no. 1, pp. 10–12, Jan. 1999.

[6] T. R. LaRocca, A. C. Reyes, and S. M. El-Ghazaly, "Analysis of electromagnetic wave propagation on coplanar waveguides on doped semiconductor substrates," in *IEEE MTT-S International Microwave Symposium Digest*, vol. 1, San Francisco, CA, June 1996, pp. 295–298.

[7] L. G. Chambers, "Propagation in waveguides filled longitudinally with two or more dielectrics," *British Journal of Applied Physics*, vol. 4, no. 2, p. 39, Sep. 1953.

[8] S. Ahmed and P. Daly, "Finite-element methods for inhomogeneous waveguides," *Proc. Institution of Electrical Engineers*, vol. 116, no. 10, pp. 1661–1664, Oct. 1969.

[9] Z. J. Csendes and P. Silvester, "Numerical solution of dielectric loaded waveguides: Ii - modal approximation technique," *IEEE Transactions on Microwave Theory and Techniques*, vol. 19, no. 6, pp. 504–509, June 1971.

[10] R. Collin, *Field Theory of Guided Waves.* IEEE Press, 1991.

[11] T. Itoh, *Numerical Techniques for Microwave and Millimeter-Wave Passive Structures.* Wiley, 1989.

[12] K. Chang, *Encyclopedia of RF and Microwave Engineering.* Wiley, 2005.

[13] J. D. Craggs, "Fields and waves in modern radio," *Physics Bulletin*, vol. 5, no. 51, p. 50, 1954.

[14] D. Pozar, *Microwave Engineering, 4th Edition.* Wiley, 2011.

[15] S. J. Orfanidis, *Electromagnetic Waves and Antennas.* Rutgers University, 2014.

[16] D. Deslandes, "Etude et developpement du guide d'ondes integre au substrat pour la conception de systemes en ondes millimetriques," Ph.D. dissertation, Ecole Polytechnique, Montreal, 2005.

[17] J. Attari, T. Djerafi, and K. Wu, "Fast and accurate simulation of novel millimeter-wave circuits based on commercial software package," *IEEE Microwave Magazine*, vol. 14, no. 2, pp. 106–111, Mar. 2013.

References

[18] J. M. Pinheiro, M. V. Pelegrini, L. Amorese, P. Ferrari, G. P. Rehder, and A. L. C. Serrano, "Nanowire-based through substrate via for millimeter-wave frequencies," in *Proc. IEEE MTT-S International Microwave Symposium (IMS)*, San Francisco, CA, May 2016, pp. 1–4.

[19] A. L. C. Serrano, A. L. Franc, D. P. Assis, F. Podevin, G. P. Rehder, N. Corrao, and P. Ferrari, "Slow-wave microstrip line on nanowire-based alumina membrane," in *Proc. IEEE MTT-S International Microwave Symposium (IMS2014)*, Tampa Bay, FL, June 2014, pp. 1–4.

[20] M. V. Pelegrini, J. M. Pinheiro, L. G. Gomes, G. P. Rehder, A. L. C. Serrano, F. Podevin, and P. Ferrari, "Interposer based on metallic-nanowire-membrane (mnm) for mm-wave applications," in *Proc. 46th European Microwave Conference (EuMC)*, London, United Kingdom, 2016.

[21] R. A. Woode, E. N. Ivanov, M. E. Tobar, and D. G. Blair, "Measurement of dielectric loss tangent of alumina at microwave frequencies and room temperature," *Electronics Letters*, vol. 30, no. 25, pp. 2120–2122, Dec. 1994.

[22] S. Yang, A. Elsherbini, S. Lin, A. E. Fathy, A. Kamel, and H. Elhennawy, "A highly efficient vivaldi antenna array design on thick substrate and fed by siw structure with integrated gcpw feed," in *Proc. IEEE Antennas and Propagation Society International Symposium*, Honolulu, HI, June 2007, pp. 1985–1988.

[23] R. Kazemi, A. E. Fathy, S. Yang, and R. A. Sadeghzadeh, "Development of an ultra wide band gcpw to siw transition," in *IEEE Radio and Wireless Symposium*, Santa Clara, CA, Jan. 2012, pp. 171–174.

[24] P. Souzangar and M. Shahabadi, "Numerical multimode thru-line (tl) calibration technique for substrate integrated waveguide circuits," *Journal of Electromagnetic Waves and Applications*, vol. 23, no. 13, pp. 1785–1793, Sep. 2009.

[25] G. F. Engen and C. A. Hoer, "Thru-reflect-line: An improved technique for calibrating the dual six-port automatic network analyzer," *IEEE Transactions on Microwave Theory and Techniques*, vol. 27, no. 12, pp. 987–993, Dec. 1979.

[26] Ansoft, "ANSYS HFSS, 3D Full-wave Electromagnetic Field Simulation." [Online]. Available: http://www.ansoft.com/products/hf/hfss/

[27] C. J. Chen and T. H. Chu, "Design of a 60-ghz substrate integrated waveguide butler matrix, a systematic approach," *IEEE Transactions on Microwave Theory and Techniques*, vol. 58, no. 7, pp. 1724–1733, July 2010.

Chapter 6

Conclusion

The work presented in this thesis was mainly oriented in two directions. As a conclusion, the different developments concerning these two orientations are recalled and several prospects are proposed.

First, a specific topology of miniaturized substrate integrated waveguide based on a slow wave effect in printed-circuit-board technology was analysed. This topology relies on the insertion of blind via holes inside the waveguide, resulting in a confinement of electric field in the upper part of the waveguide.

Starting from theoretical considerations, an interpretation of its slow-wave properties was introduced. By adopting an ideal framework in a parallel-plate waveguide configuration, an explicit formulation of the slow-wave factor was derived, as well as results concerning field amplitudes, impedance and losses contributions. The underlying requirement of energies separation was highlighted. Then, the impacts of several geometric parameters on the velocity reduction and attenuation were analysed. Most of the modelling aspect was performed at low frequencies to get rid of the dispersion. However, the derived model already provides a good estimation of the phase constant at microwave frequencies where dispersion is still limited.

This work forms a basis for eventual future works which could include the following orientations. In order to complete the definition of the model, a more detailed analysis of the currents distribution could possibly lead to an analytical estimation of metallic attenuation. In combination with all previous results, an estimation of the SW-SIW quality factor based on all geometric parameters would be obtained. In all of that, the dispersion influence could also be analysed in further details. In the long term, the performance of the SW-SIW may be improved by considering dielectric constant and loss tangent variations among the different layers. For instance, the upper layers of the waveguide could be made of a low loss substrates, that may provide a solution to avoid the proportionality relation between dielectric attenuation and velocity reduction. Air-filled based technologies could also be considered in this context. Finally, a study of the power handling capabilities of the SW-SIW may be performed based on the results derived in this thesis.

Then, the first concrete realizations in SW-SIW were presented along with their SIW counterparts. More precisely, the slow-wave concept was applied to the design of 0-dB and 3-dB couplers based on the short-slot topology. Using a homogeneous distribution of blind via holes, an equivalent substrate was used to reduce the optimization procedure time. Measurements showed a miniaturization of more than 65% while maintaining reasonable insertion loss. This miniaturization factor is very close to what was obtained in the state-of-the-art couplers by combining the half-mode topology with the ridge waveguide. An even greater miniaturization could be achieved by using a half-mode slow-wave waveguide. Based on the obtained results, the design of more complex circuits such as feeding networks for antenna arrays could be considered. Local modifications of the slow-wave factor may also be used to create compact phase shifters.

The miniaturization potential of SW-SIW was also demonstrated for filter applications. Based on the existing synthesis methods, a modified approach adapted to SW-SIW filters was defined. In particular, this design method aims at reducing both design time and complexity related to the waveguide periodicity. Several passband

filters were fabricated in X-band. Measurement results showed a good agreement with the simulation after taking into consideration fabrication variations. Once again, a high miniaturization was obtained. Following these first results, the synthesis method could be adapted to more complex coupling schemes than the ladder topology. Also, an analytical research of the optimum blind via holes geometric dimensions and distribution could be performed to minimize insertion loss for a given filter.

Finally, the last chapter was dedicated to the realization of integrated waveguides at very high frequencies, namely from 60 GHz up to sub-THz bands. Before introducing slow-wave effect or more complex topologies, it was decided to begin the evaluation of two different technologies for regular integrated waveguides. Because of process requirements, a multilayer configuration had to be considered. A theoretical analysis was therefore carried out to provide a better understanding of the propagation characteristics and field distribution. Measurements were carried out for the alumina technology, validating the propagation of guided modes. However process issues were also observed and are currently being solved. The measurement of IHP technology circuits is planned in the near future. Depending on the obtained performance, the design of more complex passive functions could be implemented later. During this thesis, two projects were initiated on the development of advanced integrated waveguide technologies. The first one ("Terapacipode") aims at investigating the possibilities offered by a benzocyclobutene (BCB) interposer for sub-THz electronics. The second one ("Tricot") deals with the integration of miniaturized slow-wave waveguides using carbon nano-tubes, in which carbon nano-tubes are grown. Today, many technologies are now competing at millimeter-wave frequencies and above, these works will help evaluating their respective performance.

Publications

Conference papers published during the thesis:

M. Bertrand, Z. Liu, E. Pistono, D. Kaddour and P. Ferrari, "A compact slow-wave substrate integrated waveguide cavity filter," 2015 IEEE MTT-S International Microwave Symposium, Phoenix, AZ, 2015, pp. 1-3.

M. Bertrand, Z. Liu, E. Pistono, D. Kaddour and P. Ferrari, "Filtre compact en technologie SIW à ondes lentes," 19èmes Journées Nationales Micro-Ondes, Bordeaux, France, June, 2015.

M. Bertrand, G. Rehder, A. Serrano, N. Kabbani, E. Pistono, D. Kaddour, V. Puyal and P. Ferrari, "Intégration de guides d´onde rectangulaires dans une membrane nano-poreuse d´alumine pour les applications en bande millimétrique," 20èmes Journées Nationales Micro-Ondes, Saint-malo, France, Mai, 2015.

M. Bertrand, G. Rehder, A. Serrano, N. Kabbani, E. Pistono, D. Kaddour, V. Puyal and P. Ferrari, "Intégration de guides d´onde rectangulaires dans une membrane nano-poreuse d´alumine pour les applications en bande millimétrique," 20èmes Journées Nationales Micro-Ondes, Saint-malo, France, Mai, 2015.

Journal articles under review:

M. Bertrand, E. Pistono, D. Kaddour and P. Ferrari, "A Filter Synthesis Procedure for Slow-Wave Substrate Integrated Waveguide Based on a Distribution of Blind Via Holes", in IEEE Transactions on Microwave Theory and Techniques.

Journal articles under writing:

M. Bertrand, E. Pistono, D. Kaddour and P. Ferrari, "Analytical modelling of slow-wave substrate integrated waveguide and application to the design of couplers".

Abstract : The last decades have seen the evolution of communication networks toward greater complexity and efficiency, being now able to carry significant data rates. This evolution is the result of both scientific and technological breakthroughs. Thanks to the wide bandwidths available at millimeter-wave frequencies, the future generations will be able to supply for the the increasing demand in multimedia services, especially high-definition videos. The design of wireless systems which operate at high frequencies with acceptable efficiency, costs, and minimum size thus constitute a decisive challenge. In this context, this work focuses on the development of passive circuits such as filters, couplers and waveguides which address these issues. We developed a miniaturization technique for printed circuits technology, which in a first step is dedicated to frequencies below 20 GHz. This technique is based on a slow-wave concept, defined as the property of any structure which impose lower velocities to the electromagnetic waves. A theoretical analysis, as well as design methods were established and confirmed by measurements. Secondly, we proposed two distinct technological solutions for the integration of efficient waveguides at millimeter-wave frequencies. This work was achieved in collaboration with two other laboratories. A theoretical study, design of test features and measurements were performed. These results intend to constitute a basis for the future realization of miniaturized slow-wave circuits at millimeter-wave frequency bands.

Résumé : Du fait de nombreuses avancées technologiques et scientifiques, l´ensemble du réseau de télécommunications a évolué vers une complexité croissante intégrant désormais des débits très importants. Grâce aux larges bandes passantes offertes par les bandes de fréquences millimétriques, les prochaines générations visent à permettre l´augmentation du nombre de services multimédias et de partage de contenus en haute définition. Cette évolution pose la problématique de concevoir des systèmes sans-fils capables de fonctionner en haute fréquence avec des rendements et coûts acceptables, ainsi qu´un encombrement minimum. Ce travail se situe dans le cadre du développement de circuits passifs, de types filtres, coupleurs et guides d´ondes qui répondent à ces défis. Nous avons développé une technique de miniaturisation pour des dispositifs en technologie imprimée, dans un premier temps dédiée aux fréquences inférieures à 20 GHz. Celle-ci repose sur la notion d´onde lente, définie comme la capacité d'une structure à ralentir la propagation des ondes la traversant. Une analyse théorique ainsi que des méthodes de conception ont été développées, puis validées par des mesures. Dans un second temps, nous avons proposé deux technologies distinctes permettant l´intégration de guides d´ondes performants en bande millimétrique en collaboration avec deux laboratoires partenaires. Une étude théorique, la conception de motifs de test et les résultats de mesure sont présentés. Ces travaux constituent une base pour la réalisation ultérieure en bande millimétrique de topologies miniaturisées grâce aux ondes lentes.